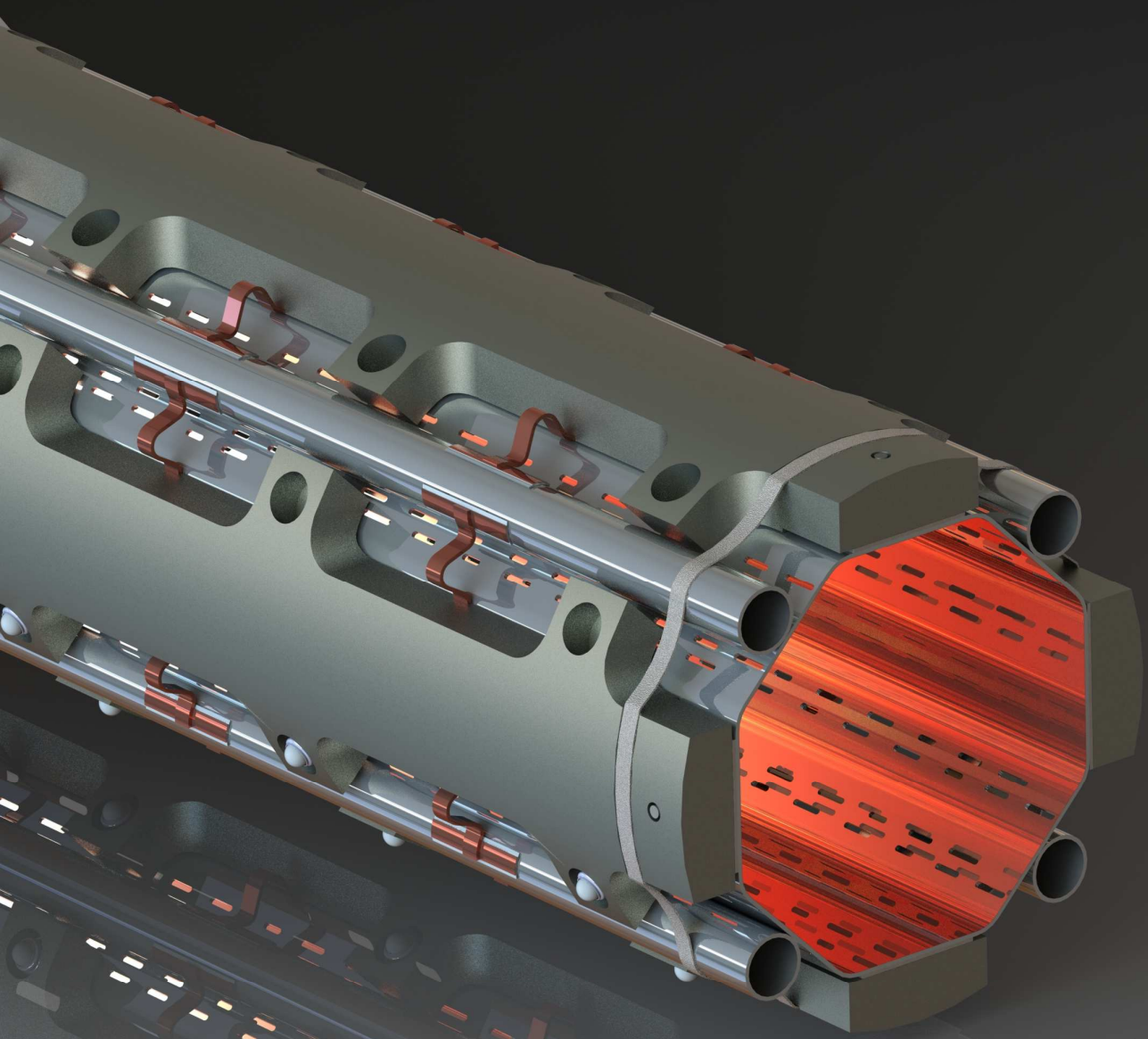
Thermomechanical study of complex structures in the aperture of superconducting magnets:

Application to the design of the High-Luminosity Large Hadron Collider shielded beam screen



Marco Morrone

IMPERIAL COLLEGE LONDON

Thermomechanical study of complex structures in the aperture of superconducting magnets: Application to the design of the High-Luminosity Large Hadron Collider shielded beam screen

by

Marco Morrone

A thesis submitted for the degree of
Doctor of Philosophy

in the
Faculty of Engineering
Department of Mechanical Engineering

January 2018

IMPERIAL COLLEGE LONDON

ABSTRACT

FACULTY OF ENGINEERING
DEPARTMENT OF MECHANICAL ENGINEERING

Doctor of Philosophy

Thermomechanical study of complex structures in the aperture of superconducting magnets: Application to the design of the High-Luminosity LHC shielded beam screen

by Marco Morrone

In the framework of the High-Luminosity Large Hadron Collider (HL-LHC) project, a complex structure, known as the beam screen, will be installed by 2024 in the aperture of the inner triplet superconducting magnets nearby the ATLAS and CMS experiments. The beam screen is an octagonal shaped pipe that shields the 1.9 K magnet cryogenic system from the heat loads and damage to the magnet coils that would be otherwise induced by the highly penetrating collision debris. It also ensures that the vacuum conditions, required for the stability of the beam, are met. This thesis describes the design of the beam screen and proposes extensions to important components and features. The unknown physical properties of the beam screen materials have been characterised. The thermal behaviour of the beam screen during normal working conditions has been optimised by simulations and validated by measurements. The behaviour of the beam screen during a magnet quench, a resistive transition of the superconducting magnet, has been studied. Two magnet quench protection systems have been considered: the Quench Heaters (QH) by themselves and in conjunction with the Coupling Loss Induced Quench (CLIQ) device. To this purpose two innovative coupled multiphysic models have been developed, which have been verified by comparison with a closed form expression showing the advantages of considering self-inductance phenomena. In the case of the QH the force distribution per quadrant gives rise to forces up 330 N/mm in the beam screen closest to the interaction point, while in the case of the CLIQ a torque load-type is induced, whose maximum intensity is around 2 N m/mm. With the new multiphysic models an unprecedented level of accuracy has been achieved, which has permitted to demonstrate the mechanical integrity of the proposed beam screen design during a quench.

Contents

List of Figures ix

List of Tables xvii

Declaration of Originality xix

Copyright Declaration xxi

Acknowledgements xxiii

1 Introduction 1
- 1.1 The Large Hadron Collider . . . 1
- 1.2 The High-Luminosity LHC upgrade . . . 2
- 1.3 The beam screen . . . 3
- 1.4 Definition of the problem . . . 4
- 1.5 Objectives of the work . . . 5
- 1.6 Content of the thesis . . . 5
- 1.7 Key results and relevance of the present work . . . 5
- 1.8 Structure of the thesis . . . 6

2 The beam screen 9
- 2.1 Main functions of the beam screen . . . 9
  - 2.1.1 Cold mass shielding . . . 9
  - 2.1.2 Vacuum stability . . . 10
- 2.2 History of the beam screen . . . 11
  - 2.2.1 Superconducting Super Collider liner . . . 11
  - 2.2.2 Square design . . . 12
  - 2.2.3 Round flattened design . . . 12
  - 2.2.4 The need for a new beam screen . . . 13
- 2.3 The HL-LHC beam screen . . . 14
  - 2.3.1 Functional requirements . . . 14
  - 2.3.2 The shielded beam screen . . . 15
  - 2.3.3 Beam screen dimensions . . . 16
  - 2.3.4 Self-weight deformation and aperture reduction . . . 18
  - 2.3.5 Description of the HL-LHC beam screen components . . . 18
- 2.4 Conclusions . . . 27

3 Material characterisation 31
- 3.1 Material definition . . . 31
- 3.2 Mechanical properties . . . 31
- 3.3 Magnetic properties . . . 32
- 3.4 Thermal properties . . . 33
- 3.5 Electrical properties . . . 33

3.6 Conclusions . . . 33

4 Thermal transfer performance during operation 37
4.1 Thermal requirements of the beam screen assembly . . . 37
4.2 Model definition . . . 39
4.3 Thermal link . . . 40
4.3.1 Thermal link versions . . . 41
4.3.2 Thermal link optimisation . . . 42
4.4 Test setup . . . 44
4.4.1 Small-scale test . . . 44
4.4.2 Real-scale test . . . 45
4.5 Thermal behaviour of the beam screen . . . 46
4.5.1 Small-scale sample (FEM + test) . . . 46
4.5.2 Real-scale sample (FEM) . . . 51
4.6 Heat transfer to the cold bore . . . 52
4.6.1 Small-scale sample (FEM + test) . . . 52
4.6.2 Heat transferred by radiation to the cold bore . . . 56
4.7 Conclusions . . . 57

5 Beam screen behaviour during a magnet quench with quench heaters 59
5.1 Quench heaters . . . 59
5.2 Multiphysics modelling . . . 60
5.2.1 Beam screen modelling . . . 60
5.2.2 Multiphysics modelling relevant to the beam screen problem . . . 61
5.3 Constitutive and governing equations . . . 64
5.3.1 Magnetic physics . . . 64
5.3.2 Thermal physics . . . 69
5.3.3 Solid mechanics physics . . . 70
5.4 Multiphysics FEM model . . . 72
5.4.1 Model algorithm . . . 72
5.4.2 Solvers . . . 73
5.4.3 Time dependent solver algorithm . . . 73
5.4.4 Mesh . . . 75
5.4.5 Model input: material properties and magnet gradient decay . . . 76
5.4.6 Analytical description of the forces induced during a quench . . . 76
5.5 Analysis of the multiphysics FEM model . . . 81
5.5.1 Analytical verification and convergence analysis of the FEM model . . . 81
5.5.2 Self-inductance effects . . . 82
5.5.3 Magnetic and thermal coupling: one-way vs two-way . . . 84
5.5.4 Magnetic and mechanical coupling: one-way vs two-way . . . 84
5.5.5 Comparison between the 2D and 3D version of the FEM model . . . 85
5.6 Results and discussion . . . 86
5.6.1 Q1 beam screen . . . 89
5.6.2 Q2 beam screen . . . 91
5.6.3 D1 beam screen . . . 97
5.6.4 Gap analysis . . . 104
5.6.5 Modal analysis . . . 104
5.6.6 Mechanical analysis at the interface of the colaminated copper layer . . . 108
5.6.7 Thermal link . . . 113
5.6.8 Summary of the mechanical response . . . 121
5.7 Conclusions . . . 122

6 Beam screen behaviour during a magnet quench with quench heaters and CLIQ 123

6.1 CLIQ . . . 123
6.2 Model definition . . . 123
6.3 Preliminary considerations . . . 128
6.4 Magneto-thermal analysis . . . 130
6.4.1 Q1 beam screen . . . 132
6.4.2 Q2 beam screen . . . 135
6.5 Mechanical analysis . . . 137
6.5.1 Equivalent force method . . . 138
6.5.2 Calibration between the 2D and 3D FEM model . . . 139
6.6 Results and discussion . . . 143
6.6.1 Q1 beam screen . . . 143
6.6.2 Q2 beam screen . . . 152
6.6.3 Heat absorber - cold bore interaction . . . 159
6.6.4 Cold bore - magnet coil interaction . . . 159
6.6.5 Fracture mechanics analysis . . . 164
6.6.6 Buckling analysis . . . 167
6.6.7 Magnet coil electrodynamcis . . . 167
6.6.8 Thermal link . . . 169
6.6.9 Summary of the mechanical response . . . 173
6.6.10 Summary of the changes of the beam screen design due to CLIQ . . . 173
6.7 Experimental setup of the magnet quench test . . . 182
6.8 Conclusions . . . 184

7 Conclusions and discussion **185**
7.1 Summary of key results . . . 185
7.1.1 Beam screen design . . . 185
7.1.2 Beam screen material characterisation . . . 185
7.1.3 Beam screen behaviour during normal operation . . . 186
7.1.4 Beam screen behaviour during a magnet quench (quench heaters) . . . 186
7.1.5 Beam screen behaviour during a magnet quench (quench heaters + CLIQ) . . . 186
7.2 Discussion . . . 187
7.3 Future work . . . 189
7.4 Conclusions . . . 189
7.5 Contributions and impact . . . 189
7.6 Publications and awards . . . 190

List of Figures

1.1 LHC layout with the the main experiments and utility insertions. . . . 1
1.2 LHC cell layout. . . . 2
1.3 LHC timeline. The HL upgrade will take place during the third long shut down (LS3). . . . 3
1.4 Schematic of the HL-LHC inner triplet layout for point 1 and 5. Q1 and Q3 are focusing magnets, Q2a and Q2b are defocusing magnets, CP is the higher order corrector package, and D1 is the separation/recombination dipole. . . . 4
1.5 Flow chart of the chapters constituting the thesis. . . . 8

2.1 Gas dynamics phenomena within the cold bore and the LHC beam screen. Image taken from [20]. 11
2.2 First concept of beam screen theorised at the SCC. Image taken from [21]. . . . 11
2.3 Square beam screen developed at CERN. . . . 12
2.4 Round flattened beam screen. . . . 13
2.5 Standard cross section of the LHC dipole. The beam screen label is highlighted in red. . . . 13
2.6 First concept of the HL-LHC beam screen. . . . 15
2.7 HL-LHC beam screen placed in the Q1 magnet. . . . 16
2.8 Cross section of the new Q1 type and Q2x - Q3- CP- D1 type HL-LHC beam screen. The layout of the triplet region is shown below the cross sections. The dimensions of the beam screens are reported in mm. . . . 17
2.9 Cross section of the Q1-MQXF magnet including the cold bore and the beam screen. . . . 17
2.10 Q1 beam screen unloaded in (a) and with gravity load in (b). The magnification factor is 100. The deformation of the beam screen in (c) is expressed in mm, while the von Mises stress in (d) is expressed in MPa. . . . 18
2.11 Rendering of the Q1 and Q2 beam screen. . . . 19
2.12 Overlapping of two consecutive heat absorbers over one single centring pin. . . . 21
2.13 Elastic ring made of titanium grade 5. . . . 21
2.14 Simplified setup of the beam screen to simulate the stress of the elastic ring during a magnet quench. . . . 22
2.15 Von Mises stress in the titanium ring of the Q1 beam screen (a) and Q2 beam screen (b). . . . 22
2.16 Cross section along the thermal link of the Q1 and Q2 beam screen in (a) and in (b), respectively. In (b) the multilayer structure of the lateral part of the link is highlighted. . . . 23
2.17 Brazing and welding position of the Q2 thermal link. . . . 23
2.18 Thermal links of the Q1 and Q2 beam screen with the relative interface pads in (a) and in (b), respectively. . . . 24
2.19 Displacement, in mm, of the Q2 bulky thermal link in (a) and multilayer thermal link in (b) due to the elastic ring acting onto the heat absorber. . . . 25
2.20 Supporting system for the Q1 beam screen in (a) and Q2 beam screen in (b). . . . 25
2.21 Cross section of the Q1 beam screen. The supporting mechanism is magnified in the red box. . . . 26
2.22 Von Mises stress [MPa] due to the maximum displacement of the Q1 spring (a) and Q2 spring (b). 26
2.23 Dimensions (in mm) of the Q1 spring (a) and Q2 spring (b). . . . 27

3.1 Materials used for the beam screen. . . . 32
3.2 Magnetic permeability of the tungsten alloy. . . . 33

3.3 Thermal conductivity of the austenitic stainless steels (316 LN and P506) (a), the titanium grade 5 (b), the copper OFE RRR 100 (c) from 4 K to 80 K. 34
3.4 Thermal conductivity of the tungsten alloy (a) and the zirconia (b) has been measured from 4 K to 80 K. 35
3.5 Heat capacity at constant pressure of the materials used for the beam screen from 4 K to 100 K. . . 36
3.6 Electrical resistivity for the beam screen from 4 K to 100 K. 36

4.1 Allowed temperature profile along the total length of the beam screens (60 m). The maximum drop along the cooling tube (C.T.) is 15 K, while the temperature of the beam screen (BS) can be up to 5 K higher. 37
4.2 Cross section of the beam screen in (a) depicting the various components involved in the heat transfer. From the two areas highlighted in (b) two small-scale samples have been extracted to characterise the heat transfer from the heat absorber to the cooling tube and from the beam screen to the cold bore. 38
4.3 Sample representing one eight of the Q2 beam screen 40 mm long. 39
4.4 Mesh of the sample by second-order tetrahedral elements. 41
4.5 Thermal link pad welded on the octagonal pipe in (a) and on the cooling tube in (b). 41
4.6 Parameters of the thermal link affecting the heat transfer; t: thickness of the link, h: width of the link, b: length of the pad, a: length of the co-laminated copper layer. 42
4.7 Impact of the thermal link and pad dimensions on the temperature of the heat absorber. The type of weld is analysed in (a), the thickness of the pad in (b), the coverage of the Cu layer on the pad in (c), the thermal link width in (d). For the evaluation of each dimension, the remaining ones are kept constant and are shown at the bottom of each graph. 43
4.8 Best trade-off of the thermal link system in terms of thermal transfer and ease of assembly. The dimensions are reported next to each component. 44
4.9 In (a) small-scale sample and position of the temperature sensors. In (b) copper rod fitted into the cooling tube to cool down the tube. In (c) cross section of the cooling tube. 45
4.10 Setup configuration of the small-scale thermal test. 46
4.11 In (a) mounting sequence of the beam screen assembly into the vacuum vessel of the cryostat. In (b) section of the real-scale sample setup. 47
4.12 Beam screen prototype for the thermal test. 48
4.13 CAD model for the simulation in (a) and (b) and real model for the test in (c) and (d) of the two small-scale samples. 48
4.14 Measuring points of the small-scale samples whose thermal link is welded on the octagonal pipe (a) or on the cooling tube (b). 49
4.15 Thermal link welded on the pipe with nominal compression force (1.82 N). Temperature of the probe points according to the initial temperatures of 50 K (a), 60 K (b), 70 K (c), and 80 K (d).The power given to the heat absorber is 0.05 W, 0.1 W, 0.2 W, and 0.4 W. The profile of the measured data are represented by the continuous line while the numerical ones by the dashed lines. 50
4.16 Thermal link welded on the cooling tube without compression force. Temperature of the probe points according to the initial temperatures of 50 K (a), 60 K (b), 70 K (c), and 80 K (d). The power given to the heat absorber is 0.05 W, 0.1 W, 0.2 W, and 0.4 W. The profile of the measured data are represented by the continuous line while the numerical ones by the dashed lines. 51
4.17 Thermal link welded on the cooling tube with nominal compression force. Temperature of the probe points according to the initial temperatures of 50 K (a), 60 K (b), 70 K (c), and 80 K (d). The power given to the heat absorber is 0.05 W, 0.1 W, 0.2 W, and 0.4 W. The profile of the measured data are represented by the continuous line while the numerical ones by the dashed lines. 52
4.18 Temperature distribution [K] simulated for a quarter of a Q1 and Q2-Q3-D1 beam screen 400 mm long whose thermal links are welded on the cooling tube. 53
4.19 3D printed titanium grade 5 springs in (a), setup to assess the heat transfer through the zirconia sphere in (b), full CAD model of the experimental setup in (c), and its simplified version adopted in the simulations in (d). 54
4.20 In (a) mesh of the contact interface between the zirconia sphere and the plate. In (b) contact surface between the sphere and the plate. 55
4.21 Heat load transferred to the cold bore through the Q1 and Q2 zirconia spheres. 55

4.22 Contact between the first stainless steel plate and the spring in (a), contact between the spring and the zirconia sphere in (b), contact between the sphere and the stainless steel plate in (c). 56

5.1 Magnet gradient decay of a quadrupole magnet in (a) and magnetic field decay of a dipole magnet in (b) during a magnet quench of the inner triplet area when only quench heaters are used as protection scheme. 59
5.2 Electric size of the beam screen. 65
5.3 Simplification in (a) of the beam screen geometry in a dipole magnet through the perfect magnetic conductor, in green at $180°$ angle, and the magnetic insulation, in blue at $90°$ angle. The geometry discretisation reduced to a quarter in (b). 68
5.4 Simplification in (a) of the beam screen geometry in a quadrupole magnet through two insulation conditions, in blue at $45°$ and $135°$ angle. The geometry discretisation reduced to a quarter in (b). 68
5.5 External magnetic vector potential condition, in blue, applied on the modelling domain of the dipole in (a) and of the quadrupole in (b). 69
5.6 Thermal insulation of the beam screen. 70
5.7 In (a) mechanical contacts (in blue) implemented between the bottom side of the heat absorber and the octagonal pipe as well as between the round side of the absorber and the inner part of the cold bore. In (b) the mesh used in the mechanical physics. 71
5.8 Flow chart of the 2D model algorithm during a time step of the magnet quench. 74
5.9 In (a) mesh used in the magnetic and thermal module and in (b) the one used in the mechanical module. In the red box the mesh is zoomed to highlight the elements used in the inner copper layer. 75
5.10 Magnetic field decay, B, due to the dipole magnet quench and $B\frac{\partial B}{\partial t}$ evolution. 76
5.11 Magnet gradient decay, G, due to the quadrupole magnet quench and $G\frac{\partial G}{\partial t}$ evolution. 77
5.12 Annular sectors accounted in the analytical formulation to derive the expression of the forces induced during a dipole magnet quench in (a) (from 0 to $\pi/4$) and a quadrupole magnet quench in (b) (from $\pi/4$ to $3\pi/4$). 77
5.13 Vectors of the currents and forces induced in an annular geometry during a dipole magnet quench. The forces are referred to the deformed geometry. 79
5.14 Vectors of the currents and forces induced in an annular geometry during a quadrupole magnet quench. The forces are referred to the deformed geometry 82
5.15 Mesh convergence in (a) and time-step convergence in (b) of the numerical solution to the analytical one. 83
5.16 In (a) comparison between the maximum analytical and numerical forces for electrical conductivities ranging from 10^2 to 10^{10} S/m. In (b) the evolution on time of the numerical forces are normalised and compared for electrical conductivities ranging from 10^8 to 10^{10} S/m. 83
5.17 Colour map of the magnetic field around the annulus sector after 50 ms from the start of the magnet quench. The electrical conductivity of the portion in (a) is 10^7 S/m, while the one in (b) is 10^{10} S/m. In the magnification in (a), the Lorentz forces follow the typical pattern of a quadrupole magnet quench decay while in the magnification in (b), the forces are bent because of the magnetic perturbation due to the high eddy currents (blue area). 84
5.18 Comparison between the one-way and two-way coupling of the magnetic and thermal physics. . . 85
5.19 Comparison of the couplings between the magnetic and mechanical interface. 86
5.20 Deformation of a quadrant of the octagonal pipe. 86
5.21 Comparison of the radial component of the forces integrated from $\pi/4$ to $3\pi/4$ between the cold bore (in black) and the heat absorber (in red) according to the 2D (continuous line) and 3D (dashed line) versions of the model. The 2D model is compared with the 3D model without periodic conditions in (a) and with periodic conditions in (b). 87
5.22 Current distribution induced in one quarter of the Q1 beam screen. At the extremities of the assembly the currents wrap up in order to close the circuit if no periodic conditions are implemented in (a), while they are not perturbed in case of periodic conditions in (b). 87
5.23 Internal radius of the cold bore and external radius of the heat absorber in (a). Contact between the heat absorber and the cold bore resulting in a radial gap of 0.33 mm at the extremity of the wings in (b). 88
5.24 Distribution of the induced forces in the Q1 beam screen during a magnet quench. 90

5.25 Evolution on time of the main physical quantities induced in the Q1 beam screen during a magnet quench. . . . 92
5.26 Distribution of the main physical quantities induced in the Q1 beam screen at 55 ms. . . . 93
5.27 Evolution on time of the equivalent and principal stress induced in all the components of the Q1 beam screen. The contact force is shown between the heat absorber and the cold bore. The kinetic energy is shown for the heat absorber. . . . 94
5.28 In (a) von Mises stress on the Q1 octagonal pipe fitted with pumping holes. In (b) stress concentration on the rear part of the most critical slot. . . . 95
5.29 Q1 heat absorber. From top to bottom: von Mises stress on the external side of the heat absorber; von Mises stress on the internal side of the heat absorber; maximum principal stress. . . . 96
5.30 Distribution of the induced forces in the Q2 beam screen during a magnet quench. . . . 97
5.31 Evolution on time of the main physical quantities induced in the Q2 beam screen during a magnet quench. . . . 98
5.32 Distribution of the main physical quantities induced in the Q2 beam screen at 55 ms. . . . 99
5.33 Evolution on time of the equivalent and principal stress induced in all the components of the Q2 beam screen. The kinetic energy is shown only for the heat absorber and the contact force between the heat absorber and the cold bore. . . . 100
5.34 In (a) von Mises stress on the Q2 octagonal pipe fitted with pumping holes. In (b) stress concentration on the rear part of the most critical slot. . . . 101
5.35 Q2 heat absorber. From top to bottom: von Mises stress on the external side of the heat absorber; von Mises stress on the internal side of the heat absorber; maximum principal stress. . . . 102
5.36 Distribution of the induced forces in the D1 beam screen during a magnet quench. . . . 103
5.37 Evolution on time of the main physical quantities induced in the D1 beam screen during a magnet quench. . . . 105
5.38 Distribution of the main physical quantities induced in the D1 beam screen at 152 ms. . . . 106
5.39 Evolution on time of the equivalent and principal stress induced in all the components of the D1 beam screen. The kinetic energy is shown only for the heat absorber and the contact force between the heat absorber and the cold bore. . . . 107
5.40 In (a) von Mises stress on the D1 octagonal pipe fitted with pumping holes. In (b) stress concentration on the rear part of the most critical slot. . . . 108
5.41 D1 heat absorber. From top to bottom: von Mises stress on the external side of the heat absorber; von Mises stress on the internal side of the heat absorber; maximum principal stress. . . . 109
5.42 Kinetic energy of the heat absorber for the Q1, Q2, and D1 beam screen as a function of the gap between the cold bore and the heat absorber itself (in the x-axis C.B. and H.A. stand for cold bore and heat absorber, respectively). . . . 110
5.43 Maximum displacement and equivalent stress for the cold bore of the Q1, Q2, and D1 beam screen as a function of the gap between the cold bore and the heat absorber. . . . 111
5.44 Local stress at the interface between the copper layer and the Q1 octagonal pipe during the quench at 55 ms (a,b) and after the quench (c,d). The x-axes of the graphs corresponds between each other. 112
5.45 Local stress at the interface between the copper layer and the Q2 octagonal pipe during the quench at 55 ms (a,b) and after the quench (c,d). The x-axes of the graphs corresponds between each other. 113
5.46 Local stress at the interface between the copper layer and the D1 octagonal pipe during the quench at 152 ms (a,b) and after the quench (c,d). The x-axes of the graphs corresponds between each other. . . . 114
5.47 Plastic strain amplitude versus cycles to failure of OFHC copper at room temperature. Image taken from [131]. . . . 114
5.48 Currents, forces and magnetic field in a generic thermal link. . . . 115
5.49 Distribution and norm of the magnetic field [T] for the Q1 beam screen. . . . 116
5.50 Distribution and norm of the magnetic field [T] for the Q2 beam screen. . . . 116
5.51 Distribution and norm of the magnetic field [T] for the D1 beam screen. . . . 117
5.52 Profile of the total forces induced in the Q1, Q2, and D1 thermal links. . . . 117
5.53 Profile of the total forces induced in the Q2 thermal links of width 3, 5, and 10 mm. . . . 118
5.54 Current path and forces distribution in (a). Regions where the forces are integrated: over a quarter of the thermal link (b) or in a small portion to limit border effects (c). . . . 118

5.55 Profile of the total forces induced in the Q2 thermal links of width 3, 5, and 10 mm with and without the effects of the temperature increase. . . . 119
5.56 Fixed constraints (in orange) used in the mechanical analysis of the thermal link. . . . 120
5.57 Domain discretisation of the thermal link along its thickness. . . . 120
5.58 Von Mises stress for a thermal link of a width of 3 mm (a), 5 mm (b), and 10 mm (c). . . . 120
5.59 Axial stress in the thermal link cross section. It is worth noting the classical butterfly profile due to the bending. . . . 121

6.1 Nominal (a) and ultimate (b) current discharge for the poles 1 - 3 and 2 - 4 upon the activation of CLIQ. . . . 124
6.2 Geometrical structure of the model representing the quadrupole magnet. . . . 124
6.3 In (a) main regions of the equivalent quadrupole magnet. In (b) dimensions of the equivalent structure. . . . 126
6.4 In (a) magnetic field lines generated by the equivalent COMSOL model. In (b) real coil structure generating the magnetic field in ROXIE, taken as reference. . . . 127
6.5 In (a) comparison of **B** monitored on the 26 points between COMSOL and ROXIE. In (b) comparison of the $B\dot{B}$ factor monitored on the same points between COMSOL and ROXIE. . . . 128
6.6 In (a) the normalised profile of the magnet current discharge in case of CLIQ along with the quench heaters and in case of quench heaters only as a protection scheme. In (b) the $I\dot{I}$ factor for the current discharge of the two protection schemes. . . . 128
6.7 In (a) current loops in the octagonal pipe induced during the first phase of the CLIQ discharge. The adjacent flows of the (yellow and blue path) have opposite direction. In (b) the current loops induced in case of the quench heaters. The adjacent flows have the same direction. . . . 129
6.8 In (a) current density distribution induced at 5 ms in the beam screen inserted in a magnet equipped with CLIQ. In (b) current density distribution induced during a monotonic magnetic field decay. . 129
6.9 Current induced in a quarter of the beam screen whose limits in the colour map is set to $1 \cdot 10^3$ A and $-1 \cdot 10^3$ A. . . . 131
6.10 In (a) Lorentz force distribution induced in the heat absorber at 5 ms whose resultant force is decomposed in a normal and tangential component. In (b) it is shown the equivalent force distribution represented by a torque and a tangential force. . . . 131
6.11 Percentage of current and force unbalance between the right and left side of the heat absorber delimited by the intersection with the y-axis. . . . 132
6.12 Evolution of the normal and the tangential forces induced in the Q1 cold bore (a), heat absorber (b), octagonal pipe (c), and inner layer (d) during the CLIQ discharge. Black vertical lines determine regions of interest of the CLIQ discharge. The red bars and their relative values indicate the highest difference of forces for each region. . . . 133
6.13 Distributions of the forces induced in the heat absorbers of the Q1 beam screen with respect to each region of the CLIQ discharge. . . . 134
6.14 Evolution of the induced currents integrated over the two sides of the Q1 cold bore (CB) and heat absorber (HA) in (a), the octagonal pipe (OP) and the inner layer (IL) in (b). The electromagnetic heating (c) and the maximum temperature (d) refer to each quarter of the beam screen components. 135
6.15 Evolution of the normal and the tangential forces induced in the Q2 cold bore (a), heat absorber (b), octagonal pipe (c), and inner layer (d) during the CLIQ discharge. The regions of the CLIQ dischargeare identified by the black vertical line. The red bars and their relative values indicate the highest difference of the normal forces. . . . 136
6.16 Evolution of the induced currents integrated over the two sides of the Q2 cold bore (CB) and heat absorber (HA) in (a), the octagonal pipe (OP) and the inner layer (IL) in (b). The electromagnetic heating (c) and the maximum temperature (d) refer to each quarter of the beam screen components. 137
6.17 Integrated forces induced in the cold bore decomposed in the normal (blue) and tangential (orange) component. The normal forces generate a torque (blue circles) in each quadrant, numbered from 1 to 4. The tangential forces generate two counteracting torques (orange circles) numbered as 1-3 and 2-4. . . . 140
6.18 Real force distribution and equivalent system of forces for the heat absorber (a-b), octagonal pipe (b-c) and cold bore (d-e). The distance of the centroids and the equivalent one (represented by orange dots) is indicated. . . . 141

6.19 Specific vertexes of the beam screen section chosen to monitor the deformation of the beam screen components during the CLIQ discharge between COMSOL and Ansys. 142
6.20 Comparison of the radial displacement of the vertexes chosen to monitor the mechanical response of each beam screen component between COMSOL and Ansys. The type of the component is shown at the top of each graph. 144
6.21 Evolution of the highest von Mises stress in the cold bore computed by Ansys and COMSOL. . . 145
6.22 Stress state of the cold bore hit by the heat absorber at 5 ms in Ansys in (a) and in COMSOL in (b). 145
6.23 Original pin design and integration with the interfacing systems. In (c) the force distribution around the pin with or without CLIQ. 146
6.24 On top, von Mises stress state of the Q1 octagonal pipe at 5 ms. On the bottom, cross section view of the octagonal pipe. The upper bound of the legend is set to 1350 MPa, elastic limit of the material, to highlight plastically deformed regions. 147
6.25 New concept of the pin to withstand the CLIQ discharge and integration with the interfacing systems. In (c) the force distribution around the pin with or without CLIQ. 148
6.26 Equivalent stress of the Q1 beam screen, in particular: octagonal pipe (a), cross section of the beam screen (b), bottom face of the pin (c), cross section of the octagonal pipe and pin (e), and cross section of the pin itself (f). The shear stress of the bottom face of the pin on the XZ plane is in (d). The elastic limit is set to 1350 MPa on the legend to highlight the regions that undergo plastic deformations (in red). 149
6.27 Reinforcement plates added on the octagonal pipe. In (a) the thickness is 1 mm while in (b) it is 2 mm. 152
6.28 Equivalent stress of the Q1 beam screen equipped with a reinforcement plate 1 mm thick: octagonal pipe (a), cross section of the beam screen (b), bottom face of the reinforcement plate (c), cross section of the octagonal pipe and pin (e), and cross section of the pin itself (f). The shear stress of the bottom face of the reinforcement plate on the XZ plane is in (d). The elastic limit is set to 1350 MPa on the legend to highlight the regions that undergo plastic deformations (in red). 153
6.29 Equivalent stress of the Q1 beam screen equipped with a reinforcement plate 2 mm thick: octagonal pipe (a), cross section of the beam screen (b), bottom face of the reinforcement plate (c), cross section of the octagonal pipe and pin (e), and cross section of the pin itself (f). The shear stress of the bottom face of the reinforcement plate on the XZ plane is in (d). The elastic limit is set to 1350 MPa on the legend to highlight the regions that undergo plastic deformations (in red). 156
6.30 Cross section of the Q2 beam screen equipped with the straight pin in (a) and with the double diameter pin in (b). 159
6.31 In (a) von Mises stress state of the Q2 octagonal pipe at 5 ms. In (b) cross section view of the octagonal pipe. The upper bound of the legend is set to 1350 MPa, elastic limit of the material, to highlight plastically deformed regions. 160
6.32 Equivalent stress of the Q2 beam screen, in particular: octagonal pipe (a), cross section of the beam screen (b), bottom face of the pin (c), cross section of the octagonal pipe and pin (e), and cross section of the pin itself (f). The shear stress of the bottom face of the pin on the XZ plane is in (d). The elastic limit is set to 1350 MPa on the legend to highlight the regions that undergo plastic deformations (in red). 161
6.33 Shape of the cold bore squeezed at 45° angle in the first region of the CLIQ discharge. 164
6.34 In (a) radial displacement of the cold bore during the CLIQ discharge for the Q1 cold bore in case of the Q1 beam screen equipped with or without reinforcements plate. In (b) radial displacement of the Q2 cold bore. 164
6.35 Equivalent and maximum principal stress of the Q1 heat absorber (a,b) and of the Q2 heat absorber (c,d), respectively. The upper bound of the legend is set to 500 MPa to better visualise high-stress regions. 165
6.36 In (a) equivalent stress of the cold bore hit by the Q1 heat absorber. In (b) equivalent stress of the cold bore hit by the Q2 heat absorber. 165
6.37 Ansys model to account for the force transmitted to the supporting pin placed at $+/- 45^\circ$ angle in the magnet poles. Periodic conditions (PC) are applied on the eternal faces of the assembly. 166
6.38 Cross section of one quarter of the Q1 beam screen assembly which includes the supporting pins. . 166

6.39 In (a) regions of the beam screen (in violet) where the force distribution of the octagonal pipe and the inner layer cause the compression of the pipe itself. In (b) critical load factor and total displacement calculated through the linear buckling analysis. 167
6.40 Current $[A]$ circulating in the HL-LHC magnet coil after 5 ms the initiation of the CLIQ discharge in (a). Current density $[A/m^2]$ induced in the beam screen after 5 ms the initiation of the CLIQ discharge in (b). 168
6.41 Thermal link position with respect to the magnet poles. In the links facing the poles 1 and 3 the magnetic field increases locally, while for the poles 2 and 4 it decreases. 169
6.42 Distribution of the forces in the thermal link side brazed underneath the heat absorber (a), facing the poles 2 or 4 (b), and the poles 1 or 3 (c). 170
6.43 Portion of the thermal link used to integrate the Lorentz forces. 170
6.44 Evolution of the longitudinal forces integrated over each portion of the thermal link 1 mm thick and 3 mm wide facing the poles 1 or 3, and 2 or 4. 171
6.45 Evolution of the longitudinal forces integrated over each portion of the thermal link 1 mm thick and 5 mm wide facing the poles 1 or 3, and 2 or 4. 172
6.46 Evolution of the longitudinal forces integrated over each portion of the thermal link 1 mm thick and 10 mm wide facing the poles 1 or 3, and 2 or 4. 172
6.47 Buckling analysis performed on a 10 mm wide thermal link. 173
6.48 Von Mises stress for a thermal link layer 0.1 mm thick and 3 mm wide in (a), 5 mm in (b), and 10 mm in (c). The upper limit of the colour map is set to 35 MPa to highlight the regions of plastic deformations. 173
6.49 Bottom side of the heat absorber. One slot of the pins is ovally shaped to allow a stress-free thermal contraction during the cooling down of the magnet. 175
6.50 Octagonal pipe of the Q1 beam screen in (a), equipped with the heat absorbers in (b) in the case of quench heaters used as a quench protection scheme. 176
6.51 Octagonal pipe of the Q1 beam screen in (a), equipped with the heat absorbers in (b) in the case of CLIQ used as a quench protection scheme. 177
6.52 Rendering of the Q1 beam screen inserted in the cold bore in (a) and of the new pin geometry in (b). 178
6.53 Octagonal pipe of the Q2 beam screen in (a), equipped with the heat absorbers in (b) in the case of quench heaters used as a quench protection scheme. 179
6.54 Octagonal pipe of the Q2 beam screen in (a), equipped with the heat absorbers in (b) in the case of CLIQ used as a quench protection scheme. 180
6.55 Rendering of the Q1 beam screen inserted in the cold bore in (a) and of the new pin geometry in (b). 181
6.56 Cross section of the MQXFS magnet whose aperture accommodates the beam screen. 182
6.57 Measuring probe inserted in the the beam screen. 183
6.58 Measuring probe instrumented with 8 titanium strips. The right side measures the rotation of the heat absorber while the left side measures the displacement of the octagonal pipe. 183

List of Tables

1.1 Objectives of the thesis with the relative methods, results, and the chapters in which these are treated. In the table BS stands for beam screen. 6

2.1 Thermal loads estimated for the inner triplet of point 1 and 5. The synchrotron radiation loads are from [17], the impedance and electron cloud loads are from [18], and the nuclear debris loads are from [16]. 10
2.2 Summary of the dimensions and tolerances of the triplet area HL-LHC beam screens and cold bores. 18

3.1 Materials used for each component of the HL-LHC beam screen. 31
3.2 Mechanical properties of the materials used for the HL-LHC beam screen. 32

4.1 Cooling scheme characteristics of the LHC and HL-LHC beam screens [51] [26]. 38
4.2 Temperature increase measured for the relevant Q2 beam screen spots (Inermet and BS thermal link points in Fig. 4.14) for a nominal heat load of 15 $\mathrm{W\,m^{-1}}$ with and without compression force. 49
4.3 Measured maximum temperature increase of relevant Q2-type beam screen components with the thermal link welded on the cooling tube, for a nominal heat load of 15 $\mathrm{W\,m^{-1}}$. 51

5.1 Features of the multiphysics models to study the beam screen during quench up to 2017. Legend, Mf: magnetic fields, Th: thermal, Mech: mechanical. 61
5.2 Physical variables needed for each interface used in the model. 76
5.5 Comparison of the highest force, stress, displacement induced in each component of the Q1,Q2, and D1 beam screen subject to the relative magnetic field decay. 121

6.1 Summary of the highest forces (ΔF_n and F_t) induced in the Q1 beam screen with respect to the four regions of the CLIQ discharge. The normal forces induced during the monotonic magnetic field decay analysed in chapter 5 (NO CLIQ) are presented for comparative purposes. 134
6.2 Summary of the highest forces (ΔF_n and F_t) induced in the Q2 beam screen with respect to the four regions of the CLIQ discharge. The normal forces induced during the monotonic magnetic field decay analysed in chapter 5 (NO CLIQ) are presented for comparative purposes. 136
6.3 Maximum torque induced in the Q1 and Q2 beam screen components during the CLIQ discharge of region 1. 140
6.5 Comparison of the highest force, stress, and displacement induced in each component of the Q1 (reinforcement plate 1 mm thick) and Q2 beam screen subject to the CLIQ discharge. For the Q1 beam screen, these quantities are reported also by considering the magnet electrodynamics. 174

Declaration of Originality

I, Marco Morrone, declare that this thesis entitled *Thermomechanical study of complex structures in the aperture of superconducting magnets: Application to the design of the High-Luminosity Large Hadron Collider shielded beam screen* and the work presented in it are my own and has been generated by me as the result of my own original research. I confirm that where I have consulted the published work of others, this is always clearly attributed.

Copyright Declaration

The copyright of this thesis rests with the author and is made available under a Creative Commons Attribution Non-Commercial No Derivatives licence. Researchers are free to copy, distribute or transmit the thesis on the condition that they attribute it, that they do not use it for commercial purposes and that they do not alter, transform or build upon it. For any reuse or redistribution, researchers must make clear to others the licence terms of this work.

Acknowledgements

I consider myself truly privileged to have embarked on this PhD experience in an extremely stimulating environment provided by CERN and Imperial College. On reflection, I would like to acknowledge a few people that made this possible.

I am very grateful to Dr. Cedric Garion, my supervisor at CERN, that throughout my entire PhD guided me on a daily basis with professionalism and kindness. His sharp observation and pragmatism have certainly left a big mark on me.

I am equally grateful to Dr. Marco Aurisicchio, my supervisor at Imperial College. Although we have worked from distance, we have always found a way to have fruitful communications. His support on my research activities has been outstanding and his continuous pursuit of accuracy remarkable.

I also want to thank Dr. Catrin Mair Davies, my second supervisor at Imperial College, for her valuable help in the characterisation of some beam screen materials at university.

A special mention goes to Paolo Chiggiato, the head of Vacuum, Surface and Coating group at CERN. His busy agenda has never been an obstacle for him to follow and support my activities. I am very grateful to Paolo for the numerous times he gave me advice and especially when I was afraid of making mistakes.

I want to thank my colleagues of my group and section at CERN with whom I had pleasure to work with. They have helped me a lot and played an extraordinary role in my research project. I also thank my colleagues in various groups at CERN that I have worked with, in particular, those of the TE-CRG, TE-MSC, and EN-MME groups whom I have been collaborated with on many experimental activities.

A huge thank you to my friends of CERN. It is renowned that doing a PhD is not an easy task but with their energy and enthusiasm they have helped me cope. A normal lunch or an evening out have always been a lot of fun.

I would like to acknowledge my family of their unwavering support and for forging me to become the person I am today.

And finally you, Tessa! Thank you for your patience, understanding, and relentless encouragement throughout these intense years. Words cannot express the extent of my gratitude and you definitely deserve the most important acknowledgement of this thesis.

Chapter 1

Introduction

1.1 The Large Hadron Collider

The Large Hadron Collider (LHC) is the largest particle accelerator ever built for scientific purposes. Its 27 km long ring extends about 100 m underground along the French-Swiss border close to Geneva and is run by the European Organisation of Nuclear Research (CERN). The LHC is a particle-particle collider and consists of two counter rotating beam crossing at four points where huge detectors track the interaction products [1].

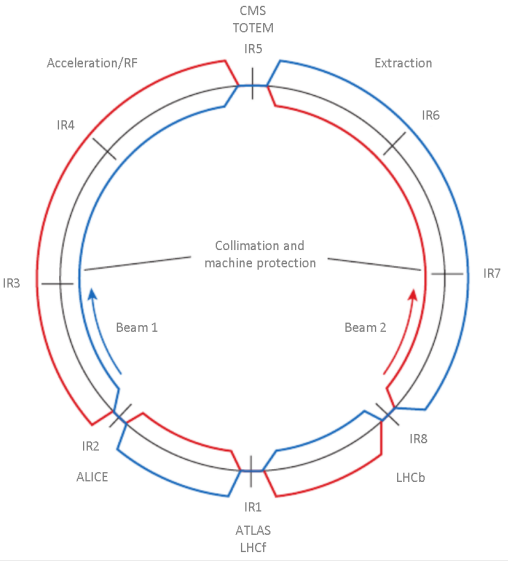


FIGURE 1.1: LHC layout with the the main experiments and utility insertions.

The LHC, shown in Fig. 1.1, is not a perfect circle but is made of eight arcs and eight Long Straight Sections (LSS). Each arc is 2.45 km long while the LSS is 545 m.

The arc, in turn, is made of 23 regular arc cells about 110 m long which contain dipole, quadrupole and other multipole magnets, see Fig. 1.2. In total each arc contains 154 dipole bending magnets needed to steer the beam around the accelerator.

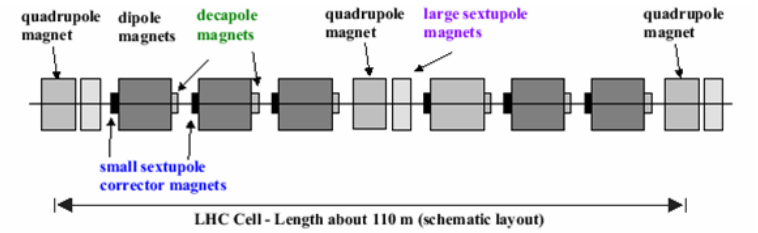


FIGURE 1.2: LHC cell layout.

The layout of the LSS is not uniquely defined as it can serve as an experimental or utility insertion. Two counter-rotating beams collide in four Interaction Regions (IR). The two high-luminosity experimental insertions are the ATLAS (IR1) and CMS (IR5) experiments. There are other two low luminosity experimental insertions ALICE (IR2) and LHCb (IR8) which contain also the injection system for beam 1 and beam 2, respectively. The two beams do not interact in the remaining four straight sections. IR3 and IR7 accommodate collimation and machine protection systems. IR4 contains the RF system while IR6 serves to extract the beam by means of fast pulsed magnets (kickers).

The area of the experimental insertions close to the Interaction Points (IP) is the so called inner triplet region providing the final focusing of the beam. This is obtained through powerful quadrupole magnets that reduces the size of the beam from about 0.2 mm to 16 μm resulting in an increased number of collisions (luminosity) at a centre-of-mass energy of 13-14 TeV.

1.2 The High-Luminosity LHC upgrade

The LHC started operating in 2009 and has since widened the knowledge of particle physics. The 2012 confirmation of the existence of the Higgs boson demonstrated the machine potential, giving hope for future discoveries [2]. In addition, it inspired a long-term exploration of higher-energy phenomena through a consistent upgrade called High-Luminosity Large Hadron Collider (HL-LHC) that will take place around 2024. The project aims to increase the integrated luminosity by a factor of 10 beyond the current design value. The luminosity, L, is a parameter representing the performance of particle accelerators. It indicates the number of collisions per square centimetre per second and determines, along with the cross section σ_p, the number of useful interactions per second, dR/dt, according to [3]:

$$\frac{dR}{dt} = L\sigma_p. \tag{1.1}$$

The timeline of the LHC program is shown in Fig. 1.3. After an increase of the nominal design luminosity by a factor of two in 2019, a further major leap will take place following three years of technical upgrade, from 2024 to mid 2026. During such time, the integrated luminosity will achieve an impressive target of 3000 fb^{-1} in 10 years[1] [4, 5]. This luminosity is more than ten times the luminosity reach of the first 10 years of the LHC lifetime.

After 2020 the statistical gain in running the accelerator without a significant luminosity increase beyond its design value will become marginal. The running time necessary after 2020 to halve the statistical error in measurements will be more than ten years [6]. Therefore, the luminosity increase is needed to maximize the machine exploitation and is hence crucial to keep the scientific progress relevant. The technological development

[1] fb^{-1} is a unit of measure of the integrated luminosity, a quantity proportional to the number of recorded collisions.

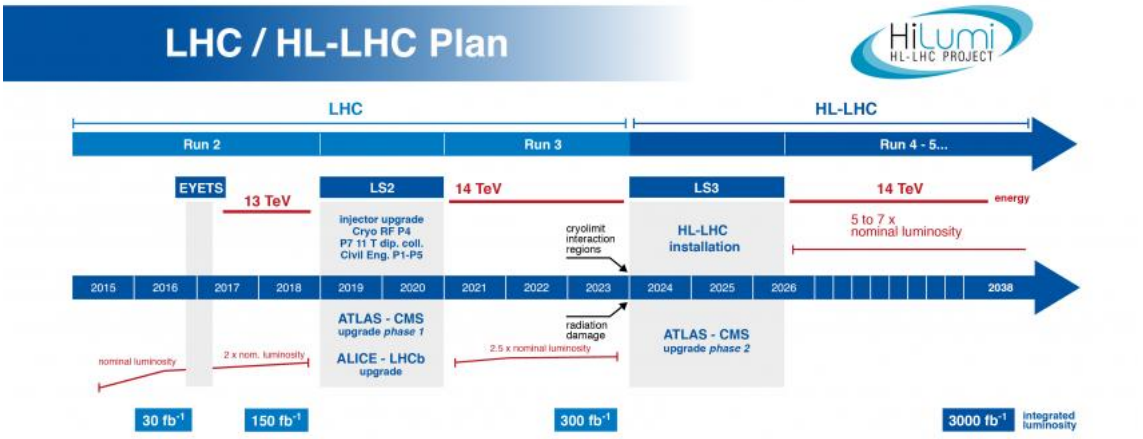


FIGURE 1.3: LHC timeline. The HL upgrade will take place during the third long shut down (LS3).

required to cope with such a challenge is considerable and will hinge on a series of cutting-edge applications spanning over different domains of science. Many upgrades on superconducting magnets, vacuum, cryogenics, machine protection, collimation and diagnostics will be implemented by 2024. The LHC is a very powerful particle accelerator, to give an idea of its proportions, by the end of 2012 its integrated luminosity was equal to 22 fb^{-1}, while that for the entirety of hadron colliders in the world was 10 fb^{-1}. In 2017, the LHC has reached 50 fb^{-1}, exceeding the target of 45 fb^{-1}. The LHC represents a high priority project for the European Research Area (ERA) and the HL upgrade will guarantee the European leading position in high-energy physics for another 20 years [7].

1.3 The beam screen

In the framework of the HL-LHC project, new beam screens will be installed by 2024 within the beam pipe of the superconducting magnets, a few tens of meters from the proton beam interaction points 1 and 5, *i.e.* the ATLAS and CMS experiment.

The beam screen is a liner that shields the 1.9 K magnet cryogenic system from the beam-induced heat loads and damage to the magnet coils that would be otherwise induced by the highly penetrating collision debris. It also ensures that proper vacuum conditions required for the stability of the beam are met.

New shielded beam screens will replace those of the inner triplet and the D1 separation/recombination dipoles of point 1 and 5. The inner triplet consists of three quadrupole optical elements made of four magnets (Q1, Q2a, Q2b, Q3) and several corrector magnets.

The layout of the triplet region which comprises two focusing magnets, *i.e.* Q1 and Q3, and two defocusing magnets, *i.e.* Q2a and Q2b is shown in Fig. 1.4.

Within the ambitious HL machine upgrade, the beam screen plays a dominant role for the fulfilment of the project.

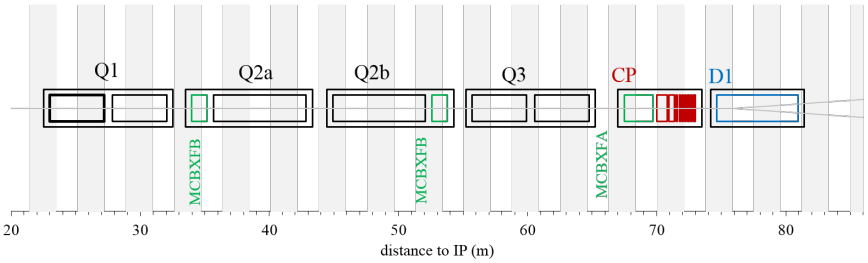


FIGURE 1.4: Schematic of the HL-LHC inner triplet layout for point 1 and 5. Q1 and Q3 are focusing magnets, Q2a and Q2b are defocusing magnets, CP is the higher order corrector package, and D1 is the separation/recombination dipole.

1.4 Definition of the problem

The HL-LHC upgrade calls for a new mechanical design of the beam screens close to point 1 and 5 of the LHC.

Amongst the beam-induced heat loads, the increased and highly penetrating collision debris must be efficiently intercepted by the beam screen to lower the dramatic energy consumption that would be required otherwise by the cryogenic system at 1.9 K. At this temperature, the cooling energy to dissipate 1 W is nearly 1kW [8]. Any thermal load should be intercepted through the beam screen coupled with an active cooling system at a higher temperature to improve the Carnot efficiency of the cryogenic cycle [9]. In addition, the nuclear shower would undermine the integrity of the delicate magnet coils that therefore need to be shielded. The beam screen must ensure also proper vacuum conditions for the stability of the high-energy beam. In conclusion, the design of the new beam screen has to satisfy these requirements to guarantee the normal operation of the LHC.

In the event of a magnet quench [10], a resistive transition of the superconducting coils, possible failures of the beam screen may occur. During this transition, high magnitude currents and forces are induced in the conductive components of the beam screen. These forces could endanger the assembly itself and the magnet coils. Therefore, a robust design that guarantees the mechanical integrity of the beam screen is mandatory to secure LHC availability to particle physics research.

FEM modelling can be a useful tool to establish the mechanical integrity of a complex assembly whose design hinges on the accurate prediction of the magnet quench effects. However, in the context of the beam screen design, this poses five main modelling challenges. First, considering the very low electrical resistivity of some components, self-inductance effects need to be considered. Second, during a quench the resistive losses of the induced currents cause a temperature increase which in turn influences the material properties of some beam screen components. In particular, the eddy currents depend on the variation of the electrical resistivity. Hence, the analysis has to be setup in a way that the material properties are constantly updated. A two-way coupling is therefore needed between the magnetic and thermal modules. At the same time, a two-way coupling between the magnetic and structural modules is necessary to investigate the dependence between the displacement of the assembly and the induced forces. Third, as a result of components coming into contact, the mechanical response of the assembly should be studied dynamically over the whole evolution of the magnet quench. Fourth, since the assembly is non-geometrically uniform along the beam axis, a complementary three dimensional model is required. Fifth, highly non-linear contacts between the opposing components have to be setup adding complexity to the model, whose overall convergence is strongly dependent on the fine tuning of such contacts.

1.5 Objectives of the work

The aim of this research is to develop a new beam screen design for the inner triplet and the D1 magnet able to satisfy the requirements of the HL-LHC upgrade and to study the behaviour of the beam screen in normal working conditions and in the case of a magnet quench. The research aim is broken down into four main objectives:

- Describe and define the design of the new triplet area beam screens able to address the requirements of the HL-LHC upgrade;
- Characterise at cryogenic temperatures the materials used in the beam screen including determining their mechanical, magnetic, electric, and thermal properties;
- Assess the heat transfer within the beam screen assembly and optimise the temperature distribution due to the beam-induced heat loads to guarantee the normal operation conditions;
- Understand the magnetic, thermal and mechanical behaviours of the beam screen assembly during a magnet quench to enable its effective design and operation.

1.6 Content of the thesis

A review of previous beam screen is provided to outline the elements of novelty introduced by the HL-LHC beam screen. The functional requirements of the new beam screen are reported and discussed. The design of the new beam screen is presented and the functions of each component described. For sake of brevity only the final design of the beam screen will be defined.

The material property of the beam screen components not found in literature have been measured and given as input to the numerical models. Therefore, the magnetic permeability, the electrical resistivity and the thermal conductivity have been measured from 4.4 K to 300 K. Tensile and fracture mechanics tests have been performed at 4.4 K, 77 K, and 300 K.

The heat transfer is assessed within the beam screen by simulations and experiments. The radiative heat transfer to the cold mass is estimated analytically instead. Tests have been carried out on a representative portion of the beam screen to preliminarily validate design features. Thermal contacts have been implemented in the FEM model to account for the actual beam screen characteristics. Comparisons with experimental results are presented.

The effects of the magnet quench on the beam screen in the case of two magnet quench protection systems are studied: the quench heaters [11], and the quench heaters coupled with the recently developed Coupling-loss-Induced Quench (CLIQ) [12]. The beam screen has been designed originally to cope with quench heaters only. Subsequently, it has then been modified in order to be compatible also with CLIQ. The two designs are outlined throughout the thesis and the differences are highlighted. The experimental setup of the magnet quench test for the beam screen is introduced.

1.7 Key results and relevance of the present work

Table 1.1 reports the four aims of this thesis, the methods adopted to fulfil them, the results, and the relative chapter.

Objective	Methods	Results	Chapter
Beam screen design	FEM	Self-weight deformation, thermal link design 1, supporting system design	2
BS material characterisation	literature review, measurements	Physical properties: magnetic, mechanical, thermal, electrical	3
BS behaviour during normal operation	FEM, measurements	Thermal model, thermal link design 2, BS temperature profile	4
BS behaviour during a magnet quench (quench heaters)	literature review, FEM	Multiphysics model 1, magneto-thermal and mechanical response of the BS	5
BS behaviour during a magnet quench (quench heaters + CLIQ)	FEM	Multiphysics model 2, magneto-thermal and mechanical response of the BS	6

TABLE 1.1: Objectives of the thesis with the relative methods, results, and the chapters in which these are treated. In the table BS stands for beam screen.

The design of the triplet area beam screen is described and its features are discussed. In particular, the self-weight deformation of the assembly has been assessed and the design of sub-components such as thermal links and supporting systems has been defined.

Several experimental campaigns have been conducted to complete the characterisation, where missing in literature, of the materials used in the beam screen. In particular, mechanical, thermal, magnetic, and electrical tests have been performed over a wide range of temperatures spanning from 4.4 K to 300 K.

The optimisation of the thermal transfer within the beam screen has been performed through simulation which has allowed to limit the number of costly experiments.

Similarly, FEM modelling has been used as a tool to establish the mechanical integrity of the beam screen whose design hinges on the accurate prediction of the magnet quench effects. In particular, two innovative multiphysics models have been developed to assess the magneto-thermo mechanical behaviour of the beam screen during a magnet quench. One model is devoted to the analysis of the beam screen when the magnet is protected by the classical quench heaters, while the other accounts for the magnet protected by the quench heaters and CLIQ. Compared to the analytical formulations used to design the beam screen currently installed in the LHC, the multiphysics FEM models developed in this research introduces multiple elements of novelty. First, self-inductance effects that reduce the induced forces are taken into account. Second, the one-way and two-way coupling of the magnetic physics with the mechanical and thermal ones are explored and the best trade-off is outlined. Third, the mechanical response of the assembly is evaluated dynamically over the whole evolution of the magnetic field decay rather than in a quasi-static way. Fourth, three dimensional geometries can also be studied allowing the design of the components placed along the beam axis. Finally, the mechanical integrity of the new beam screen has been demonstrated and a less conservative design has been obtained, which has permitted to relax the tight constraints on interfacing systems.

1.8 Structure of the thesis

The thesis is composed of seven Chapters. The structure of the thesis is shown in the flow chart of Fig. 1.5.

In Chapter 2 the history of the beam screen is introduced and the new HL-LHC triplet area beam screen requirements are presented. The components of the beam screen are described in detail and some FEM results are provided.

In Chapter 3, the measured physical properties of the materials used for the beam screen are reported. The material properties found in literature are included as well for comparison purposes.

In Chapter 4, the optimisation of the thermal behaviour of the beam screen during normal operation is presented. In addition, the experimental results are provided and compared with the numerical ones.

In Chapter 5, the magneto-thermo-mechanical response of the beam screen undergoing a magnet quench with quench heaters is illustrated. A description of the numerical model developed in COMSOL to study the beam screen is provided.

In Chapter 6 the magneto-thermo-mechanical behaviour of the beam screen in the case of a magnet quench, where CLIQ and the quench heaters are used as protection system, is described. The numerical model to study the effects of the this magnet protection scheme has been developed in COMSOL and Ansys. A description of the model is provided.

In Chapter 7, the final conclusions of the thesis are presented.

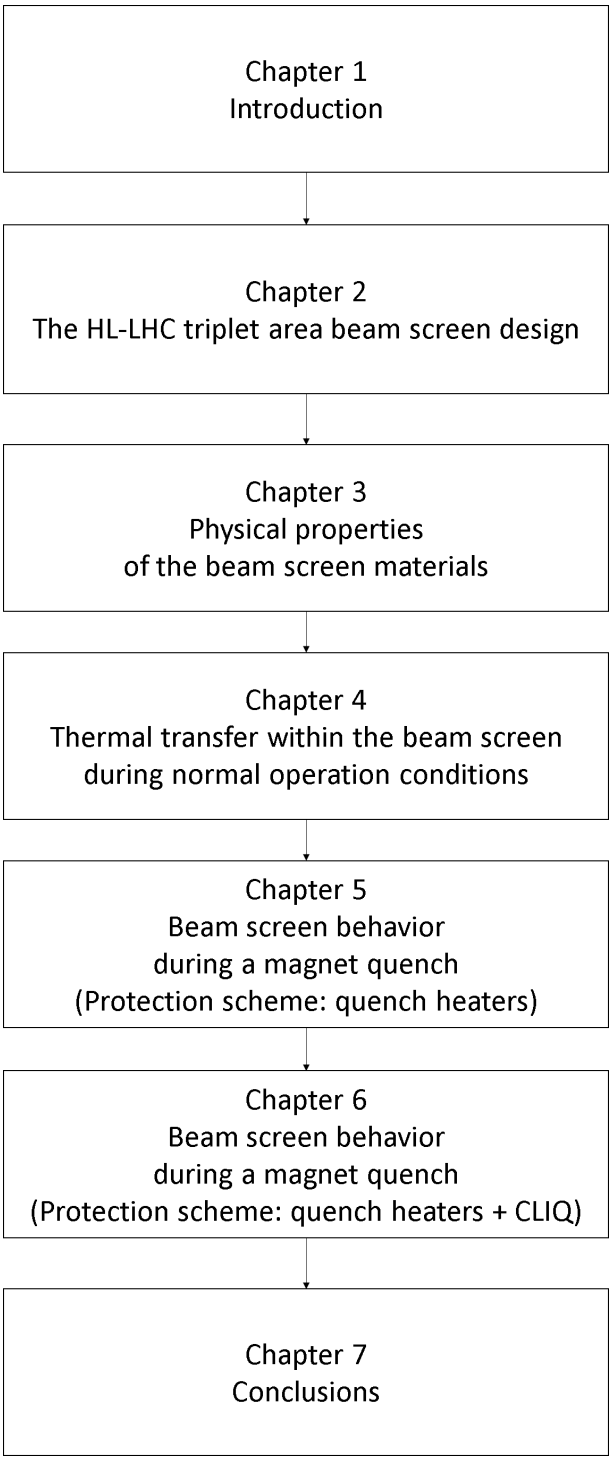


FIGURE 1.5: Flow chart of the chapters constituting the thesis.

Chapter 2

The beam screen

2.1 Main functions of the beam screen

2.1.1 Cold mass shielding

Beam-induced thermal loads would be entirely dissipated in the main beam pipe at 1.9 K if these are not shielded by the beam screen. Intercepting these loads at a more efficient temperature is not only convenient for energy consumption but also to passively reduce the risk of a magnet quench. In fact, the temperature increase of the magnet helium bath due to energy depositions is reduced, providing more margin of operation. The thermal loads are generated by the following phenomena:

- Synchrotron radiation:
  In circular accelerators, in particular in the dipole magnets, synchrotron radiation is emitted tangentially to the circular trajectories. This type of radiation, typical of particle accelerators, is represented by the critical photon energy which is the median of the continuous emitted spectrum. The radiated power, P, is given by $P = 6.0317 \cdot 10^{-12}\gamma^4/R$. It is proportional to the fourth power of γ, a relativistic factor, and inversely proportional to the accelerator radius R [13]. In the inner triplet region some synchrotron radiation is emitted due to the strong optics layout;

- Beam image currents:
  Image currents are induced by the charge of the beam along the pipe walls. Due to the current flow, the resistive nature of the pipe material gives rise to ohmic losses, which are proportional to the proton beam charge squared and to the electrical resistivity of the vacuum chamber wall material [8]. This calls for a lower resistivity of the wall material, hence a lower temperature;

- Electron cloud:
  Free electrons, within the LHC, are mainly the result of photons released by synchrotron radiations and beam ionisation that hit the chamber surface. The impingement of these electrons on the pipe wall surface can foster the release of secondary electrons according to a parameter defined as Secondary Electron Yield (SEY). The SEY depends on the energy of the incident electrons and on the surface characteristics [14]. This mechanism, known as electron cloud, can lead to severe energy depositions on the cold walls and dangerous vacuum instabilities that can threaten the beam lifetime [15].

Region	Length [m]	Beam-induced heat sources [W]			
		Synchrotron radiation	Impedance T BS= 70 K	Electron cloud (SEY = 1.1)	Nuclear debris
Q1 (Q1a +Q1b)	4.2 + 4.2	0.032	3	43.7	338
Q2a + corrector	7.2	0.075	2.7	17.3	130
Q2b + corrector	7.2	0.094	2.7	27.4	185
Q3 (Q3a +Q3b)	4.2 + 4.2	0.039	2.6	26.8	148
CP	11.2	-	0.8	2.2	111
D1	6.3	0.997	2	11.4	102
Beam pipe extensions	17.7	-	5.5	39.4	136

TABLE 2.1: Thermal loads estimated for the inner triplet of point 1 and 5. The synchrotron radiation loads are from [17], the impedance and electron cloud loads are from [18], and the nuclear debris loads are from [16].

- Debris from nuclear collisions (triplet area only):
  A consistent amount of physical debris coming from particle collisions are deposited in the vicinity of the interaction points resulting in the highest heat load amongst the above mentioned ones [16].

The estimated thermal loads corresponding to the above mentioned phenomena are summarised in Table 2.1 for the HL-LHC beam screen.

2.1.2 Vacuum stability

The beam screen has to ensure adequate vacuum conditions within the beam pipe. The gas desorption induced by photons and ions would raise the internal pressure to an unacceptable limit leading to beam degradation. At cryogenic temperatures, such a requirement is expressed in terms of equivalent hydrogen gas density and the upper-bound limit to attain the beam lifetime of 100 h is 10^{15} H_2/m^3 [8]. The extraction process of gas molecules from the beam screen walls is caused by photons and ionized particles [19]. Photons emitted by synchrotron radiation hit the surfaces and cause electrons and gas molecules to desorb. Subsequently, some molecules are cryopumped via physisorption on the same walls with a weak binding energy of around 100 meV. Some physisorbed particles will be redesorbed due to the unceasing particle bombardment (photons-electrons). However, the particle coverage will keep growing on the beam screen giving rise to a vapour pressure incompatible with that required for the targeted beam lifetime. To counteract this cascade effect, many oval slots are positioned along the beam screen to allow the cold bore to pump more efficiently and, as a consequence, obtain a better beam vacuum. On the cold bore the vapour pressure budget is negligible due to the very low temperatures (1.9 K). In addition, desorbing phenomena cannot occur since the condensed layer of particles is concealed from desorbing elements and synchrotron radiation. Fig. 2.1 shows the mechanisms of particle bombardment, desorption and physisorption in LHC dipoles. The holes ensure an equilibrium between the gas load and the beam screen pumping speed because, after a while, all the desorbed particles are pumped away by the slots [20].

The beam screen temperature plays an important role as it determines the pumping speed of the holes and the saturated vapour pressure within the pipe. The greater the temperature, the quicker the equilibrium is reached. A slow pumping speed would lead to unsuitable vapour pressures for the beam [13].

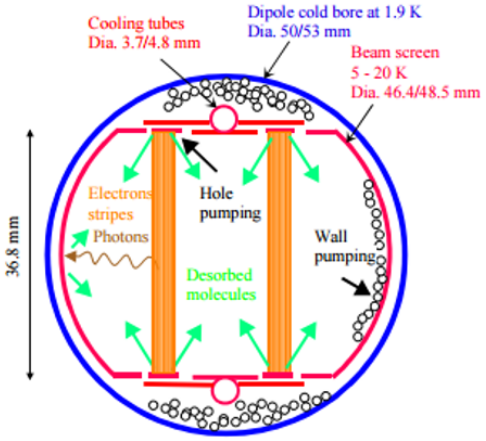


FIGURE 2.1: Gas dynamics phenomena within the cold bore and the LHC beam screen. Image taken from [20].

2.2 History of the beam screen

2.2.1 Superconducting Super Collider liner

The first example of beam screen was theorised during the design phase of the Superconducting Super Collider (SSC) in Texas, USA. Several studies demonstrated that the photon flux would have greatly increased the surface coverage of physisorbed particles on the cold bore and affected its pumping speed because of saturation. Since the cooling temperature was set to 4.2 K, the saturated vapour pressure would have not been compatible with the required beam vacuum conditions. Without any shielding, the upper boundary pressure could have been exceeded even by a factor of fifty. Following these considerations, the concept of a *beam screen* to be placed inside the magnet bore emerged. It was originally called liner and was partly perforated to ensure faster pumping of the recycled particles. This would have hidden the main beam pipe from particle impingement avoiding further desorbing mechanisms. This shielding mechanism is shown in Fig. 2.2. The liner was never realized because the U.S Congress suspended the funds for the SCC project. However, this concept paved the way for the actual beam screen used at CERN [21].

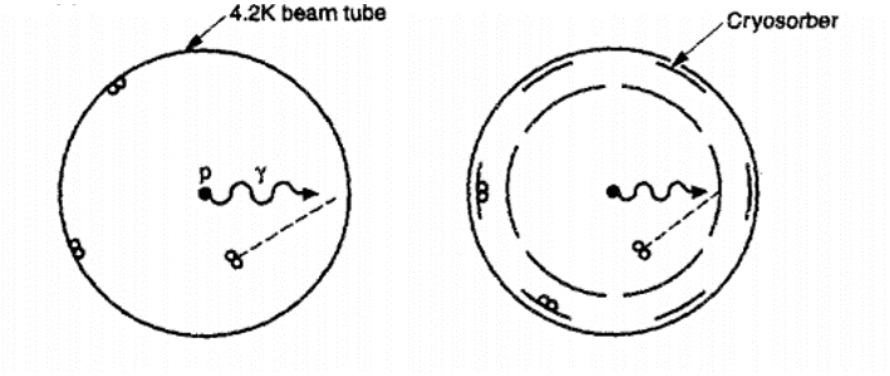
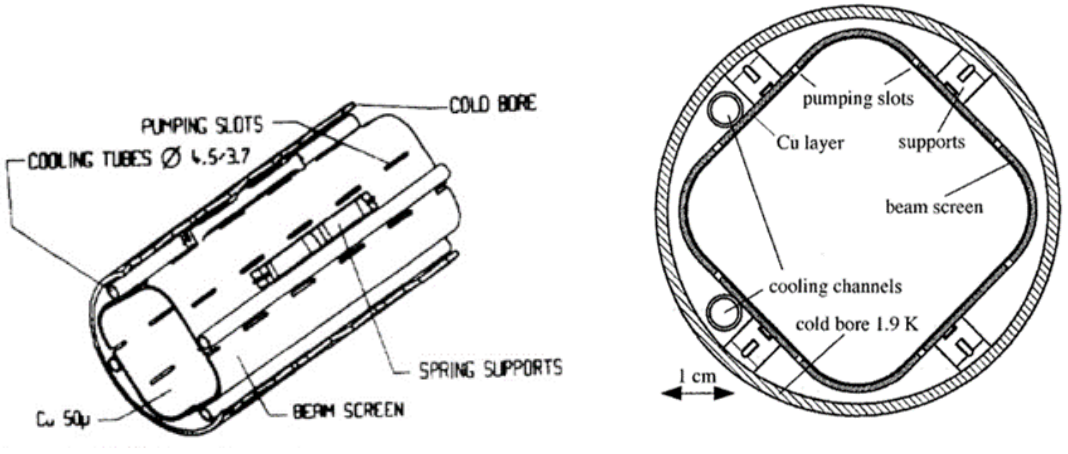


FIGURE 2.2: First concept of beam screen theorised at the SCC. Image taken from [21].



(A) (B)

FIGURE 2.3: Square beam screen developed at CERN.

2.2.2 Square design

The first prototype of beam screen was proposed at CERN for the LHC. Fig. 2.3 shows the square cross section of the assembly, chosen to maximize the horizontal and vertical aperture for the beam [22]. It was designed to intercept beam-induced thermal loads as well as to limit gas dynamics phenomena. This translated into multiple technical requirements. Firstly, the need to intercept and dissipate the beam-induced heat loads was met by keeping the beam screen at temperatures higher than those for the cold bore, namely from 5 to 40 K. This requirement was satisfied by means of super critical helium flowing in four capillaries welded on the main structure of the screen. To comply with the vacuum requirements, oval-shaped holes (amounted to 4% of the total surface coverage) were perforated in the shell of the screen to minimise thermal leaks to the cold bore.

A sufficient clearance was ensured between the screen and the main beam pipe to facilitate assembly operations. The internal surface of the beam screen was co-laminated with copper from 50 μm to 100 μm thick. However, the copper highly affected the induced currents and forces during a magnet quench and, consequently, a suitable trade-off was considered. In addition, all the materials used for the beam screen should not interact or influence the direction of the magnetic field within the beam pipe. To ensure the required magnetic field quality, the magnetic permeability of the materials had to be below 1.005.

2.2.3 Round flattened design

A 10 year-long research has been conducted for the development of the beam screen currently installed in the LHC machine. Important aspects such as gas dynamics, energy deposition, beam-impedance analysis and mechanical investigations have been taken into account. Due to the revision of mechanical and optical tolerances, the square cross section shape was abandoned [23]. Machine optics calculations showed that critical beam apertures would occur between dipole and quadrupole magnets. To solve this issue the horizontal physical aperture needed to be enlarged. Fig. 2.4 shows the new solution based on a cylinder flattened at the bottom and at the top to accommodate two cooling capillaries.

The supporting system is based on sliding rings made of a low thermal conductivity material. The capillaries are laser welded on the flat surfaces while the beam screen is formed by bending flat stainless sheets 1 mm thick,

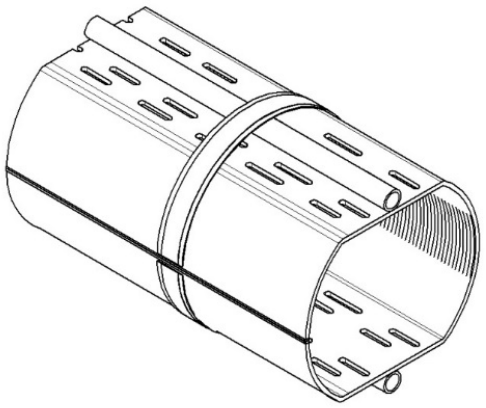


FIGURE 2.4: Round flattened beam screen.

co-laminated with a copper layer 75 µm thick. Lateral welds assure the closure of the beam screen. This assembly is placed in the superconducting dipole and quadrupole magnets of LHC along 2 * 22 km of the LHC, see Fig. 2.5.

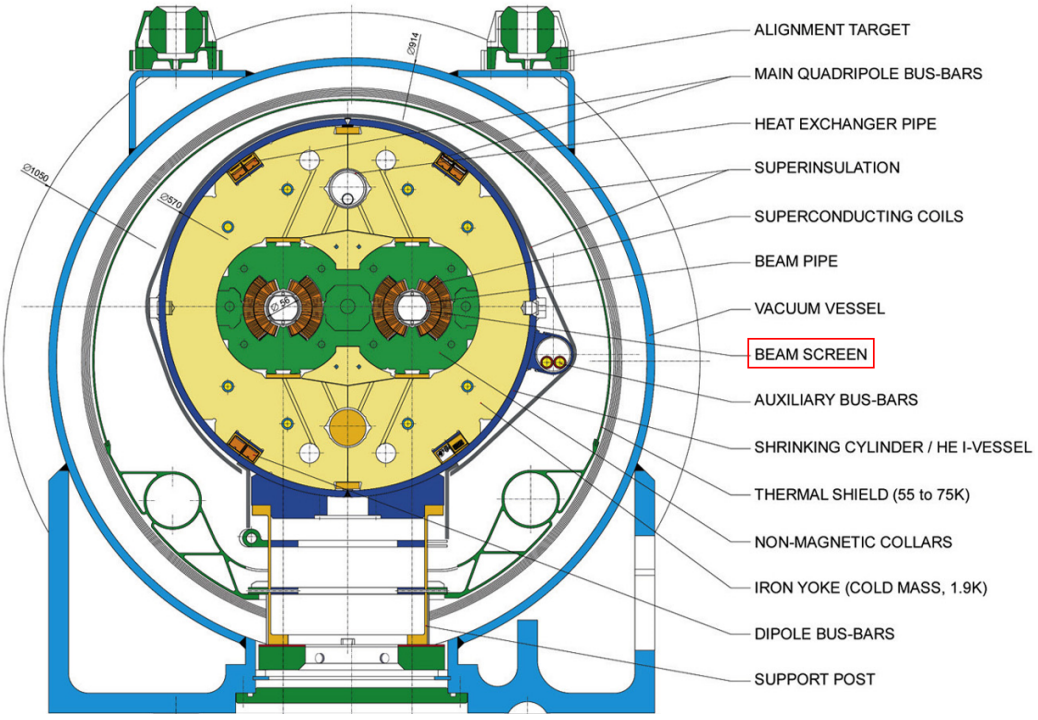


FIGURE 2.5: Standard cross section of the LHC dipole. The beam screen label is highlighted in red.

2.2.4 The need for a new beam screen

In the framework of the HL-LHC upgrade, several studies based on the investigation of the collision debris trajectories have shown unprecedented energy depositions in the vertical and horizontal plane of the beam screen close to the main experiments, *i.e.* ATLAS and CMS [24]. The scattering would affect the cryogenic system surmounting its tolerated power absorption. In addition, the superconducting magnets would not bear this severe burden and would be damaged under the continuous radiation bombardment. The thermal load and gas rise would

also cause magnet quenches leading to the interruption of the machine operation. Therefore, a new beam screen ensuring the shielding of collision debris needed to be designed.

2.3 The HL-LHC beam screen

The design of the LHC beam screen has laid the foundation for the new HL-LHC beam screen. However, considering the higher energy deposition the new design calls for an integrated shielding system for the assemblies located in the triplet region and in the D1 separation/recombination dipole. Also the D2 and Q4 beam screens will be replaced with octagonal shaped screens. These will have a larger aperture than the current ones but without shielding inserts.

2.3.1 Functional requirements

The functional requirements of the new beam screens are [25] reported below:

- The system lifetime must be greater than that of the inner triplet life time, namely 20 years of operation and 50 quenches;
- The system must fulfil the required performance in terms of vacuum stability, beam lifetime, and background to the experiments;
- The shielded beam screen must be perforated (or shadowing) to fulfil the vacuum performance, *i.e.* allow pumping of the molecules onto the cold bore;
- The cold bore temperature must be held below 3 K to allow cryosorption of all molecules with the exception of helium;
- The shielded beam screen must be heatable to allow a flushing of the physisorbed gas onto the shielded beam screen towards the cold bore during machine stops;
- The vacuum surface of the shielded beam screen must withstand a dose of several hundred MGy during its life time;
- The shielded beam screen must withstand the Lorentz forces induced by the eddy current during a quench;
- The temperature of the shielded beam screen must be actively controlled in a given temperature range;
- To minimise the heat load on the shielded beam screen due to electron cloud, a coating, *e.g.* amorphous carbon or a clearing electrode system, must be studied, validated, and implemented;
- The system must be compatible with impedance performance;
- The system must be compatible with the machine aperture.

2.3.2 The shielded beam screen

The major feature introduced by the HL-LHC beam screen is the exploitation of tungsten-based inserts (known also as heat absorbers) used as shielding material. The selected tungsten alloy, having a high atomic number, is a suitable material to absorb the larger heat generated by the particle collisions debris of the HL upgrade. The new HL-LHC beam screen has come a long way from its first conceptual design consisting of a circular pipe made of stainless steel and round heat absorbers made of a tungsten alloy [26], see Fig. 2.6. This solution has been abandoned due to the complexity of the heat absorbers manufacturing.

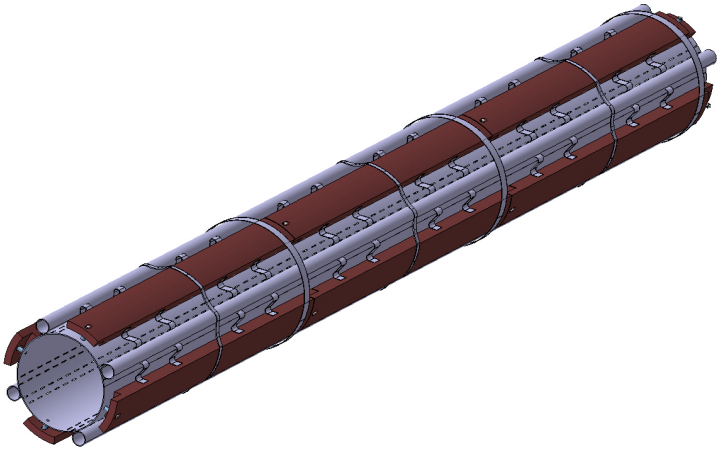


FIGURE 2.6: First concept of the HL-LHC beam screen.

The first evolution of the design was driven by the need to simplify the geometry of the heat absorbers. For this purpose an octagonal shaped pipe has been developed. In this way, the surface of the heat absorber leaning on the pipe is flat and, therefore, easier to manufacture. A further evolution of the design has been driven by the need to increase the flexibility of the beam screen assembly. This has been obtained by connecting mechanically the heat absorbers to the octagonal pipe and not by brazing them as initially foreseen [27]. This has allowed a reduction of the octagonal pipe thickness and therefore a gain in the aperture.

The current beam screen design, shown in Fig. 2.7, is a complex octagonal shaped pipe made of stainless steel P506 inserted into the cold bore of the triplet area superconducting magnets. The high Mn and N content of the P506 grade guarantees the austenitic phase stability and, therefore, a low impact on the magnetic field quality. The shielding action of the 1.9 K cold mass from physics debris and beam-induced heating is obtained by placing four heat absorbers on the vertical and horizontal flat surfaces of the octagonal pipe.

The four tungsten alloy blocks are simply laid along the longitudinal walls of the screen, centred by pins welded on the screen and kept firmly in place by titanium rings. This solution enables to overcome soldering issues between stainless steel and tungsten that would give rise to high residual stress during cooling down. In fact, the thermal contraction of the tungsten alloy is around 0.09 % while that of stainless steel is 0.29 % at 50 K.

The heat retained by the absorbers is dissipated through a stand-alone cooling circuit at a thermodynamically efficient temperature set between 60 K and 80 K. Highly conductive copper links connect the blocks to the stainless

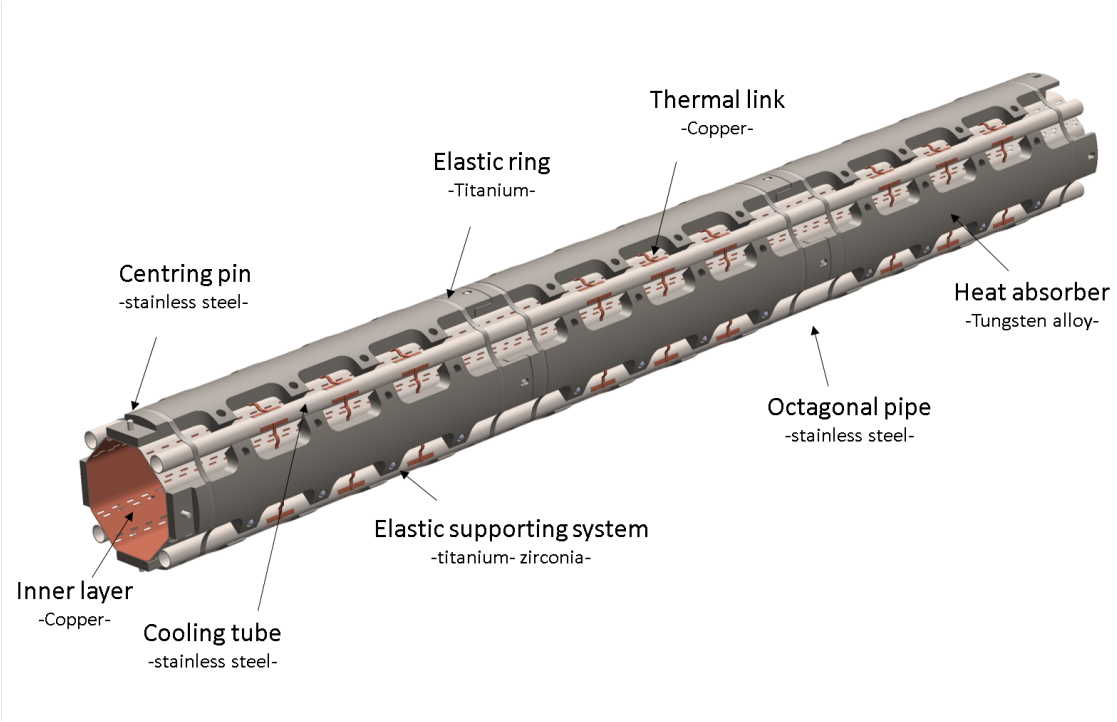


FIGURE 2.7: HL-LHC beam screen placed in the Q1 magnet.

steel cooling tubes placed on the surfaces of the pipe tilted at a $+/-45°$ angle. To limit the heat transfer to the cold bore supporting systems composed by titanium springs and ceramic balls are positioned in the lateral extension of the heat absorbers. This enables to leave a 1.5 mm gap between the heat absorbers and the cold bore, avoiding any contact between the warm heat absorbers and the cold mass. The internal surface of the beam screen is covered by 75 μm of co-laminated Oxygen-Free Electronic (OFE) copper with a Residual-resistivity ratio (RRR) equal to 100 to minimise resistive wall losses and coupling impedance. The assembly guarantees a good vacuum stability for the beam lifetime through slots distributed along the surfaces of the screen tilted at $+/-45°$ angle. The beam-induced particles escaping randomly through the slots are trapped indefinitely on the walls of the cold bore at 1.9 K.

2.3.3 Beam screen dimensions

Two beam screens have been designed for the HL-LHC triplet region due to different shielding and aperture requirements. In the Q1 magnet, the closest to the interaction point, the need of shielding material is higher than in the other beam screens due to a denser nuclear scattering than at longer distance from the interaction point. The beam screen positioned in the Q2a and Q2b, Q3, CP, and D1 magnet need, therefore, less shielding material. This results, in turn, into a wider beam aperture than for the Q1 type. It is worth noting that the Q2a, Q2b, Q3, CP, and D1 beam screens share the same design. Consequently, any reference throughout the text to the Q2x shape will be valid also to the CP, Q3 and D1 beam screens, unless otherwise specified. In Fig. 2.8 the cross sections of the two beam screen versions are shown, while in Table 2.2 the dimensions and the tolerances are reported.

The Q1 beam screen is inserted in the so called MQXF single-bore magnet, see Fig. 2.9.

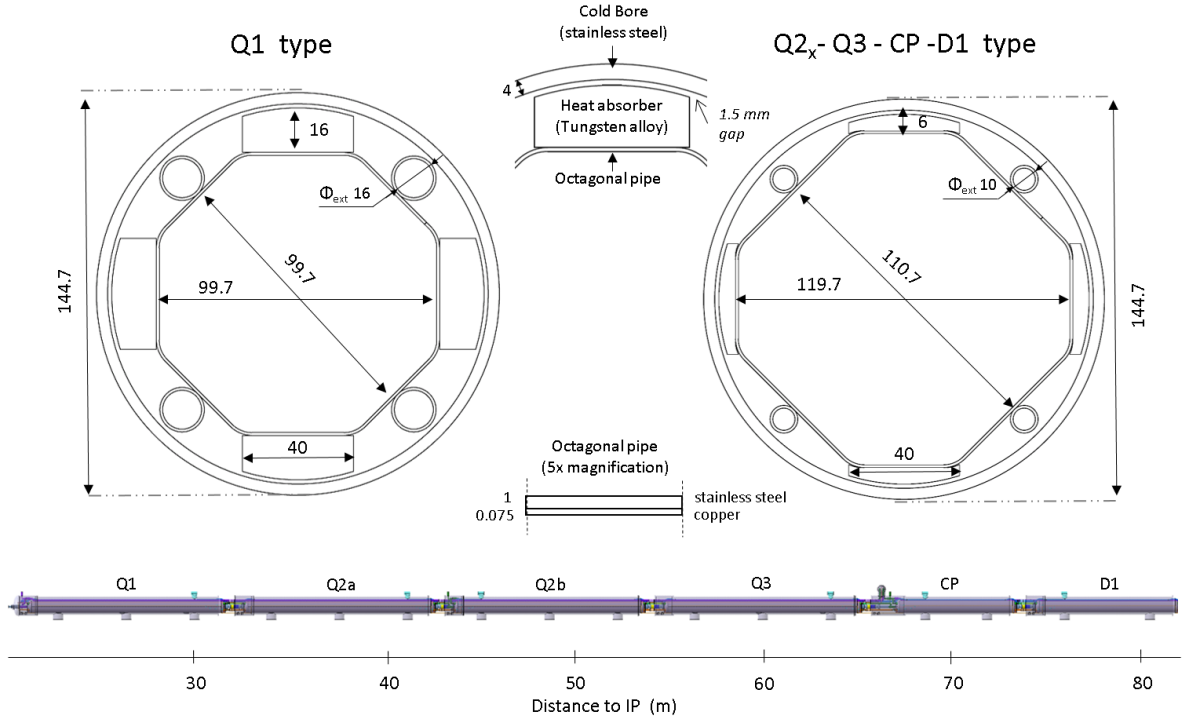


FIGURE 2.8: Cross section of the new Q1 type and Q2x - Q3- CP- D1 type HL-LHC beam screen. The layout of the triplet region is shown below the cross sections. The dimensions of the beam screens are reported in mm.

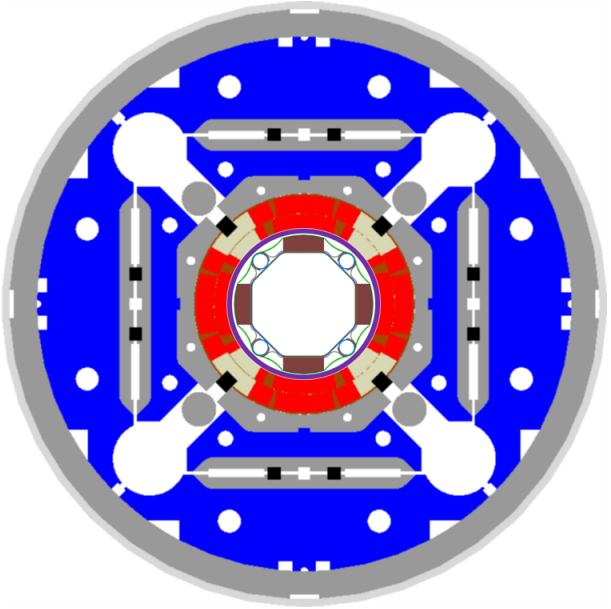


FIGURE 2.9: Cross section of the Q1-MQXF magnet including the cold bore and the beam screen.

Beam screen version	Cold bore		Beam screen						
	Inner diameter	Thick-ness	Aperture +/ −45°	Vertical		Horizontal		Cool. tubes	Shield. height
				Shape	Position	Shape	Position		
Q1	136.7 H8	4 +0.35	99.7; 99.7	± 1.15	-1.23 +0	±1.1	+ 0.65	16*1	16
Q2a	136.7 H8	4 +0.35	119.7; 110.7	± 1.15	-1.05 +0.11	±1.1	+ 0.65	10*1	6
Q2b	136.7 H8	4 +0.35	119.7; 110.7	± 1.15	-1.05 +0.11	±1.1	+ 0.65	10*1	6
Q3	136.7 H8	4 +0.35	119.7; 110.7	± 1.15	-1.05 +0.11	±1.1	+ 0.65	10*1	6
CP	136.7 H8	4 +0.35	119.7; 110.7	± 1.15	-1.05 +0.11	±1.1	+ 0.65	10*1	6
D1	136.7 H8	4 +0.35	119.7; 110.7	± 1.15	-1.05 +0.11	±1.1	+ 0.65	10*1	6

TABLE 2.2: Summary of the dimensions and tolerances of the triplet area HL-LHC beam screens and cold bores.

2.3.4 Self-weight deformation and aperture reduction

The weight of the Q1 version beam screen is 51.04 $\mathrm{kg\,m^{-1}}$, while that of the Q2 version is 21.2 $\mathrm{kg\,m^{-1}}$. The weight of the cold bore is 13.62 $\mathrm{kg\,m^{-1}}$. Fig. 2.10 shows the deformation and the von Mises stress due to the weight of the heaviest beam screen, namely the Q1 version. aa

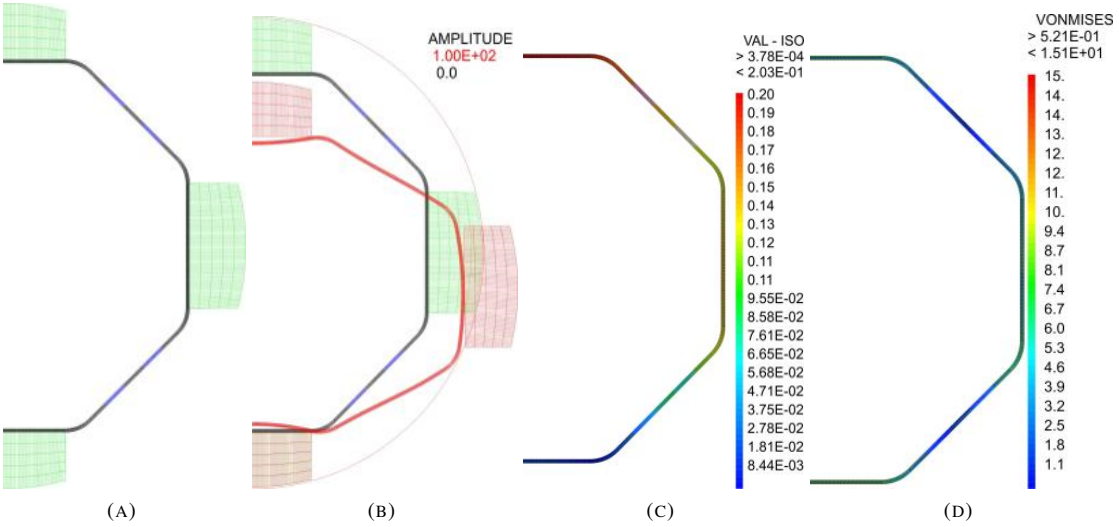
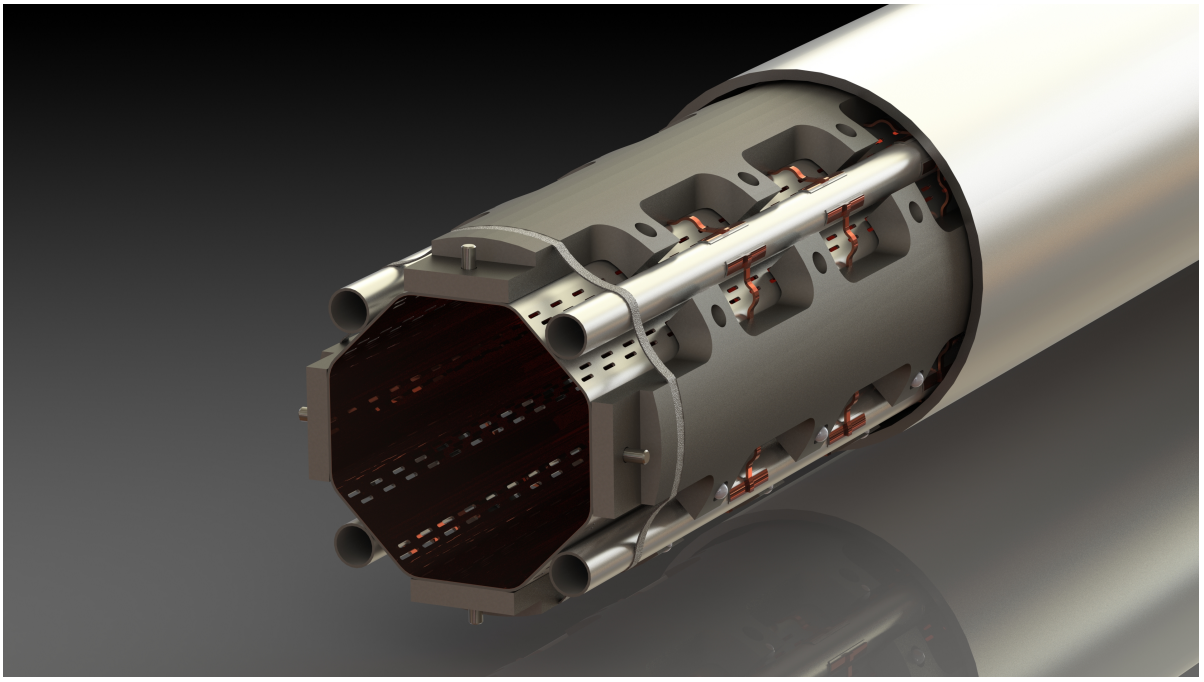


FIGURE 2.10: Q1 beam screen unloaded in (a) and with gravity load in (b). The magnification factor is 100. The deformation of the beam screen in (c) is expressed in mm, while the von Mises stress in (d) is expressed in MPa.

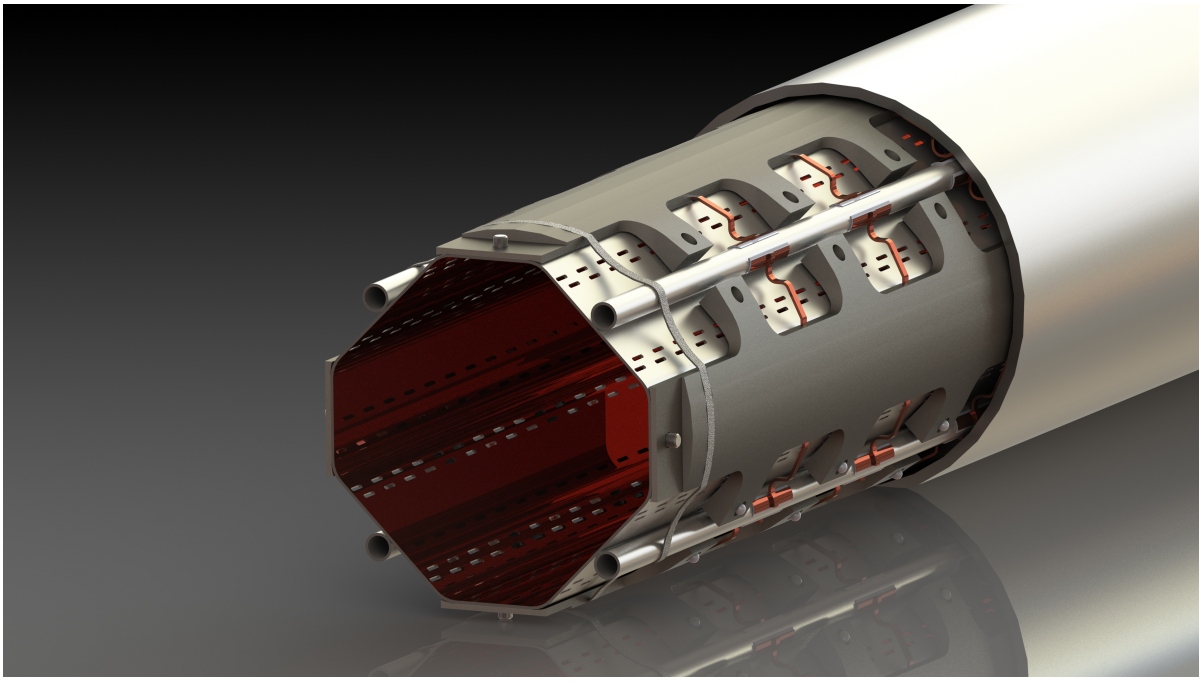
The deformation of the beam screen due to its weight causes a reduction of aperture. For the Q1 beam screen it is -0.2 mm, while for the Q2 it is -0.07 mm. Further aperture reductions are due to thermal contractions, for the Q1 it is -0.26 mm and for the Q2 is -0.31 mm. The copper layer thickness causes an aperture reduction for all the beam screens of 0.15 mm.

2.3.5 Description of the HL-LHC beam screen components

The Q1 and Q2 versions of the beam screen are illustrated in Fig. 2.11.



(A)



(B)

FIGURE 2.11: Rendering of the Q1 and Q2 beam screen.

Octagonal pipe

The octagonal pipe is made of the austenitic stainless steel P506 1 mm thick co-laminated with 75 μm of high purity copper. The inner copper layer minimises the electrical resistance of the internal walls and, therefore, the resistive heat load due to image currents. The pumping slot scheme located at +/- 45° orientation has a random pattern and is obtained from a flat sheet by means of a punch press. Subsequently, the octagonal pipe is obtained by a bending sequence of the sheet aimed at obtaining two half shells. The pipe is composed of two half shells 6 m long welded on the longitudinal sides. To minimise the heat load on the shielded beam screen due to electron cloud, an amorphous carbon layer will be coated on the internal walls of the pipe [28]. The specially developed austenitic stainless steel grade ensures a magnetic permeability at the operating beam screen temperature below the 1.005 limit [29]. Pumping slots along the length of the beam screens result in an effective pumping speed for the desorbing particles that can leave the pipe and are then trapped into the opposing cold bore wall at 1.9 K.

Centering pins

The centering pins are made of the austenitic stainless steel P506 welded by electrical discharge on the surfaces of the octagonal pipe. The function of the pin is to position the tungsten blocks longitudinally.

Cooling tubes

Four cooling tubes made of the austenitic stainless steel P506 are laser spot welded on the octagonal pipe at +/ -45° angle. These are part of the active cooling system that keeps the temperature of the beam screen within the required range (60 - 80 K).

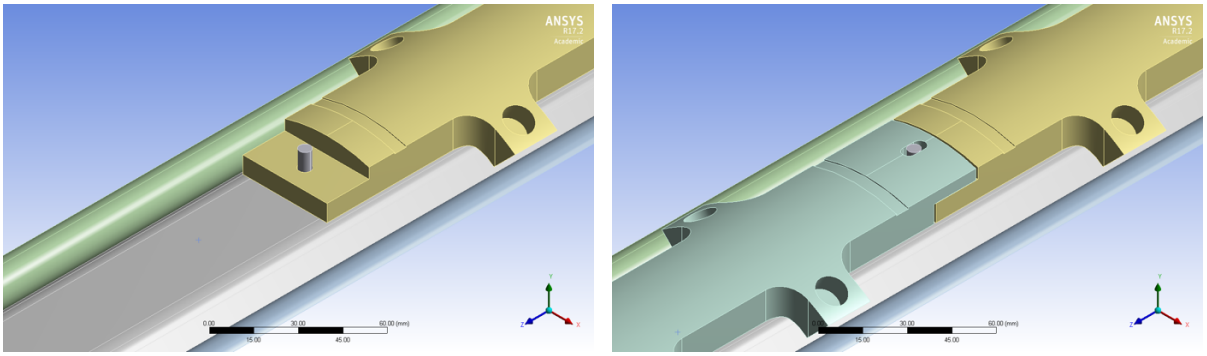
Heat absorber

The heat absorbers are made of a tungsten alloy made of 95 % tungsten, and 5 % of nickel and copper. The length of the absorber, 400 mm, is imposed by limitations of the manufacturing processes. The absorbers are positioned along the vertical and horizontal planes in accordance to the debris trajectories [16]. The absorbers present some lateral extensions over 20 % of their total length to intercept the debris that are directed at +/ -45° angle. The thickness of the absorber is determined by the intensity of the collision debris [16] and, therefore, by the distance from the interaction point. As shown in Fig. 2.12 the geometrical configuration of the rear and front part of the heat absorbers enables an overlap so that one single pin can hold two absorbers at the same time. This halves the number of total pins needed to position the absorbers.

Elastic rings

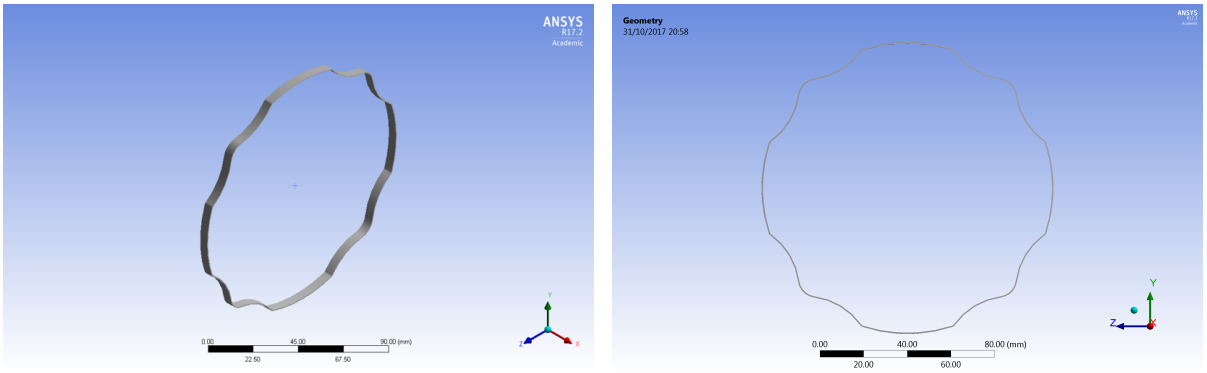
The elastic ring, shown in Fig. 2.13, is made of titanium grade 5. It is 0.5 mm thick and 5 mm wide. Two rings per block keep the heat absorbers firmly on the octagonal pipe during operation. At the same time the shape of the elastic ring provides enough flexibility to allow the expected displacement of the absorbers with no permanent damage during a magnet quench. The rings are manufactured by 3D printing technology.

A FEM analysis has been carried out to assess the mechanical stress in the elastic ring during a magnet quench when the heat absorbers are expected to move outwardly, as shown in Fig. 2.14, and impact on the cold bore.



(A) (B)

FIGURE 2.12: Overlapping of two consecutive heat absorbers over one single centring pin.



(A) (B)

FIGURE 2.13: Elastic ring made of titanium grade 5.

The displacement imposed on the heat absorbers is 1.7 mm (1.5 mm gap + 0.2 mm cold bore deformation). The analysis is simplified as only the heat absorbers and the titanium rings are considered. The four red edges shown on the bottom right side of Fig. 2.14 are considered fixed to represent the cooling tubes.

The highest von Mises stress is shown in Fig. 2.15 for the Q1 and Q2 ring, respectively. The highest stress in the areas not affected by the boundary conditions is 1160 MPa for the Q1 and 1210 MPa for the Q2 ring. Therefore, the rings should not undergo any failure or plastic deformation as the elastic limit of titanium grade 5 is around 1500 MPa at 60 K.

The spring constant of the two rings has been calculated according to the configuration shown in Fig. 2.14 by considering the ratio between the load and the relative displacement. It turns out that for the Q1 version $k_{Q1} = 132$ N/mm, while for the Q2 version $k_{Q2} = 188$ N/mm.

Thermal link

The thermal links are made of OFE copper RRR 100 1mm thick and 3 or 5 mm wide (according to the quench protection system). Their requirements are multiple as they have to transfer the heat from the absorbers to the cooling tube, withstand the effects of a magnet quench without undergoing plastic deformations, and be flexible enough to not hinder the movement of the heat absorber along its normal direction. In fact, during a quench the

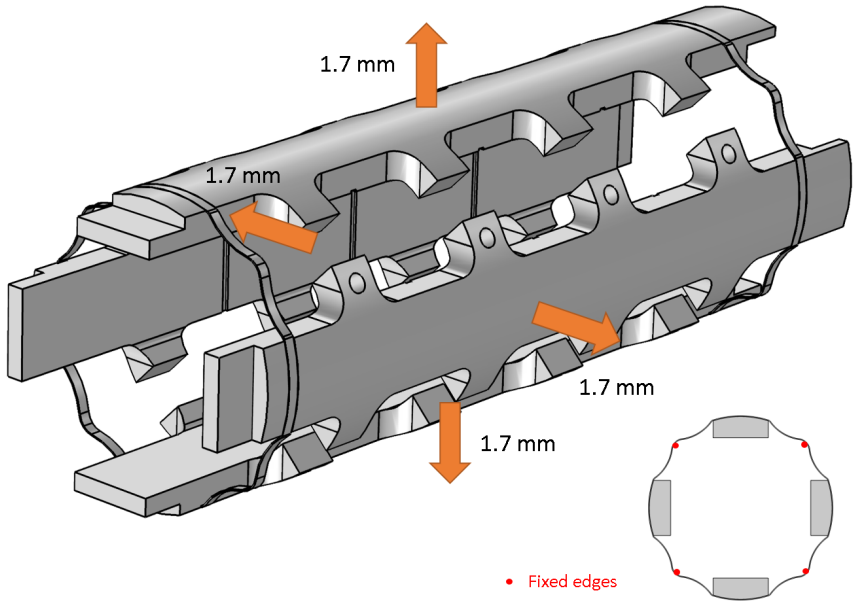
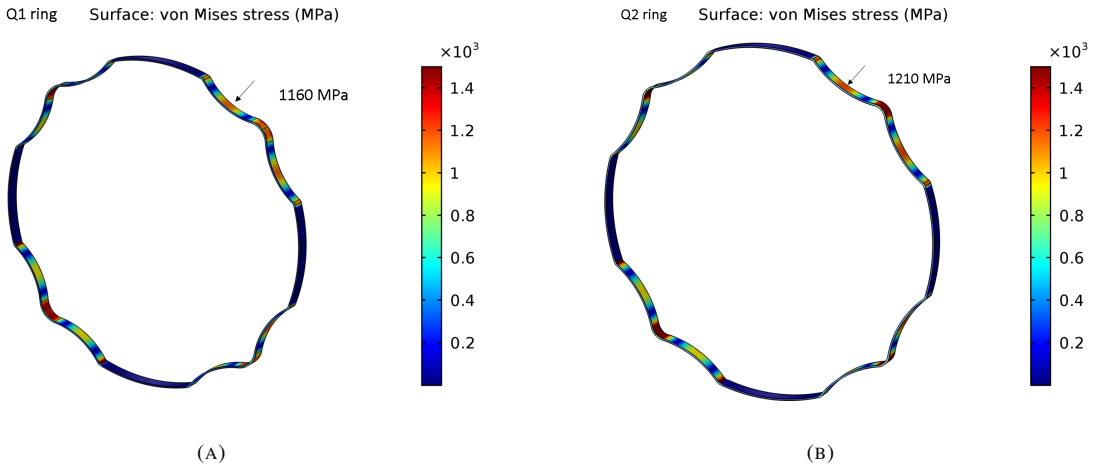


FIGURE 2.14: Simplified setup of the beam screen to simulate the stress of the elastic ring during a magnet quench.

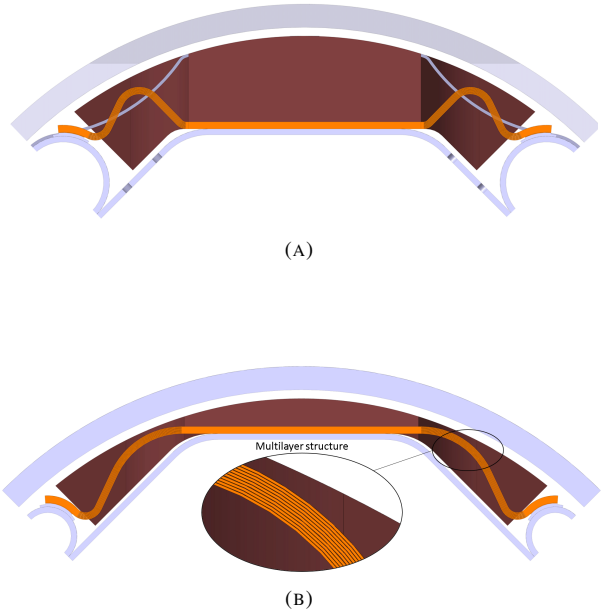


(A) (B)

FIGURE 2.15: Von Mises stress in the titanium ring of the Q1 beam screen (a) and Q2 beam screen (b).

absorber moves outwardly and a stiff link would not allow the absorber to return to its original position. This would cause a failure in the collision debris absorption and, consequently, higher thermal load to the cold bore.

The required flexibility is obtained by piling up ten copper layers, each 0.1 mm thick, in the two lateral sides of the thermal link, see Fig. 2.16. The extremities of this multilayer structure are welded to a bulk central strip and two other bulk lateral elements, see Fig. 2.17. The central part of the link is brazed underneath the heat absorber in a dedicated groove. The round plates, called *interfacing pads*, are made of P506 0.6 mm thick co-laminated with 75 µm of copper to allow the brazing with the bulk elements at the extremities of the link. The stainless steel edges of the interfacing pads are ultimately laser welded on the cooling tubes. The Q1 and Q2 versions of the thermal link are sown in Fig. 2.18. It is worth noting that the unfolded dimensions of the two links are the same.



(A)

(B)

FIGURE 2.16: Cross section along the thermal link of the Q1 and Q2 beam screen in (a) and in (b), respectively. In (b) the multilayer structure of the lateral part of the link is highlighted.

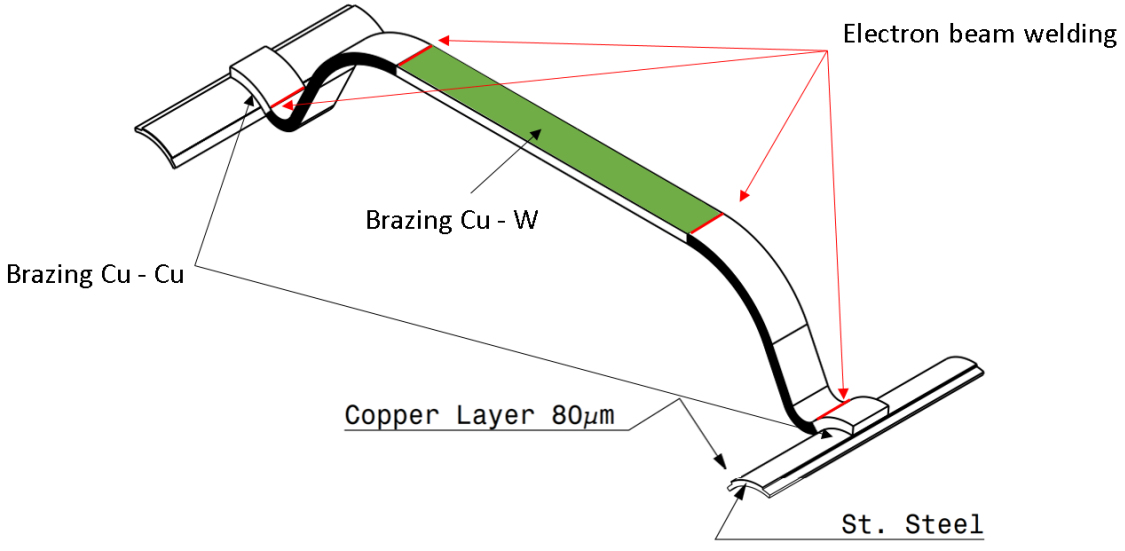


FIGURE 2.17: Brazing and welding position of the Q2 thermal link.

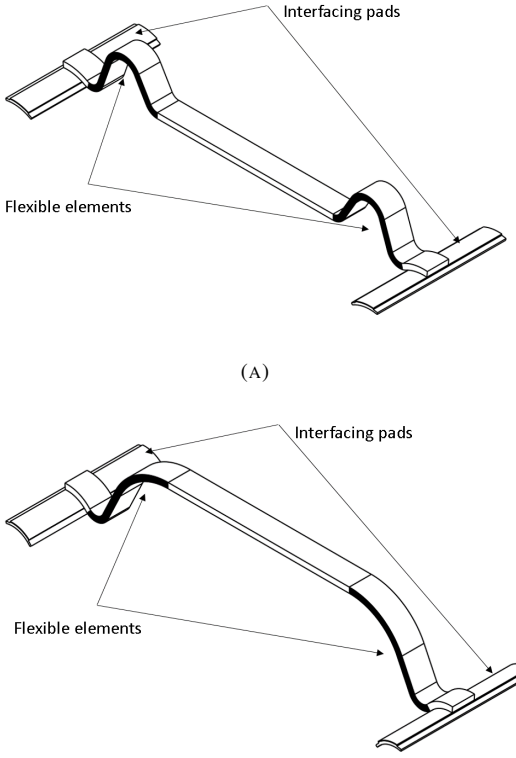
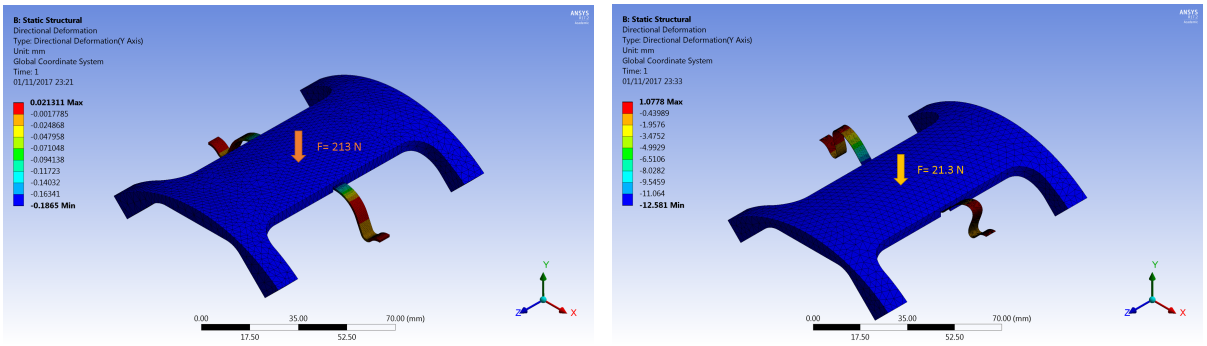


FIGURE 2.18: Thermal links of the Q1 and Q2 beam screen with the relative interface pads in (a) and in (b), respectively.

The flexibility of the multilayer thermal link has been demonstrated through a FEM analysis by comparison with a bulky link 5 mm wide. After a quench, the force acting on the thermal link is the contribution of the weight of the heat absorber and of the spring-back of the elastic ring. The simulations have been performed for the stiffest thermal link, namely the one of the Q2 beam screen. Knowing the spring constants, the elastic force given by the ring due to a normal displacement of the heat absorber of 1.7 mm is 320 N. Considering that one absorber is kept firmly in place by two rings, the total elastic force is then 640 N. For sake of simplicity, one single thermal link has been considered in the FEM analysis. As there are three links per block, the consequent compression force is then one third, namely 213 N. Such a force is applied on the heat absorber to quantify the displacement of a bulky copper thermal link and a flexible one. In this analysis, the force due to the weight of the absorber is negligible. For the multilayer link, one tenth of the force is applied on the heat absorber as only one layer 0.1 mm thick has been considered in the simulation. The displacement of the heat absorber for the two cases is shown in Fig. 2.19. It turns out that the bulky thermal link does not enable the heat absorber to recover the 1.7 mm gap as the maximum vertical stroke is around 0.19 mm. The multilayer link allows a stroke of 12.5 mm instead. Therefore, this analysis demonstrates the need of a flexible thermal link.

Supporting system

The supporting system of the beam screen is integrated in the lateral extensions of the heat absorbers. It supports the whole assembly in a way to keep the required gap of 1.5 mm from the cold bore and limit, therefore, the heat transfer to the cold mass. The mechanism consists of a titanium spring and a zirconia sphere. The stiffness of the



(A) (B)

FIGURE 2.19: Displacement, in mm, of the Q2 bulky thermal link in (a) and multilayer thermal link in (b) due to the elastic ring acting onto the heat absorber.

spring needs to be tailored to the weight of the beam screen in order to sustain the static load of the assembly as well as to leave the gap.

The design of the spring has been carried out by means of numerical simulations in order to determine the suitable shape, the maximum stroke, and the displacement associated with the weight of each beam screen type. These parameters have to be compatible with the dedicated dimensions of the holes integrated in the lateral extensions of the heat absorbers. It is worth noting that the maximum stroke of the spring has to be sufficiently larger than the displacement associated with each beam screen weight. In fact, during a quench the heat absorber and the cold bore come into contact causing an additional contraction of the spring-sphere system. In this case, the sphere needs to be pushed inside the hole by 1.5 mm without any contact between the spires of the spring. These requirements are addressed by the conical spring shown in Fig. 2.20 specifically manufactured through 3D printing technology. The maximum stroke of the Q1 spring is 2.7 mm, while that of the Q2 is 2.05 mm.

The heat transfer to the cold bore is limited by the low conductive ceramic spheres. Only the bottom side of the assembly is equipped with the spring, see Fig. 2.21. This translates in 40 spheres per meter in contact with the cold bore.



(A) (B)

FIGURE 2.20: Supporting system for the Q1 beam screen in (a) and Q2 beam screen in (b).

From simulations, the stiffness of the Q1 and Q2 springs turns out to be 17.46 N/mm and 15.76 N/mm, while the relative compression due to the weight of each beam screen type is 1.06 mm and 0.48 mm, respectively. Knowing the total height of the spring and the compression due to the beam screen weight, the depth of the heat

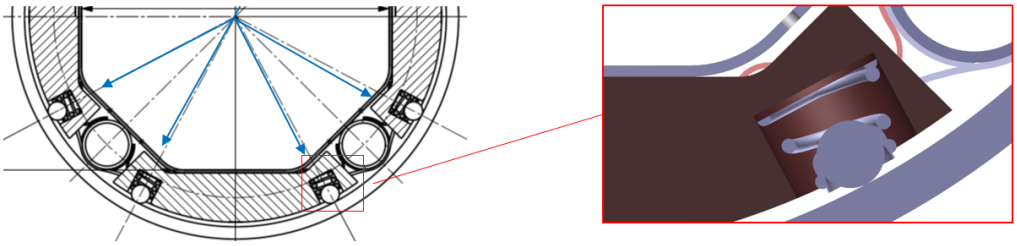
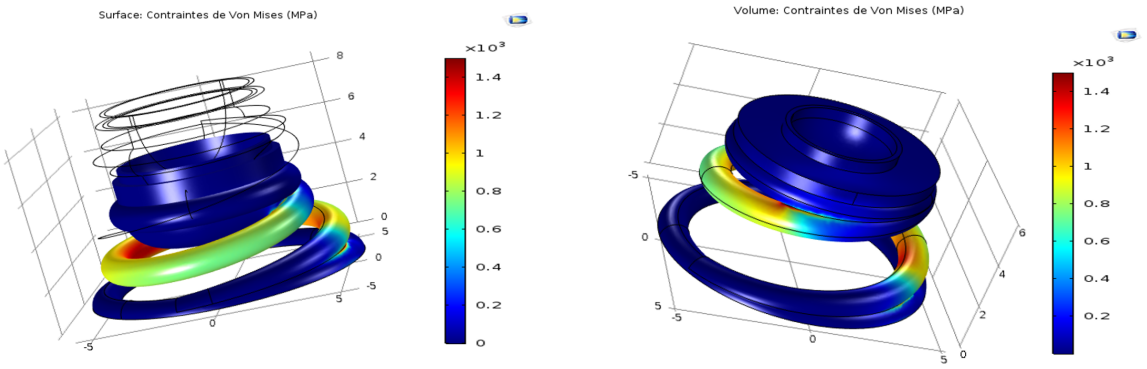


FIGURE 2.21: Cross section of the Q1 beam screen. The supporting mechanism is magnified in the red box.

absorber hole to guarantee the 1.5 mm gap with the cold bore has been determined. It is 8.5 mm for the Q1 block and 5.7 mm for the Q2 block.

The mechanical stress corresponding to the weight of the beam screen and the additional 1.5 mm compression during the quench is shown in Fig. 2.22 for the Q1 and Q2 spring, respectively. The stress is 1350 MPa for the Q1 version and 1300 MPa for the Q2 version. These values are both below the elastic limit of titanium grade 5 at 100 K (around 1500 MPa) [30].

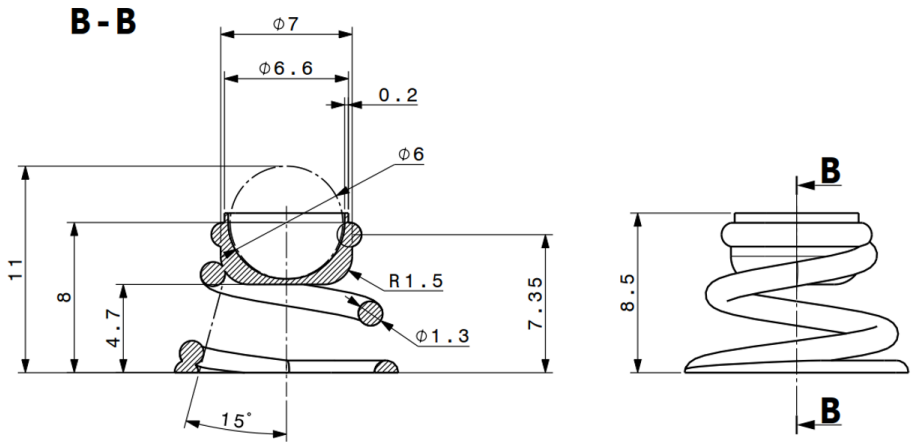


(A) (B)

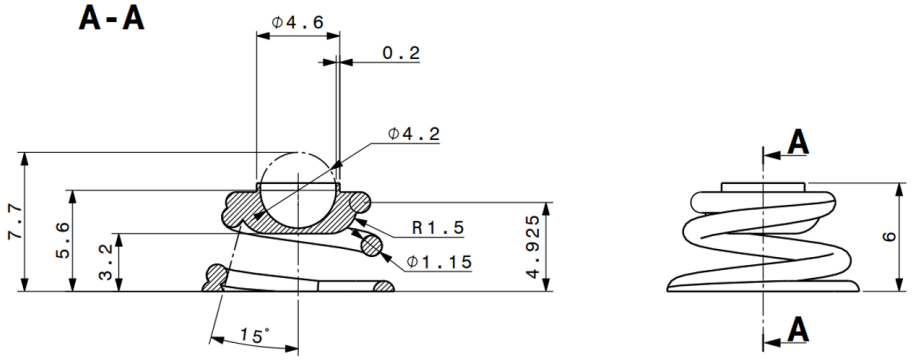
FIGURE 2.22: Von Mises stress [MPa] due to the maximum displacement of the Q1 spring (a) and Q2 spring (b).

The dimensions of the Q1 and Q2 springs satisfying the design requirements are reported in Fig. 2.23a and in Fig. 2.23b, respectively.

Several prototypes of the springs have been manufactured and the relative stiffness has been measured. For the Q1 spring the stiffness is 16.27 $\pm$ 0.8 N/mm while for the Q2 spring is 15.75 $\pm$ 0.26 N/mm. For the Q1 spring the value is slightly lower than expected. This might due to mechanical precision faults of the 3D additive manufacturing.



(A)



(B)

FIGURE 2.23: Dimensions (in mm) of the Q1 spring (a) and Q2 spring (b).

Cold bore

The cold bore is a tube 4 mm thick with no welds made of stainless steel 316 LN. It houses the beam screen assembly and guarantees mechanical stability under the external helium bath pressure of 20 bar. According to standard EN13445-3 (non fired pressure vessel), a thickness of 4 mm leads to a safety factor of 2.35.

2.4 Conclusions

This chapter has presented the functional requirements of the new HL-LHC beam screen placed in the inner triplet of the ATLAS and CMS experiment. Amongst these, the two most important ones have been explored in detail, *i.e.* the cold mass shielding and the vacuum stability. The beam screen shields the cryogenic system from several beam-induced heat loads, such as electron cloud, synchrotron radiation, image currents and collision debris. To dissipate the 1 W heat rate without the beam screen, a cooling energy of nearly 1 kW would be required by the cold bore at 1.9 K. With the beam screen, the heat is intercepted at a higher temperature to improve the Carnot efficiency of the cryogenic cycle. The required vacuum stability is obtained through pumping slots placed on the

screen. In this way, the desorbing particles within the beam screen can escape through the slots and be trapped on the cold bore at 1.9 K. In fact, at this temperature a cold surface acts as a pump for many gases.

The historical evolution of the beam screen has been described. The first concept, theorised for the SCC, is based on the idea of concealing the cold bore from the photon flux and therefore from the surface coverage of physisorbed particles. The application of this concept was implemented at CERN through two actively cooled devices, namely a squared-shape and a round flattened beam screen. The former has been rejected due to optics reason, while the latter has become the standard beam screen currently in use in the LHC. However, in the framework of the HL-LHC upgrade it has been found that the increased luminosity calls for a completely new design, characterised by tungsten-based inserts intercepting the increased collision debris and a wider aperture due to the stronger focusing magnets.

The design of the new HL-LHC beam screen has been presented. The new beam screen is an octagonal shaped pipe made of a 1 mm thick austenitic stainless steel. The screen is co-laminated with 75 μm of OFE copper to lower the impedance seen by the beam. In addition, a pattern of pumping slots is punched on the tilted sides of the screen to ensure the required vacuum stability for the high-energy beam. Tungsten-based inserts are laid on the flat surfaces of the octagonal pipe and positioned by centring pins to intercept the collision debris. The aperture of the beam screen is determined by the thickness of the absorbing inserts. The beam screen closest to the interaction point, *i.e.* the Q1 beam screen, must intercept more debris compared to those placed further away, *i.e.* the Q2, Q3 and D1 beam screen, and therefore requires thicker inserts.

For the Q1 beam screen, the thickness of the insert is 16 mm and the aperture at a $+/- 45^{\circ}$ angle is 99.7 mm. For the Q2, Q3 and D1 beam screens, the thickness of the insert is 6 mm and the aperture at $+/- 45^{\circ}$ angle is 119.7 mm and 110.7 mm. Therefore, the different requirements in terms of absorbing power result in two versions of the beam screen for the inner triplet. Although the two versions share the same design, the Q1 beam screen has a smaller aperture, while the Q2, Q3, and D1 screens have a larger aperture. Four cooling tubes 1mm thick are laser welded on the tilted surface of the screen. These regulate the temperature of the assembly in the range between 60 K and 80 K. For the Q1 version the external diameter is 16 mm as it needs to dissipate more heat, while for the other version is 10 mm. The tungsten-based inserts are kept firmly in place by titanium rings. Such rings are elastic enough to allow the beam screen to deform during a magnet quench with no permanent damage. The aperture reduction due to the weight of the heat absorbers has been calculated through simulation. The heat absorbed by the inserts is transferred to the cooling tubes through thermal links made of copper. The thermal link has been designed to satisfy multiple requirements. Beyond the primary function to transfer heat, these have to withstand the effects of a magnet quench without undergoing plastic deformations and be flexible enough not to hinder the movement of the heat absorber along its normal direction. In fact, during a quench the absorber moves outwardly and a stiff link would not allow it to return to its original position. This would cause a failure in the collision debris absorption and, consequently, a higher thermal load transferred to the cold bore. The need for a flexible thermal link has been successfully addressed by proposing a multi-layer structure. In general, the design of the thermal link has required extensive exploration of solution options and compromise. For example, a wider link would foster better heat transfer but would hinder at the same time the capability to withstand a quench. The remaining requirements of the thermal link are investigated in the next chapters. To avoid a detrimental thermal contact between the absorbers and the cold bore, the beam screen needs to be insulated by a vacuum gap. For this purpose, this chapter has described a supporting system composed of titanium springs and ceramic spheres which holds the beam screen suspended in the cold bore. The system is integrated in dedicated slots of the lateral extensions of the heat absorbers. The heat transfer to the cold bore is limited by low conductive ceramic spheres, which are in contact with the cold bore itself. The shape of the spring for the Q1 and Q2 versions of the beam

screen has been determined by simulation and validated experimentally to ensure that the required gap with the cold bore is obtained and a full compression during quench is achieved.

Chapter 3

Material characterisation

3.1 Material definition

The HL-LHC beam screen is made of six different materials. The material of each beam screen component are listed in Table 3.1 and shown in Fig. 3.1 with respect to the Q1 version of the beam screen.

The mechanical, magnetic, thermal, and electric properties of the beam screen materials are paramount for the design of the assembly. The physical properties that have not been found in literature for the operating temperature of the beam screen (60 - 80 K) have been measured. This allows to properly set up the numerical simulations.

A common requirement for each material is related to the relative magnetic permeability which has to be lower than a certain threshold to avoid perturbations of the magnetic field. The maximum acceptable value depends also on the geometry of the component. In general, the limit of the materials of non-cylindrical geometry (and welds) should not exceed 1.005 [31]. Cylindrical geometry like the cold bore can have higher values of magnetic permeability.

3.2 Mechanical properties

The mechanical properties of the materials used for the beam screen are summarised in Table 3.2. The data concerning the P506 have been found in [32], the 316 LN in [33], the copper in [34], Ti-6Al-4V (also know as titanium grade 5) in [30], and zirconium oxide (also known as zirconia) in [35].

Material	Beam screen component
Tungsten alloy	Heat absorber
St. st. P506	Octagonal pipe, centring pin
St. st. 316 LN	Cold bore, cooling tube
Copper OFE (RRR 100)	Inner layer, thermal link
Ti-6Al-4V	Elastic ring, supporting system spring
Zirconium dioxide	supporting system sphere

TABLE 3.1: Materials used for each component of the HL-LHC beam screen.

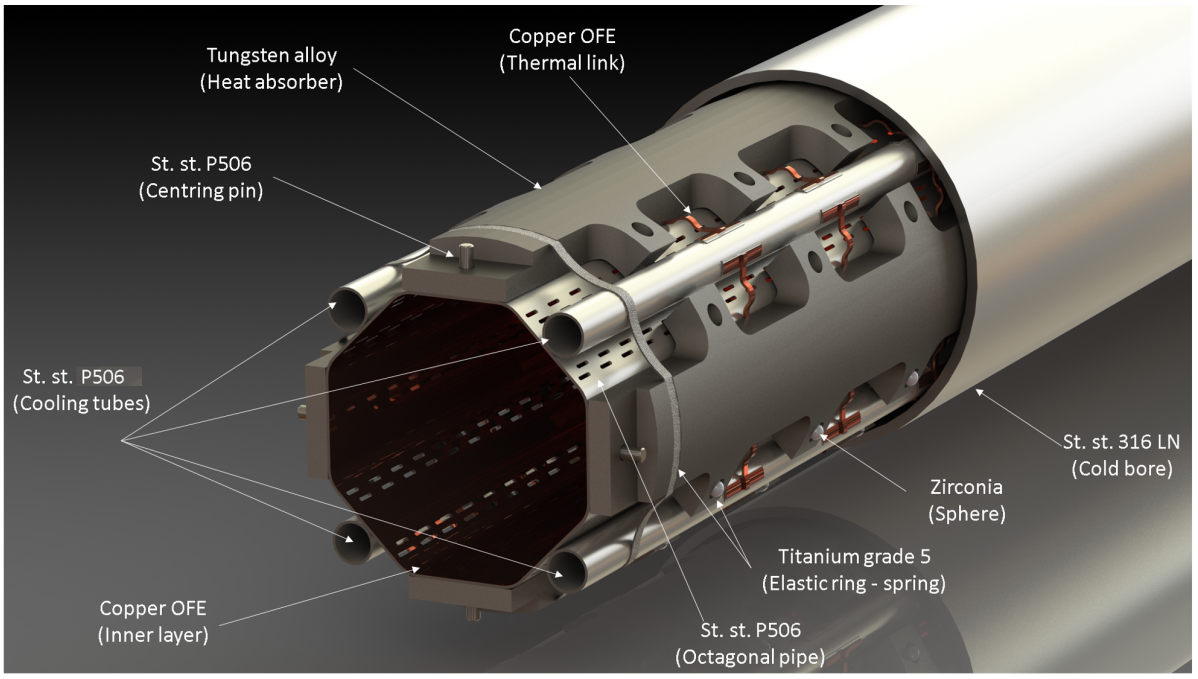


FIGURE 3.1: Materials used for the beam screen.

Material	Temperature [K]	E [GPa]	$R_{0.2}$ [MPa]	R_m [MPa]	A [%]	k_c [MPa m^{-1}]	J_Q [kJ/m^2]
Tungsten alloy	4.2	-	-	1085	0	21.3	-
Tungsten alloy	77	-	-	1284	0	29	-
Tungsten alloy	293	415	788	973	7.6	34.2	-
P506	4.2	240	1620	2115	18	-	-
P506	77	240	1180	1760	57	-	-
P506	293	190	405	730	47	-	-
316 LN	4.2	-	862	1759	59.9	-	~ 200
316 LN	77	-	726	1532	61.8	-	~ 400
316 LN	293	-	329	653	79.6	-	~ 1000
Copper OFE (Annealed)	77	130	35	320	77	110	-
Ti-6Al-4V	4.2	-	1650	1698	-	78	-
Ti-6Al-4V	293	-	881	957	-	61	-
Zirconium dioxide	293	220	540	6000	-	10	-

TABLE 3.2: Mechanical properties of the materials used for the HL-LHC beam screen.

The mechanical properties of the tungsten alloy have been measured as just a few data at room temperature are available [36] [37] [38]. At cryogenic temperatures the tungsten alloy shows better performance than at room temperature. However, at 4.2 K there is drop of mechanical strength and fracture toughness than at 77 K. This is due to a intra-grain fracture propagation which prevails on the inter-grain mechanism. A detailed description of the measurement setup and a discussion of the results can be found in [39].

3.3 Magnetic properties

The relative magnetic permeability of the stainless steel 316 LN is higher than 1.005 [40]. However this does not pose a problem as the 316 LN is used for a cylindrical tube as the cold bore. The magnetic permeability of the

other materials used for the beam screen are lower than 1.005. The data for the stainless steel 316 LN can be found in [41] [40], for the P506 in [42] [32] [40], for the titanium grade 5 in [43], and for the copper OFE in [34]. The magnetic permeability of the tungsten alloy, shown in Fig. 3.2, has been measured from 4 K to 300 K. The details of this measurement can be found in [39].

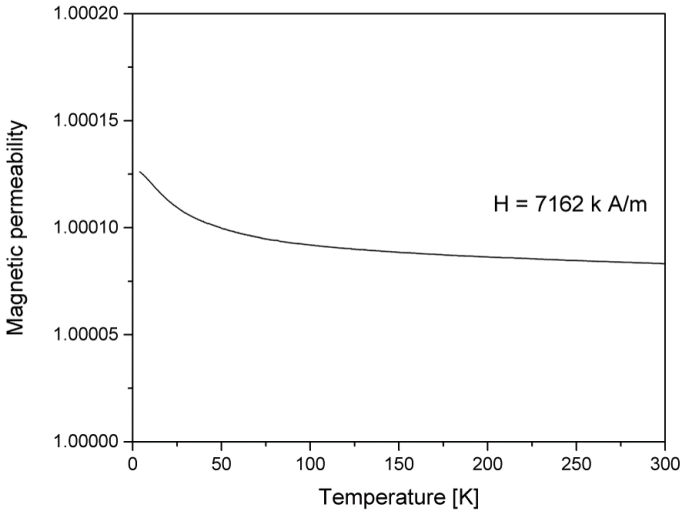


FIGURE 3.2: Magnetic permeability of the tungsten alloy.

3.4 Thermal properties

The thermal conductivities of the austenitic stainless steel (316 LN and P506) [44], the titanium grade 5 [45], and the copper OFE [34], are shown in Fig. 3.3.

The thermal conductivities of the tungsten alloy and the zirconia, shown in Fig. 3.4, have been measured from 4 K to 300 K. The details of the measurement can be found here [39].

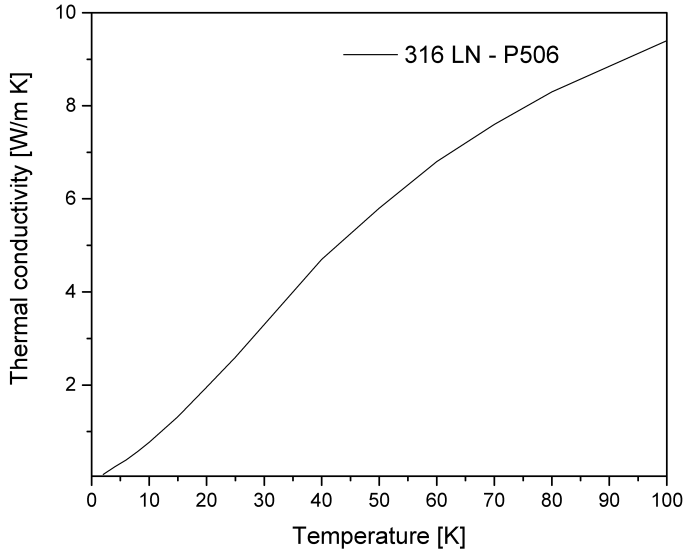
In Fig. 3.5 the heat capacities of the austenitic stainless steel (316 LN and P506) [46], the titanium grade 5 [47], the copper OFE (RRR 100) [48], and of the tungsten alloy [48] are shown.

3.5 Electrical properties

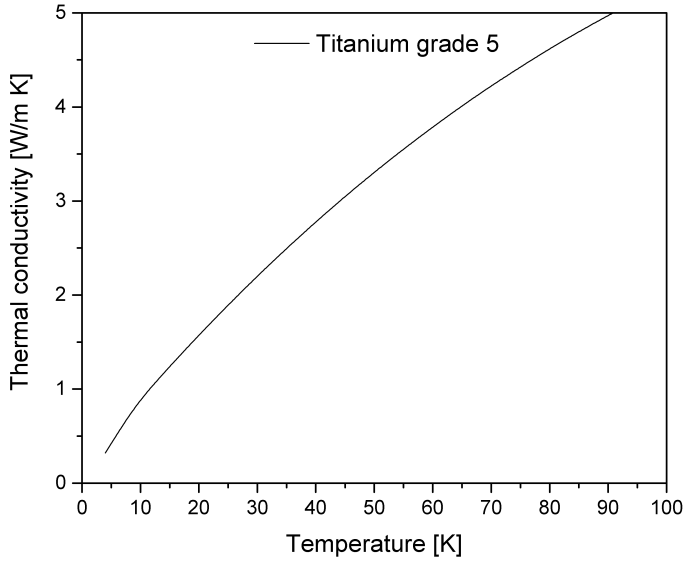
The electrical resistivity of the tungsten alloy has been measured and it is shown in Fig. 3.6 along with the one of the copper OFE (RRR 100) [34] and the austenitic stainless steel (316 LN and P506) [49]. The details of the electrical resistivity measurement of the tungsten alloy can be found in [39].

3.6 Conclusions

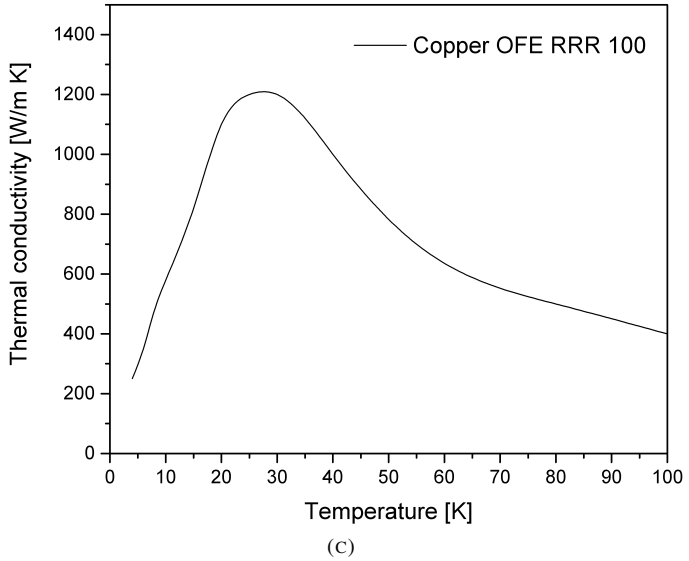
Understanding the physical properties of the materials used for the HL-LHC beam screen is essential to validate their suitability to the new design and to accurately predict the behaviour of the assembly by simulation. In particular, adequate mechanical, magnetic, thermal and electric properties are needed to develop a robust design.



(A)



(B)



(C)

FIGURE 3.3: Thermal conductivity of the austenitic stainless steels (316 LN and P506) (a), the titanium grade 5 (b), the copper OFE RRR 100 (c) from 4 K to 80 K.

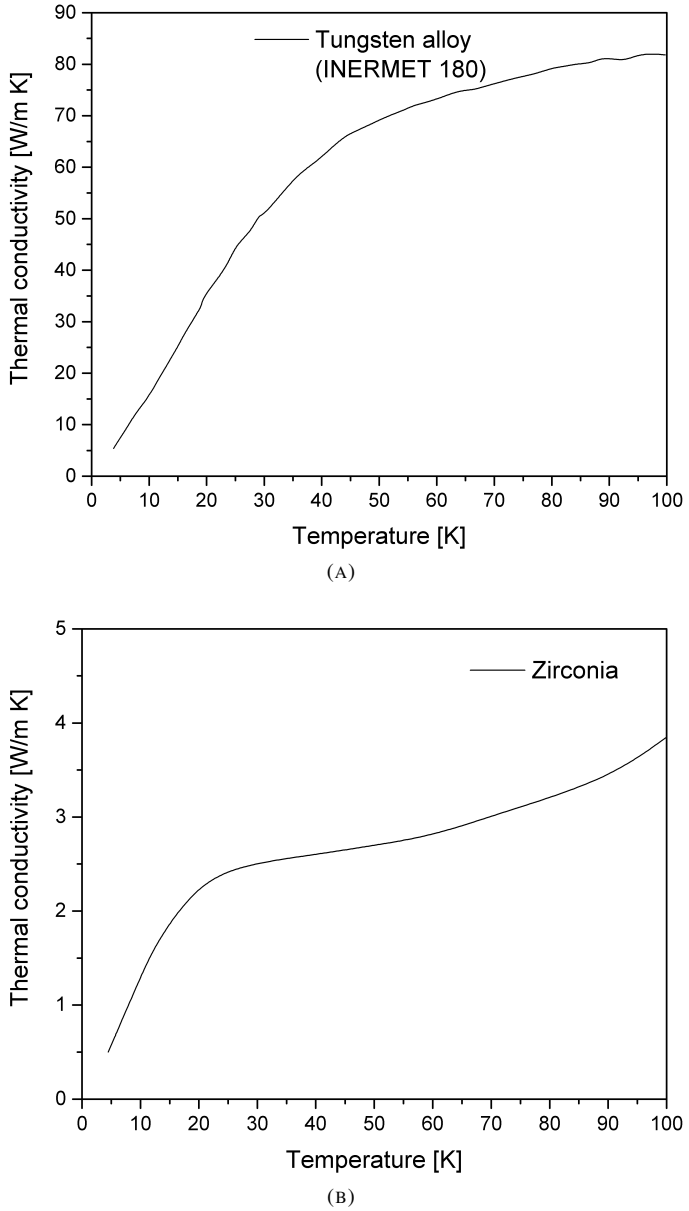


FIGURE 3.4: Thermal conductivity of the tungsten alloy (a) and the zirconia (b) has been measured from 4 K to 80 K.

The beam screen is composed of six different materials: a tungsten alloy for the heat absorbers, the P506 austenitic stainless steel for the octagonal pipe, the cooling tubes and the positioning pins, the 316LN austenitic stainless steel for the cold bore, the OFE copper (RRR 100) for the inner layer and the thermal links, the titanium grade 5 for the elastic rings and the supporting springs, and the zirconia for the spheres of the supporting system.

The material properties not found in the literature have been measured. However, all the material properties needed for the design have been reported for reference purposes. The measurements are mainly related to the tungsten alloy and the zirconia.

The mechanical behaviour of the tungsten alloy makes it a suitable material to withstand the effects of a magnet quench. The magnetic permeability fulfils the requirements of field quality as it is well below 1.005 at cryogenic temperatures. The electrical resistivity is rather flat in the temperature range of interest, namely from 40 K to 100 K. Finally, the thermal conductivity is satisfactory for the thermal transfer to the cooling tubes through the thermal

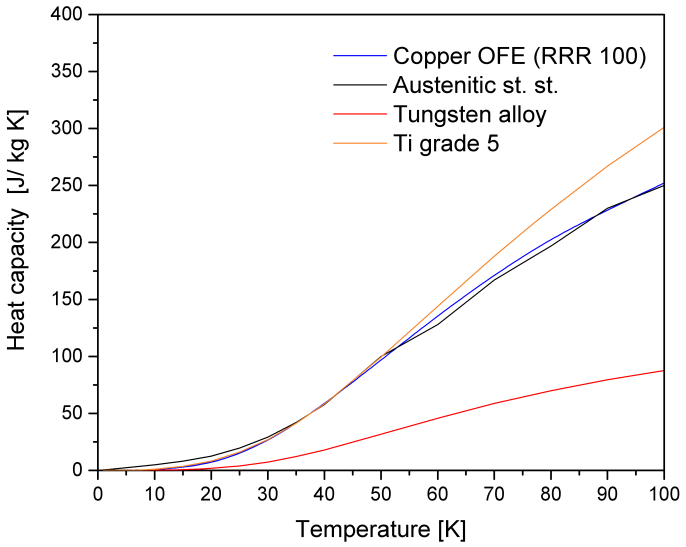


FIGURE 3.5: Heat capacity at constant pressure of the materials used for the beam screen from 4 K to 100 K.

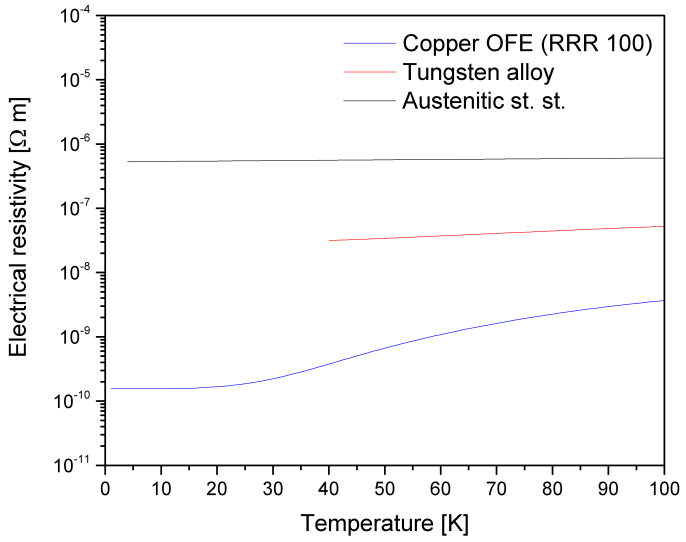


FIGURE 3.6: Electrical resistivity for the beam screen from 4 K to 100 K.

links. On the contrary, the thermal transfer of the zirconia, as typically for ceramic materials, hinders significantly the heat transfer to the cold bore. It is, therefore, a very appropriate choice for an interface material between the cold bore and the beam screen assembly.

Chapter 4

Thermal transfer performance during operation

4.1 Thermal requirements of the beam screen assembly

The thermal design of the HL-LHC beam screen, based on connecting through copper links the heat absorbers with the cooling tubes, is substantially more complex than the LHC counterpart. A comparison of the thermal parameters for both beam screens is given in Table 4.1.

Due to cryogenic and thermodynamic reasons the nominal temperature of the beam screen has been set between 60 K and 80 K [50]. The heat load generated by the collision debris has to be absorbed by the tungsten blocks and has been predicted for nominal conditions through simulations. These are 15 $\mathrm{W\,m^{-1}}$ for the Q2 to the D1 beam screens and 25 $\mathrm{W\,m^{-1}}$ for the Q1 beam screens [16]. The main requirement of the beam screen from a thermal performance standpoint is that the temperature of the copper inner layer remains in the temperature window of 60 to 80 K all along the triplet area. The 20 K range is shared in a temperature gradient of super fluid helium along the triplet equal to 15 K and a temperature difference between the super fluid helium and the copper layer equal to 5 K. Therefore, the inner layer of the beam screen can increase 5 K at most with respect to the relative temperature of the helium circulating in the cooling tubes, *i.e.* if the temperature of the He gas is 60 K, the inner surface of the beam screen should be kept below 65 K, see Fig. 4.1.

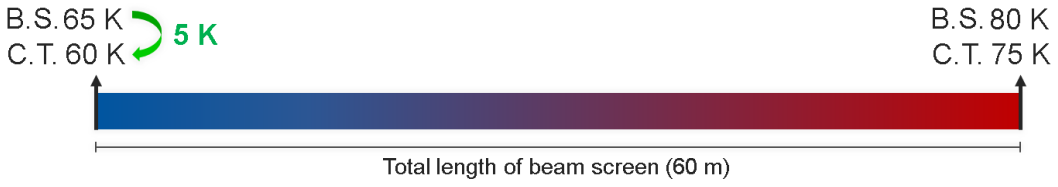


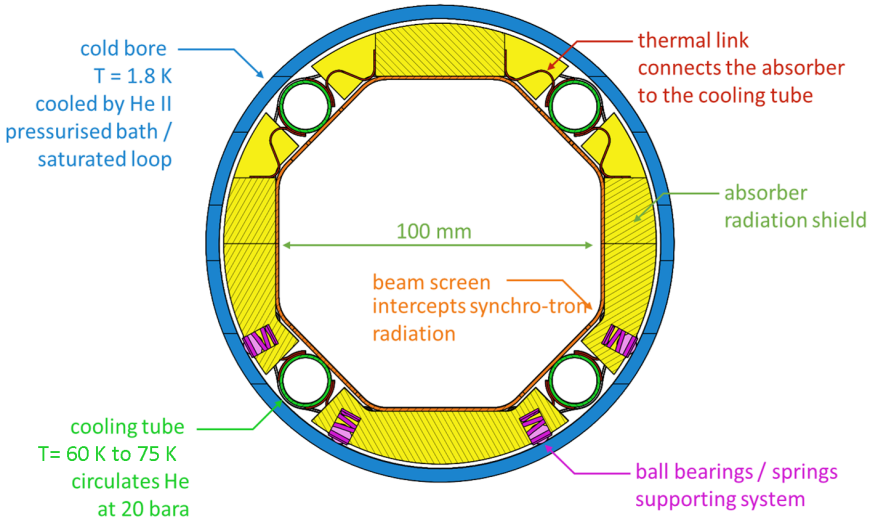
FIGURE 4.1: Allowed temperature profile along the total length of the beam screens (60 m). The maximum drop along the cooling tube (C.T.) is 15 K, while the temperature of the beam screen (BS) can be up to 5 K higher.

Although there is no specific limit imposed on the heat absorber temperature, this should be evaluated and kept below reasonable values so that the heat transferred to the 1.9 K cold bore either by radiation or by conduction through the supporting structure is minimised and particle desorption is kept to a minimum.

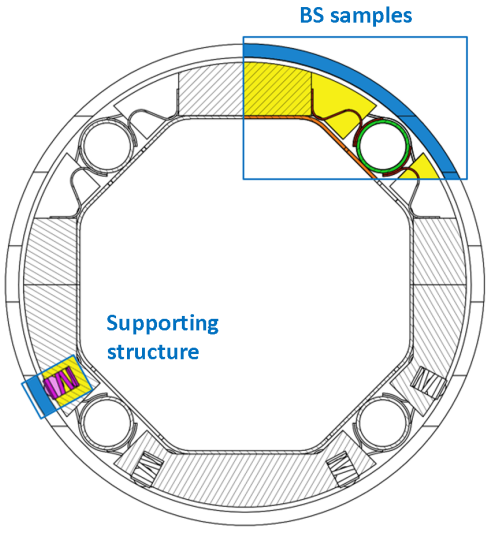
	LHC beam screen	HL-LHC beam screen
Operating temperature	4.6 K to 20 K	60 K to 80 K
Nominal heat load	1 $\mathrm{W\,m^{-1}}$	15 $\mathrm{W\,m^{-1}}$ (Q2 to D1), 25 $\mathrm{W\,m^{-1}}$ (Q1)
Cooling fluid	supercritical He	supercritical He
Operating pressure	3 bar	20 bar
Mass flow rate	1 $\mathrm{g/\,sec}$	10 $\mathrm{g/\,sec}$ to 20 $\mathrm{g/\,sec}$
Absorber material	none	Tungsten alloy

TABLE 4.1: Cooling scheme characteristics of the LHC and HL-LHC beam screens [51] [26].

The thermal behaviour of the beam screen is characterised through a small-scale and a real-scale beam screen sample. In this chapter, the heat transfer from the heat absorber to the cooling tubes and from the supporting structure to the cold bore is presented, see Fig. 4.2.



(A)



(B)

FIGURE 4.2: Cross section of the beam screen in (a) depicting the various components involved in the heat transfer. From the two areas highlighted in (b) two small-scale samples have been extracted to characterise the heat transfer from the heat absorber to the cooling tube and from the beam screen to the cold bore.

Numerical simulations have been carried out to assess and optimise the heat transfer of the assembly. Experiments have been conducted to validate the design of the thermal link and the supporting system. The heat transferred through radiation has been estimated through an analytical formulation.

4.2 Model definition

The FEM thermal model has been developed in COMSOL Multiphysics. The constitutive equation of the thermal transfer module is based on the Fourier's law that reads:

$$\mathbf{Q} = -kA\frac{\Delta T}{\Delta x} \tag{4.1}$$

where **Q** is the heat transferred per unit of time [W], k is the material thermal conductivity [$\mathrm{W\,m^{-1}\,K^{-1}}$], A is the cross section of reference [$\mathrm{m^2}$], ΔT the temperature difference [K] and Δx the distance between two endpoints [m].

The small-scale sample used to optimise the heat transfer from the heat absorber to the cooling tube is shown in Fig. 4.3.

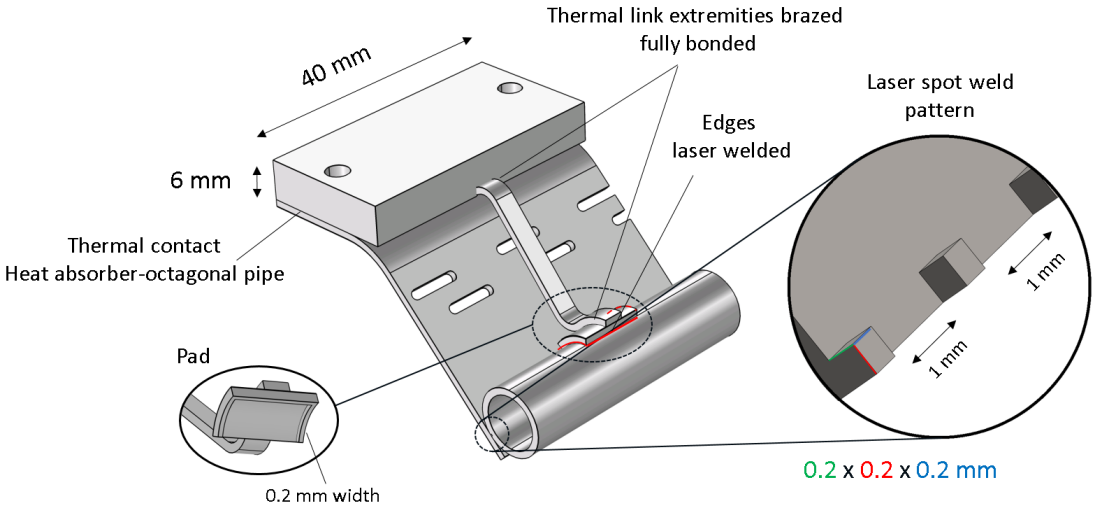


FIGURE 4.3: Sample representing one eight of the Q2 beam screen 40 mm long.

Considering a mass flow rate of 10-12 g/s, the convection heat transfer coefficient, h, is 800-920 $\mathrm{W\,m^{-2}\,K^{-1}}$ and is assigned only to the internal side of the cooling tube (Dittus-Boelter [52], Colburn [53]). A thermal insulation condition has been assigned to the remaining external faces of the model to represent the vacuum environment.

To implement the actual welding scheme of the beam screen components some modelling *tricks* have been adopted. Fig. 4.3 shows how the components are bonded together in the sample used to optimise the heat transfer between the heat absorber and the cooling tube. To simulate the spot welds of the cooling tubes on the octagonal pipe, 0.2 mm cubes are placed every 1 mm along the pipe which the tubes are considered fully bonded to. To

simulate the continuous welds of the thermal link pads on the cooling tubes, only the external edges of the pad 0.2 mm wide are considered fully bonded. This is possible because the remaining part of the pad is not in contact with the tube. The brazing of the thermal link with the pad and the heat absorber is considered fully bonded instead.

As the heat absorber is laid on the octagonal pipe a thermal contact model based on the Cooper *et al.* [54] work is considered. According to this model and the study of Grujicic *et al.* [55] and Zheng *et al.* [56] the heat transfer depends on the joint conductance, h, which is composed by three terms: the constriction conductance of the contact points, h_c, the gap conductance related to the fluid at the interstitial space, h_g, and the radiative conductance, h_r:

$$h = h_c + h_g + h_r \tag{4.2}$$

Since the beam screen works at cryogenic temperatures and is placed in vacuum h_r and h_g are neglected. Therefore, only h_c takes part in the thermal transfer between two contacting surfaces by means of a finite number of spots.

The parameters affecting the conductance are:

- Contact pressure;
- Microhardeness;
- Surface roughness (RMS average, σ_{asp});
- Surface roughness slope (RMS average, m_{asp});

h_c is determined by the Cooper-Mikic-Yovanovich (CMY) correlation as:

$$h_c = 1.25 k_{contact} \frac{m_{asp}}{\sigma_{asp}} (\frac{p}{H_c})^{0.95} \tag{4.3}$$

where H_c is the micro-hardness of the softer material, p is the contact pressure, and $k_{contact}$ is the harmonic mean of the contacting surface conductivities, which reads to:

$$k_{contact} = \frac{2 k_u k_d}{k_u + k_d} \tag{4.4}$$

It turns out that the contact pressure and the surface roughness are the parameters mostly affecting the conductance and therefore the heat transfer.

The sample has been meshed with $5.8 \cdot 10^5$ second-order tetrahedral elements, see Fig. 4.4.

4.3 Thermal link

The design of the thermal link is a complex trade-off which relies on the optimisation of the heat to be transferred from the tungsten absorber to the cooling tube, the ease of assembly, and the mechanical integrity during a magnet quench.

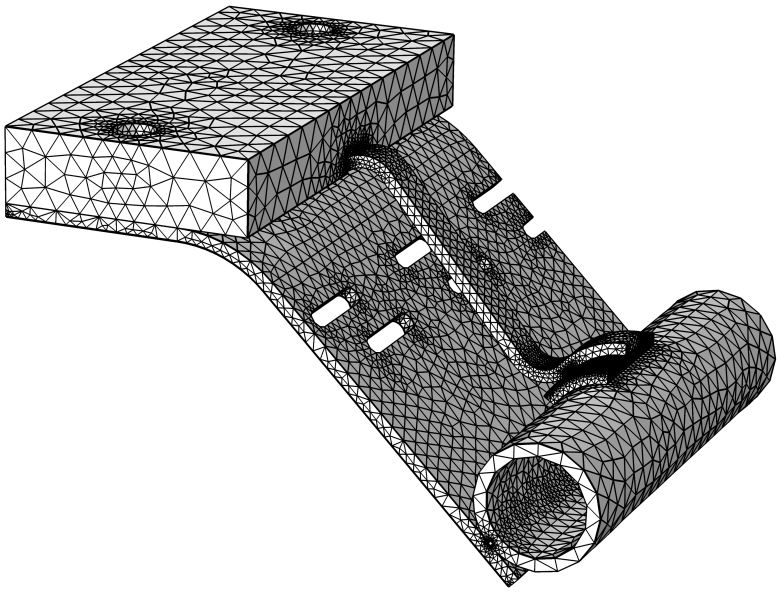
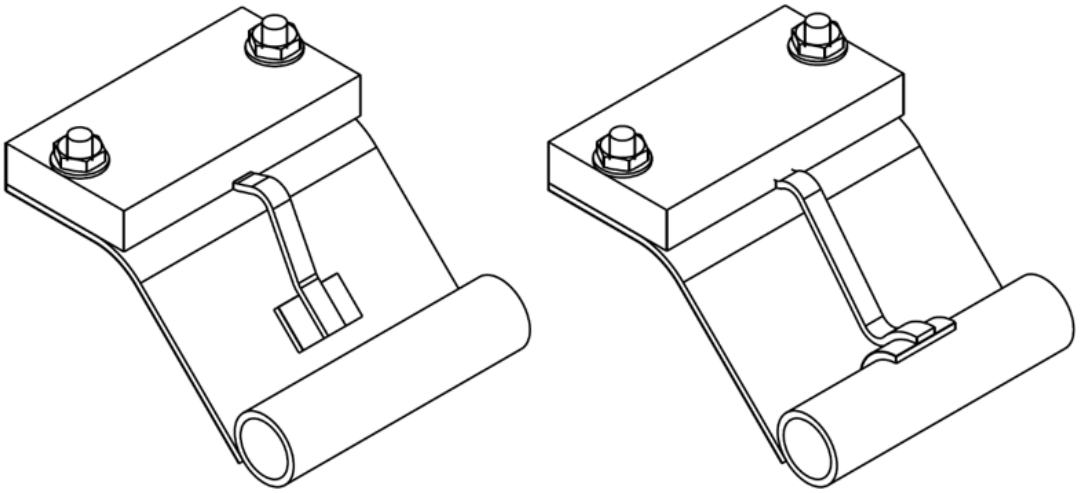


FIGURE 4.4: Mesh of the sample by second-order tetrahedral elements.

4.3.1 Thermal link versions

Two versions of the thermal link have been investigated. In one case the pad of the link is welded directly on the octagonal pipe, while in the other case it is welded on the cooling tube, see Fig. 4.5. During the welding phase, the pad welded on the octagonal pipe eliminates the risk of perforating the cooling tubes. However, the heat transfer to the cold source is limited due to the non-direct connection. On the contrary, the pad welded on the cooling tube has a direct and efficient connection to the cold source but introduces the risk of perforating the tube.



(A) (B)

FIGURE 4.5: Thermal link pad welded on the octagonal pipe in (a) and on the cooling tube in (b).

4.3.2 Thermal link optimisation

The optimisation of the thermal link design has been performed by simulation for the most efficient version of the link, namely the one welded on the cooling tube. To this purpose, a parametric analysis has been carried out by varying the characteristic dimensions of the link and its pad, see Fig. 4.6. The aim of this study is to find the best geometrical configuration of the thermal link allowing an efficient heat transfer and a reduced number of experiments. It is worth to note, as shown in Fig. 4.6, that in this study the pad has been further optimised to limit the potential risk of perforating the tubes. In fact, the thickness of the external edges of the pad have been reduced to 0.2 mm so that the welding of such thin band on the cooling tube 1 mm thick can be performed perpendicularly by laser. This limits the risk to perforate the tube as the energy to weld 0.4 mm is of course lower than to weld 0.6 mm on a 1 mm thick tube.

In the simulations, the properties of copper refer to a temperature of 40 K, see section 3.4. The thermal power assigned to the heat absorber is 0.15 W, the initial temperature of the sample is 50 K, and the convection heat transfer coefficient, h, of the cooling tube is 800 $\mathrm{W\,K^{-1}\,m^{-2}}$.

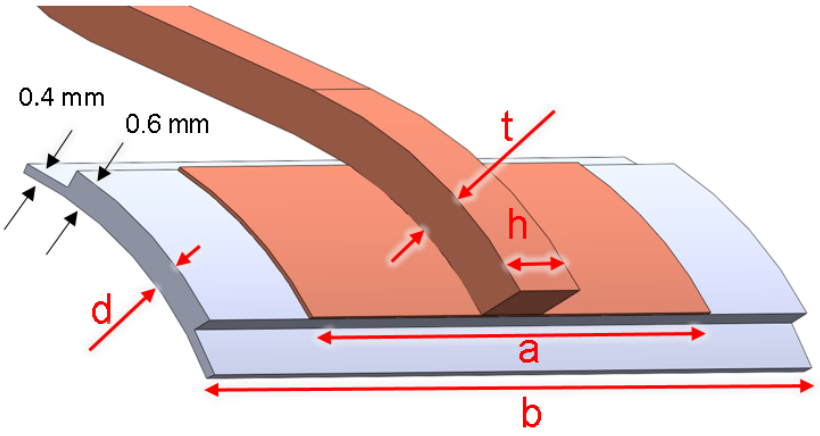


FIGURE 4.6: Parameters of the thermal link affecting the heat transfer; t: thickness of the link, h: width of the link, b: length of the pad, a: length of the co-laminated copper layer.

The impact of each thermal link parameter is shown in Fig. 4.7. The heat transfer efficiency can be assessed by evaluating the maximum temperature of the heat absorber. A high temperature corresponds to a low efficiency, vice versa, a low temperature corresponds to a high efficiency.

Fig. 4.7a shows that the heat transfer depends on the length of the pad and on how many welding lines are used to bond the pad to the cooling tube. It turns out that the number of welds and the length of the pad represent a real *bottleneck* for the heat transfer efficiency. This is due to the thermal conductivity of the welded edges (stainless steel) which is much lower than the one of the thermal link (copper). Therefore, the heat transfer efficiency increases by extending the length of the pad and the number of welded edges.

The width of the thermal link is assessed in Fig. 4.7b for a 30 mm long pad welded on its three external edges. It turns out that the temperature of the heat absorber drops significantly by increasing the thermal link width from 1 mm to 3 mm. From 3 mm to 10 mm the change in temperature is minimal meaning that the thermal link capacity of transferring heat is limited by the welds of the pad.

The effects of the copper layer 75 µm co-laminated on the 30 mm long pad are shown in Fig. 4.7c. It turns out that the extension of such a layer can lower dramatically the temperature of the heat absorber. In fact, the heat from the thermal link hardly diffuses in a pad without the co-laminated layer resulting, therefore, in lower performance for longer pads.

Finally, the influence of the pad thickness is shown in Fig. 4.7d, which results in a better heat transfer for the 0.6 mm thick pad rather than that 1 mm thick due to a reduction of low conductive material.

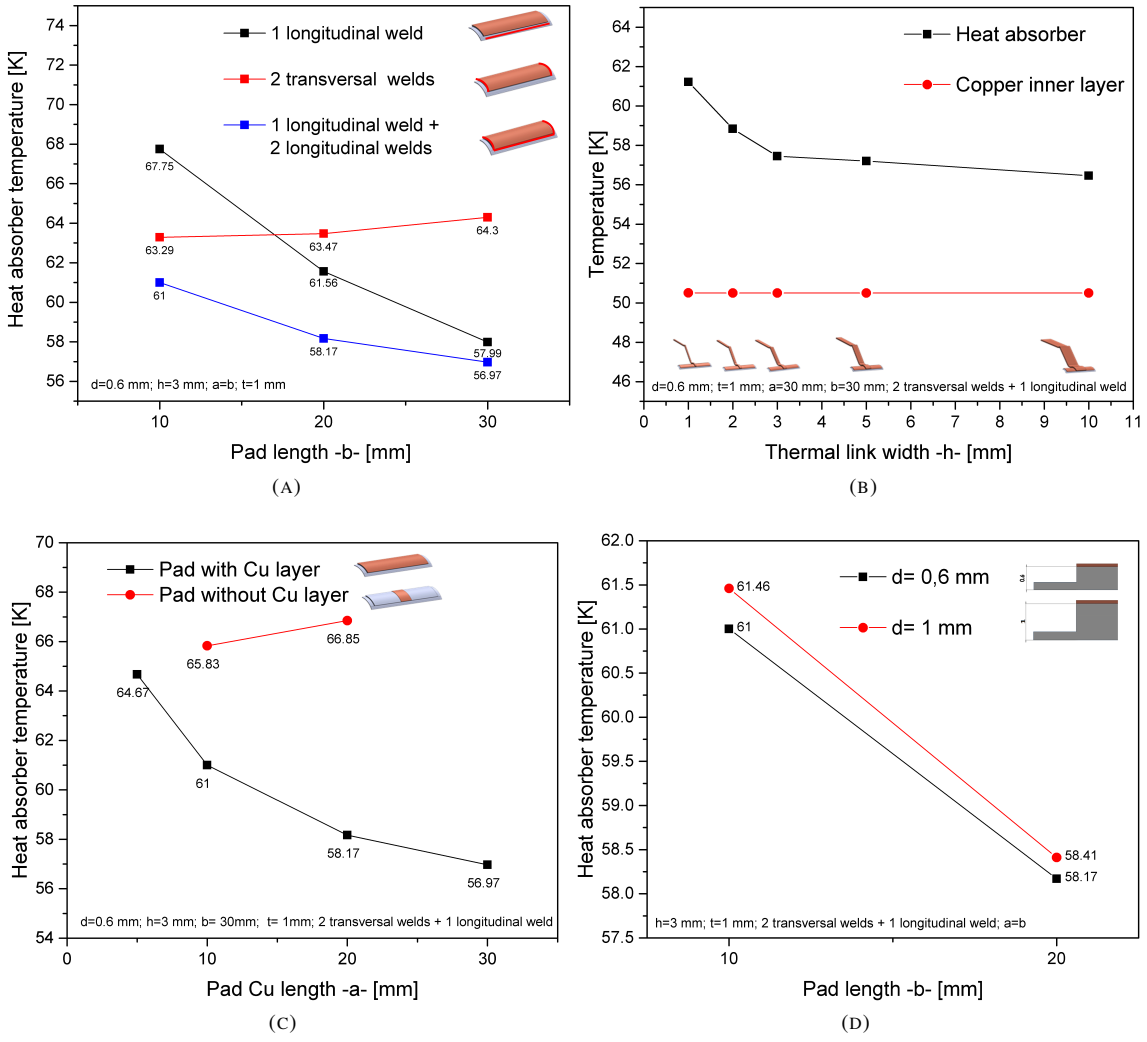


FIGURE 4.7: Impact of the thermal link and pad dimensions on the temperature of the heat absorber. The type of weld is analysed in (a), the thickness of the pad in (b), the coverage of the Cu layer on the pad in (c), the thermal link width in (d). For the evaluation of each dimension, the remaining ones are kept constant and are shown at the bottom of each graph.

Therefore, for the above mentioned initial conditions the thermal link shown in Fig. 4.8 represents the best trade-off in terms of thermal efficiency and width. The optimised thermal link is made of 10 copper layers 0.1 mm thick whose width can vary between 3 and 5 mm. The pad, co-laminated by 75 µm of copper, needs to be 30 mm long and welded longitudinally on the cooling tubes.

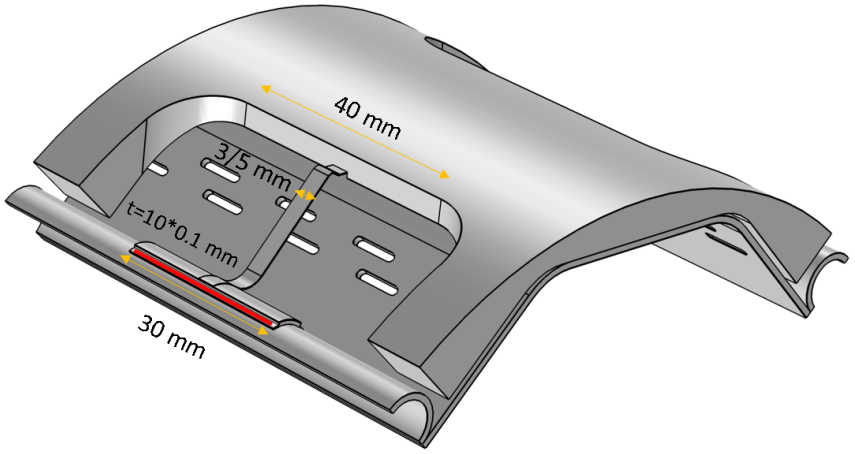


FIGURE 4.8: Best trade-off of the thermal link system in terms of thermal transfer and ease of assembly. The dimensions are reported next to each component.

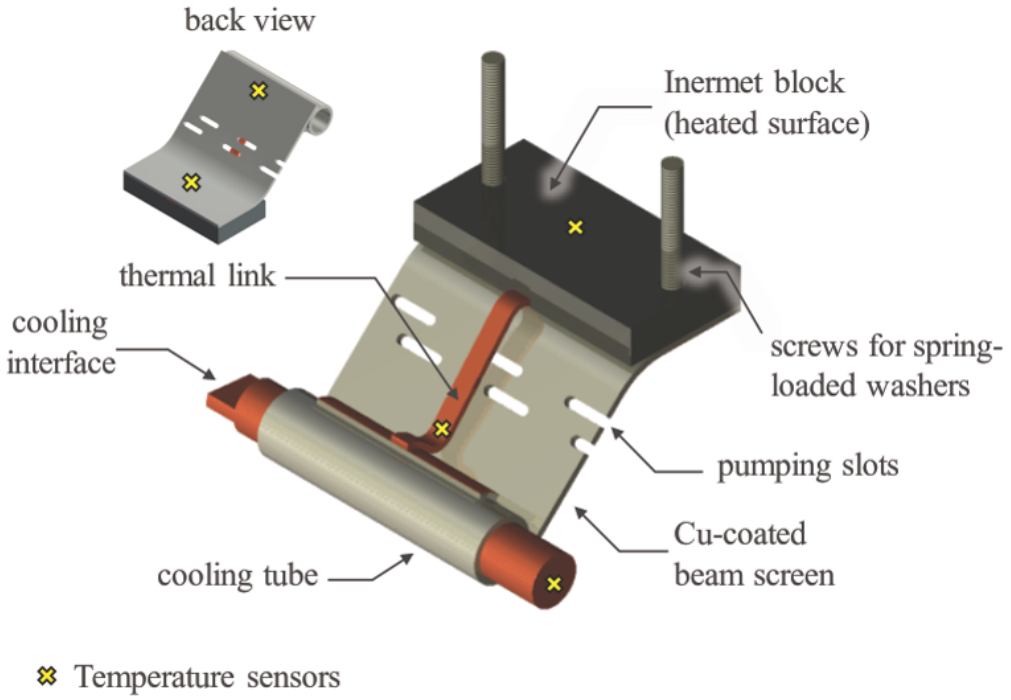
4.4 Test setup

4.4.1 Small-scale test

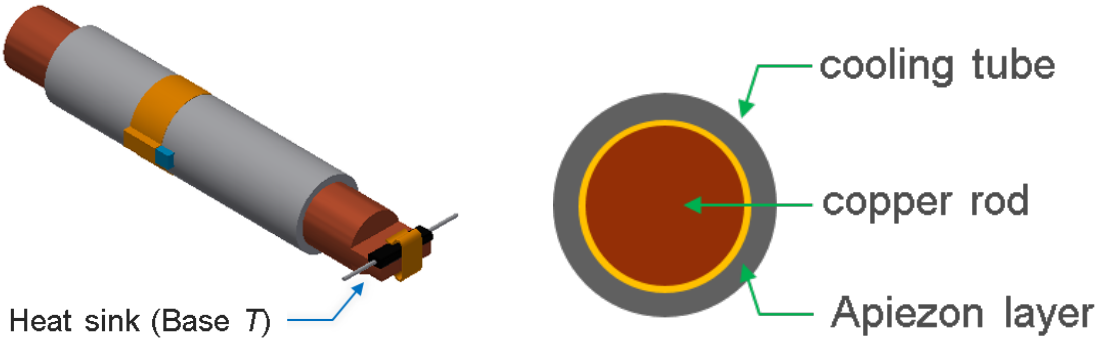
Each sample has been instrumented with six temperature probes, placed on the heat absorber, two points on the octagonal pipe, the thermal link, the cooling tube, and the heat sink. To apply a compression force on the tungsten block, two springs have been mounted on a set of screws welded to the octagonal pipe portion. The springs apply a nominal compression of 1.82 N to the tungsten block against the octagonal pipe. The heat load applied on the tungsten block ranges from 0 mW to 400 mW, which corresponds to a distributed load on the whole beam screen spanning from 0 $\mathrm{W\,m^{-1}}$ to 25 $\mathrm{W\,m^{-1}}$. The heat load has been calculated by considering that each 0.8 m section of beam screen contains eight tungsten blocks and, in turn, each of them is equipped with 6 thermal links. By way of example, for a heat load of 25 $\mathrm{W\,m^{-1}}$ each thermal link needs to transfer $\dot{Q} = 25 \times \frac{0.4}{6\times4} = 417\ \mathrm{mW}$ from the tungsten block to the cooling tube.

The small-scale sample used in the measurements is showed in Fig. 4.9. A copper rod has been fitted into the cooling tube as a way to represent the super fluid helium. An apiezon layer is placed at the interface between the rod and the cooling tube to guarantee a good thermal contact. The heat transfer coefficient between the copper rod, the apiezon layer and cooling tube at 50 K is h= 1000 $\mathrm{W\,m^{-2}\,K^{-1}}$. The heat transfer coefficient for He gas at 20 bar and 50 K, considering a mass flow rate of 10-12 g/s, is h= 800-920 $\mathrm{W\,m^{-2}\,K^{-1}}$ (Dittus-Boelter [52], Colburn [53]).

Measurements were carried out on a Sumitomo Heavy Industries two-stage pulse tube refrigerator (PTR), see Fig. 4.10, that can provide up to 1 W of cooling power at 4.2 K on the second stage and a no-load temperature of 2.6 K. A detailed description of the measurement can be found in [57].



(A)



(B) (C)

FIGURE 4.9: In (a) small-scale sample and position of the temperature sensors. In (b) copper rod fitted into the cooling tube to cool down the tube. In (c) cross section of the cooling tube.

4.4.2 Real-scale test

A horizontal cryostat has been set up for the real-scale sample measurement, see Fig. 4.11. A pulse tube refrigerator and a cold circulator to condition the flow on the beam screen have been used to reproduce the real temperature of the cold bore. The 80 cm long beam screen, shown in Fig. 4.12, will be inserted into a double-walled cold bore that contains the pressurised helium bath, that is, in turn, connected to the helium saturated bath by the heatmeter. *The thermal measurement using this setup will be performed by May 2018.*

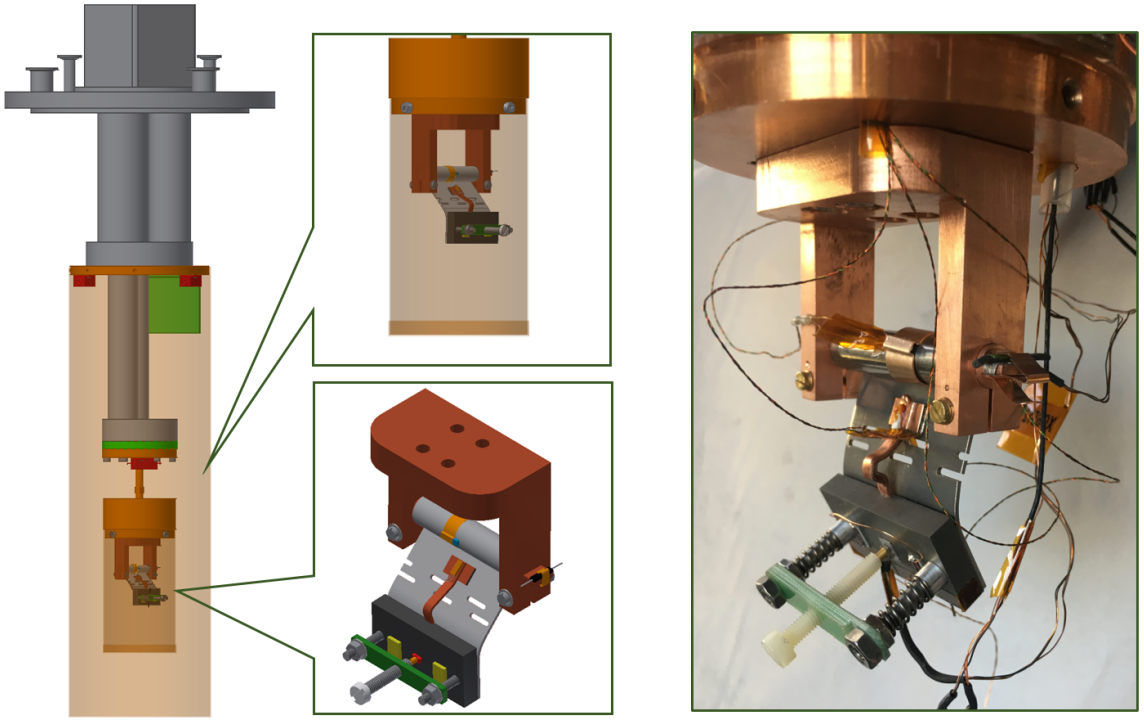


FIGURE 4.10: Setup configuration of the small-scale thermal test.

4.5 Thermal behaviour of the beam screen

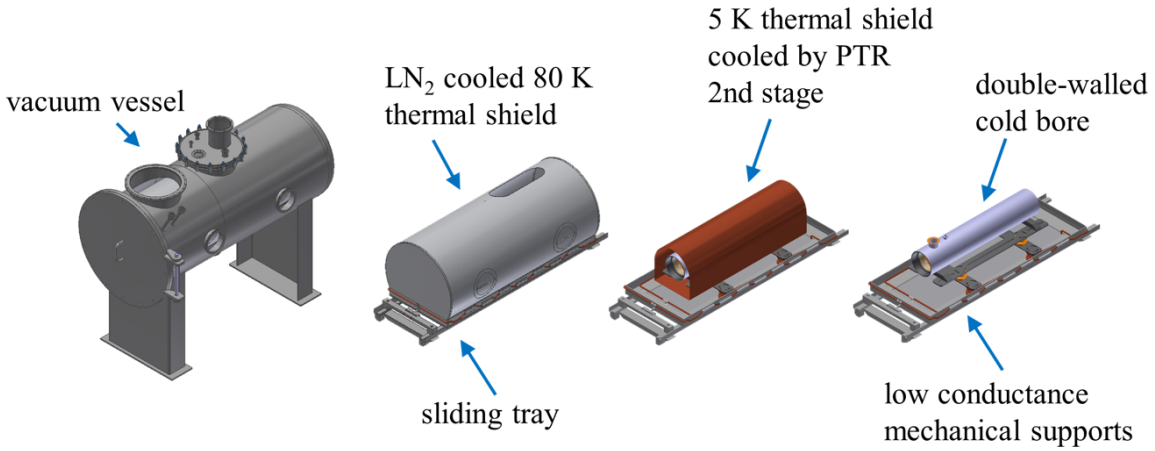
4.5.1 Small-scale sample (FEM + test)

The thermal behaviour of the beam screen has been predicted by simulation and then assessed by measurement through two small-scale samples depicted in Fig. 4.13. Each sample is 40 mm long and represents one eighth of the Q2 beam screen. The thermal link is 3 mm wide and composed of 10 layers 0.1 mm thick. The aim of the analyses is to assess the thermal efficiency of the thermal link welded on the cooling tube and on the octagonal pipe. The sample with the thermal link welded on the cooling tube has been further optimised as shown in section 4.3.2. The simulated and measured temperature for the two versions of the thermal links are compared in the points outlined in Fig. 4.14. The measurements and the work presented in this chapter have been performed with the support of the TE-CRG group at CERN [58].

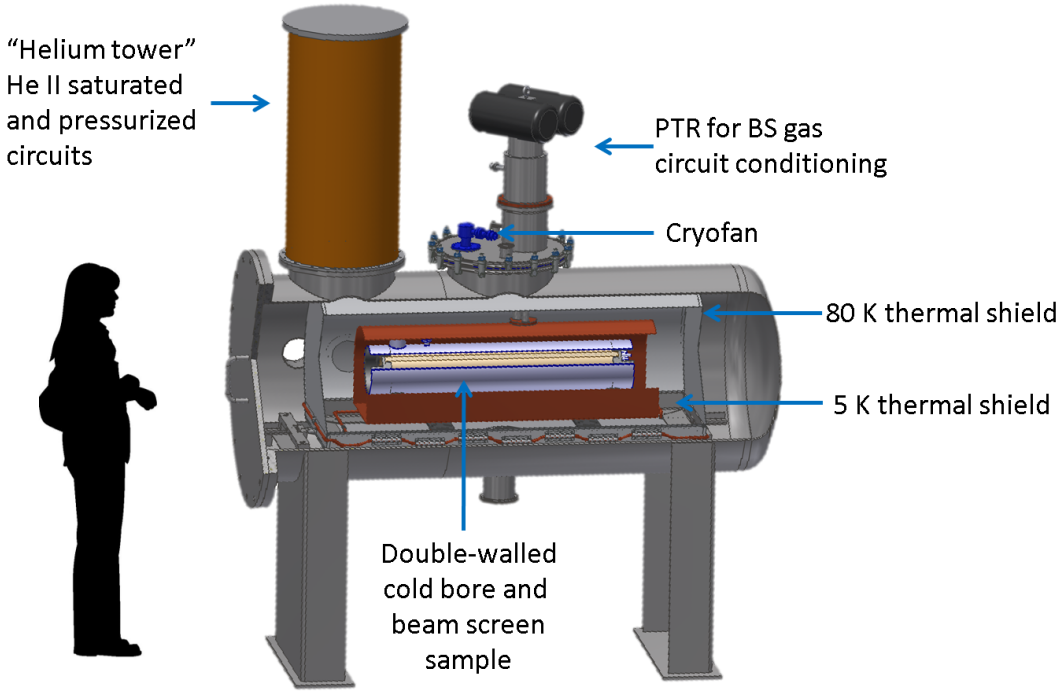
Thermal link welded on the pipe

The temperatures of the beam screen sample whose thermal link is welded on the octagonal pipe is shown in Fig. 4.15. The initial temperature of the cooling tube ranges from 50 to 80 K.

The numerical results show an excellent agreement with the experimental ones. In fact, the temperature difference spans from 8 % for the heat absorber (Inermet in Fig. 4.14) to 25 % for the thermal links (BS thermal link in Fig. 4.14).



(A)

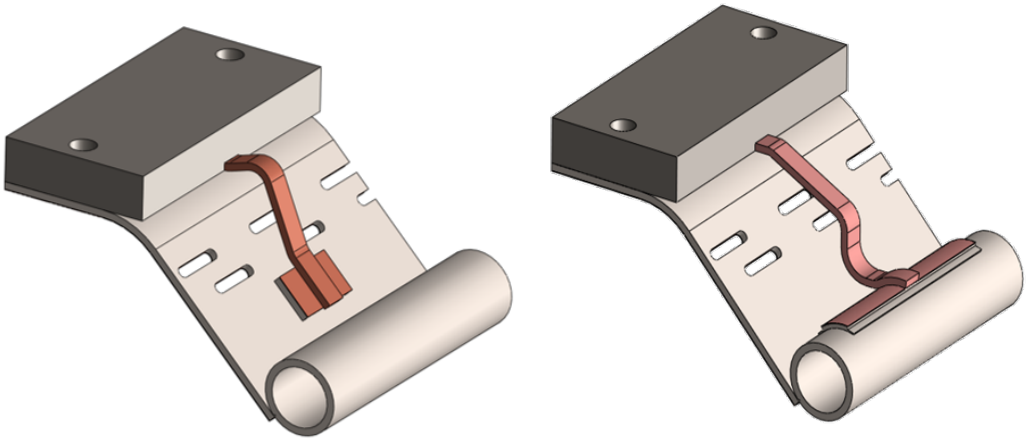


(B)

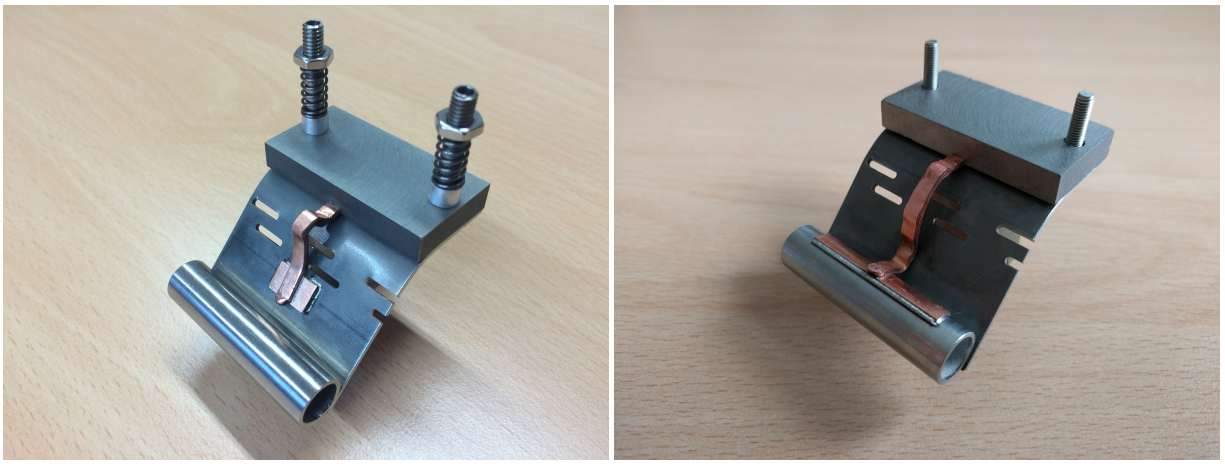
FIGURE 4.11: In (a) mounting sequence of the beam screen assembly into the vacuum vessel of the cryostat. In (b) section of the real-scale sample setup.



FIGURE 4.12: Beam screen prototype for the thermal test.

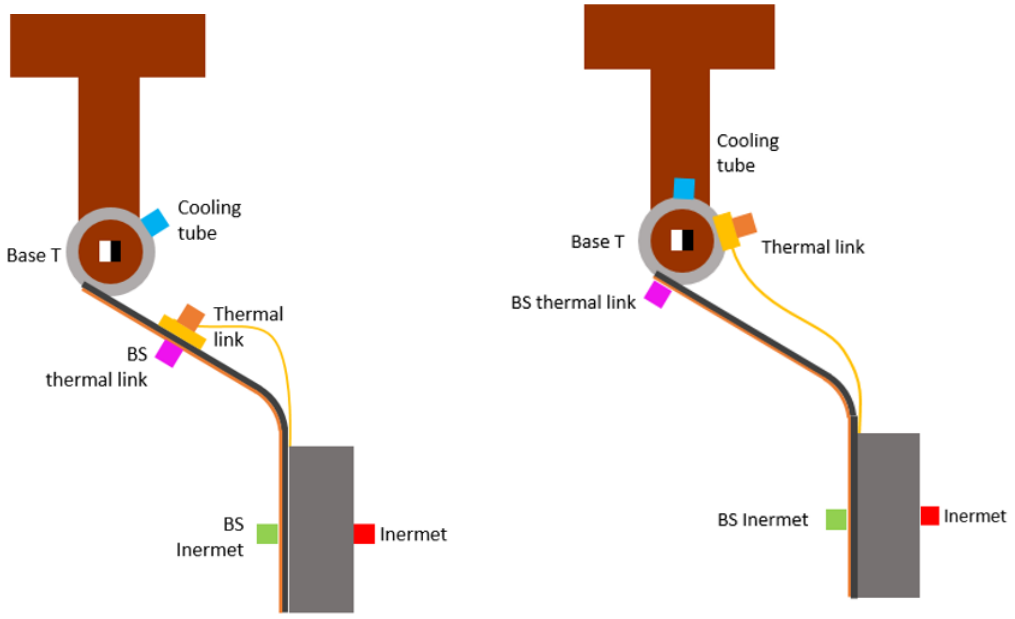


(A) (B)



(C) (D)

FIGURE 4.13: CAD model for the simulation in (a) and (b) and real model for the test in (c) and (d) of the two small-scale samples.



(A) (B)

FIGURE 4.14: Measuring points of the small-scale samples whose thermal link is welded on the octagonal pipe (a) or on the cooling tube (b).

	Nominal compression		No compression	
Base T	W block ΔT	Octagonal pipe ΔT	W block ΔT	Octagonal pipe ΔT
(60.00 $\pm$ 0.16) K	(15.00 $\pm$ 0.06) K	(8.20 $\pm$ 0.04) K	(17.00 $\pm$ 0.06) K	(9.20 $\pm$ 0.04) K
(75.00 $\pm$ 0.23) K	(15.00 $\pm$ 0.09) K	(8.00 $\pm$ 0.03) K	(16.50 $\pm$ 0.09) K	(8.50 $\pm$ 0.03) K

TABLE 4.2: Temperature increase measured for the relevant Q2 beam screen spots (Inermet and BS thermal link points in Fig. 4.14) for a nominal heat load of 15 W m^{-1} with and without compression force.

Table 4.2 reports the measured increase of temperature for the heat absorber and the octagonal pipe for the nominal heat load equal to 15 W m^{-1}. The base temperatures are 60 K and 75 K, namely at the beginning and at the end of the triplet area, while the forces are 1.82 N (nominal compression) and 0 N (no compression). In case of nominal compression for both base temperatures the increase is around 15 K for the heat absorber and 8.2 K for the inner side of the octagonal pipe. If no force is applied, the temperature increase of the heat absorber is higher, *i.e.* around 17 K, as well as the one of the pipe, *i.e.* around 9 K. The local temperatures are lower in the case of nominal compression as the heat is more uniformly distributed on the upper side of the pipe. However, since the temperature of the pipe (inner copper layer) exceeds the maximum allowed increase of 5K, the thermal link welded on the upper side of the octagonal pipe has been disregarded.

Thermal link welded on the cooling tube

The temperature increase of the beam screen sample whose thermal link is welded on the cooling tube is shown in Fig. 4.16 without any compression force and in Fig. 4.17 with nominal compression force. The initial temperature of the cooling tube ranges from 50 to 80 K.

The comparison of the experimental data with the simulated ones is worse than in the previous case (up to 45 %). This is probably due to a bad quality of the brazing between the thermal link and the heat absorber or a bad

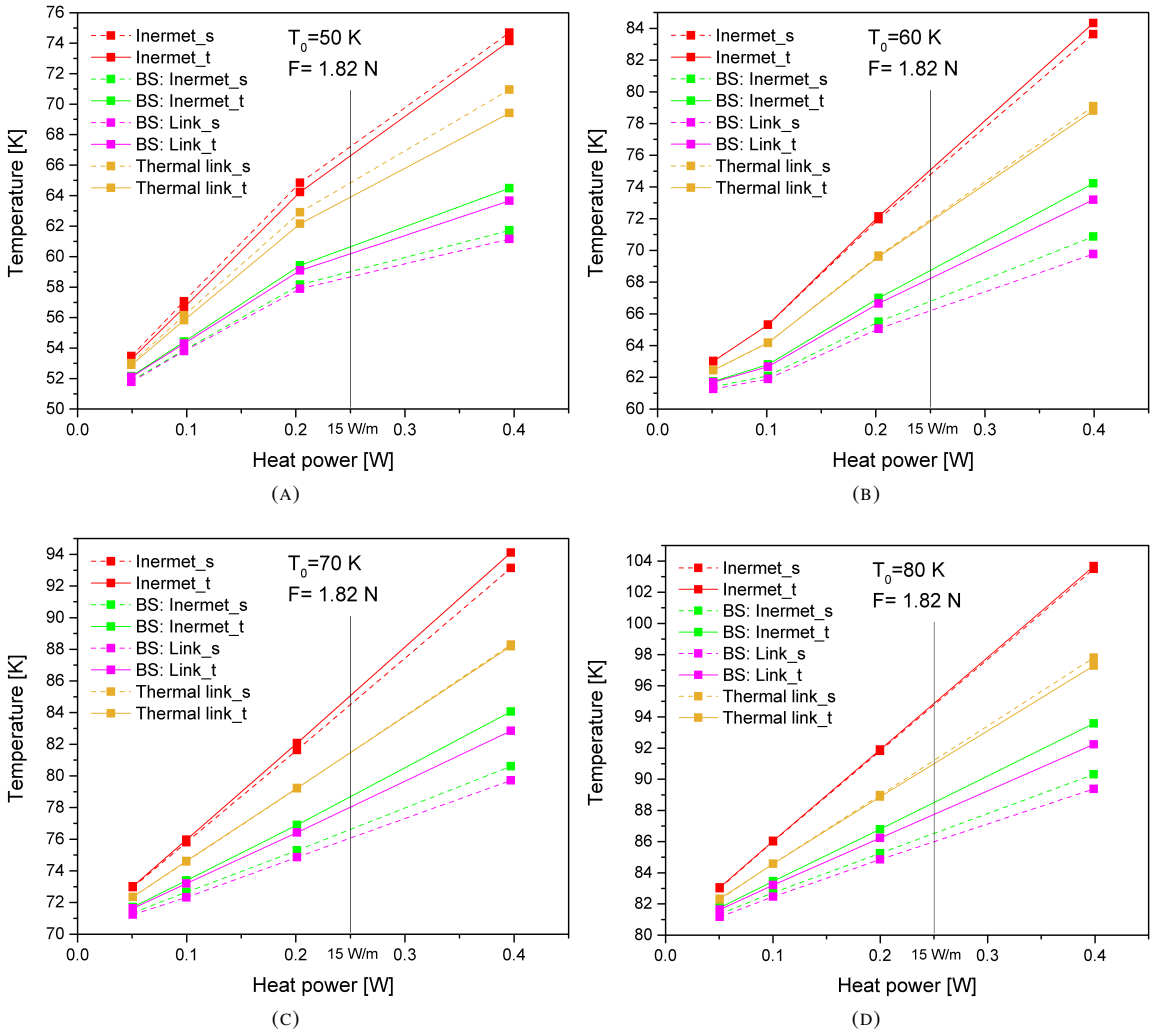


FIGURE 4.15: Thermal link welded on the pipe with nominal compression force (1.82 N). Temperature of the probe points according to the initial temperatures of 50 K (a), 60 K (b), 70 K (c), and 80 K (d).The power given to the heat absorber is 0.05 W, 0.1 W, 0.2 W, and 0.4 W. The profile of the measured data are represented by the continuous line while the numerical ones by the dashed lines.

welding of the thermal link pad on the cooling tube. In addition, the sample presented a manufacturing defect as the pin holding the heat absorber was in full contact with the inner copper layer.

The compression force of 1.82 N has an impact on the temperature of the inner side of the octagonal pipe which results to be at most 32 % higher in comparison to the case when no force is applied. The initial temperature has a negligible effect on the net temperature increase within each beam screen component.

Table 4.3 reports the measured temperature increase of the heat absorber and the octagonal pipe for a nominal heat load equal to 15 $\mathrm{W\,m^{-1}}$. The base temperatures are 60 K and 75 K, namely at the beginning and at the end of the triplet area, and the forces are 1.82 N (nominal compression) and 0 N (no compression). In case of nominal compression for both base temperatures the increase is around 14 K for the heat absorber and 3.4 K for the inner side of the octagonal pipe. If no force is applied, the temperature increase of the heat absorber is slightly lower, *i.e.* around 13.5 K, as well as the one of the pipe, *i.e.* around 2.3 K. For the no-compression case the local temperatures are lower as the heat is transferred only to the cooling tube and not to the pipe. Therefore, since the temperature of

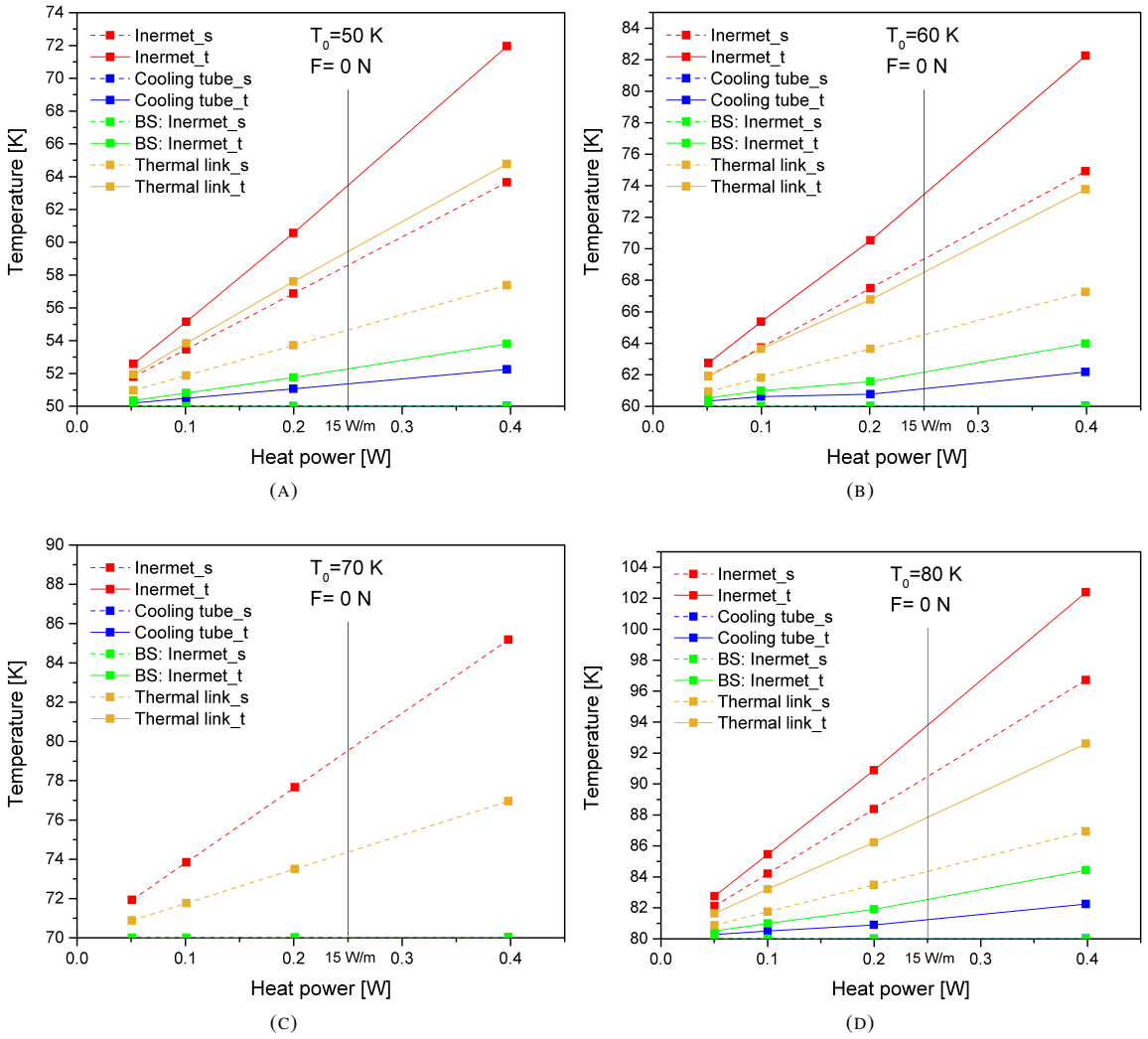


FIGURE 4.16: Thermal link welded on the cooling tube without compression force. Temperature of the probe points according to the initial temperatures of 50 K (a), 60 K (b), 70 K (c), and 80 K (d). The power given to the heat absorber is 0.05 W, 0.1 W, 0.2 W, and 0.4 W. The profile of the measured data are represented by the continuous line while the numerical ones by the dashed lines.

	Nominal compression		No compression	
Base T	W block ΔT	Octagonal pipe ΔT	W block ΔT	Octagonal pipe ΔT
(60.00 $\pm$ 0.16) K	(14.00 $\pm$ 0.06) K	(3.20 $\pm$ 0.04) K	(13.50 $\pm$ 0.06) K	(2.20 $\pm$ 0.04) K
(75.00 $\pm$ 0.23) K	(14.00 $\pm$ 0.09) K	(3.40 $\pm$ 0.03) K	(13.50 $\pm$ 0.09) K	(2.30 $\pm$ 0.03) K

TABLE 4.3: Measured maximum temperature increase of relevant Q2-type beam screen components with the thermal link welded on the cooling tube, for a nominal heat load of 15 W m^{-1}.

the pipe (inner copper layer) is within the maximum allowed 5K increase, the thermal link welded on the cooling tube is a suitable solution to guarantee an efficient thermal transfer within the HL-LHC beam screen.

4.5.2 Real-scale sample (FEM)

The temperature distribution of the assembly has been simulated for one eight of the Q1 and Q2 beam screens which are 400 mm long (periodic unit of the beam screen). The considered thermal link is 3 mm wide, 1 mm thick,

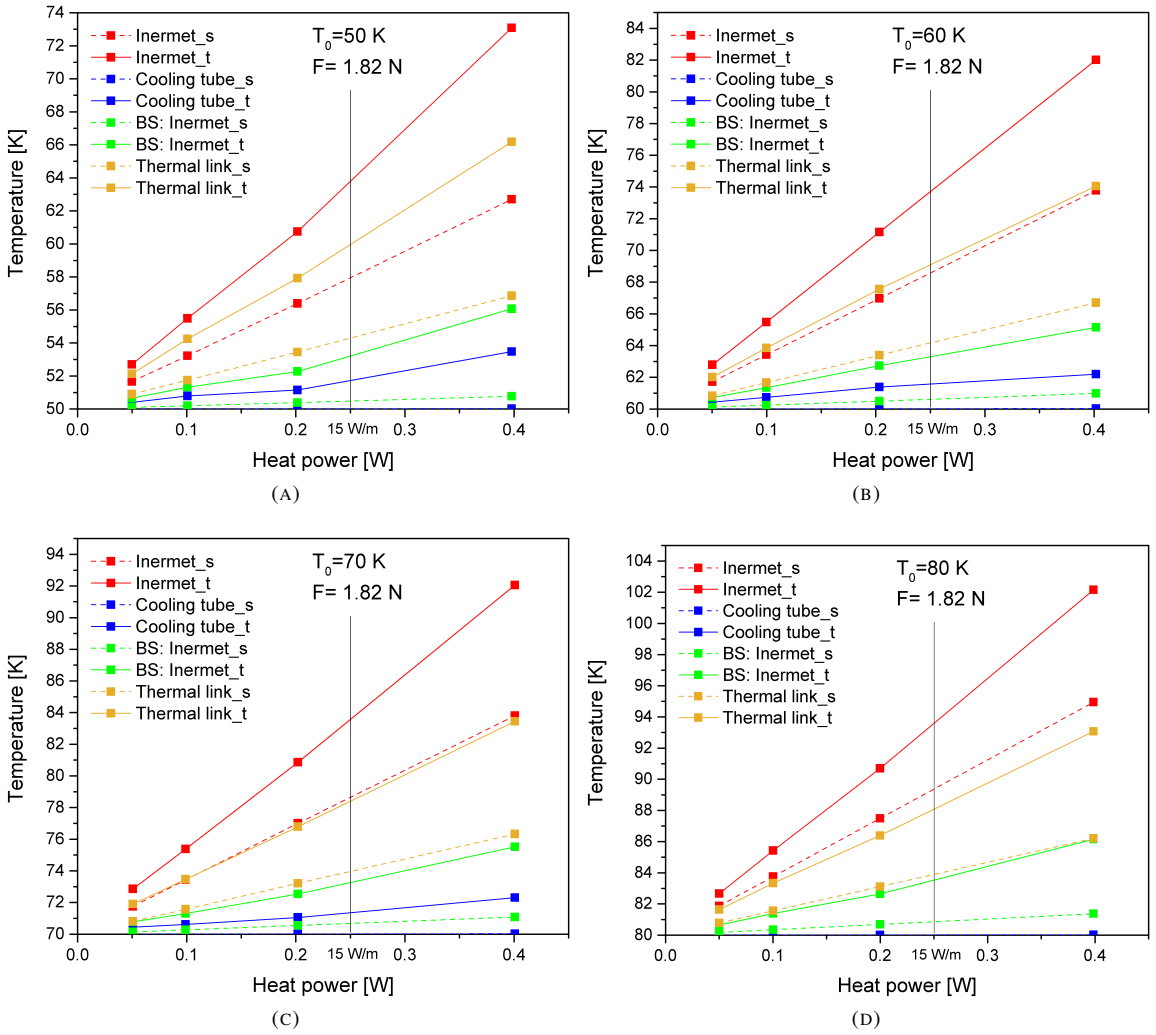


FIGURE 4.17: Thermal link welded on the cooling tube with nominal compression force. Temperature of the probe points according to the initial temperatures of 50 K (a), 60 K (b), 70 K (c), and 80 K (d). The power given to the heat absorber is 0.05 W, 0.1 W, 0.2 W, and 0.4 W. The profile of the measured data are represented by the continuous line while the numerical ones by the dashed lines.

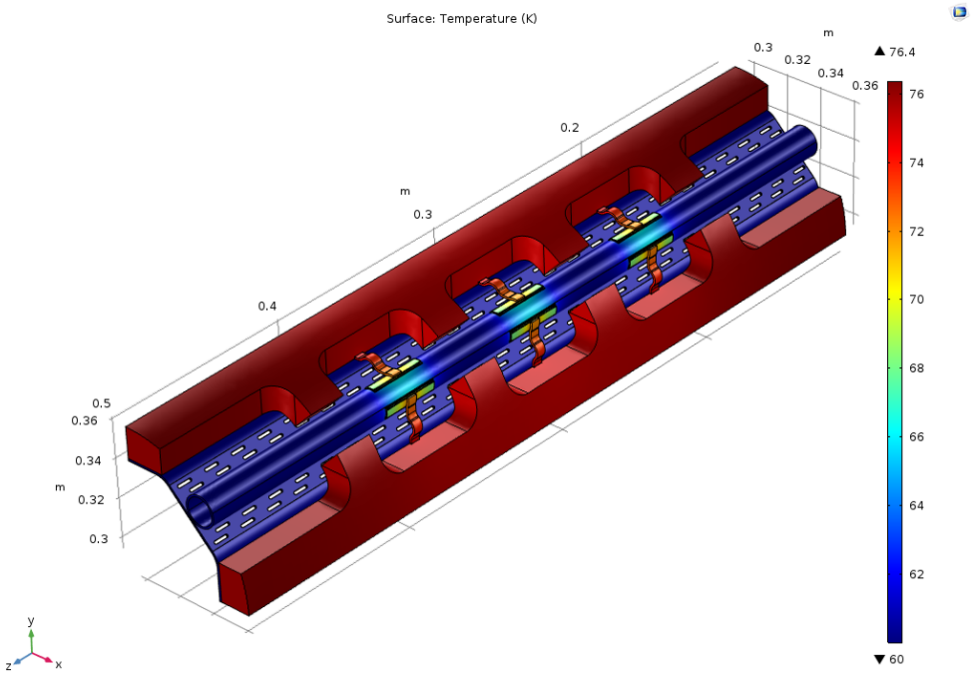
and welded on the cooling tubes. For the Q1 beam screen the heat load is 25 $\mathrm{W\,m^{-1}}$ and the initial temperature is set to 60 K while for the Q2 version beam screen the heat load is 15 $\mathrm{W\,m^{-1}}$ and the initial temperature is 75 K.

The temperature distribution is shown in Fig. 4.18 for the two beam screen types. For the Q1 version the maximum temperature is 76.4 K, while for the Q2 version is 86.7 K. The temperature of the inner copper layer is for both versions well below 5 K.

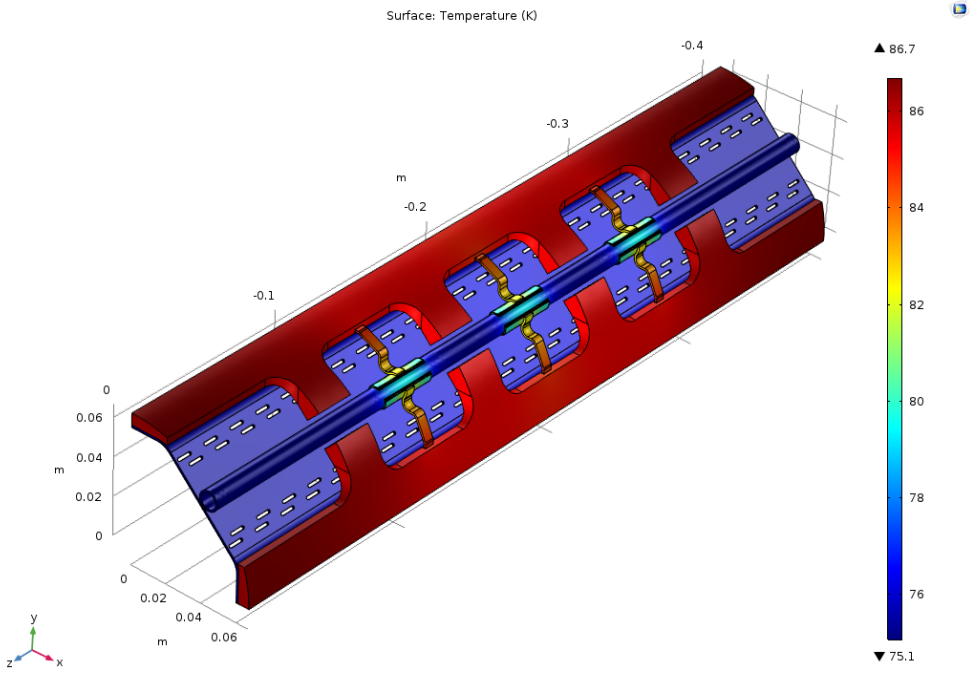
4.6 Heat transfer to the cold bore

4.6.1 Small-scale sample (FEM + test)

The heat transfer through the supporting springs has been measured by means of a specific sample equipped with a set of six springs, see Fig. 4.19. These have been assembled onto a sample holder in a symmetrical configuration



(A)



(B)

FIGURE 4.18: Temperature distribution [K] simulated for a quarter of a Q1 and Q2-Q3-D1 beam screen 400 mm long whose thermal links are welded on the cooling tube.

so that the heated side of the springs is thermally decoupled from the rest of the setup. The heat transfer occurs only through the supporting system. The ZrO_2 spheres are in contact with a stainless steel plate which represents the cold bore. Heat losses through the cabling wires for the electric heater and temperature sensor have been taken into account and compensated for. Measurements have been carried out on a Sumitomo Heavy Industries two-stage pulse tube refrigerator (PTR) that can provide up to 1 W of cooling power at 4.2 K on the second stage and a no-load temperature of 2.6 K. A detailed description of the measurement setup can be found in [57]. Numerical simulations have been performed to evaluate the heat transfer to the cold bore through the simplified version of the sample holder shown in Fig. 4.19d.

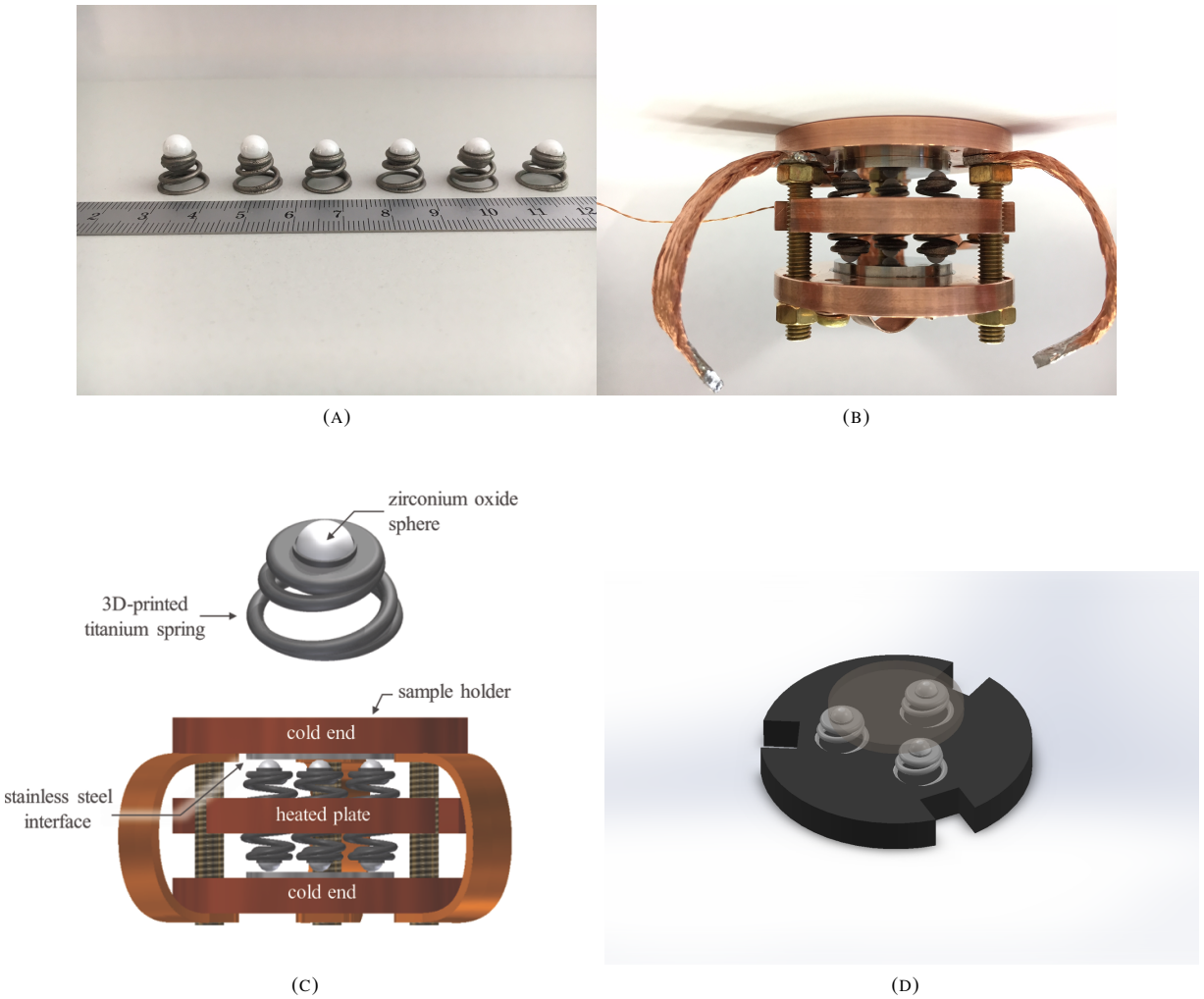
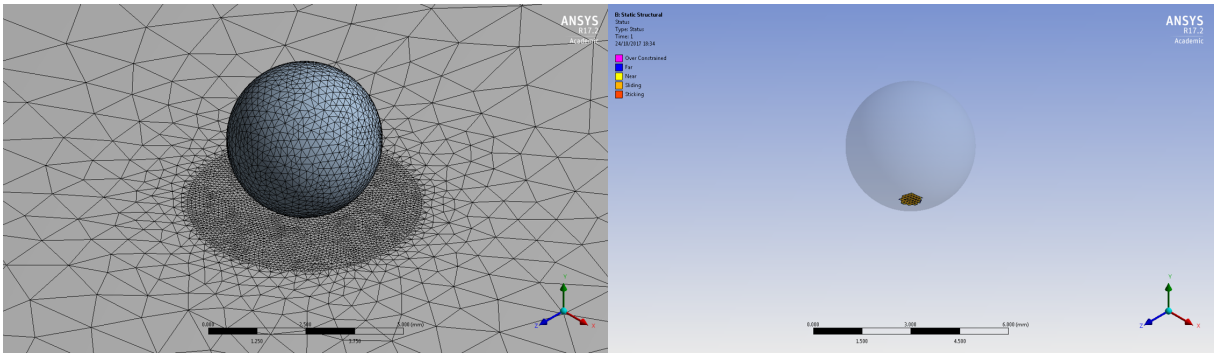


FIGURE 4.19: 3D printed titanium grade 5 springs in (a), setup to assess the heat transfer through the zirconia sphere in (b), full CAD model of the experimental setup in (c), and its simplified version adopted in the simulations in (d).

The thermal contacts considered in the FEM model are depicted in Fig. 4.22. These refer to the contacts of the Q2 spring between the heated plate and the zirconia sphere as well as the contact of the sphere with the cold end. The contact surface between the ceramic sphere and the end plate has been estimated by means of a linear-elastic FEM simulation, see Fig. 4.20. The normal load applied in the simulation is 7.5 N (nominal compression), which results into a contact surface of 0.38 mm^2.

The supporting structure made of zirconia spheres and titanium springs has been characterised for both the nominal compression of the Q2 (7.5 N) and Q1 springs (18.5 N). Fig. 4.21 shows the heat load transferred



(A) (B)

FIGURE 4.20: In (a) mesh of the contact interface between the zirconia sphere and the plate. In (b) contact surface between the sphere and the plate.

to the cold bore per supporting system, as a function of the hot side temperature (*i.e.* tungsten block). For each measurement, the cold end temperature has been maintained between 2.7 K and 3 K. Overall conductance increases with increasing temperature, which stabilizes for temperatures higher than 80 K where it reaches values in the range of 0.08 $\mathrm{mW\,K^{-1}}$. The heat load transferred from the heat absorber to the cold bore surface per spring varies between 5 mW and 7 mW at the operating range of the heat absorber temperature (75 K to 95 K). As the beam screen is sustained in the cold bore by 40 springs per meter, this results in a maximum heat transfer equal to 280 $\mathrm{mW\,m^{-1}}$.

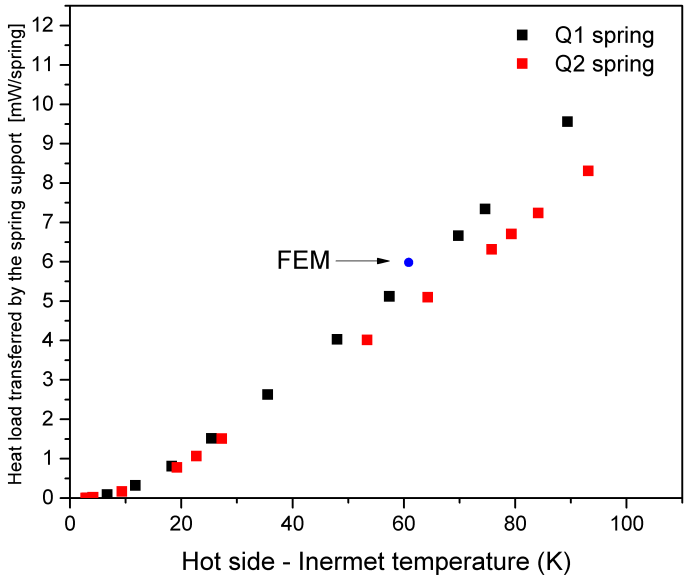


FIGURE 4.21: Heat load transferred to the cold bore through the Q1 and Q2 zirconia spheres.

A close analogy has been found between measurement and simulations. The heat transferred through a Q2 zirconia sphere is equal to 6.9 mW. The simulations account for the thermal contact shown in Fig. 4.22. The initial temperature has been set to 60 K for the heated plate and 2 K for the cold plate.

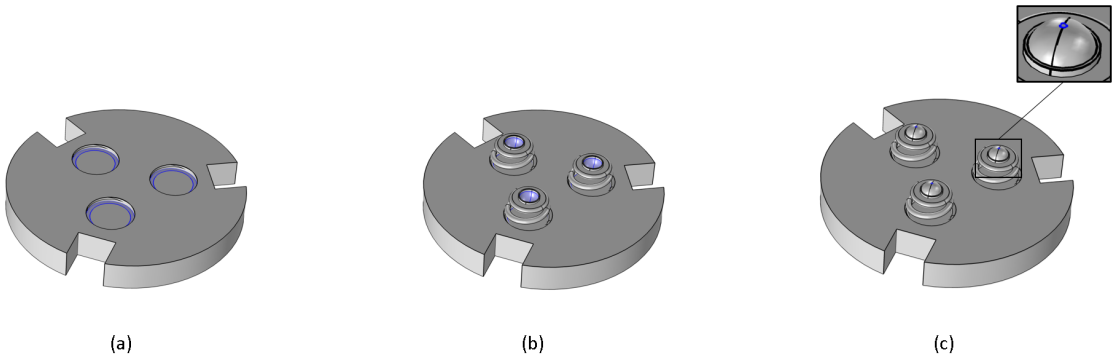


FIGURE 4.22: Contact between the first stainless steel plate and the spring in (a), contact between the spring and the zirconia sphere in (b), contact between the sphere and the stainless steel plate in (c).

4.6.2 Heat transferred by radiation to the cold bore

The radiative heat transferred to the cold bore has been calculated analytically as done in [59].

The radiative heat load to the cold bore is given by:

$$Q_{rcb} = \frac{\epsilon_{cb}\epsilon_{ha}}{\epsilon_{ha} + (1-\epsilon_{ha})\epsilon_{cb}} A\sigma(T_{ha}^4 - T_{cb}^4) \tag{4.5}$$

where:

- Q_{rcb} : radiative heat load to the cold bore (in W)
- ϵ_{cb} : emissivity of the cold bore tube ($\epsilon_{cb} = 0.1$, see [59])
- ϵ_{bs} : emissivity of the heat absorbers ($\epsilon_{ha} = 0.032$, see [60])
- A : cold bore area (A = 0.43 m^2 per aperture and per meter)
- σ : Stephan-Boltzmann constant ($\sigma = 5.67 \cdot 10^{-8} \mathrm{W\,m^{-2}\,K^4}$)
- T_{cb} : cold bore temperature (T_{cb}=1.9 K)
- T_{ha} : heat absorber temperature (in K)

The analytical formula is based on the heat transferred between two concentric tubes. Therefore, it is an approximation for the HL-LHC beam screen which is octagonally shaped and presents non uniform heating sources.

The radiative heat load turns out to be 60 $\mathrm{mW\,m^{-1}}$ if the beam screen was uniformly covered by heated elements. However, since there are only four tungsten blocks the radiative load is lower than 60 $\mathrm{mW\,m^{-1}}$.

4.7 Conclusions

In this chapter the thermal transfer between the heat absorbers and the cooling tubes has been optimised through a FEM model, which allows to specify the thermal contacts.

Two types of thermal links have been tested. In one case the extremities of the link are welded on the octagonal pipe and in the other case on the cooling tubes. The thermal link welded on the octagonal pipe has been rejected as the temperature of the inner copper layer exceeds the 5K threshold. The most efficient way to transfer the heat by welding the thermal links to the cooling tubes. Specifically these are first brazed under the tungsten blocks and then welded to the tubes. To allow the connection of the thermal links with the cooling tubes, a round 0.6 mm thick interface pad made of stainless steel co-laminated with 75 $\mu\mathrm{m}$ of copper has been used. The pad is brazed to the thermal link on the copper side and welded to the tube on the stainless steel side. To reduce the risk of perforating the tubes during the welding phase, the thickness of the pad has been reduced of 0.2 mm along its long edges. This makes the welding safer as the laser energy needed to weld the pad is tailored on a 0.4 mm thick layer to be joined to a 1 mm thick tube. The bottleneck of the heat transfer was found to be related to the length of the welding lines on the interface pad. This is due to a difference of around two order of magnitude between the thermal conductivity of the copper and stainless steel. Therefore, the interface pad has been extended up to 30 mm in order to transfer the heat carried by the copper link. It has also been found that the co-laminated copper layer of the interface pad enhances significantly the thermal transfer due to a more uniform thermal distribution. The optimisation of the thermal link has been validated by experiments reproducing the operational conditions on a small-scale sample. The requirement that the temperature of the inner copper layer does not exceed 5 K has been fulfilled with six thermal links per heat absorber. The minimum width of each link is 3 mm, while its thickness is 1 mm. The thermal link needs to be necessarily welded on the cooling tube.

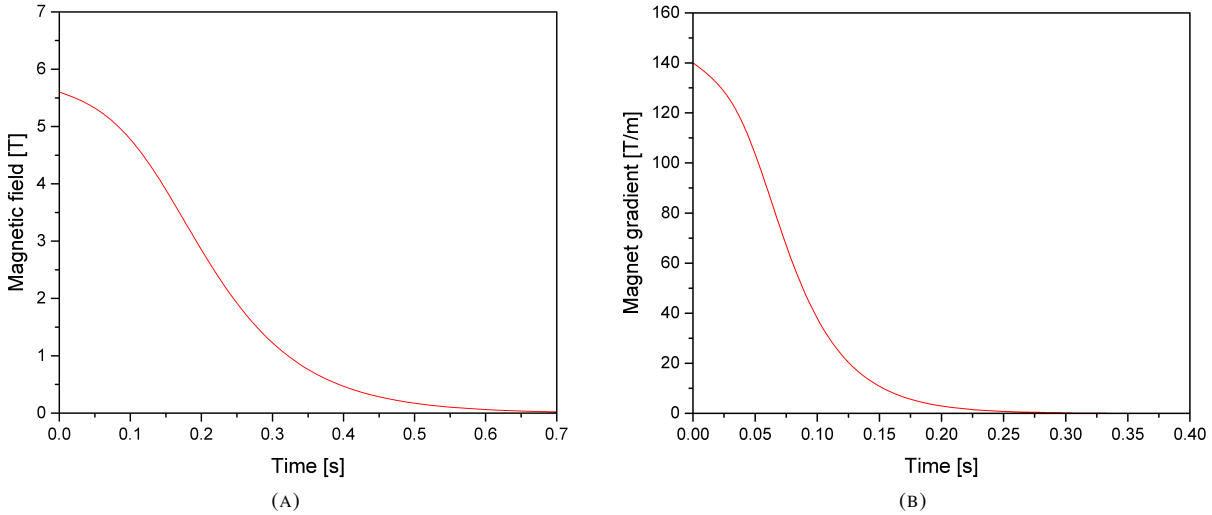
The heat transfer from the supporting system to the cold bore has been measured. The heat varies between 5 mW and 7 mW per spring. A good agreement with the numerical results has been found, which further proves the validity of the thermal contacts in the FEM model. This makes the estimation of the beam screen temperature reliable and efficient.

Chapter 5

Beam screen behaviour during a magnet quench with quench heaters

5.1 Quench heaters

The resistive transition of a magnet quench causes an excessive voltage and overheating that might locally damage the insulation material or even melt the superconducting cable. Quench heaters are stainless steel foils plated with copper used to protect the superconducting magnets in case of a quench. External power supplies energise the heater strips inside the magnet as soon as the quench is detected. The initial power density and the current decay time determine the quench heater effectiveness. By this means the propagation of the quench is enhanced as the stored energy is distributed over a larger volume, which results in lower hot-spot temperatures [61] [62]. About 2000 dipole and quadrupole magnets are equipped in the LHC with quench heaters mounted inside and/or outside the magnet coils. The magnetic field and magnet gradient decays in the case of a magnet quench for the HL-LHC inner triplet magnets are reported in Fig. 5.1.



(A) (B)

FIGURE 5.1: Magnet gradient decay of a quadrupole magnet in (a) and magnetic field decay of a dipole magnet in (b) during a magnet quench of the inner triplet area when only quench heaters are used as protection scheme.

5.2 Multiphysics modelling

5.2.1 Beam screen modelling

Multiple analytical models have been developed at CERN for the beam screens currently installed in the LHC. The features of the models are now reviewed in turn and a summary of the main features is provided in Table 5.1 for comparison.

Rathjen [63] developed an analytical formulation to evaluate bending moments, deformations and stress for 2D geometries. The work has been conducted for circular and racetrack shaped screens. This approach enables fast calculations and it is ideal for parametric and optimisation studies. However, the electrical resistivity was kept constant since resistive losses were not accounted for. In addition to that, only the case when the thickness of the screen is smaller than the size of the entire structure was considered. To this end, the forces are applied on the neutral fibre of the structure. In addition, Rathjen used a quarter of the beam screen geometry to fully define its response during a magnet quench. This can be done as the symmetry conditions related to the geometry and the magnetic field are mutually valid. The principle of virtual work has been adopted in his study to characterise the mechanical response of the structure. The maximum horizontal deformation is 0.86 mm for a screen immersed in a dipolar field. The maximum stress is in correspondence of the horizontal direction and the stress concentration due to the pumping slots has been estimated. This estimation is based on the fact that the induced energy does not vary significantly with the holes and that for a certain percentage of slot coverage the proportion of regions characterised by higher stress is the same.

The variations of electrical and thermal properties as a function of temperature have been considered by Valbuena [64] in his two-dimensional model based also on analytical formulations. In addition, the magneto-resistivity has been considered too. His method consists of justifying the typical nonlinearities of a multiphysics problem by a two-way coupling between the magnetic and thermal physics. The similarity between the electric and thermal fields has enabled to easily couple them so that the temporal evolution of the power losses, temperature and forces can be derived. This approach results in induced forces that are twice less intensive than those found in Rathjen's model. The equations have been implemented in a FEM platform called CASTEM 2000 [65]. The electro-thermal calculation has been performed in a time dependent study while the mechanical analysis has been performed in a stationary study. It is noteworthy that only the highest force field induced during the quench has been given to the mechanical calculations as input.

A simplified approach has been pursued by Ferrer [66] and Darve [67] to evaluate the influence of the pumping holes on the deformation of the beam screen. The electrical resistivity of the materials used in the model has been assumed to be constant. This approach can be seen as a sort of numerical extrusion of the Valbuena model but applied to a 3D geometry. The stress state around the pumping holes has been assessed for different pattern schemes.

Darve concluded that the presence of the side slots on the beam screen samples does not affect the ratio between the vertical and the horizontal deformation of the beam screen cross section. However, the models currently developed at CERN still have limitations and these are summarised below:

- Magnetic self-inductance phenomena are not accounted for;
- The two-way coupling between the magnetic and mechanical module has never been implemented;

Model	Solving approach		Model space		Mf-th coupling		Mf-mech coupling		Mech response		Electro-dynamics
	Analytic	FEM	2D	3D	One way	Two way	One way	Two way	Sta-tic	Dyna-mic	self-inductance
Rathjen [63]	✓		✓		✓		✓		✓		
Valbuena [64]	✓		✓			✓	✓		✓		
Ferrer [66]	✓			✓	✓		✓		✓		
Darve [67]	✓			✓	✓		✓		✓		
Garion [39]	✓		✓			✓	✓			✓	

TABLE 5.1: Features of the multiphysics models to study the beam screen during quench up to 2017. Legend, Mf: magnetic fields, Th: thermal, Mech: mechanical.

- The mechanical response of the beam screen is evaluated according to a quasi-static approach. Therefore, the highest magnetic force will always give the most severe mechanical response. The evolution is obtained simply by interpolating of the static responses at each interval of time. With this approach, the dynamic effects due to the inertia of the components are not considered;
- The behaviour of components placed along the beam axis cannot be assessed as a 3D model has never been developed.

A first attempt to overcome the quasi-static approach has been successfully proposed by Garion [26] [39] by expanding the standard analytical formulations. However, the remaining three restrictions are too critical to be neglected in the design of the new HL-LHC beam screen and an advancement of the modelling techniques is required to address the limitations of current models.

5.2.2 Multiphysics modelling relevant to the beam screen problem

Eddy current problem on multiply-connected domains

The model described in this thesis hinges on the application of Maxwell's equations. In the literature their implementation for finite element methods can be found in the works of Monk [68] and Bossavit [69]. In particular, the eddy current problem on multiply-connected domains has been thoroughly treated by Ledger [70] [71] through an efficient computational approach based on the **A** formulation, *hp*-finite element discretisation, and a novel preconditioning technique. On this subject many authors have proposed different numerical formulations in terms of primal and potential variable.

Bossavit and Verite [72] proposed a method in three dimensions based on a FEM and BEM approach. Such a method hinges on the field H as state variable. To confine the magnetic field, a scalar magnetic potential in the non-conducting region has been used. The outer boundary of the modelling region has been discretised by boundary elements instead. This enables to reduce the computational load of the simulation as less elements are used to mesh the entire domain.

Morisue and Fukumi [73] analysed the eddy current problem by means of the continuous magnetic vector potential and the discontinuous magnetic vector potential. The former case results in no-cutting regions between multiply connected domains but the electric scalar potential needs to be included in the equations of the problem. The latter requires the cutting between different domains but the electric scalar potential can be neglected if the electrical conductivity is constant.

Kameari [74] developed a method to treat the eddy current whose equations have been expressed in terms of magnetic vector potential and electric scalar potential in the conductive domains and a reduced magnetic scalar potential in the non-conductive domain. This solution proved to be numerically stable especially for regions characterised by discontinuities and different materials. It turns out that such a method agrees well with analytical solutions. However, there are some disadvantages, mainly related to the large number of variables to solve and to the fact that the matrix is not always positively definite.

Biro and Preis [75] [76] reviewed various magnetic vector potential formulations in three dimensions. The conditions that guarantee the uniqueness of the numerical solution have been shown. This has been obtained by setting the normal component of the vector potential to zero along the interface of regions modelled with different potentials. In addition, the vector potential has been introduced also in non-conducting regions, which simplifies the definition of the normal component of the potential. These conditions allow to obtain a stable numerical solution with respect to frequency.

Webb and Forghani [77] treat time-harmonic eddy current problems by means of edge elements capable to cope better with different values of electrical conductivity and magnetic permeability. However, in no-conducting domains the scalar potential is the most reliable approach to reach fast convergence. Sources of currents can be handled easily without domain partitions nor specific electrical circuits.

Kanayama *et al.* [78] have formulated the eddy current problem at high frequency by magnetic vector potential together with the electric scalar potential and by magnetic vector potential only. The displacement current is, therefore, accounted for. The problem has been implemented through finite element methods. The converge of the problem is reached for a wider range of frequencies by using the magnetic vector and the scalar electric potentials.

Zheng *et al* [79] developed an adaptive formulation with respect to error estimation of the magnetic field (for conductive domains) and the magnetic scalar potential (for non-conductive domains) on multiply connected regions. This solution proved to be computationally efficient for problems with local singularities.

Multiphysics problems and couplings

One of the most important aspects concerning the design of the beam screen during the quench is the influence that the temperature rise and the displacements have on the induced forces. In the literature there is a vast and increasing number of multiphysics models to investigate these as well as other interactions. This approach is becoming increasingly popular amongst engineers because the prediction of complex interactions very often requires the consideration of different and interdependent phenomena [80] [81] [82].

In general, either one-way or two-way couplings are used when dealing with interaction mechanisms in unsteady multiphysics problems. In the former, a general physics is first computationally solved and the results are then transferred to the subsequent physics in a mono-directional way, *i.e.* no backwards exchange of information takes place. In the latter, a bi-directional communication between multiple physics exists. Although the computational burden of a two-way coupling approach is higher than the one-way, it is often the preferred choice because of an increased prediction of physical phenomena [83] [84]. However, depending on specific cases, a mono-directional transfer turns out to be a good trade-off when the interaction between different modules is negligible or when an iterative algorithm enables to lower the computational error for the equilibrium of coupled non-linear field equations [85].

Three-way couplings have also been found to be used in certain cases such as assessing Seebeck, Peltier and the Joule heat for steady state problems in periodic multi-phase thermoelectric devices [86]. There are several

domains where the interactions between the physical phenomena treated in this thesis are important to optimise products or technological processes.

Magneto-thermal couplings are essential to accelerate the design process of induction heating devices whose prototyping would be very expensive [87]. Most of the numerical work is based on the time harmonic approximation of the magnetic module and on a standard time-dependent study of the thermal module. This is due to the different time constants of the magnetic and thermal phenomena [88] [89]. Bay *et al.* [90] developed a complex two-dimensional numerical model of this type also including the mechanical response. In this work non-linear magnetic materials are considered and a range of frequency problems have been verified experimentally.

Magneto-mechanical couplings are widely used to improve the design of machines where magnetic field sources interact with electrical conductive structures. An example of industrial application for such couplings is magnetic resonance imaging (MRI) scanners [91] [92]. In this field, Ledger *et al.* [70] developed a customised routine based on a new fixed point algorithm and an enhanced evaluation of the mechanical stresses to better investigate unwanted effects related to the typical vibrations of these devices. Bagwell *et al.* [93] extended this work by including acoustic effects through a linearisation of the transient equations and a simplification of the solving algorithm. Additionally, the acoustic physics in MRI scanners has been fully coupled in transient simulations by Rausch *et al.* [94] where a combination of solvers has been used to obtain a stable solution for 2D and 3D geometries. Schinnerl *et al.* [95] proposed a multigrid calculation scheme where electromotive forces, Lorentz forces, magnetic interface forces, and the large displacement of the geometry are fully coupled. An iterative solver couples the dynamical magnetic field with the mechanical problem. The mechanical part is meshed with nodal elements, while the magnetic one with edge elements. One advantage of this strategy is that the mesh size can be adapted independently, *i.e.* where most of the result accuracy is needed. The multigrid simulation scheme provides incomparable gain in terms of computational load, which has been verified by three different examples.

Strong magneto-mechanical couplings also denote the behaviour of magnetostrictive materials [96] [97], whose implementation in numerical codes has enabled the optimization of actuators, force sensors, and rotating electric machines [98] [99]. In particular, Yang *et al.* [100] compared experimental and numerical results, based on magneto-mechanical interfaces strongly coupled, of a force sensor equipped with giant magnetostrictive materials. The coupling does not rely on the transfer of displacement and vector potential between the two physics but rather on the magnetic and mechanical energy. It turns out that results are in good agreement.

Electrodynamic loudspeakers, fast-switching electromagnetic valves, and power transformers are examples of additional industrial applications where magneto-mechanical couplings have been applied to improve their design [101] [102].

The couplings between the magnetic, thermal and mechanical physics are important for the design of electromagnetic forming systems. In 2001, El-Azab *et al.* [103] stated that a numerical solution to solve such a problem was not achieved yet. In 2015, Alves and Bay *et al.* [104] developed a numerical tool composed of two platforms, one for coupled thermo-mechanical problems of large material deformations, and the other for magnetic field problems. The solver of the two platforms runs separately according to a loosely coupled cycle. One advantage of this approach is that the non-conducting domain is accounted for only in the magnetic platform and not in the thermo-mechanical one, implying that each platform is meshed differently.

5.3 Constitutive and governing equations

5.3.1 Magnetic physics

An electromagnetic problem subjected to certain boundary conditions can be formulated through the well-known Maxwell equations [105]. From these equations the Maxwell-Ampere law can be stated as:

$$\nabla \times \mathbf{H} = \mathbf{J} + \frac{\partial \mathbf{D}}{\partial t} \tag{5.1}$$

where **H** is the magnetic field, **J** the current density and **D** the electric displacement or electric flux density.

It is important to point out that the time derivative of the electrical displacement $\frac{\partial \mathbf{D}}{\partial t}$ has been neglected due to the quasi-static approximation [106]. This approximation makes also the equation of continuity equal to $\nabla \times \mathbf{J} = 0$. It can be used when the currents and the electromagnetic fields change in time so slowly that the delay of the wave propagation can be neglected. This is true when the dimensions of the geometry to be studied are very small in comparison with the wavelength of the electromagnetic field. It is as if the device does not see the wave oscillations but only a uniform time varying field, see Fig. 5.2. In particular, the quasi-static approximation is valid when the electric size of the structure is up to $\frac{1}{10}$. The electric size is the ratio between the largest distance of the geometry and the wavelength of the field. The wavelength of an electromagnetic wave is given as [107]:

$$\lambda = \frac{c}{f} \tag{5.2}$$

where c is the speed of light and f the frequency content of the magnetic field decay. Therefore, considering the maximum distance between two points of the beam screen cross section and the frequency spectrum of the magnet quench (2.5 Hz), the electric size of the studied problem is $1 \cdot 10^{-9}$. Such approximation is then largely justified.

The Faraday's law is equal to:

$$\nabla \times \mathbf{E} = -\frac{\partial \mathbf{B}}{\partial t} \tag{5.3}$$

where **E** is the electric field and **B** the magnetic flux density.

To form an independent system the first two equations have to be combined with one of the two Gauss' laws either in the magnetic or electric form:

$$\nabla \cdot \mathbf{D} = \rho \tag{5.4}$$

$$\nabla \cdot \mathbf{B} = 0 \tag{5.5}$$

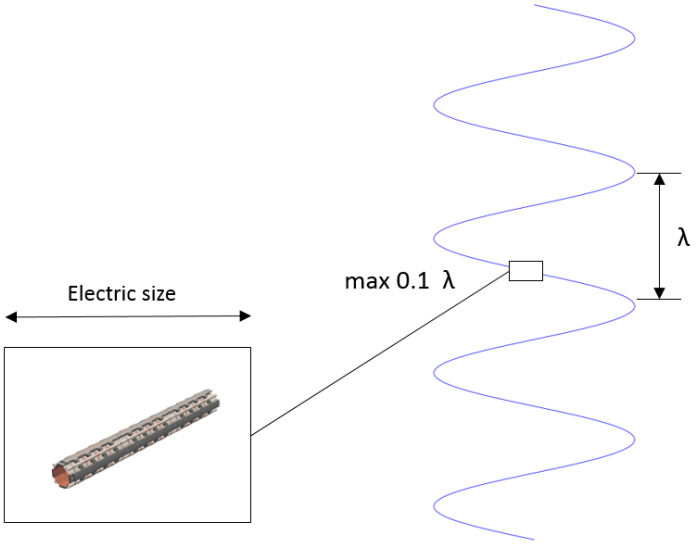


FIGURE 5.2: Electric size of the beam screen.

Alternatively the system becomes independent with the equation of continuity:

$$\nabla \cdot \mathbf{J} = -\frac{\partial \rho}{\partial t} \tag{5.6}$$

where ρ is the electric charge density.

Constitutive relationships are needed to define the physical properties of the medium and to obtain a closed system. For the electric and magnetic fields these relations can be generalized respectively as:

$$\mathbf{D} = \epsilon_0 \epsilon_r \mathbf{E} + \mathbf{D}_r \tag{5.7}$$

$$\mathbf{B} = \mu_0 \mu_r \mathbf{H} + \mathbf{B}_r \tag{5.8}$$

where μ_r is the relative magnetic permeability, μ_0 is the magnetic permeability of vacuum equal to $4\pi \cdot 10^{-7}$H/m , while ϵ_r is the relative magnetic permittivity and ϵ_0 is the permittivity of vacuum that can be derived from the following expression:

$$\epsilon_0 = \frac{1}{c_0^2 \mu_0} = 8.854 \cdot 10^{-12} [F/m] \tag{5.9}$$

The remanent displacement $\mathbf{D}_r$ as well as the remanent magnetic flux density $\mathbf{B}_r$ refer to the electric and magnetic flux density when no electric or magnetic field is present. In the case study considered in this thesis these values are zero.

If $\epsilon_0\epsilon_r$ and $\mu_0\mu_r$ are defined as electrical permittivity, ϵ, and magnetic permeability, μ, the constitutive relations can be written as:

$$\mathbf{D} = \epsilon\mathbf{E} \tag{5.10}$$

$$\mathbf{B} = \mu\mathbf{H} \tag{5.11}$$

Both ϵ and μ are scalar and equal to 1 for the isotropic and homogeneous materials of the beam screen.

In the proposed numerical model the Maxwell's equations are formulated through the magnetic vector potential $\mathbf{A}$, so that:

$$\mathbf{B} = \nabla \times \mathbf{A} \tag{5.12}$$

where $\mathbf{B}$ is the magnetic flux density. The model neglects the magnet coils generating the field as the discretisation of these would considerably increase the complexity and the computational load of the multiphysics algorithm. Therefore, the magnetic field decay, which is given as input to the problem has been conveniently considered as a known background field by which only a non-conducting region containing the beam screen needs to be modelled. For this purpose, the reduced magnetic vector potential (RMVP) has been adopted [108] [109] [110]. The magnetic vector potential is split in two terms, namely the reduced potential, $\mathbf{A}_{red}$, and the known background field, $\mathbf{A}_{ext}$, so that $\mathbf{A}$ can be written as:

$$\mathbf{A} = \mathbf{A}_{red} + \mathbf{A}_{ext}. \tag{5.13}$$

The strategy is to solve only the induced field (reduced) $\mathbf{A}_{red}$. Therefore, the governing equation in the conducting region becomes:

$$\nabla \times \mu^{-1}\nabla \times (\mathbf{A}_{red} + \mathbf{A}_{ext}) = \mathbf{j}^0 + \mathbf{j}^s + \mathbf{j}^l = -\sigma\frac{\partial(\mathbf{A}_{red} + \mathbf{A}_{ext})}{\partial t} \tag{5.14}$$

while the equation of the non-conducting region:

$$\nabla \times \mu^{-1}\nabla \times (\mathbf{A}_{red} + \mathbf{A}_{ext}) = 0 \tag{5.15}$$

where σ is the electrical conductivity and μ is the magnetic permeability. In general, the current density $\mathbf{j}$ is composed of three terms: the contribution of the eddy currents $\mathbf{j}^0 = -\sigma\partial(\mathbf{A}_{red} + \mathbf{A}_{ext})/\partial t$, the current source $\mathbf{j}^s$ which is not present in the problem, and the Lorentz currents $\mathbf{j}^l = \sigma\mathbf{v} \times (\nabla \times \mathbf{A})$ that is deemed negligible for this application, where $\mathbf{v}$ is the velocity of the conductor.

Considering the regions as homogeneous and isotropic, constitutive relationships are needed to define the physical properties of the medium and to obtain a closed system. For the electric field $\mathbf{E}$ and magnetic field $\mathbf{H}$ these relations can be generalized respectively as $\mathbf{B} = \mu\mathbf{H}$ and $\mathbf{j} = \sigma\mathbf{E}$. The magnetic permeability $\mu = \mu_0$ is equal to $4\pi \cdot 10^{-7}$ H/m as the relative magnetic permeability, μ_r is considered equal to 1 for all the beam screen materials.

To reproduce the magnetic field component, B_y, of a dipole magnet, $\mathbf{A}_{ext}$ has to be written as:

$$\mathbf{A}_{ext} = \begin{bmatrix} 0 \\ 0 \\ kx \end{bmatrix} \tag{5.16}$$

where k is the magnitude of the field.

In a magnet quadrupole the components of the magnetic flux density depend on the distance from the origin according to the classical relations [105]:

$$B_x = Gy \tag{5.17}$$

$$B_y = Gx. \tag{5.18}$$

To reproduce the quadrupole field $\mathbf{A}_{ext}(t)$ can be written as:

$$\mathbf{A}_{ext}(t) = \begin{bmatrix} 0 \\ 0 \\ \frac{1}{2}G(t)(x^2 - y^2) \end{bmatrix} \tag{5.19}$$

where $G(t)$ is the evolution on time of the quadrupole magnet gradient.

The Lorentz forces are calculated in the magnetic interface through the relation:

$$\mathbf{f} = \mathbf{j} \times \mathbf{B}. \tag{5.20}$$

The calculation of the forces through this formulation turns out to be very accurate in electrical conducting domains.

Boundary conditions

Two symmetry conditions can be used to lower the computational load of magnetic simulations, namely the magnetic insulation boundary condition:

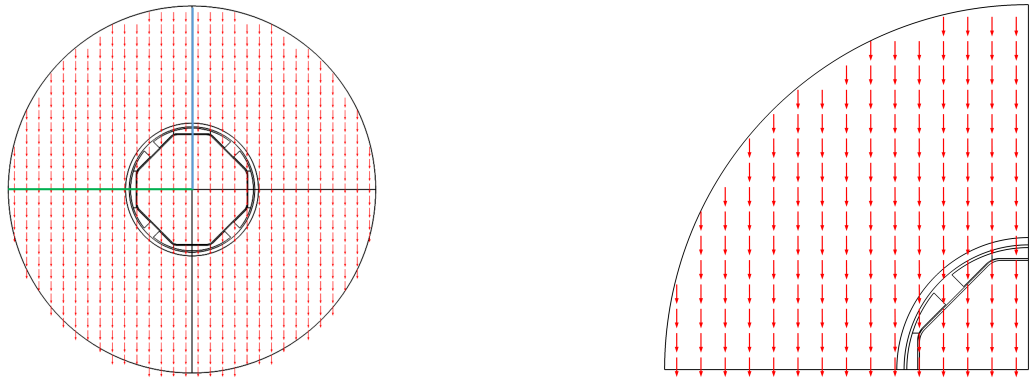
$$\mathbf{n} \times \mathbf{A} = 0 \tag{5.21}$$

and the perfect magnetic conductor boundary condition:

$$\mathbf{n} \times \mathbf{H} = 0 \tag{5.22}$$

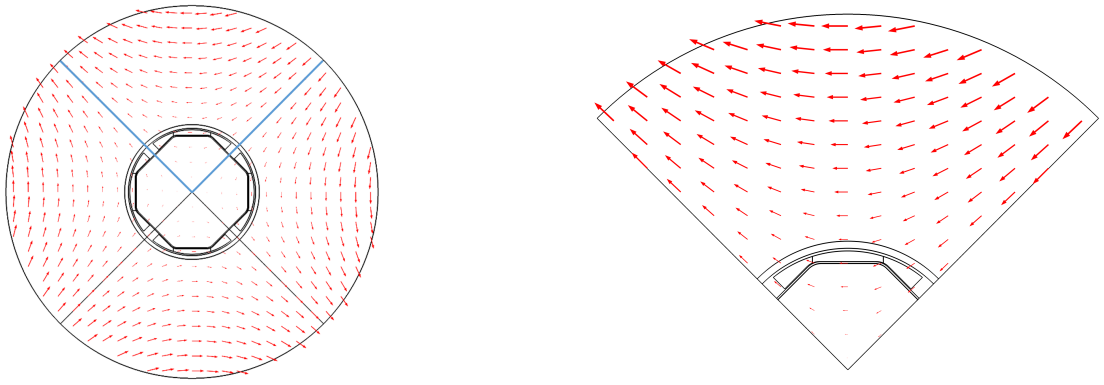
where **n** is the outer normal vector of the selected boundary.

These conditions depend strictly on the distribution of the magnetic field. The former can be used only where the magnetic field is uniformly parallel along a segment or surface and is zero in the normal direction. The latter



(A) (B)

FIGURE 5.3: Simplification in (a) of the beam screen geometry in a dipole magnet through the perfect magnetic conductor, in green at 180° angle, and the magnetic insulation, in blue at 90° angle. The geometry discretisation reduced to a quarter in (b).



(A) (B)

FIGURE 5.4: Simplification in (a) of the beam screen geometry in a quadrupole magnet through two insulation conditions, in blue at 45° and 135° angle. The geometry discretisation reduced to a quarter in (b).

can be used when the magnetic field is uniformly perpendicular along a segment or surface and is zero in the parallel direction.

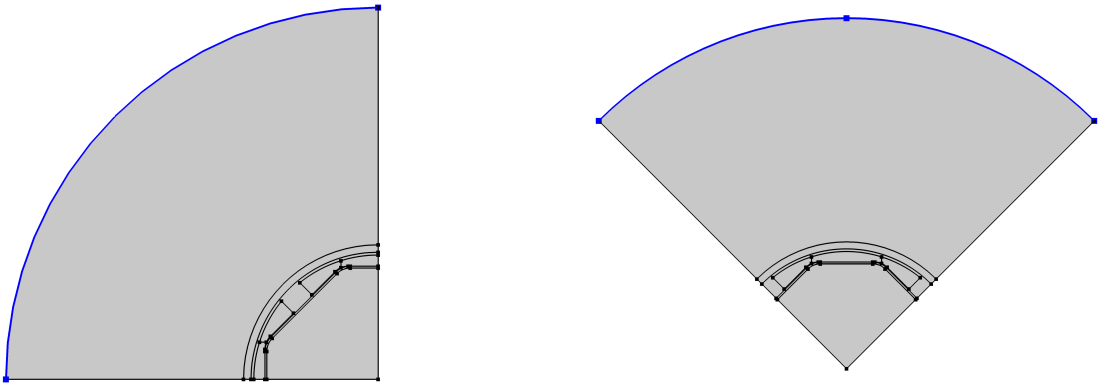
As shown in Fig. 5.3 for a dipole and in Fig. 5.4 for a quadrupole, this simplification results in modelling just a quarter of the whole beam screen. These symmetry conditions can be used only if they comply with the geometrical symmetry of the model. However, this is not an issue as the beam screen is symmetric along the magnetic ones.

Further simplifications would have been possible for the quadruple magnetic field. A perfect magnetic conductor condition placed at a 90° angle would have reduced to an eight the portion needed to give the same results as the whole domain. However, considering that a substantial reduction of the number of elements has already been achieved, this option has not been pursued due to complications in obtaining graphical results.

The RMVP can be implemented provided that a specific condition is applied along the outer boundaries of the non-conducting domain, see Fig. 5.5, that calculates to:

$$n \times \mathbf{A} = n \times \mathbf{A}_{ext} \tag{5.23}$$

This condition, known as the external magnetic vector potential, forces the total field $\mathbf{A}$ to be equal to the background field $\mathbf{A}_{ext}$.



(A) (B)

FIGURE 5.5: External magnetic vector potential condition, in blue, applied on the modelling domain of the dipole in (a) and of the quadrupole in (b).

5.3.2 Thermal physics

As the beam screen is placed in vacuum, no convective phenomena need to be accounted for. Moreover, considering that the assembly operates at cryogenic temperatures, the radiation heat transfer can be neglected. The law governing the thermal effects due to the induced currents can be written as:

$$\rho c_p(T)\frac{\partial T}{\partial t} = \nabla \cdot (k(T)\nabla T) + \mathbf{Q} \tag{5.24}$$

where T is temperature, ρ is the material density, c_p is the solid heat capacity at constant pressure, k is the thermal conductivity, and $\mathbf{Q}$ is the heat source. It is important to point out that c_p and k are temperature dependent properties. $\mathbf{Q}$ is represented by the resistive losses due to the eddy currents which are calculated in the magnetic interface as $\rho_e \mathbf{j}^2$, where ρ_e is the electrical resistivity. However, as the heat is only generated during the magnetic field decay, namely in 0.4 s, the Fourier term in eq. 5.24 can be neglected. An adiabatic approximation might be therefore valid, leading to:

$$\mathbf{Q} = \rho c_p(T)\frac{\partial T}{\partial t}. \tag{5.25}$$

with $Q_e = \rho j^2$, as the term determining the temperature profile.

Boundary conditions

Thermal insulation conditions are used along all the boundaries of the beam screen assembly, see Fig. 5.6. Such condition reflects the fact that no heat exchange takes place towards the cold bore and can be written as:

$$\mathbf{n} \cdot \mathbf{q} = 0 \tag{5.26}$$

where $\mathbf{q}$ is the heat flux by conduction. Intuitively this condition states that the temperature gradient across the boundary is zero and, therefore, the heat cannot transfer across it. The surrounding domain is not considered in thermal physics.

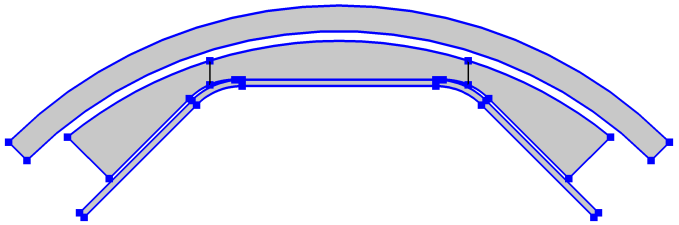


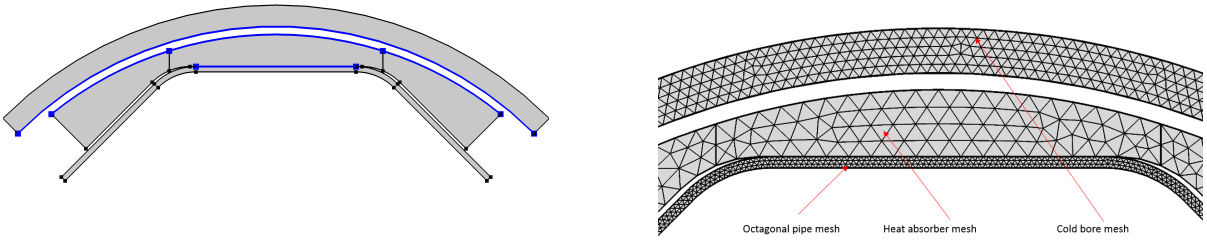
FIGURE 5.6: Thermal insulation of the beam screen.

5.3.3 Solid mechanics physics

The equation of the mechanical equilibrium is implemented in the Lagrangian form of Newton's second law. The equation is based on small deformations and takes into account the inertial effects of the beam screen component. The governing equation calculates to:

$$\rho \frac{\partial \mathbf{u}^2}{\partial \mathbf{t}^2} = \nabla \cdot FS + \mathbf{F}_V \tag{5.27}$$

where $\rho \frac{\partial \mathbf{u}^2}{\partial \mathbf{t}^2}$ is the second order time derivative of the displacement vector, F is the deformation gradient, S is the Piola-Kirchhoff stress tensor, and $\mathbf{F}_V$ is the external force vector of the magnetic interface. The force of gravity has not been accounted for. It is important to point out that the gradient operators are with respect to the material coordinates. The loads are applied as body forces instead.



(A) (B)

FIGURE 5.7: In (a) mechanical contacts (in blue) implemented between the bottom side of the heat absorber and the octagonal pipe as well as between the round side of the absorber and the inner part of the cold bore. In (b) the mesh used in the mechanical physics.

Boundary conditions

As for the magnetic interface, geometric symmetries are applied to the beam screen assembly. These refer to the same segments of the magnetic ones and have to necessarily comply with them. This is the case as the assembly is symmetric along any pair of planes perpendicular between each other along the beam axis. This condition translates into:

$$\mathbf{n} \cdot \mathbf{u} = 0 \tag{5.28}$$

meaning that the displacement along the normal direction of the boundary is zero. The heat absorber is constrained to move only along its normal direction. Mechanical contacts have been implemented on the external surfaces of the free-to-move heat absorbers targeting the cold bore and the octagonal pipe. Fig. 5.7a shows the segments in which these conditions hold. As shown in Fig. 5.7b to apply the mechanical contacts, the mesh of the adjacent contact surfaces must be disconnected. As in the thermal module, the surrounding domain is not considered in the solid mechanics physics.

The penalty contact method has been used to model these contacts. Such method can be expressed as:

$$F_c = k_c D_p \tag{5.29}$$

where $\mathbf{F}_c$ is the force needed for the algorithm to avoid penetration between two opposing surfaces, k_c is the contact stiffness (also called penalty factor) and $\mathbf{D}_p$ is the penetration at the contact elements. The method is very simple and stable. It acts as a spring between the elements coming into contact, active only in compression, so that the larger the penetration, the greater the force that guarantees the contact. Some penetration has to be expected for the method to work but very often it is negligible in comparison with the thickness of the domain. The main challenge of this method is to determine the contact stiffness value. For linear elastic isotropic materials, this is based on the Young's modulus of the destination surface. Some general recommendations have been adopted for the contacts shown in Fig. 5.7a:

- Stiffer parts need to be set as the source;
- The mesh needs to be finer at the destination ($h_{dest} < 0.5\ h_{source}$);
- The parts in contact need to be well constrained.

This translates into making the surface of the tungsten block the source and refining the mesh of the contact target, *i.e.* the cold bore.

Generally, the penalty method is strongly preferred when dealing with multiphysics problems and in time dependent studies as no special solver is needed.

5.4 Multiphysics FEM model

The numerical model presented in this thesis has been implemented in COMSOL Multiphysics [111], a commercial platform that enables to couple multiple physics into a single platform. This guarantees a level of flexibility, scalability, and longevity which is more difficult to achieve with in-house written codes. Notably, the constant development of the solver algorithm permits an increase of computational efficiency. The software is based on the finite element method to solve the partial differential equations (PDEs) governing the phenomena of each physics interface. The type of coupling between the interfaces can be chosen according to the specific needs of the user and large flexibility is given for the solver settings. If the models are computationally expensive to solve, high performance computing can be used to save time. Several studies have been performed using COMSOL and close analogies with experiments and analytical formulations have been found [112] [113] [114] [115] [116] [117].

Multiple commercial packages exist for electro-magnetic applications such as Ansys Maxwell [118], Opera [119] or NACS [120]. However, these packages require the integration of other platforms to fully obtain the multiphysics behaviour of the beam screen.

In COMSOL the model hinges on the well known Maxwell's equations implemented in the magnetic interface. For some materials of the beam screen, the electrical resistivity and the heat capacity vary considerably at cryogenic temperatures. The temperature increase due to the resistive losses is calculated in the thermal interface and, therefore, to obtain a more refined response in terms of Lorentz forces these variables need to be updated. Finally, the most important output of the model is calculated within its mechanical interface. Here it is where the Lorentz forces are received and the deformation and stress of the beam screen assembly computed.

5.4.1 Model algorithm

The algorithm of the 2D model, solving the physical interactions during a time step of the magnetic field decay, is presented in the flow chart in Fig. 5.8. The inputs of the model are the time evolution of the magnet gradient expressed in terms of $\mathbf{A}_{ext}$ and the material properties as a function of temperature, $c_p(T)$ and $\rho_e(T)$. The magnetic module, encapsulated in a thicker box in Fig. 5.8, is the effective centre of activity. It accounts for the eddy current problem and therefore gives as output the Lorentz force, $\mathbf{f}$, and the heat source, $\mathbf{Q}$, induced in the conducting components of the beam screen during the decay of the magnetic field. The temperature, T, is evaluated by the thermal module whereas the displacements, $\mathbf{u}$, by the mechanical one. These four physical quantities represent the coupling-terms between the different modules. The magnetic module can interact with the other two modules according to a one-way or a two-way coupling. The one-way coupling between the magnetic

and thermal equations implies that the heat source, **Q**, is transferred from the magnetic module to the thermal one. However, the temperature, T, is not transferred to the magnetic module and, therefore, the update of the electrical resistivity, ρ_e, cannot be considered in the following interval of time by the magnetic module. Similarly, the one-way coupling between the magnetic and solid mechanics modules translates into a uni-directional transfer of the Lorentz forces, **f**, to the mechanical module. However, the displacements of the beam screens components, **u**, are not transferred to the magnetic module. Conversely, by implementing the two-way coupling for the same interactions, the magnetic module can account for the temperature, T, and the displacements, **u**, respectively. This allows to update ρ_e and **B** for each beam screen component and to refine the estimation of the Lorentz forces (see section 5.4.6). The two-way coupling with the solid mechanics module calls for a movable mesh and it requires significant memory to be solved.

5.4.2 Solvers

Direct solver - the 2D model

The direct solver PARDISO, based on the LU decomposition of the Jacobian matrix, has been used to solve the 2D version of the model. The equations governing each module are solved simultaneously in the same matrix according to the so called *fully coupled* approach. In Fig. 5.8 this is represented by the dashed box which includes the equations governing each module. Even if each time step solution is solved in one iteration, it generally takes more time and requires extensive computational resources compared to iterative solvers. However, it guarantees an incomparable robustness to handle the couplings, the mechanical contacts, and the dynamics of the model.

Iterative solver - the 3D model

For the 3D version of the model, a direct solver would be memory and time intensive as there is an increased number of elements. Therefore, an iterative algorithm based on the Newton-Raphson method has been chosen. The magnetic and the thermal modules are coupled together in a two-way fashion according to the so called *segregated approach*. This implies that the respective governing equations are not solved simultaneouly but sequentially. The magnetic and thermal modules are based on the BiCGStab and GMRES solving algorithm, respectively. The iterative solver easily converges to a solution provided that the mechanical module is not accounted for. To compute the mechanical quantities, the highest Lorentz force field is identified between all the time intervals and given as input to the solid mechanics module in a quasi-static study. This approach is used only for the design of the components placed firmly along the beam axis where dynamic effects can be neglected.

5.4.3 Time dependent solver algorithm

The numerical integration of the differential equations solved by COMSOL is based on an implicit solver known as the Backward Differentiation Formula (BDF) . This time stepping scheme is used both for the 2D and 3D versions of the model. The time integration order goes from a minimum of one to a maximum of five. The time steps taken by the solver are divided in three ranges and reported below according to the notation (start time, step size, end time):

- range $1(0, 10^{-3}, 0.00256)$ s;

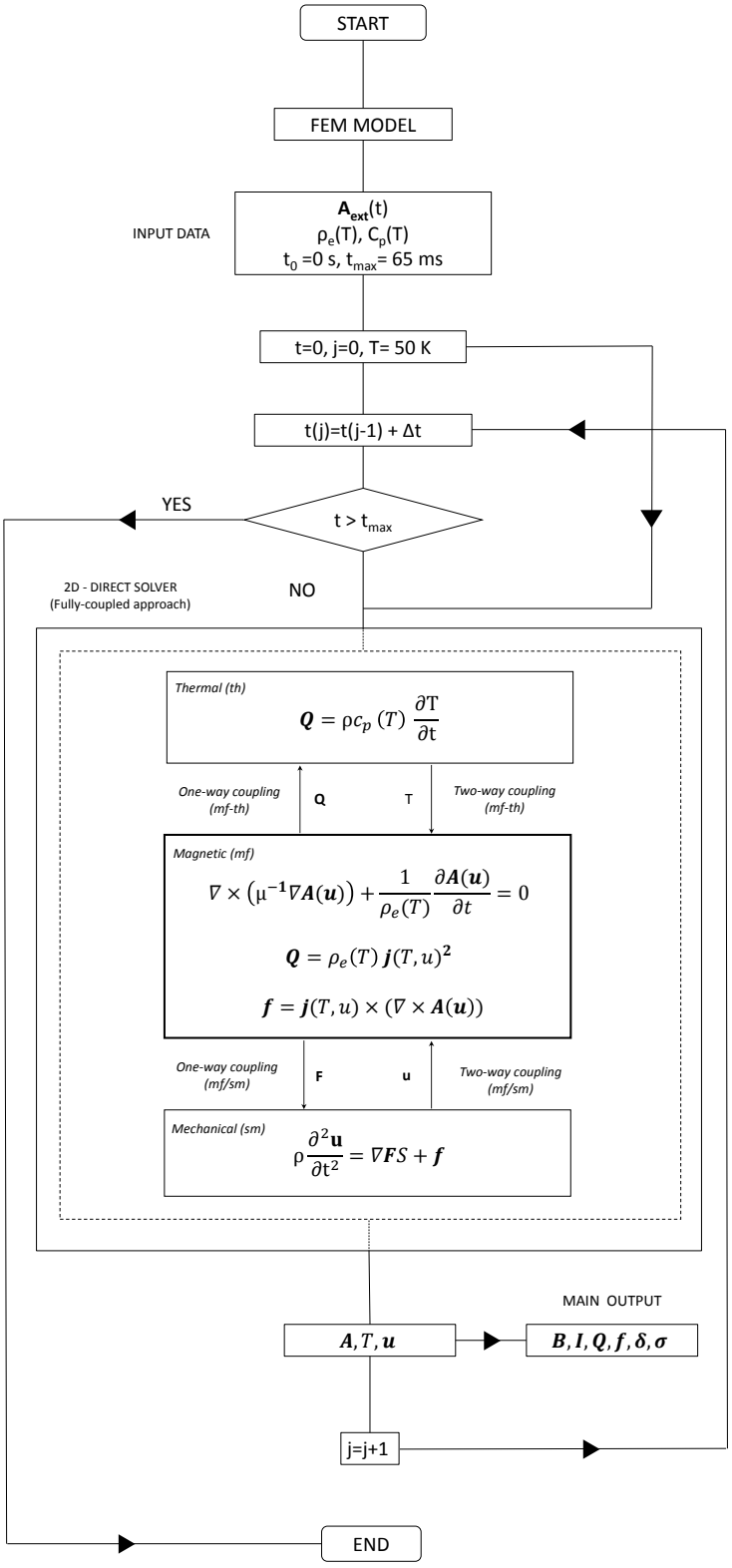
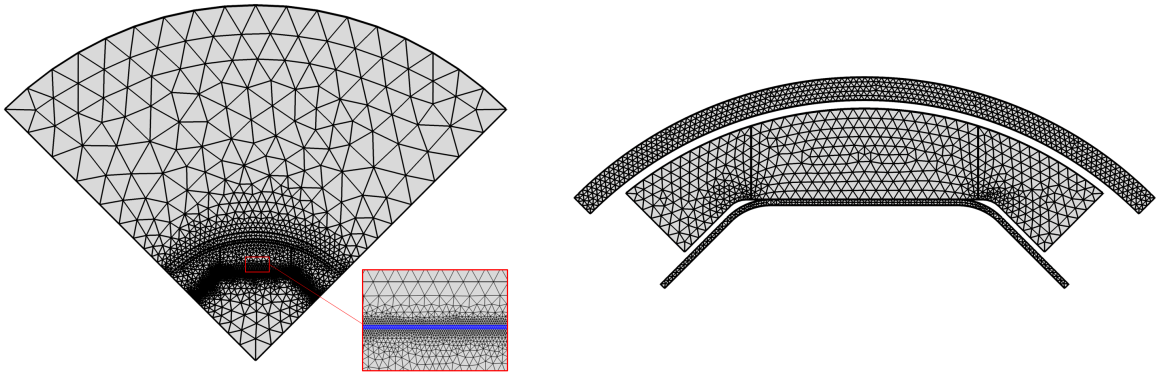


FIGURE 5.8: Flow chart of the 2D model algorithm during a time step of the magnet quench.



(A) (B)

FIGURE 5.9: In (a) mesh used in the magnetic and thermal module and in (b) the one used in the mechanical module. In the red box the mesh is zoomed to highlight the elements used in the inner copper layer.

- range 2$(0.00256, 10^{-4}, 0.01)$ s;
- range 3$(0.01, 10^{-3}, 0.065)$ s.

In the first and third range, the step size is 10^{-3} s, while in the second, it is 10^{-4} s. The second range starts when dynamic effects arise and therefore is important to capture the mechanical dynamics of the assembly through a tighter step size. The BDF solver turns out to be very stable for the multiphysics application described in this thesis.

5.4.4 Mesh

All the regions have been discretised through an unstructured mesh based on second order triangular elements in 2D and tetrahedral elements in 3D. These elements have been chosen because they guarantee an easy connection between the region containing the beam screen and the beam screen itself.

The thin 75 µm copper layer requires a considerably refined mesh. This implies that the region nearby the layer has a dense element discretisation, which increases the total amount of elements in the model. A criterion for the number of elements to be used in electromagnetic problems is based on the skin depth that calculates to:

$$\delta = \frac{\rho_e}{\pi f \mu} \tag{5.30}$$

where f is the frequency and μ the absolute magnetic permeability.

Considering the electrical resistivity of copper equal to 6.67 Ωm at 50 K and the frequency of the magnetic field decay approximated to 2.5 Hz, the skin depth of the thin copper layer is 8.23 mm. The recommendation is to use at least two linear elements per skin depth to capture the variation of the fields [121]. The mesh used for the magnetic module satisfies this requirement. Fig. 5.9 shows the mesh adopted to discretise the beam screen. The mesh used in the thermal and magnetic module is slightly different from the one of the solid mechanics module. In fact, to apply the mechanical contacts, the mesh of the beam screen domains has to be disconnected at the interface of the contact.

Physics interface	Required material properties		
Magnetic fields	Electrical conductivity	Relative permittivity	Relative permeability
Heat transfer in solids	Thermal conductivity	Heat capacity	Density [a]
Solid mechanics	Young's modulus	Poisson ratio	Initial yield stress

TABLE 5.2: Physical variables needed for each interface used in the model.

[a] property shared with solid mechanics

5.4.5 Model input: material properties and magnet gradient decay

The equations governing each module require specific material properties. Some of these properties highly depend on temperature and, therefore, have to be defined as a function of the desired range of temperature. This is particularly important for the electrical conductivity of copper, which exhibits a drastic variation for a difference of just a few degrees at around 50 K [122]. The material properties needed for each interface are summarised in Table 5.2. Magneto-resistivity effects on the beam screen materials have not been considered.

All the materials, except copper, have an elastic-linear behaviour. A perfectly elastoplastic behaviour has been assigned to copper as the stress during quench exceeds its elastic limit.

Fig. 5.10 shows the magnetic field decay for the dipole magnet and the factor $B\frac{\partial B}{\partial t}$, where $\frac{\partial B}{\partial t}$ is the time derivative of the magnetic field. Fig. 5.11 shows the decay of the quadrupole magnet gradient and the factor $G\frac{\partial G}{\partial t}$, where $\frac{\partial G}{\partial t}$ is the time derivative of the magnet gradient.

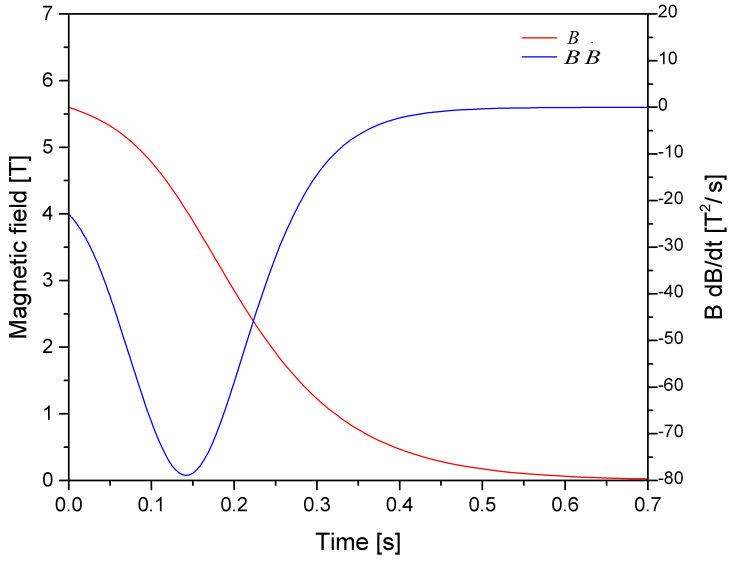


FIGURE 5.10: Magnetic field decay, B, due to the dipole magnet quench and $B\frac{\partial B}{\partial t}$ evolution.

5.4.6 Analytical description of the forces induced during a quench

For sake of simplicity, the analytical formulation of the Lorentz forces is derived only for an annular geometry as the one shown in Fig. 5.12a and 5.12b. The objective is to highlight the geometrical and physical variables

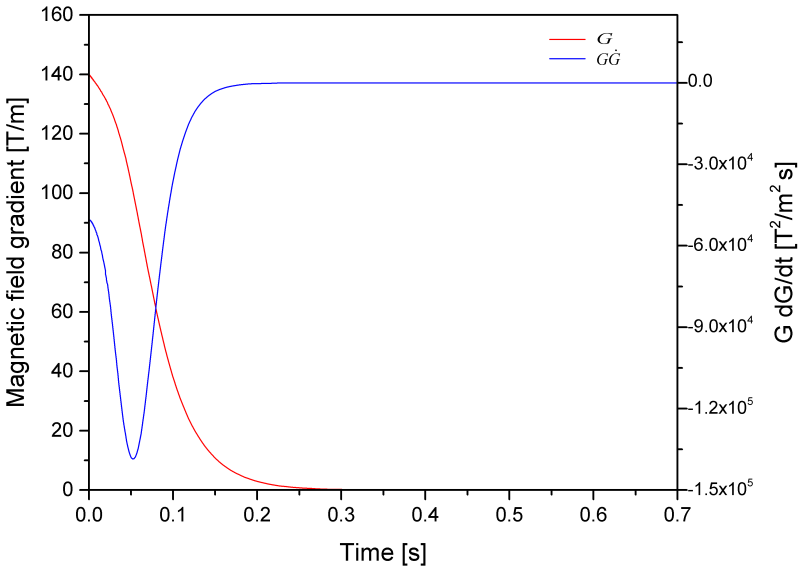
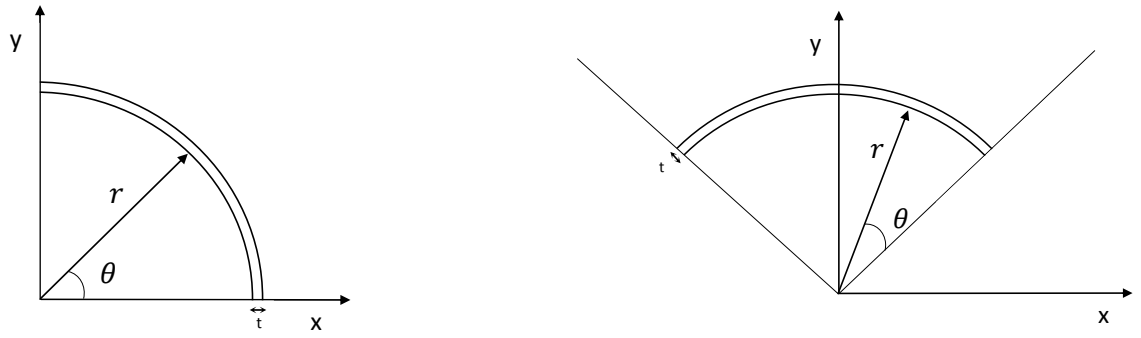


FIGURE 5.11: Magnet gradient decay, G, due to the quadrupole magnet quench and $G\frac{\partial G}{\partial t}$ evolution.

affecting the magnitude of the induced forces as well as to give a term of comparison with the numerical model treated in section 5.3.



(A) (B)

FIGURE 5.12: Annular sectors accounted in the analytical formulation to derive the expression of the forces induced during a dipole magnet quench in (a) (from 0 to $\pi/4$) and a quadrupole magnet quench in (b) (from $\pi/4$ to $3\pi/4$).

Dipole magnetic field

Known the direction of the magnetic field, the equation of Maxwell-Faraday:

$$\nabla \times \mathbf{E} = -\frac{\partial \mathbf{B}}{\partial t} \tag{5.31}$$

allows, after integration, to extract the electric field along the beam axis:

$$\frac{\partial E_z}{\partial x} = \frac{\partial B_y}{\partial t} \tag{5.32}$$

$$E_z = \frac{\partial B_y}{\partial t} x \tag{5.33}$$

Therefore, knowing the electrical resistivity of the material, the current density calculates to:

$$j_z = \frac{\partial B_y}{\partial t} \frac{x}{\rho} \tag{5.34}$$

The volumetric Lorentz forces $[\frac{N}{mm^3}]$ are given by the relation:

$$\mathbf{F}_v = \mathbf{j} \times \mathbf{B} \tag{5.35}$$

By substituting the expression of the current density the Lorentz forces can be written as:

$$F_{v_x} = -B_y \frac{\partial B_y}{\partial t} \frac{x}{\rho} \tag{5.36}$$

An easy way to integrate the forces along a quarter of the beam screen is by using the cylindrical coordinates:

$$x = r\cos(\theta) \tag{5.37}$$

$$y = r\sin(\theta) \tag{5.38}$$

The current density becomes then:

$$j_z = \frac{\partial B_y}{\partial t} \frac{r\cos(\theta)}{\rho} \tag{5.39}$$

Considering an infinitesimal portion of the annular surface $\partial S = rtd\theta$ of Fig. 5.12a, the current as a function of the angle θ can be expressed as:

$$dI(\theta) = \frac{\partial B_y}{\partial t} \frac{r^2 \cos(\theta)}{\rho} t d\theta \tag{5.40}$$

Multiplying by B_y the infinitesimal force becomes:

$$dF_x(\theta) = B_y \frac{\partial B_y}{\partial t} \frac{r^2 \cos(\theta)}{\rho} t d\theta \tag{5.41}$$

According to the right-hand rule, the direction of the force is along the x-axis. Therefore, integrating the portion of Fig.5.12a from 0 to $\pi/2$, the expression of the force assumes the following form:

$$F_x = B_y \frac{\partial B_y}{\partial t} \frac{r^2}{\rho} t \tag{5.42}$$

In Fig. 5.13 the magnetic field distribution, the induced currents and the Lorentz force direction are shown for an annular geometry. Generally, it is worth noting that any component subject to a dipole magnetic field decay is squeezed in the direction mutually perpendicular to the field and to the current flow.

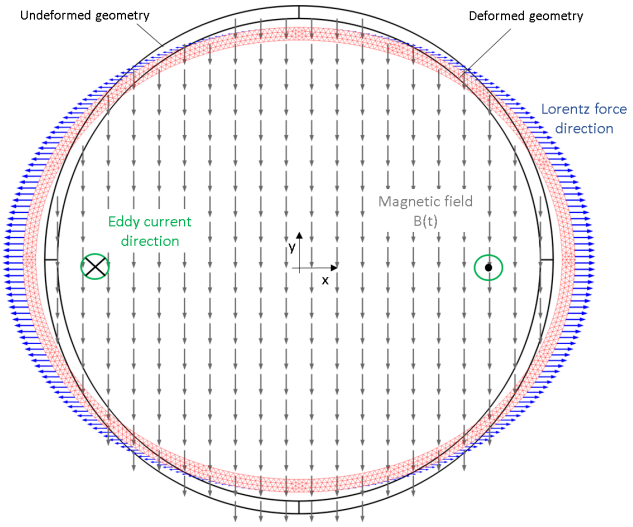


FIGURE 5.13: Vectors of the currents and forces induced in an annular geometry during a dipole magnet quench. The forces are referred to the deformed geometry.

Quadrupole magnetic field

For a magnet quadrupole the direction in space of the magnetic field is given by the relations:

$$B_x = Gy \tag{5.43}$$

$$B_y = Gx \tag{5.44}$$

where G [T/m] is the magnet gradient. From the Maxwell-Faraday equation, considering the hypothesis of a two-dimensional field **B** and that **E** has only one non-zero component along the beam axis, it becomes:

$$\frac{\partial E_z}{\partial y} = -\frac{\partial B_x}{\partial t} \tag{5.45}$$

$$\frac{\partial E_z}{\partial x} = \frac{\partial B_y}{\partial t} \tag{5.46}$$

By substituting the magnetic field components and integrating in space it is possible to derive the expression of the electric field. Hence, E_z can be written as:

$$E_z = \frac{1}{2}\frac{\partial G}{\partial t}(x^2 - y^2) \tag{5.47}$$

Therefore, knowing the electrical resistivity of the material, ρ, the current density calculates to:

$$j_z = \frac{1}{2\rho}\frac{\partial G}{\partial t}(x^2 - y^2) \tag{5.48}$$

As for the magnet dipole field, see eq. 5.39, after substituting the magnetic field components written in terms of cylindrical coordinates, the current density calculates to:

$$j_z = \frac{1}{2\rho}\frac{\partial G}{\partial t} r^2 (2\cos^2\theta - 1) \tag{5.49}$$

Considering an infinitesimal portion of the annular surface $\partial S = rtd\theta$ of Fig. 5.12b, the current as a function of the angle θ can be expressed as:

$$dI_z = \frac{t}{2\rho}\frac{\partial G}{\partial t} r^3 (2\cos^2\theta - 1) d\theta \tag{5.50}$$

The Lorentz forces acting on the x-axis and y-axis can be written as:

$$dF_x(\theta) = -dI_z B_y \tag{5.51}$$

$$dF_y(\theta) = dI_z B_x \tag{5.52}$$

and by substituting eqs.5.50, 5.44, 5.43 in the Lorentz forces expressions:

$$dF_x(\theta) = -\frac{t}{2\rho}\frac{\partial G}{\partial t} G r^4 \cos(2\theta)\cos(\theta) d\theta \tag{5.53}$$

$$dF_y(\theta) = \frac{t}{2\rho}\frac{\partial G}{\partial t} G r^4 \cos(2\theta)\sin(2\theta) d\theta \tag{5.54}$$

Integrating between $\pi/4$ and $\pi/2$ the module of the force acting along the x-axis and y-axis is:

$$F_x = \frac{\sqrt{2}-1}{6\rho}\frac{\partial G}{\partial t} G r^4 t \tag{5.55}$$

$$F_y = \frac{\sqrt{2}}{6\rho}\frac{\partial G}{\partial t} G r^4 t \tag{5.56}$$

Considering that in the quadrant shown in Fig. 5.12b, the forces along the y-axis sum up while the ones along the x-axis cancel out, the resultant force acts only on the y-axis and calculates to:

$$F_y = \frac{\sqrt{2}}{3\rho}\frac{\partial G}{\partial t} G r^4 t \tag{5.57}$$

In Fig. 5.14 the magnetic field distribution, the induced currents and the Lorentz force direction are shown for an annular geometry.

5.5 Analysis of the multiphysics FEM model

5.5.1 Analytical verification and convergence analysis of the FEM model

The numerical model presented in this thesis has been conveniently verified through the convergence analysis by comparing the Lorentz forces derived from the analytical expressions of eqs. 5.55 and 5.56. Such expressions are valid for an annular geometry provided that the thickness is much smaller than the radius. Therefore, a thickness of 1 mm and an outer radius of 300 mm have been chosen for the comparison. As seen in eq. 5.53 and 5.54, the forces are related to the product between the magnet gradient and its time derivative. The $G\frac{\partial G}{\partial t}$ factor chosen for

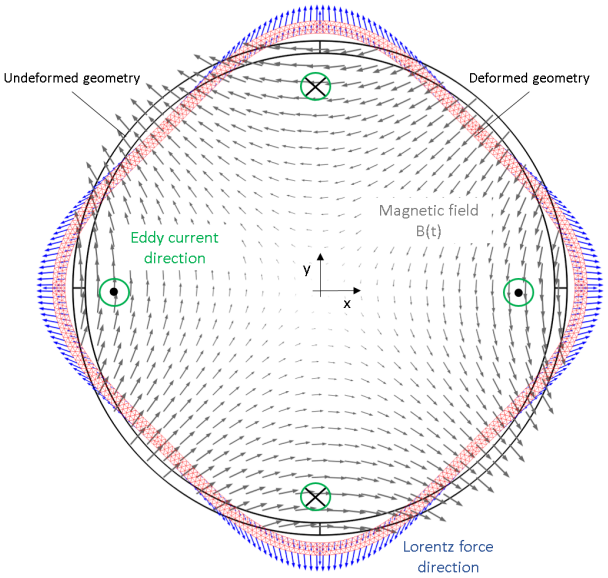


FIGURE 5.14: Vectors of the currents and forces induced in an annular geometry during a quadrupole magnet quench. The forces are referred to the deformed geometry

this correlation is $1.38 \cdot 10^5 \frac{T^2}{m^2 s}$. It corresponds to the highest $G\frac{\partial G}{\partial t}$ factor for the magnetic field decay accounted in the analysis and, therefore, it translates into considering the highest forces induced during the quench.

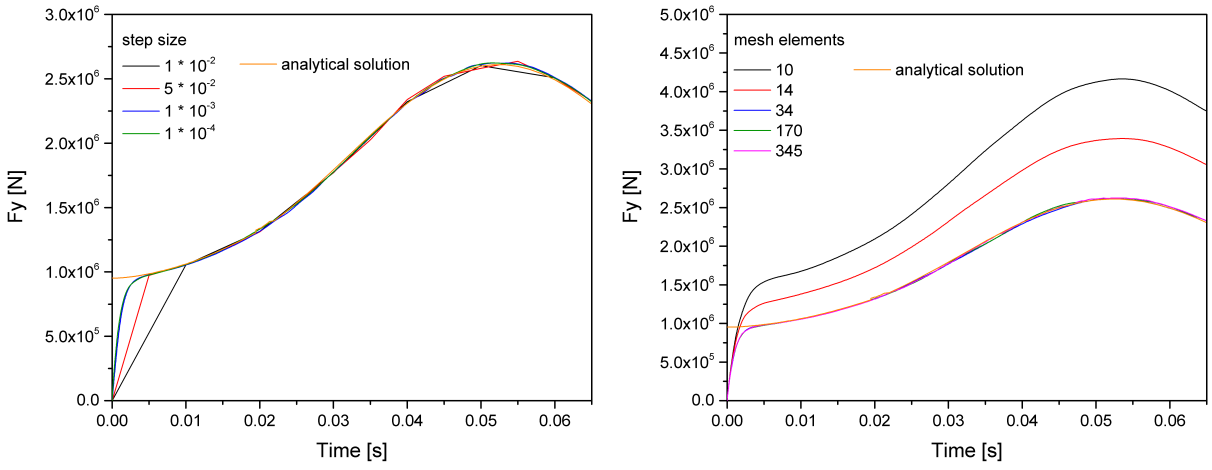
The mesh and time step convergences of the numerical solution to the analytical one are reported in Fig. 5.15. The convergence analysis is based on the radial component of the total force integrated from $\pi/4$ to $\pi/2$. For the time step convergence, step sizes ranging from 10^{-2} s to 10^{-4} s have been investigated. The electrical conductivity of the annulus is set to 10^7 S/m and 264 second order triangular elements have been used to model a quarter of the annulus. From Fig. 5.15a it can be seen that the minimum step size that allows to fully capture the analytical evolution, especially at the beginning, is 10^{-3} s. This step size is then used for the mesh convergence that has been performed with second order type elements ranging from 10 to 345. As shown in Fig. 5.15b, the exact evolution of the induced forces is captured with at least 34 elements.

Therefore, the FEM model has been verified provided that at least 34 elements and a step size of 10^{-3} s are used. It noteworthy that the analytical evolution of the Lorentz forces does not start from zero as the time derivative of the magnet gradient input is not zero.

5.5.2 Self-inductance effects

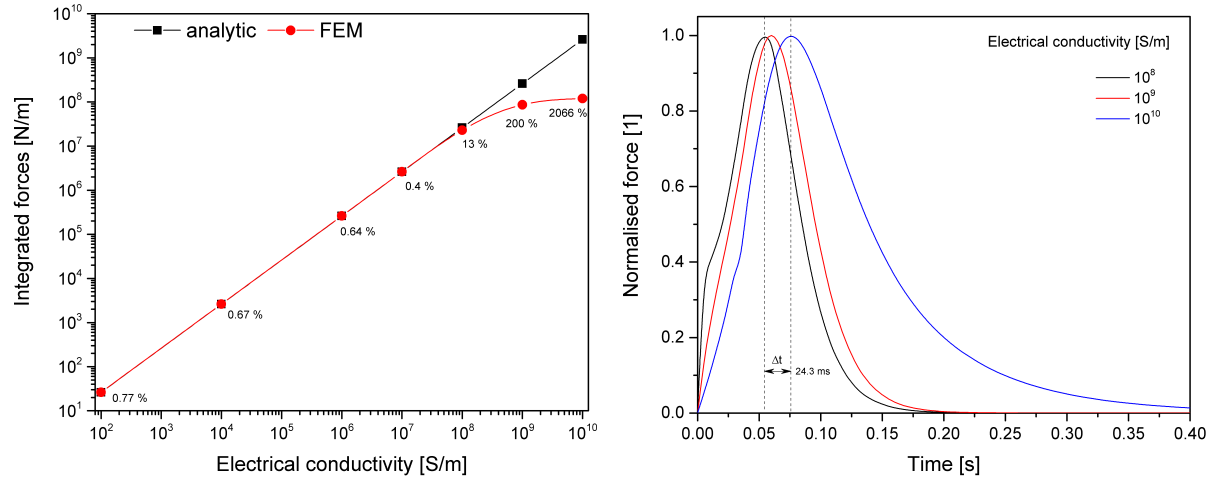
Self-inductance effects have been investigated by comparing the forces derived through the analytical formulations and the numerical model. The radial component of the forces has been integrated from $\pi/4$ to $\pi/2$ and evaluated for different electrical conductivity values ranging from 10^2 to 10^{10} S/m. In particular, the maximum force induced for each value of electrical conductivity has been accounted for in this analysis, *i.e.* when $G\dot{G}$ is the maximum.

Fig. 5.16a shows the evolution of the maximum forces for both the numerical, in red, and the analytical approach, in black. An excellent agreement is observed up to 10^7 S/m as the difference between the two approaches is lower than 1 %. After 10^7 S/m the model deviates from the analytical formulation with the difference increasing gradually for growing values of electrical conductivities. The non-linearity of the forces calculated through the



(A) (B)

FIGURE 5.15: Mesh convergence in (a) and time-step convergence in (b) of the numerical solution to the analytical one.

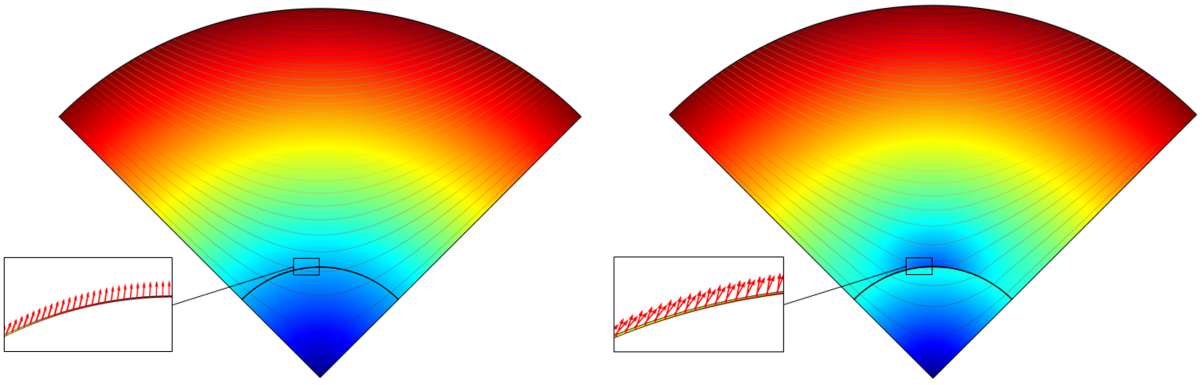


(A) (B)

FIGURE 5.16: In (a) comparison between the maximum analytical and numerical forces for electrical conductivities ranging from 10^2 to 10^{10} S/m. In (b) the evolution on time of the numerical forces are normalised and compared for electrical conductivities ranging from 10^8 to 10^{10} S/m.

model is due to self-inductance effects. The magnetic field generated by the induced currents opposes the change of the primary magnetic field (Lenz's law) resulting in a variation up to 2066 % between the two approaches at 10^{10} S/m. These transient phenomena are observed because the model accounts for the reciprocal influence of the domains [123]. This can also be visualised in the magnetic field distribution for a low and high electrical conductivity case. Fig. 5.17a shows that at 10^7 S/m the magnetic field norm increases linearly everywhere along the radius of the whole sector. However, as shown in Fig. 5.17b, a distortion of the primary field can be observed at 10^{10} S/m occurring in the central part of the annulus where the highest currents are induced. Moreover, as the field lines are perturbed, also the Lorentz force direction is modified resulting in a lower radial component of the integrated forces. This explains why the forces derived through the FEM model are lower than the ones calculated through the analytical formulation at high values of electrical conductivity.

Another effect related to the self-induction phenomena can be found in the time evolution of the forces at different values of electrical conductivity. Fig. 5.16b shows such evolutions for values of conductivity ranging



(A) (B)

FIGURE 5.17: Colour map of the magnetic field around the annulus sector after 50 ms from the start of the magnet quench. The electrical conductivity of the portion in (a) is 10^7 S/m, while the one in (b) is 10^{10} S/m. In the magnification in (a), the Lorentz forces follow the typical pattern of a quadrupole magnet quench decay while in the magnification in (b), the forces are bent because of the magnetic perturbation due to the high eddy currents (blue area).

from 10^8 S/m to 10^{10} S/m. It is worth noting that the lag in time of the peak force shifts for growing values of conductivity. The time delay from 10^8 to 10^{10} S/m is equal to 25.3 ms.

5.5.3 Magnetic and thermal coupling: one-way vs two-way

The comparison of the couplings between the magnetic and thermal interface is shown in Fig. 5.18. The radial component of the forces integrated over the $\frac{\pi}{4}$ - $\frac{3}{4}\pi$ sector of the copper inner layer is considered in the analysis. The objective of this analysis is to identify the best trade-off in terms of significant results and computational load. The reason for considering only the inner layer is because at cryogenic temperatures copper exhibits a drastic variation of electrical conductivity. By way of example, the Q1 beam screen is considered in the analysis. As seen in the eqs. 5.53 and 5.54, the Lorentz forces, among other things, depend linearly on the electrical conductivity and, therefore, the inner layer represents a good ground for the comparison. It turns out that he difference between the peaks of the two curves is 15.4 $\mathrm{N\,mm^{-1}}$. Therefore, the forces related to the one-way coupling are around 40 % higher than according to the two-way coupling. As this difference would make the model too conservative, the two-way coupling is adopted.

5.5.4 Magnetic and mechanical coupling: one-way vs two-way

During the quench, the structure deforms and the distance of the components from the origin changes.

The two-way coupling between the magnetic and mechanical modules should predict larger forces than the one-way coupling (where the geometry is always considered fixed) since the forces are induced according to a constantly updated position. To account for the two-way coupling, a movable mesh has been implemented. The couplings are compared through the safety factor (SF) related to the von Mises stress and the displacement. The von Mises SF is defined as σ_y/σ_{max}, where σ_y is the yield stress of the material and σ_{max} is the highest value of the equivalent von Mises stress during the quench. Similarly, the displacement SF is defined as d_{gap}/d_{max}, where d_{gap} is the distance not to be exceeded between the cold bore and the magnet coil (1.5 mm) and d_{max} is the largest displacement of the cold bore.

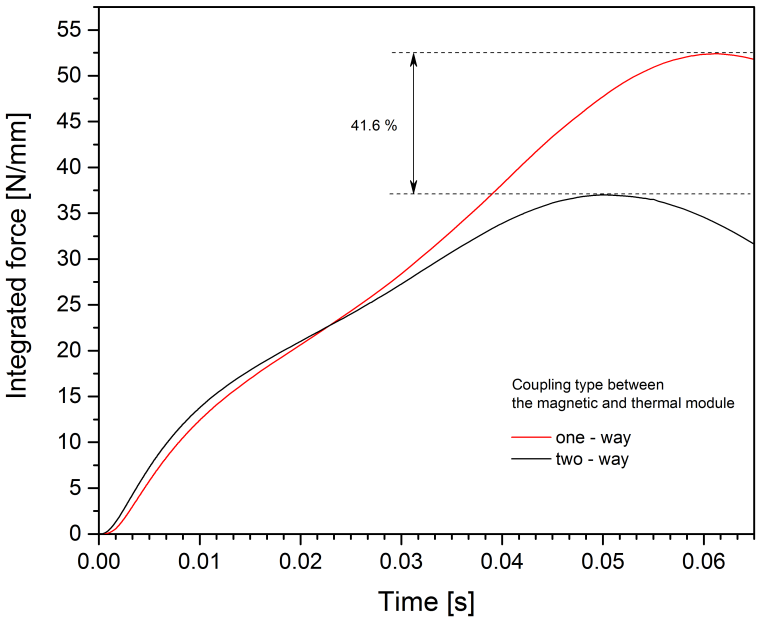


FIGURE 5.18: Comparison between the one-way and two-way coupling of the magnetic and thermal physics.

In Fig. 5.19 the von Mises SF is shown for the octagonal pipe, the heat absorber and the cold bore, while the displacement SF is reported for the cold bore only of the Q1 beam screen. As expected, the two-way coupling is less conservative than the one-way coupling although there is no considerable variation compared with the one-way coupling. Only the SFs of the heat absorber are lower. In fact, this component being simply laid on the octagonal pipe is free to move towards the cold bore covering the 1.5 mm gap.

On the other hand, the other components change shape according to the typical force distribution induced in a quadrupole magnetic field decay. As illustrated for the octagonal pipe in Fig. 5.20, this implies that the distance from the origin is not larger for the whole geometry but just for a part of it. The forces are higher in the regions that exceed the original geometry but lower in those that internally deform. In conclusion, the two-way coupling has a higher computational cost but predicts almost the same SF for the beam screen components. Since the SFs are well above any critical level, the one-way coupling between the mechanical and magnetic modules is used to simulate the behaviour of the beam screen.

5.5.5 Comparison between the 2D and 3D version of the FEM model

The radial component of the forces integrated over one quarter of the Q1 beam screen is compared between the 2D and the 3D version of the model. For the sake of simplicity, no thermal effects are considered as they would equally scale the total forces. The beam screen assembly analysed in the 3D model is 400 mm long. In 2D simulations the lateral extensions of the heat absorbers are considered. However, since these are not uniformly present along the beam axis of the component, their electrical conductivity has been assumed to be proportional to their filling ratio, namely 20%. As shown in Fig. 5.21a, the radial forces induced in the heat absorber and in the cold bore of the 3D beam screen turn out to be 65% and 10% lower than in the 2D case, respectively. The reason for such a difference has to be sought in the intrinsic characteristics of the 3D model that accounts for the closed path of the induced currents, which, as shown in Fig. 5.22a, modifies the direction of the forces. On the contrary, to avoid the formation of current loops, periodic conditions can be applied at the extremities of the model, see Fig. 5.22b, resulting in an excellent agreement with the forces of the 2D version of the model, see Fig. 5.21b.

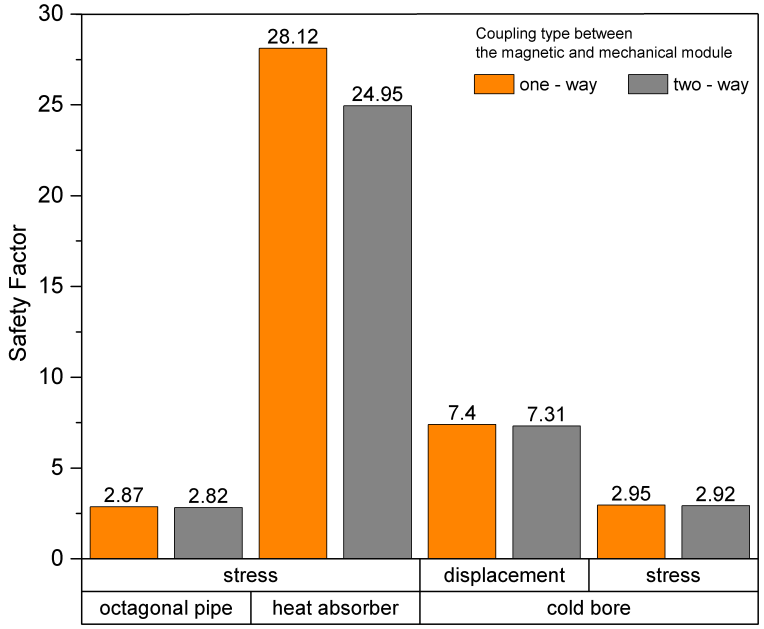


FIGURE 5.19: Comparison of the couplings between the magnetic and mechanical interface.

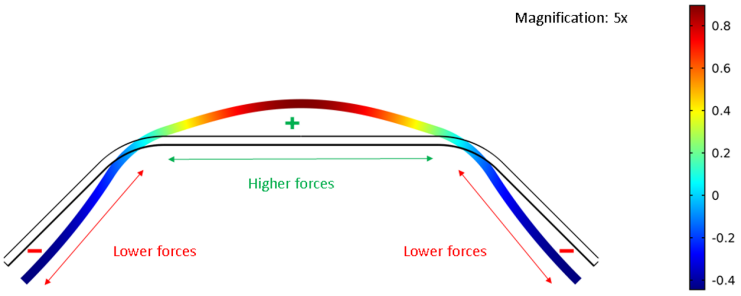


FIGURE 5.20: Deformation of a quadrant of the octagonal pipe.

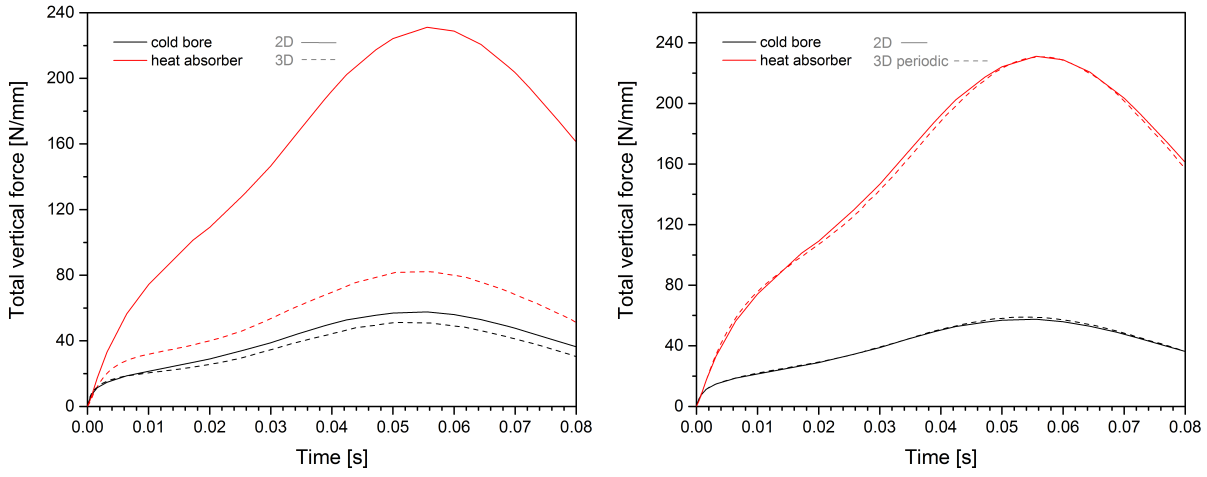
5.6 Results and discussion

In this section the results concerning the magnetic, thermal, and mechanical behaviour of the triplet area beam screens are presented and discussed. For each beam screen type the results are first presented for the 2D version of the multiphysics model and then for the 3D version, if needed.

The induced current, electromagnetic heating, temperature, force and displacement can be evaluated in 2D. These are shown in Fig. 5.25, Fig. 5.31, and Fig. 5.37 for the Q1, Q2, and D1 beam screen, respectively.

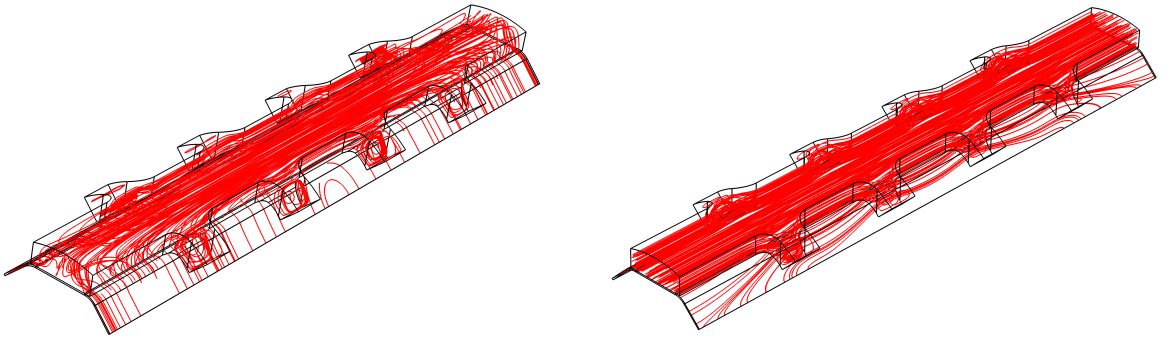
In Fig. 5.26, Fig. 5.32, and Fig. 5.38 the distribution of the relevant physical quantities are depicted also by colour maps. For the Q1 and Q2 beam screens the results refer to 55 ms and for the D1 beam screen to 152 ms, *i.e.* when the highest Lorentz forces are induced. In these maps the legend limits have been intentionally lowered to distinguish the general distribution of the induced quantities within the entire beam screen. In fact, the limits of the legend depend on the thin copper layer, where the magnitude of the induced quantities is the highest.

In Fig. 5.27, Fig. 5.33, and Fig. 5.39, the von Mises and principal stress, the kinetic energy of the heat absorber, and the contact force between the heat absorber and the cold bore are shown.



(A) (B)

FIGURE 5.21: Comparison of the radial component of the forces integrated from $\pi/4$ to $3\pi/4$ between the cold bore (in black) and the heat absorber (in red) according to the 2D (continuous line) and 3D (dashed line) versions of the model. The 2D model is compared with the 3D model without periodic conditions in (a) and with periodic conditions in (b).



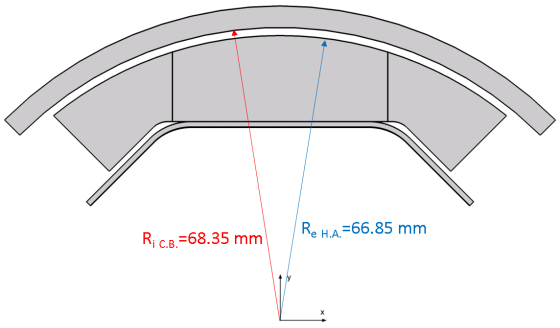
(A) (B)

FIGURE 5.22: Current distribution induced in one quarter of the Q1 beam screen. At the extremities of the assembly the currents wrap up in order to close the circuit if no periodic conditions are implemented in (a), while they are not perturbed in case of periodic conditions in (b).

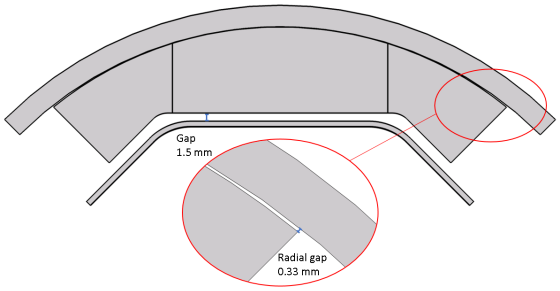
Geometrical features like the heat absorber wings and the pumping holes are not uniformly present along the beam axis and, therefore, require a 3D model to be studied.

The heat absorber wings have to be carefully assessed as these might be overly loaded during the quench due to the contact with the cold bore, which can lead to potential fracture. It is noteworthy that the wings do not bend at the first contact with the cold bore. As shown in Fig. 5.23, due to the 1.5 mm gap between the heat absorber and the cold bore, a radial gap of 0.33 mm remains at the extremity of the wings. Therefore, once this external gap is closed by the cold bore deformation, the wing is loaded.

The cold bore deformation depends on its relative Lorentz forces, on the potential impact energy of the heat absorber, and on the typical kinematics of the cold bore, (see Fig. 5.13 and Fig. 5.14, respectively). From a kinematic point of view, the external gap is closed more easily in case of a dipole as the cold bore is squeezed only



(A)



(B)

FIGURE 5.23: Internal radius of the cold bore and external radius of the heat absorber in (a). Contact between the heat absorber and the cold bore resulting in a radial gap of 0.33 mm at the extremity of the wings in (b).

in the direction perpendicular to the field. Moreover, considering that the most delicate heat absorber is the 6 mm thick version, the D1 heat absorber wings are the most loaded ones.

The heat absorber wings are modelled in Ansys as it has been observed that this software is more powerful than COMSOL to handle mechanical 3D contacts. For the Q1 and Q2 beam screen only the heat absorber has been loaded by applying the total forces derived by the COMSOL model. The octagonal pipe is not considered as it does not transmit any force to the heat absorber due to the gap that remains between the two components, see Figs. 5.25f and 5.31f. The cold bore is not loaded because the deformation caused by their relative induced forces is negligible. For the D1 beam screen, the octagonal pipe remains in contact with the heat absorber, see Fig.5.37f and its contribution is, therefore, considered. Due to symmetry reasons, the mechanical characterisation of the wings has been carried out by considering a quarter of the assembly 40 cm long.

The effects of the pumping holes (stress concentration, increased flexibility of the octagonal pipe) are evaluated in COMSOL in 3D. The octagonal pipe considered for the characterisation of the pumping holes is 80 mm long. To lower the computational load of the simulations one quarter of the assembly with periodic conditions on the longitudinal axis has been used.

5.6.1 Q1 beam screen

2D model

The current integrated in a beam screen quarter is shown in Fig. 5.25a while the current density distribution in Fig. 5.26a. The largest currents are induced in the heat absorber up to 40318 A, followed by the cold bore 10283 A, the inner layer 7267 A, and the octagonal pipe 1032 A. As seen in eqs. 5.53 and 5.54, for a given quadrupole magnetic field decay, the parameters influencing the magnitude of the current density induced in each component of the beam screen are the electrical resistivity, ρ, and geometric factors like the distance of the components from the centre, r^2, and its thickness, t. The position of the components from the origin is particularly important since its contribution on the induced currents goes with the second power while the thickness and the electrical resistivity contribute linearly instead. This explains why more currents are induced in the heat absorber, rather than in the inner copper layer. In fact, although the copper has a much lower electrical conductivity than the tungsten alloy (at 50 K, $2.93 \cdot 10^7$ vs $1.5 \cdot 10^9$ $\mathrm{S\,m^{-1}}$, respectively), the heat absorber is thicker and placed further from the origin than the inner copper layer.

The resistive heat power shown Fig. in 5.25b is derived from $Q_e = \rho \cdot j^2$. The highest heat losses per length are, 107 $\mathrm{W\,mm^{-1}}$ for the heat absorber, 29.5 $\mathrm{W\,mm^{-1}}$for the cold bore, 1.6 $\mathrm{W\,mm^{-1}}$ for the octagonal pipe, and 10.2 $\mathrm{W\,mm^{-1}}$ for the inner layer.

The maximum temperature evolution of the beam screen components are shown in Fig. 5.25c and the temperature distribution in Fig. 5.26c. The inner layer and the octagonal pipe reach 64 K, the heat absorber 60 K, while the cold bore 54 K. The temperature of the copper inner layer is the highest mainly because of the specific heat losses, see Fig. 5.25d and Fig. 5.26b.

For the inner layer the highest value of the specific heat losses are equal to 1.6 $\mathrm{W\,mm^{-3}}$, for the heat absorber 96 $\mathrm{mW\,mm^{-3}}$, for the cold bore 67 $\mathrm{mW\,mm^{-3}}$ and for the octagonal pipe 19 $\mathrm{mW\,mm^{-3}}$. In fact, the temperature rise, governed by the eq. 5.24, depends on the specific heat load as well as on the heat capacity at constant pressure of the materials. However the heat capacity is less determinant than the the specific heat load. In fact at 50 K it is about 100 $\mathrm{J\,kg^{-1}\,K^{-1}}$ for copper and stainless steel and 30 $\mathrm{J\,kg^{-1}\,K^{-1}}$ for the tungsten alloy.

The distribution of the Lorentz forces in the Q1 beam screen is shown in Fig. 5.24 while the magnitude of the total force in Fig. 5.26d

The radial component of the Lorentz forces integrated in a quarter of the assembly is shown in Fig. 5.25e. In general the largest forces are induced between 55 and 60 ms. These are 58 $\mathrm{N\,mm^{-1}}$ for the cold bore, 210 $\mathrm{N\,mm^{-1}}$ for the heat absorber, 4.7 $\mathrm{N\,mm^{-1}}$ for the octagonal pipe and 36 $\mathrm{N\,mm^{-1}}$ for the copper layer. As for the currents, the forces induced in the heat absorber are higher than those induced in the inner copper layer. As seen in eqs. 5.53 and 5.54, the general expression of the Lorentz forces $\mathbf{F} = \mathbf{I} \cdot \mathbf{B}$ implies that for a given current, the magnitude of the force depends also on the strength of the magnetic field. As shown in eqs. 5.43 and 5.44 the intensity of the magnetic field increases linearly from the origin.

The highest deformations of the beam screen components are shown in Fig. 5.25f, while in Fig. 5.26e it is depicted the deformed Q1 beam screen. The heat absorber, which is simply laid on the octagonal surface, moves independently from the rest of the assembly impacting on the cold bore multiple times during the quench. From the heat absorber impact one can determine two main phases: the first one is characterised by rapid oscillations up to 10 ms due to the violent impact of the absorber against the cold bore, while the second one by a steady contact. The highest deformation of the cold bore, equal to 0.2 mm, occurs in the first phase at 2.7 ms. At this

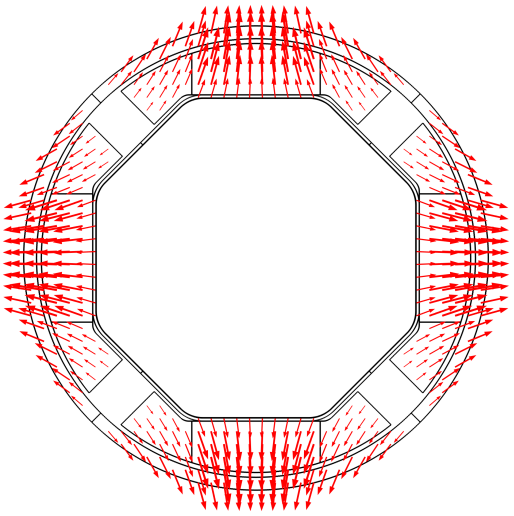


FIGURE 5.24: Distribution of the induced forces in the Q1 beam screen during a magnet quench.

stage the forces induced in the absorber are only 25.7 $\mathrm{N\,mm^{-1}}$. In the second phase, the highest deformation is 0.16 mm and takes place at 55 ms, where the induced forces in the absorber are 210 $\mathrm{N\,mm^{-1}}$. This means that the most severe deformation of the cold bore is mostly determined by the impact of the heat absorber rather than the intensity of the force itself. The reason why larger Lorentz forces cause smaller deformations is because in the second phase the cold bore and the absorber are in steady contact and, therefore, the kinetic energy is negligible. However, the highest deformation of the cold bore is within the safety margins to avoid the contact with the delicate magnet coils. The heat absorber being involved in this violent dynamics, oscillates synchronously with the cold bore attaining a peak of 1.7 mm at 2.7 ms (1.5 mm original clearance + 0.2 mm cold bore displacement). The octagonal pipe, not being involved in the impact, deforms gradually. The maximum deformation of the octagonal pipe quarter takes place at the intersection with the y-axis. It is about 0.69 mm leaving a free gap from the heat absorber equal to 0.96 mm at 50 ms.

The peak values of the von Mises stress mirror the dynamics of the displacements. Therefore, two phases can be distinguished. As shown in Fig. 5.27a several peaks occur in the first phase of the quench due to the oscillatory dynamics of the impact between the cold bore and the heat absorber. The first and highest peak of the cold bore takes place in the first phase at 2.6 ms and is equal to 524 MPa. Peaks of smaller intensity arise up to 10 ms, while the peak corresponding to the highest Lorentz forces is only 293 MPa occurring in the second phase at 55 ms. The stress of the heat absorber exhibits an oscillatory behaviour as well since it is involved in the impact with the cold bore. The highest stress observed in the first phase is about 61 MPa. The octagonal pipe exhibits a smooth stress increase instead, reaching a top value of 469 MPa, while the copper layer is limited by a perfectly plastic model to 35 MPa. All the highest values of mechanical stress are below the elastic limits of the materials used for the beam screen except for copper. Due to the thin thickness of the inner copper layer, the plastic deformations do not lead to any alarming residual stress after the quench. As shown in Fig. 5.26f the most critical areas are at the centre of the octagonal pipe and at the extremities of the cold bore quarter.

The principal stress components for the cold bore, the heat absorber, and the octagonal pipe are shown in Fig. 5.27b, 5.27c, and 5.27d, respectively.

The contact forces between the cold bore and the heat absorber is shown in Fig. 5.27e. The highest contact force is in the first phase and is equal to 345 $\mathrm{N\,mm^{-1}}$. The kinetic energy, shown in Fig. 5.27f, is given only for

the heat absorber as it is free to move during the quench. The highest kinetic energy acquired by the block is 32 $\mathrm{J\,m^{-1}}$.

3D model

Pumping holes: The von Mises stress of the octagonal pipe fitted with pumping holes is shown in Fig. 5.28a at t=50 ms, namely when the highest forces are induced in the Q1 pipe. It is worth noting that the highest stress is not along the middle plane where the highest forces are induced but around the pumping slots. In fact, such slots represent some typical stress risers. In Fig. 5.28 the stress concentration around the rear side of the slot where the most critical stress occurs is shown. This is around 850 MPa but being very local and, above all, below the elastic limit of the pipe does not constitute any concern. The pumping slots increase the flexibility of the pipe. In fact, the highest radial deformation is now 0.8 mm, 0.11 mm more than in 2D, see Fig. 5.25f.

Heat absorber wings: The distribution of the stress induced in the wings of the heat absorber of the Q1 beam screen is shown in Fig. 5.29. The maximum induced stress for the 16 mm thick wings is around 60 MPa. Such value is well below the elastic limit of the tungsten alloy.

5.6.2 Q2 beam screen

2D model

Considering the similar geometry with the Q1 beam screen and the same magnetic field decay, analogous considerations can be drawn for the results of the Q2 beam screen.

The current integrated in a beam screen quarter is shown Fig. 5.31a, while the current density distribution in Fig. 5.32a. The largest currents are induced in the heat absorber up to 18920 A, followed by the cold bore 10452 A, the inner layer 9553 A, and the octagonal pipe 1711 A.

The resistive heat power shown Fig. in 5.31b is derived from $Q_e = \rho \cdot j^2$. The highest heat losses per length are, 52.3 $\mathrm{W\,mm^{-1}}$ for the heat absorber, 30.5 $\mathrm{W\,mm^{-1}}$ for the cold bore, 3.8 $\mathrm{W\,mm^{-1}}$ for the octagonal pipe, and 18.3 $\mathrm{W\,mm^{-1}}$ for the inner layer.

The highest temperatures of the beam screen components are shown in Fig. 5.31c and the temperature distribution in Fig. 5.32c. The inner layer and the octagonal pipe reach 74 K, the heat absorber 60.2 K, while the cold bore 54.6 K. The temperature of the copper inner layer is the highest mainly because of the specific heat losses, see Fig. 5.31d and Fig. 5.32b.

For the inner layer the highest value of the specific heat losses are equal to 2.4 $\mathrm{W\,mm^{-3}}$, for the heat absorber 104 $\mathrm{mW\,mm^{-3}}$, for the cold bore 69.6 $\mathrm{mW\,mm^{-3}}$ and for the octagonal pipe 39.8 $\mathrm{mW\,mm^{-3}}$.

The distribution of the Lorentz forces in the Q2 beam screen is shown in Fig. 5.30, while the magnitude of the total force in Fig. 5.32d.

The radial component of the Lorentz forces integrated in a quarter of the assembly is shown in Fig. 5.31e. In general the largest forces are induced between 55 and 60 ms. These are 61 $\mathrm{N\,mm^{-1}}$ for the cold bore, 108 $\mathrm{N\,mm^{-1}}$ for the heat absorber, 9 $\mathrm{N\,mm^{-1}}$ for the octagonal pipe and 59.4 $\mathrm{N\,mm^{-1}}$ for the copper layer. As for the currents, the forces induced in the heat absorber are higher than those induced in the inner copper layer.

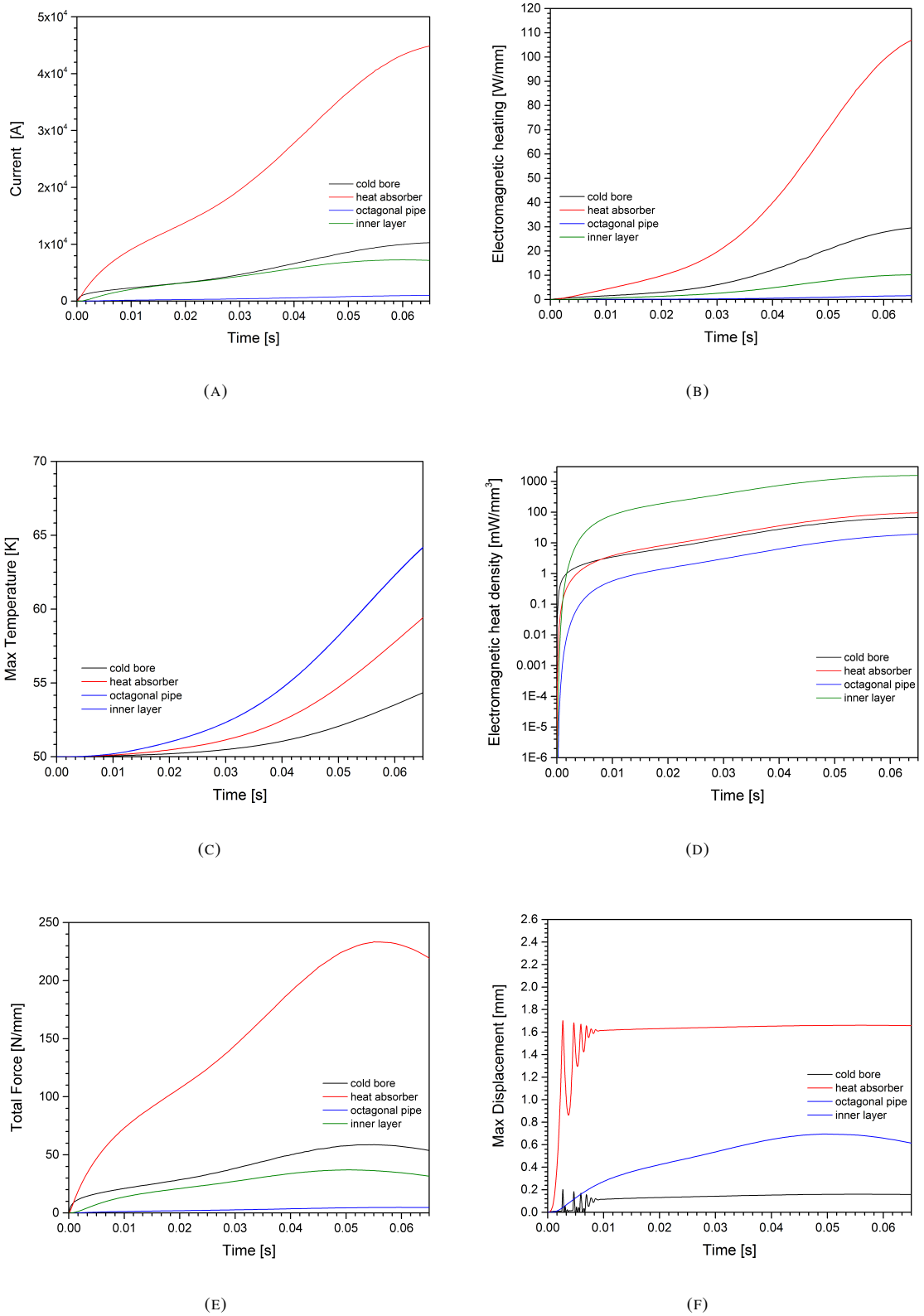


FIGURE 5.25: Evolution on time of the main physical quantities induced in the Q1 beam screen during a magnet quench.

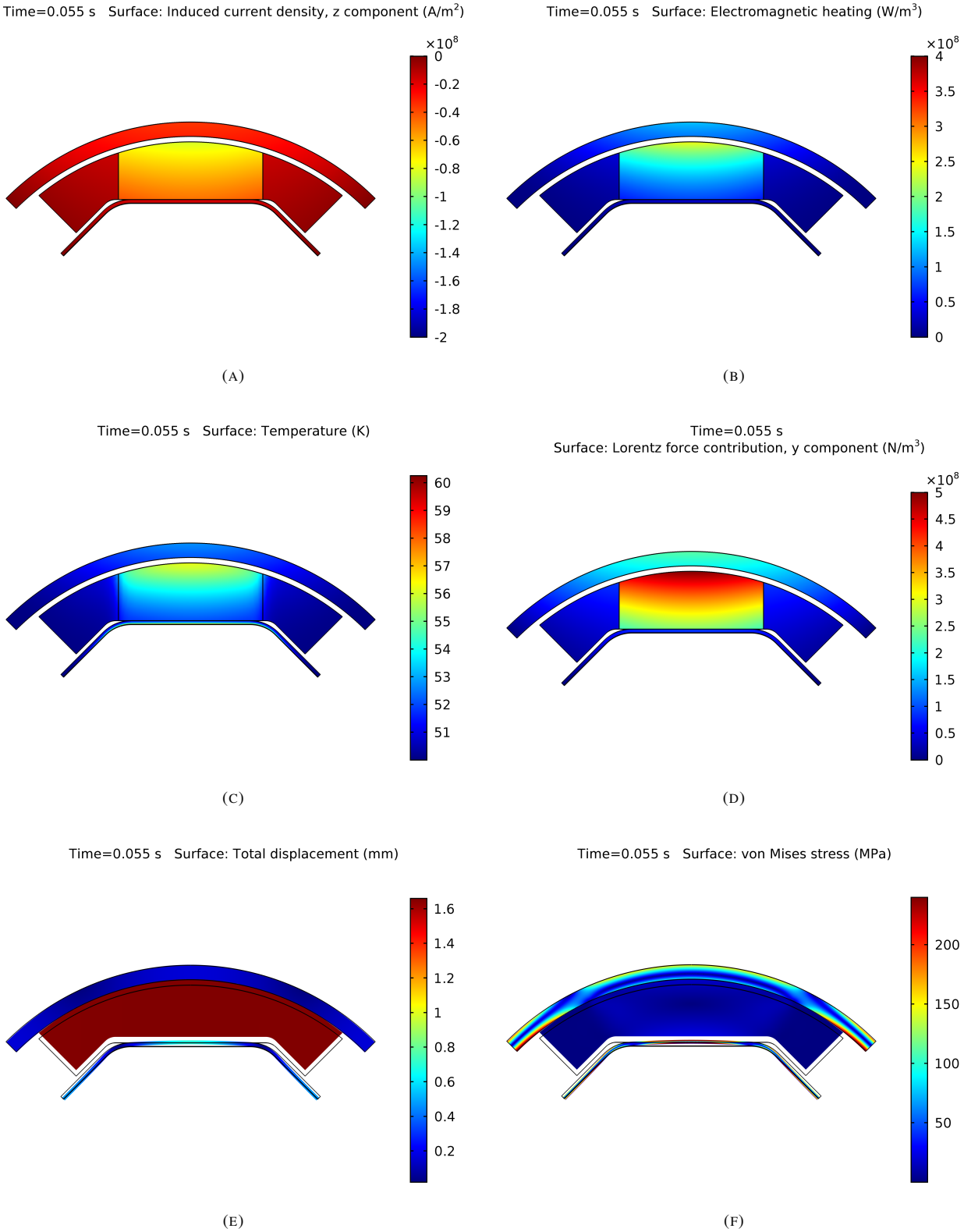


FIGURE 5.26: Distribution of the main physical quantities induced in the Q1 beam screen at 55 ms.

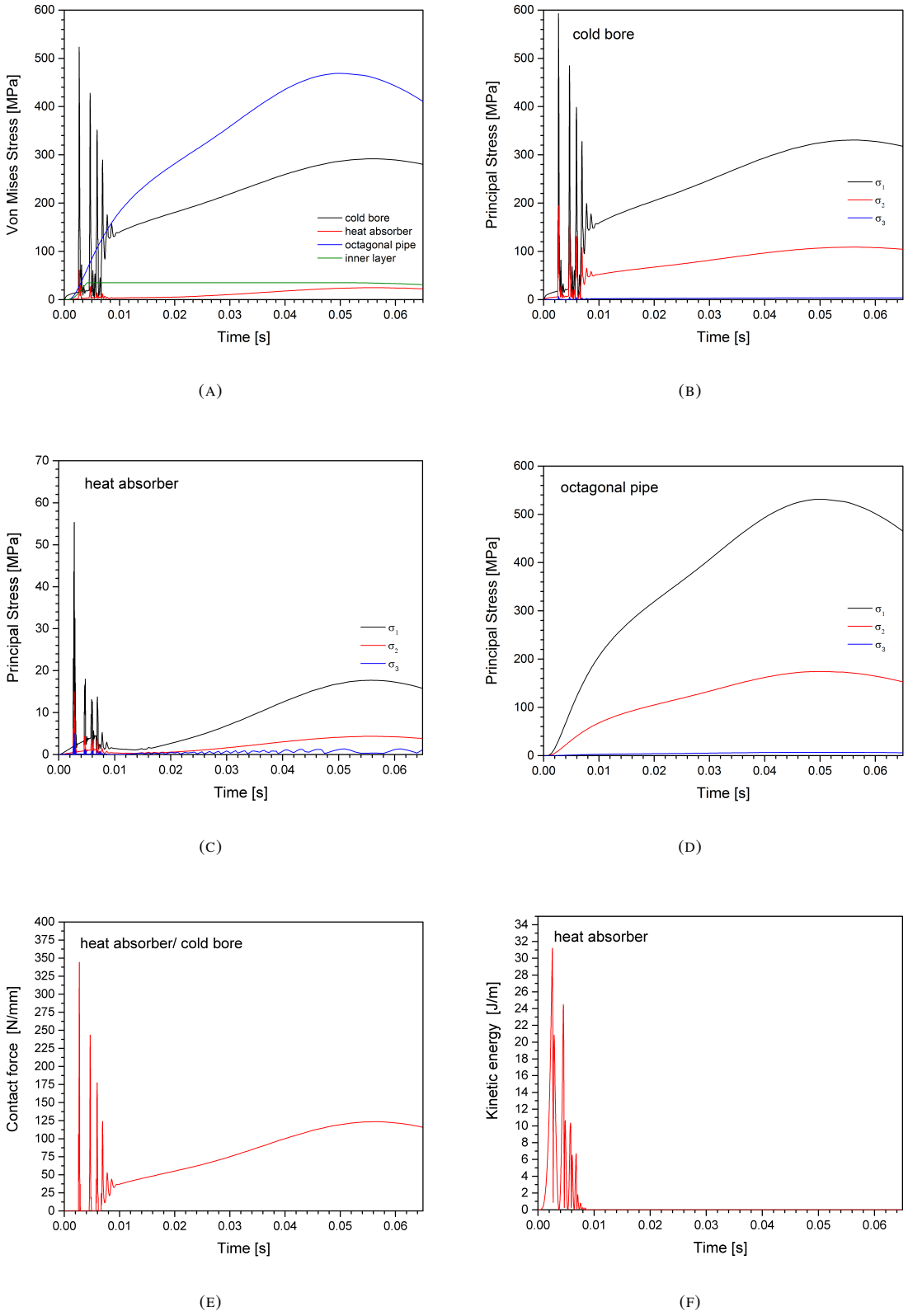
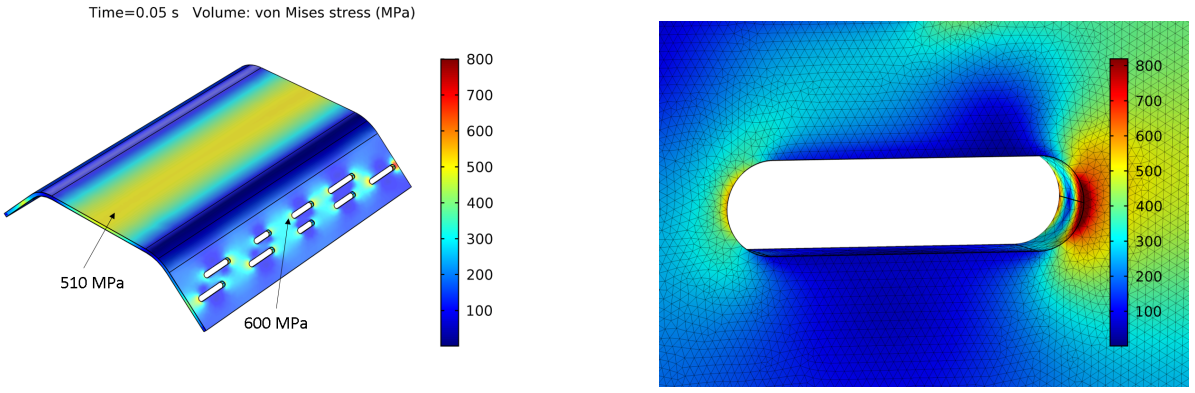


FIGURE 5.27: Evolution on time of the equivalent and principal stress induced in all the components of the Q1 beam screen. The contact force is shown between the heat absorber and the cold bore. The kinetic energy is shown for the heat absorber.

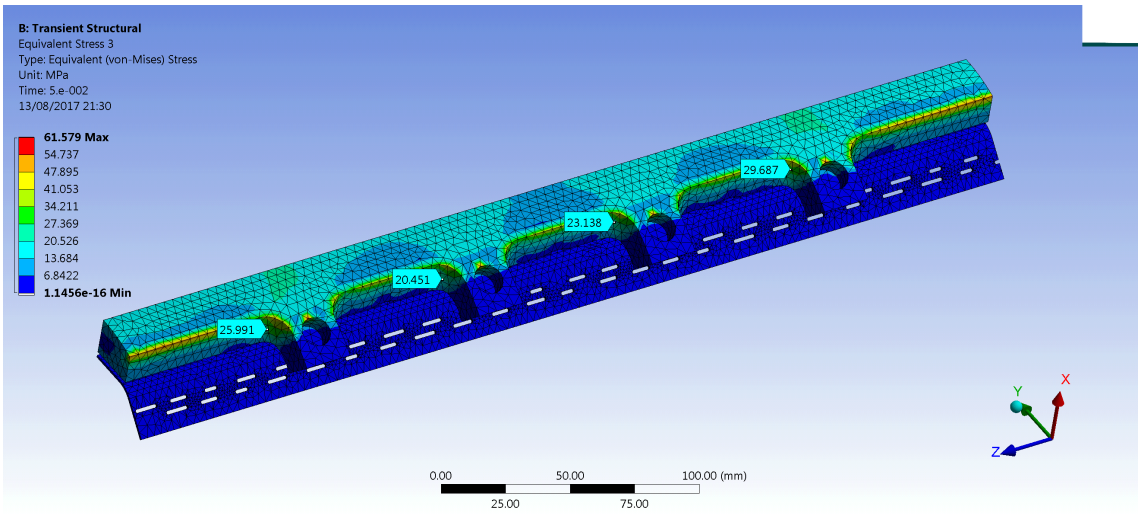


(A) (B)

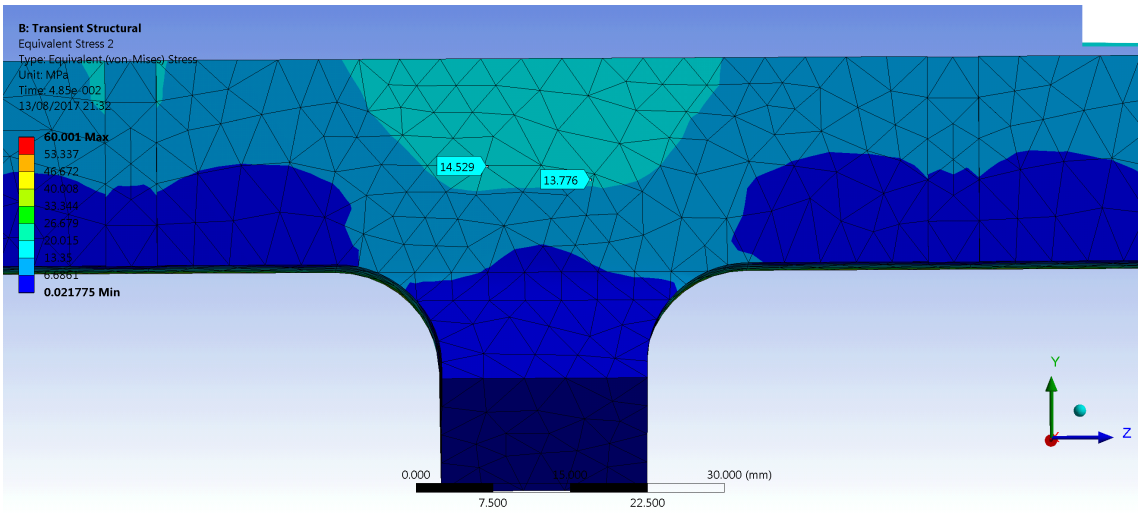
FIGURE 5.28: In (a) von Mises stress on the Q1 octagonal pipe fitted with pumping holes. In (b) stress concentration on the rear part of the most critical slot.

The highest deformations of the beam screen components are shown in Fig. 5.31f, while in Fig. 5.32e it is depicted the deformed Q2 beam screen. The heat absorber, which is simply laid on the octagonal surface, moves independently from the rest of the assembly impacting on the cold bore multiple times during the quench. From the heat absorber impact one can determine two main phases: the first one is characterised by rapid oscillations up to 8 ms due to the violent impact of the absorber against the cold bore, while the second one by a steady contact. The highest deformation of the cold bore, equal to 0.15 mm, occurs in the first phase at 2.7 ms. At this stage the forces induced in the absorber are only $15.7\mathrm{N\,mm^{-1}}$. In the second phase, the highest deformation is almost the same, namely, 0.148 mm and takes place at 54 ms where the induced forces in the absorber are 108 $\mathrm{N\,mm^{-1}}$. Like for the Q1 beam screen the most severe deformation of the cold bore is mostly determined by the impact of the heat absorber rather than the intensity of the force itself. The reason why larger Lorentz forces cause smaller deformations is because in the second phase the cold bore and the absorber are in steady contact and, therefore, the kinetic energy is negligible. However, the highest deformation of the cold bore is within the safety margins to avoid the contact with the delicate magnet coils. The heat absorber being involved in this violent dynamics, oscillates synchronously with the cold bore attaining a peak of 1.65 mm at 2.3 ms (1.5 mm original clearance + 0.15 mm cold bore displacement). The octagonal pipe, not being involved in the impact, gets deformed gradually. The maximum radial deformation reached by the octagonal pipe is about 0.67 mm leaving a free gap from the heat absorber equal to 0.96 mm at 50 ms.

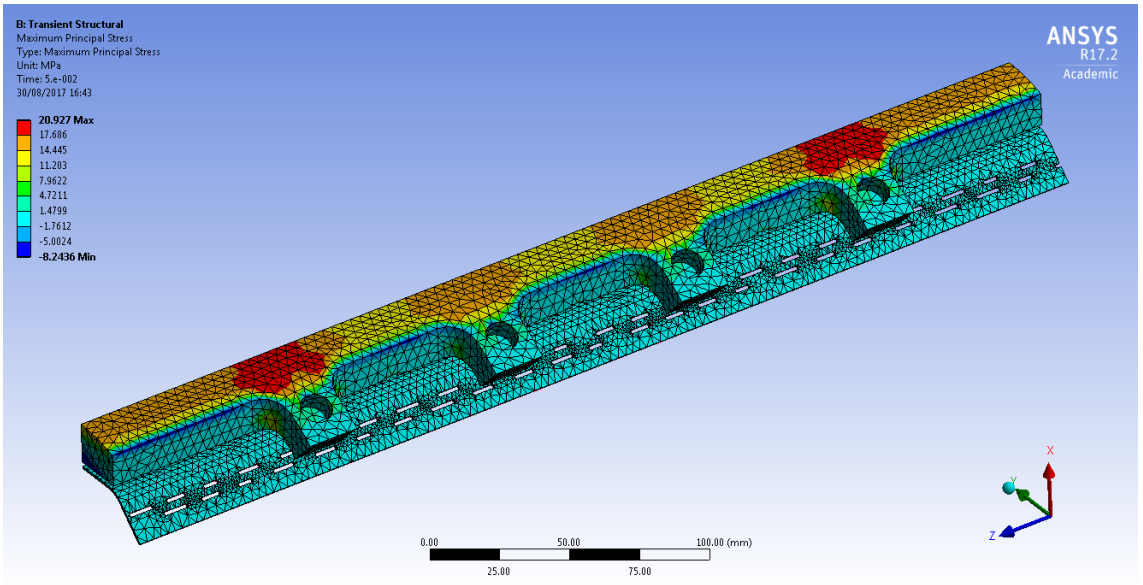
The peak values of the von Mises stress mirror the dynamics of the displacements. Therefore, as for the Q1 beam screen two phases can be distinguished. As shown in Fig. 5.33a several peaks occur in the first phase of the quench due to the oscillatory dynamics of the impact between the cold bore and the heat absorber. The first and highest peak of the cold bore takes place in the first phase at 2.3 ms and is equal to 389 MPa. Peaks of smaller intensity arise up to 8 ms, while the peak corresponding to the highest Lorentz forces is only 212 MPa occurring in the second phase at 55 ms. The stress of the heat absorber exhibits an oscillatory behaviour as well since it is involved in the impact with the cold bore. The highest stress observed in the first phase is about 138 MPa. The octagonal pipe exhibits a smooth stress increase instead, reaching a top value of 548 MPa, while the copper layer is limited by a perfectly plastic model to 35 MPa. All the highest values of mechanical stress are below the elastic limits of the materials used for the beam screen except for copper. Due to the thin thickness of the inner copper layer, the plastic deformations do not lead to any alarming residual stress after the quench. As shown in Fig. 5.32f the most critical areas are at the centre of the octagonal pipe and at the extremities of the cold bore quarter.



(A)



(B)



(C)

FIGURE 5.29: Q1 heat absorber. From top to bottom: von Mises stress on the external side of the heat absorber; von Mises stress on the internal side of the heat absorber; maximum principal stress.

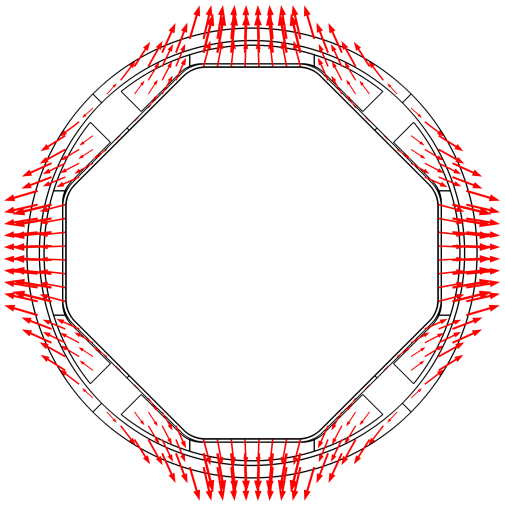


FIGURE 5.30: Distribution of the induced forces in the Q2 beam screen during a magnet quench.

The principal stress components for the cold bore, the heat absorber, and the octagonal pipe are shown in Fig. 5.33b, 5.33c and 5.33d, respectively.

The contact forces between the cold bore and the heat absorber is shown in Fig. 5.33e. The highest contact force is in the first phase and it is equal to 175 $\mathrm{N\,mm^{-1}}$. The kinetic energy, shown in Fig. 5.33f, is given only for the heat absorber as it is free to move during the quench. The highest kinetic energy acquired by the block is 16.5 $\mathrm{J\,m^{-1}}$.

3D model

Pumping holes: The von Mises stress of the octagonal pipe fitted with pumping holes is shown in Fig. 5.34a at t=40 ms, namely when the highest forces are induced in the Q2 pipe. As for the Q1, the highest stress is not along the middle plane but around the pumping slots. In Fig. 5.34 it is depicted the stress concentration around the rear side of the slot where the most critical stress occurs. This is around 950 MPa but being very local and, above all, below the elastic limit of the pipe (1350 MPa) does not constitute any concern. The pumping slots increase slightly the flexibility of the pipe. The highest radial deformation goes from 0.68 mm in 2D to 0.72 mm in 3D, see Fig. 5.31f.

Heat absorber wings: The stress induced in the wings of the heat absorber of the Q2 beam screen is depicted in Fig.5.35. The heat absorber wings whose thickness is 6 mm might break down during the violent hit of the block into the cold bore. However, the highest value is 116 MPa, which is below the elastic limit of the tungsten alloy.

5.6.3 D1 beam screen

2D model

The current integrated in a beam screen quarter is shown Fig. 5.37a, while the current density distribution in Fig. 5.38a. For the D1 beam screen the largest currents are induced in the inner layer, 5647 A, followed by the heat

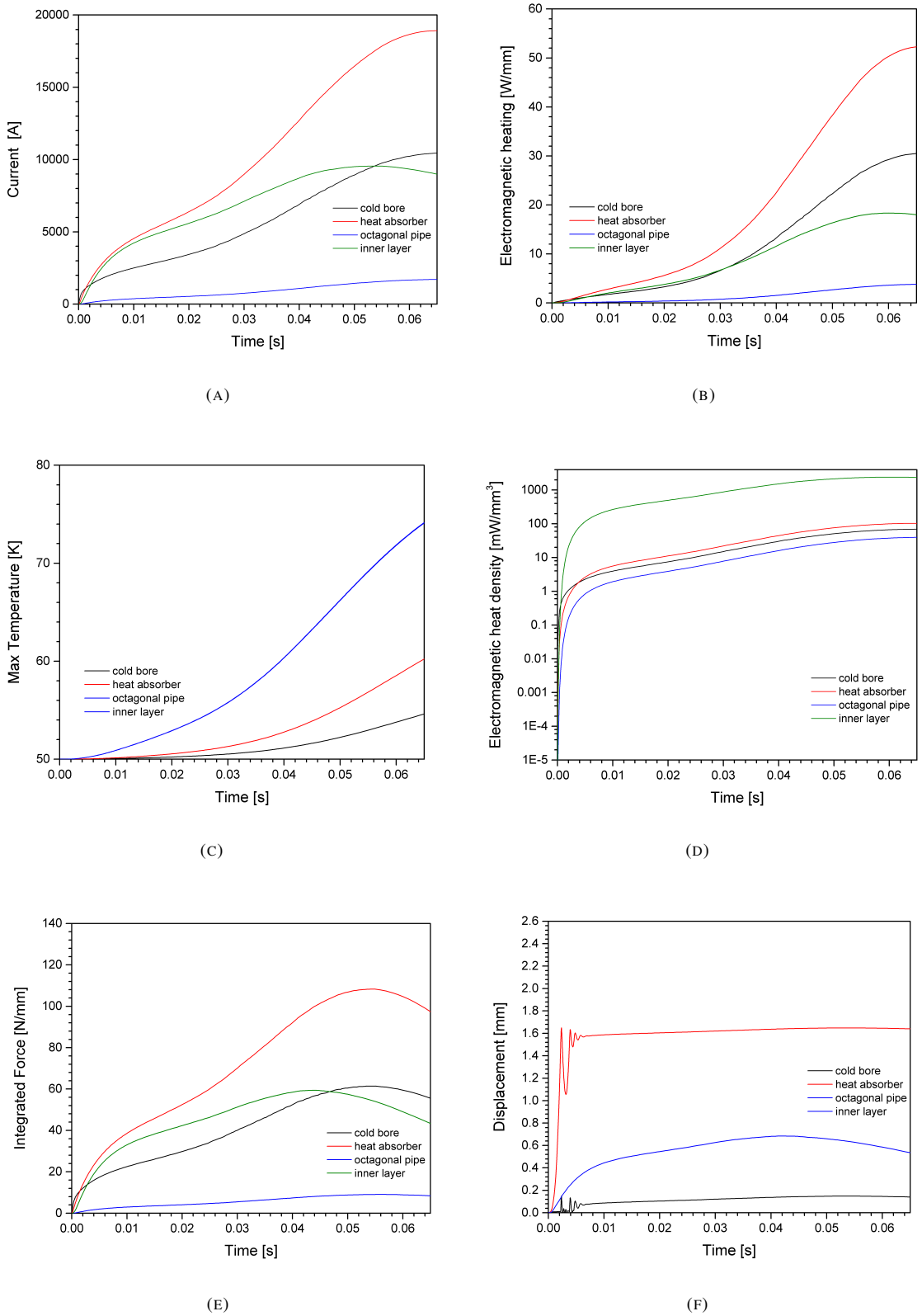


FIGURE 5.31: Evolution on time of the main physical quantities induced in the Q2 beam screen during a magnet quench.

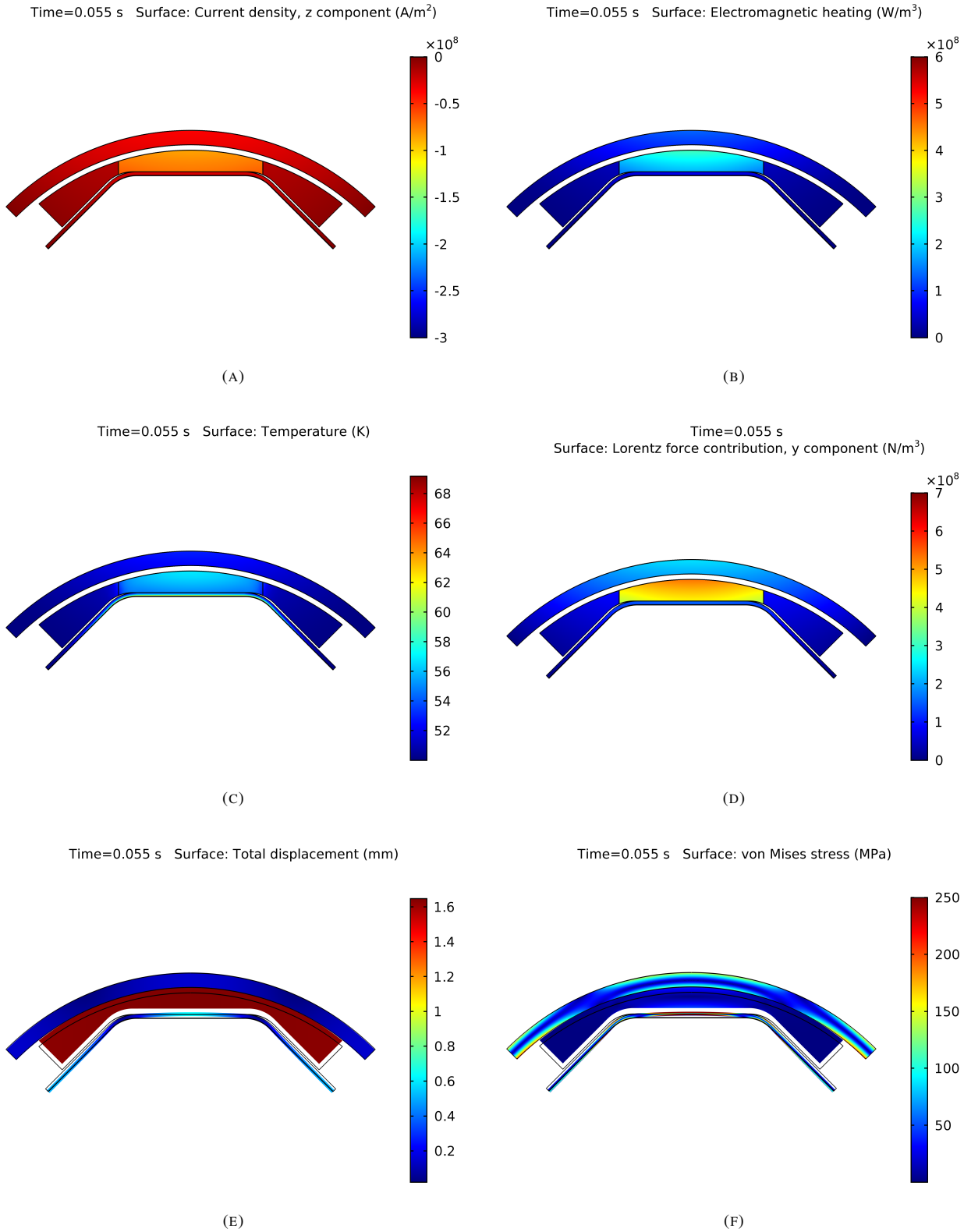


FIGURE 5.32: Distribution of the main physical quantities induced in the Q2 beam screen at 55 ms.

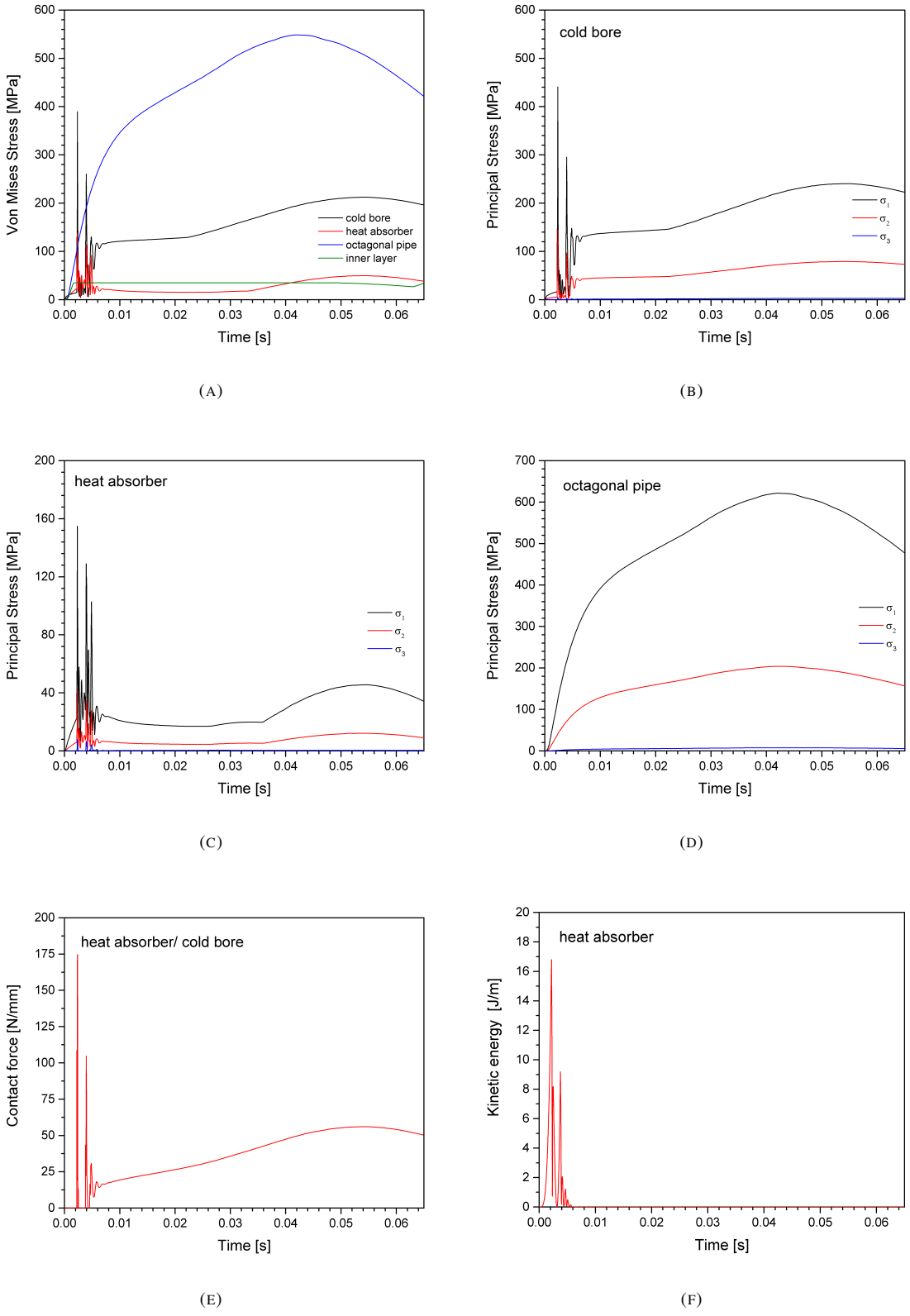
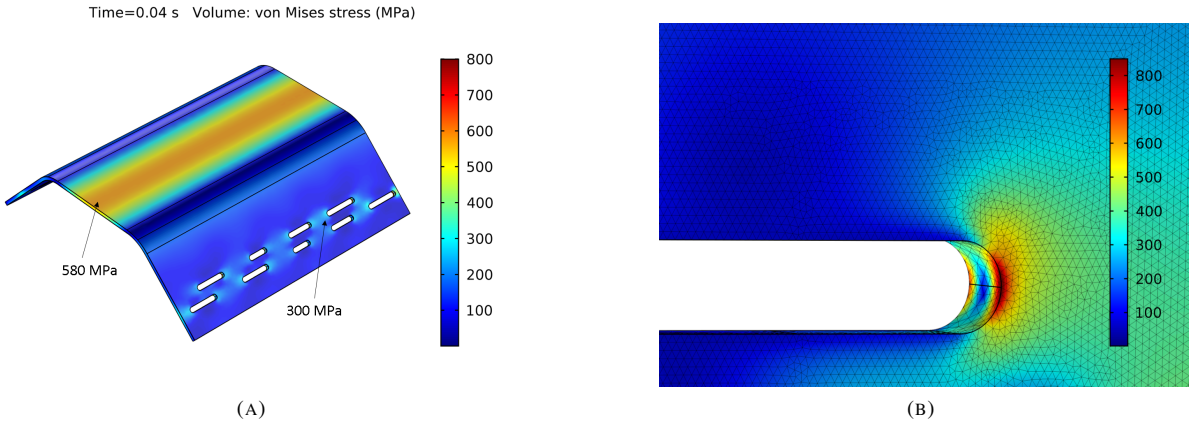


FIGURE 5.33: Evolution on time of the equivalent and principal stress induced in all the components of the Q2 beam screen. The kinetic energy is shown only for the heat absorber and the contact force between the heat absorber and the cold bore.



(A) (B)

FIGURE 5.34: In (a) von Mises stress on the Q2 octagonal pipe fitted with pumping holes. In (b) stress concentration on the rear part of the most critical slot.

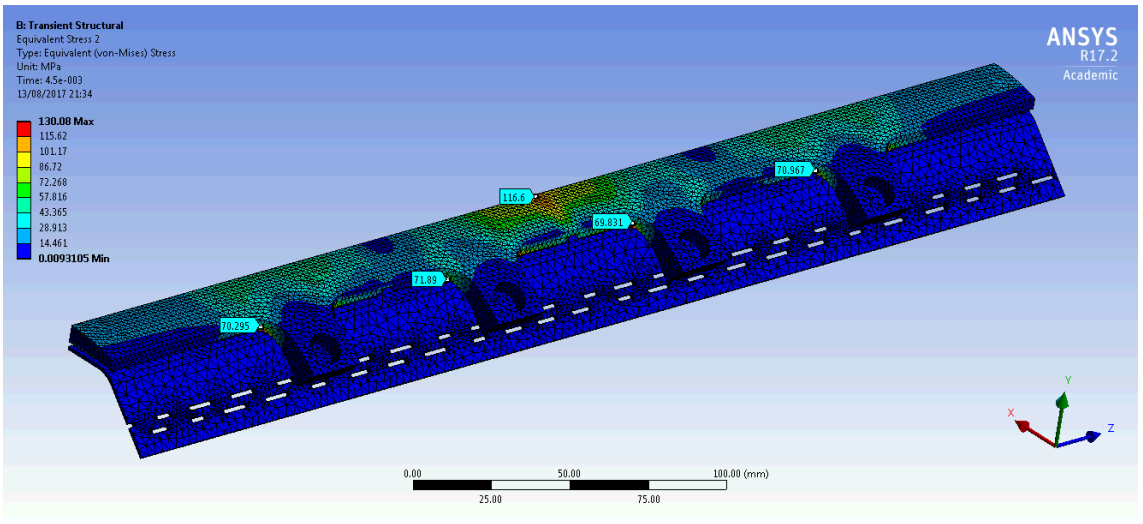
absorber 4601 A, the cold bore 3968 A, and the octagonal pipe 724 A. As seen in eq. 5.39, for a given dipolar magnetic field decay, the parameters influencing the magnitude of the currents are the electrical resistivity ρ and geometric factors like the distance of the components from the centre, r and its thickness t. It is worth noting that in comparison with the Q1 and Q2 beam screen the dependence of the distance from the origin is linear rather than quadratic. This explains why more currents are induced in the inner copper layer, rather than in the heat absorber. For the D1 beam screen the electrical resistivity of copper, which is lower than the one of the tungsten alloy (at 50 K, $2.93 \cdot 10^7$ vs $1.5 \cdot 10^9$ $\mathrm{S\,m^{-1}}$, respectively), prevails on the position and the thickness of the component.

Fig. 5.37b shows that although the currents induced in the inner layer are higher than the ones of the heat absorber, the maximum heat loss per length is 6.2 $\mathrm{W\,mm^{-1}}$ for the heat absorber and 5 $\mathrm{W\,mm^{-1}}$ for the inner layer. This is due to the electrical resistivity of the tungsten alloy, which is about two orders of magnitude higher than the one of copper. Finally, 4.4 $\mathrm{W\,mm^{-1}}$ of power is induced in the cold bore and 0.68 $\mathrm{W\,mm^{-1}}$ in the octagonal pipe.

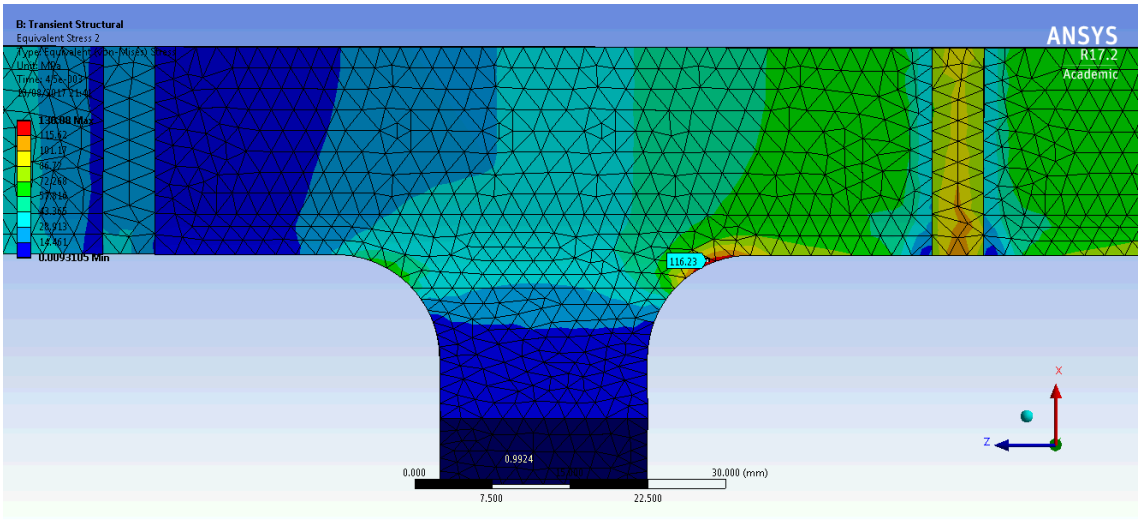
The highest temperatures of the beam screen components are shown in Fig. 5.37c and the temperature distribution in Fig. 5.32c. The highest temperature of the inner layer is 62.2 K as well as the one of the octagonal pipe because it is at the interface with the inner layer. The heat absorber reaches 54.4 K, while the cold bore 51 K. As seen also for the Q1 and Q2 beam screen, the average temperature of the copper inner layer is the highest mainly because of the specific heat losses, see Fig. 5.37d.

For the inner layer the maximum resistive losses are equal to 657 $\mathrm{mW\,mm^{-3}}$, while those for the heat absorber 12.4 $\mathrm{mW\,mm^{-3}}$, for the cold bore 010 $\mathrm{mW\,mm^{-3}}$ and for the octagonal pipe 7.1 $\mathrm{mW\,mm^{-3}}$.

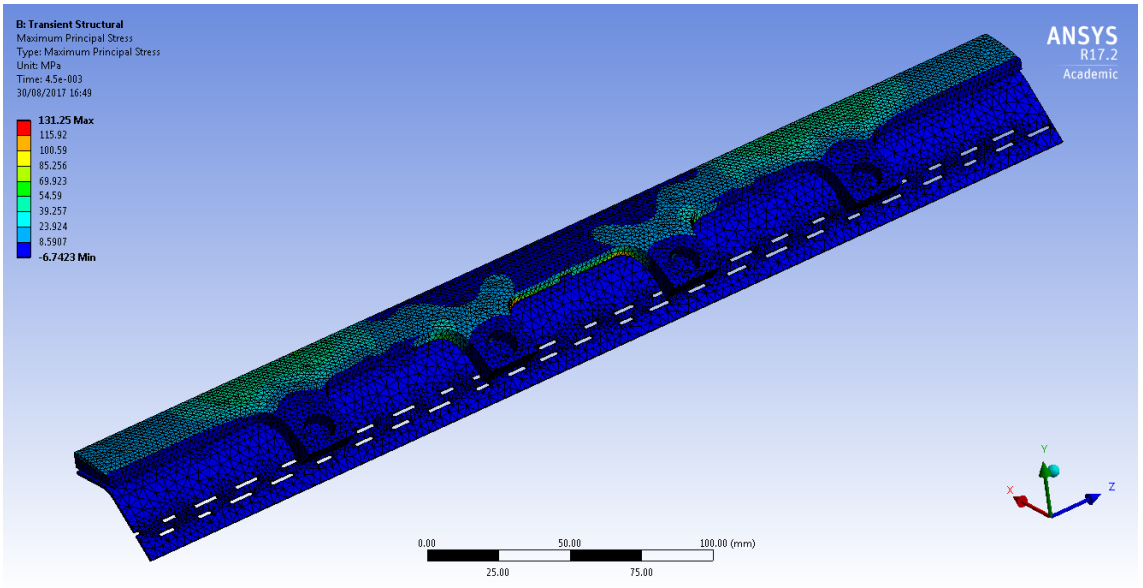
The distribution of the Lorentz forces in the D1 beam screen is shown in Fig. 5.36, while the magnitude of the F_x in Fig. 5.38d. The radial component of the Lorentz forces integrated in a quarter of the assembly is shown in Fig. 5.37e. In general, the largest forces of the beam screen components are induced between 100 and 150 ms. These are 15.3 $\mathrm{N\,mm^{-1}}$ for the cold bore, 17.9 $\mathrm{N\,mm^{-1}}$ for the heat absorber, $\mathrm{N\,mm^{-1}}$ for the octagonal pipe and 24.2 $\mathrm{N\,mm^{-1}}$ for the copper layer. As for the currents, the forces induced in the inner copper layer are higher than those induced in the heat absorber. It is important to point out that since the D1 beam screen is inserted in a dipole magnet, the intensity of the magnetic field is uniform throughout the beam pipe. Therefore, as shown in eq. 5.41, the integrated Lorentz forces depend on the second power of the distance between the component and the origin.



(A)



(B)



(C)

FIGURE 5.35: Q2 heat absorber. From top to bottom: von Mises stress on the external side of the heat absorber; von Mises stress on the internal side of the heat absorber; maximum principal stress.

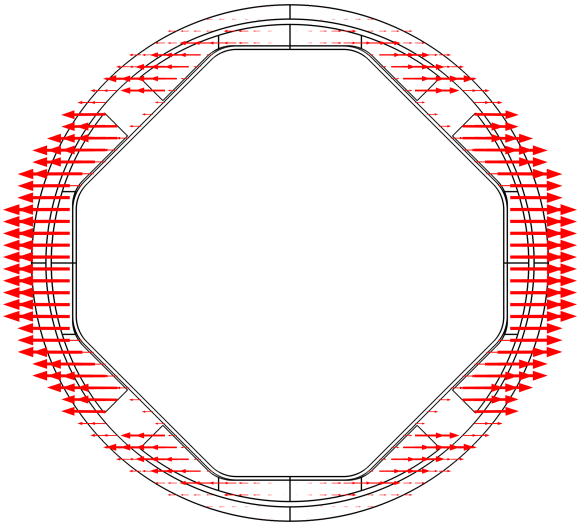


FIGURE 5.36: Distribution of the induced forces in the D1 beam screen during a magnet quench.

In Fig. 5.37f the maximum displacements of the D1 beam screen components are shown, while in Fig. 5.38e it is depicted the deformed D1 beam screen. Unlike the dynamics of the Q1 and Q2 beam screens, the heat absorber does not moves independently from the octagonal pipe but it remains always in partial contact with it. As for the Q1 and Q2 two phases can be distinguished. In the first phase, the impact of the absorber against the cold bore causes some oscillations up to 20 ms. In the second phase there are no oscillations but a partial contact between the octagonal pipe and the heat absorber is kept. In contrast to the Q1 and Q2 beam screen, the highest deformation of the cold bore, equal to 0.98 mm, occurs in the second phase of the impact at 142 ms. The reason why the D1 forces, which are lower than the ones induced in the Q1 and Q2 beam screen, cause higher displacement has to be sought in their distribution and the associated dynamics. In fact as seen in Fig. 5.36, the forces act only on the horizontal plane of the beam screen. Therefore, the deformation of the cold bore on the horizontal plane is not counteracted by any other force. Moreover, since the octagonal pipe is always in contact with the heat absorber, the force transferred to the cold bore is composed by the sum of the force of the heat absorber and the one exerted at the interface with the octagonal pipe. The heat absorber and the octagonal pipe, being in contact, exhibit the same maximum displacement attaining 2.48 mm at 142 ms.

As seen for the Q1 and Q2 beam screen, the highest value of the von Mises stress mirrors the dynamics of the displacements. This is shown in Fig. 5.27a where several peaks manifest at the beginning of the quench due to the oscillatory dynamics of the impact between the cold bore and the heat absorber. However these peaks are not higher than the ones corresponding to the highest forces (second phase). The stress in the cold bore has a maximum value of about 280 MPa, in the octagonal pipe 423 MPa, in the heat absorber 279 MPa, while in the copper layer is limited by a perfectly plastic model to 35 MPa. All the highest values of mechanical stress are below the elastic limits of the materials used for the beam screen except for copper. Due to the thin thickness of the inner copper layer, the plastic deformations do not lead to any alarming residual stress after the quench. Fig. 5.32f represents the stress of a quarter of the beam screen assembly.

The principal stress components for the cold bore, the heat absorber, and the octagonal pipe are shown in Fig. 5.39b, 5.39c, and 5.39d, respectively.

The contact forces between the cold bore and the heat absorber is shown in Fig. 5.39e. The highest contact force is in then first phase and it is equal to 59 $\mathrm{N\,mm^{-1}}$. The kinetic energy, shown in Fig. 5.39f, is given only for

the heat absorber as it is free to move during the quench. The highest kinetic energy acquired by the block is 3.5 $\mathrm{J\,m^{-1}}$.

3D model

Pumping holes: The von Mises stress of the octagonal pipe fitted with pumping holes is shown in Fig. 5.40 at t=120 ms, namely when the highest forces are induced in the D1 pipe. As for the Q1 and Q2, the highest stress is around the pumping slots. In Fig. 5.40b it is depicted the stress concentration around the rear side of the slot, where the most critical stress occurs. This is around 750 MPa but being very local and, above all, below the elastic limit of the pipe (1350 MPa) does not constitute any concern.

Heat absorber wings: The stress induced in the wings of the heat absorber of the D1 beam screen is depicted in Fig. 5.35. Only the wings placed on the horizontal plane of the assembly (along the direction of the induced forces) are affected by the hit with the cold bore. The highest von Mises stress calculates to 524 MPa on the internal side of the wing. Even if it is much higher than the Q1 and Q2 wings it is is below the elastic limit of the tungsten alloy. The maximum principal stress is 687 MPa.

5.6.4 Gap analysis

The gap between the heat absorber and the cold bore is set to 1.5 mm. However, due to mechanical tolerances (shape and straightness of the components), it might happen that this gap is reduced from one side and increased to another one. Therefore, an analysis has been conducted for all the beam screens to quantify the stress and the displacement of the cold bore as well as the kinetic energy of the heat absorber for a gap ranging from 0.5 mm to 2 mm.

The kinetic energy calculates to:

$$E_k = \frac{1}{2}\rho \cdot v^2 \tag{5.58}$$

where ρ is the mass density and v is the velocity of the component. The kinetic energy of the heat absorber corresponding to the initial contact with the cold bore is shown in Fig. 5.42. In general, as expected, the kinetic energy increases as function of the gap since the speed becomes higher. In particular, amongst all the heat absorbers, that of the Q1 is the highest due to the larger mass, followed by the Q2 and the D1. The kinetic energy of the Q2 absorber is higher than the one of the D1 because, even if they have the same mass, the speed is not the same. In fact, the higher forces induced in the Q2 absorber make it move much faster than the one of the D1.

The kinetic energy of the heat absorber has an impact on the displacement and stress of the cold bore itself. As shown in Fig. 5.43, the maximum stress and deformation of the cold bore increases for all the assemblies as a function of the gap and, therefore, of the kinetic energy.

5.6.5 Modal analysis

The frequency of the initial cold bore oscillation results to be around 1000 Hz for the Q1 and Q2, and 300 Hz for the D1 beam screen. From a modal analysis it turns out that those are close to the first two natural frequencies of the cold bore vibrational modes, namely 532 Hz and 916 Hz.

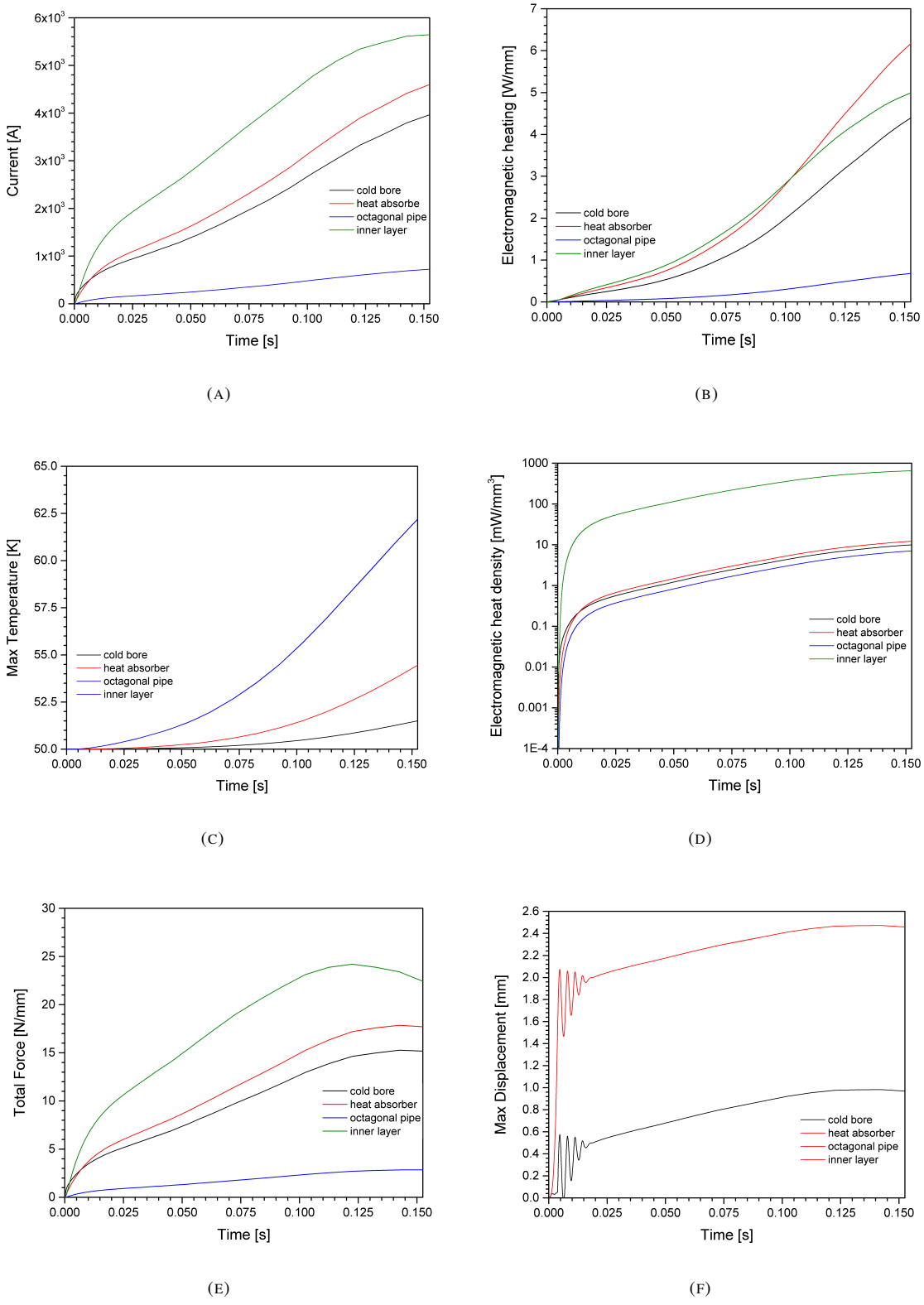


FIGURE 5.37: Evolution on time of the main physical quantities induced in the D1 beam screen during a magnet quench.

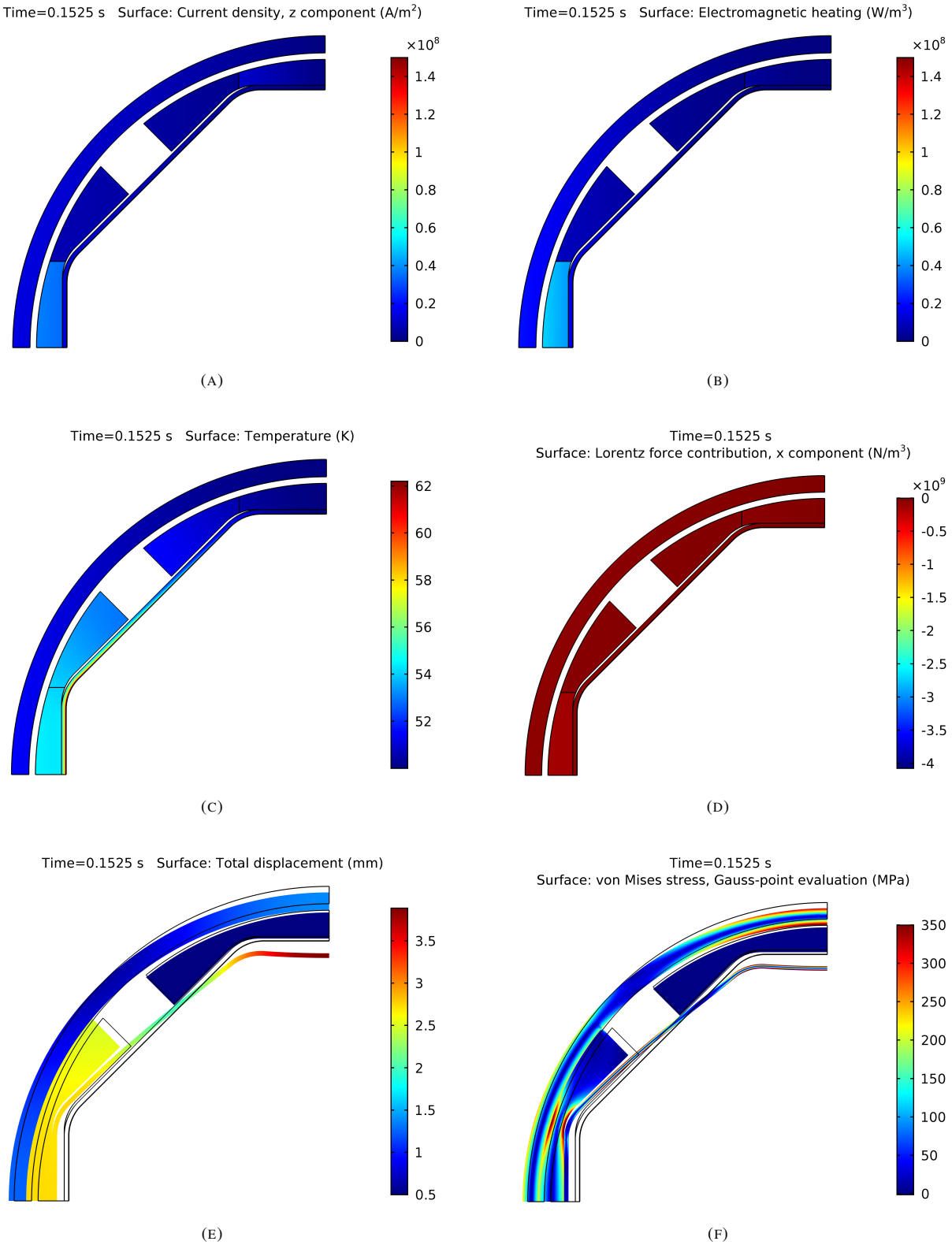


FIGURE 5.38: Distribution of the main physical quantities induced in the D1 beam screen at 152 ms.

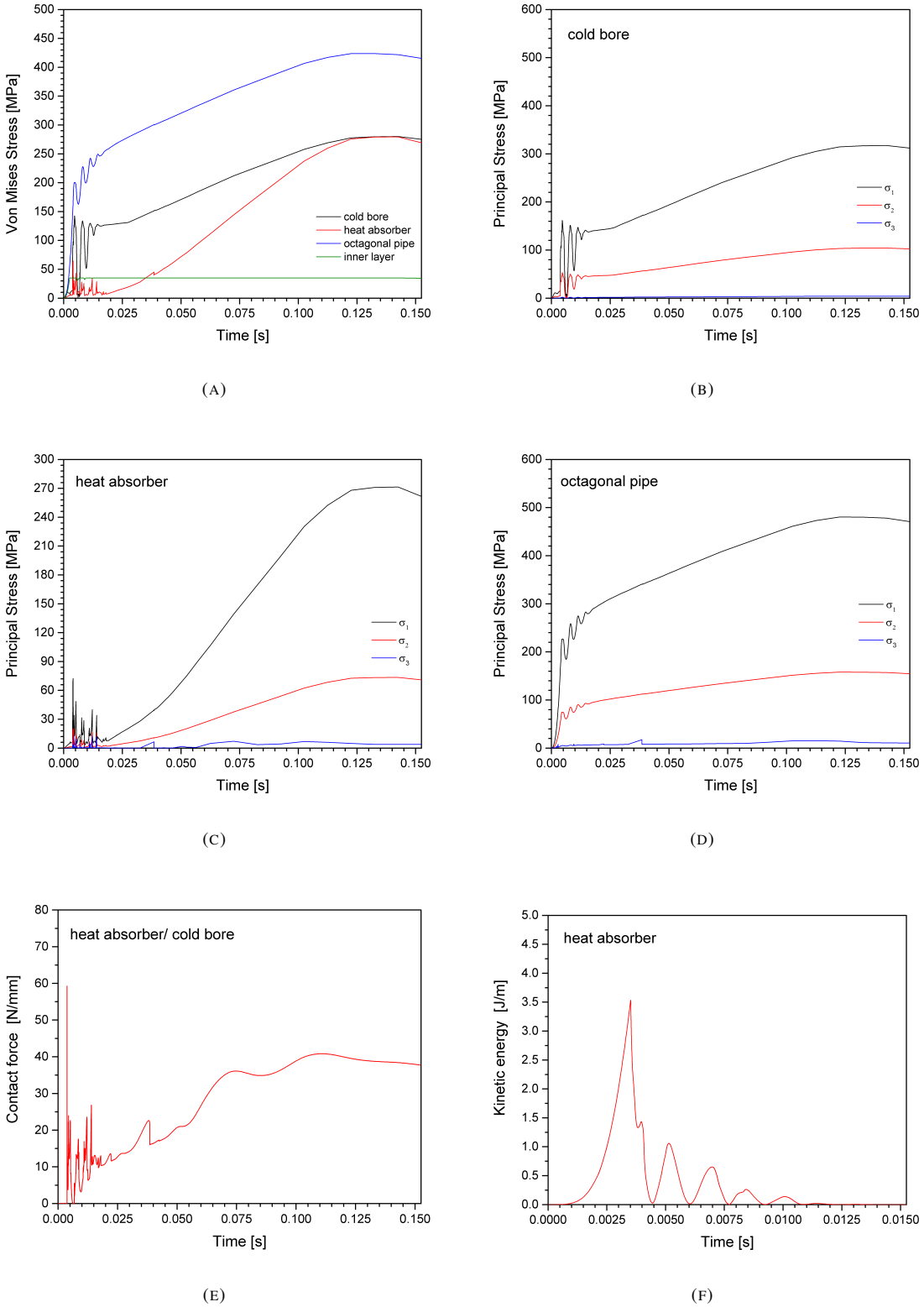
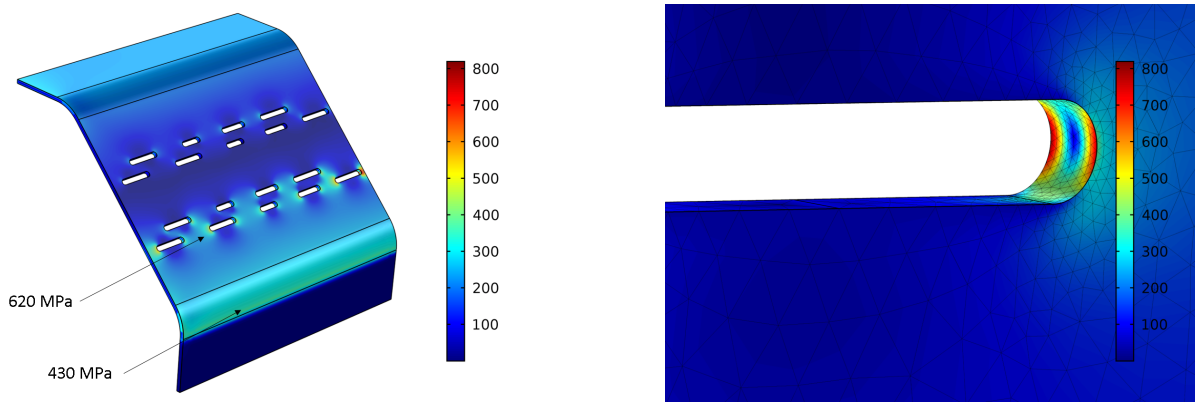


FIGURE 5.39: Evolution on time of the equivalent and principal stress induced in all the components of the D1 beam screen. The kinetic energy is shown only for the heat absorber and the contact force between the heat absorber and the cold bore.



(A) (B)

FIGURE 5.40: In (a) von Mises stress on the D1 octagonal pipe fitted with pumping holes. In (b) stress concentration on the rear part of the most critical slot.

5.6.6 Mechanical analysis at the interface of the colaminated copper layer

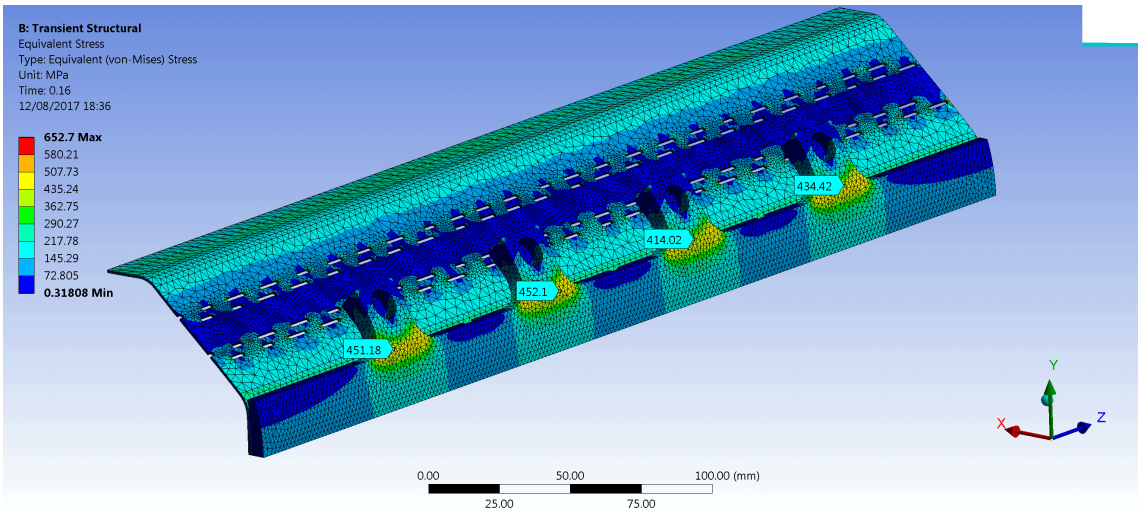
The evaluation of the stress state at the interface between the co-laminated copper layer and the octagonal pipe is important to assess potential delamination phenomena. The interface stress has been assessed during the magnet quench, when the highest forces are induced, as well as after the quench, when the forces are vanished. The analysis of this latter case is particularly interesting as the unavoidable plastic deformation of the copper layer may lead to a detrimental residual stress. The von Mises stress and the profile of the interface stress before and during the quench is shown in Figs. 5.44, 5.45, 5.46 for the Q1, Q2, D1 beam screen, respectively.

The profile of the stress enables to identify a compressive or tensile load acting at the interface between the copper layer and the octagonal pipe. The normal component $\sigma_{y\ loc}$ of the stress at the interface might be dangerous for the delamination of the copper layer. For the Q1 and Q2 beam screen the highest normal component is of tensile-type reaching 100 MPa during the quench and of compressive-type reaching 7.5 MPa after the quench, see Fig 5.44b and Fig. 5.44d for the Q1 and Fig 5.45b and Fig. 5.45d for the Q2 beam screen.

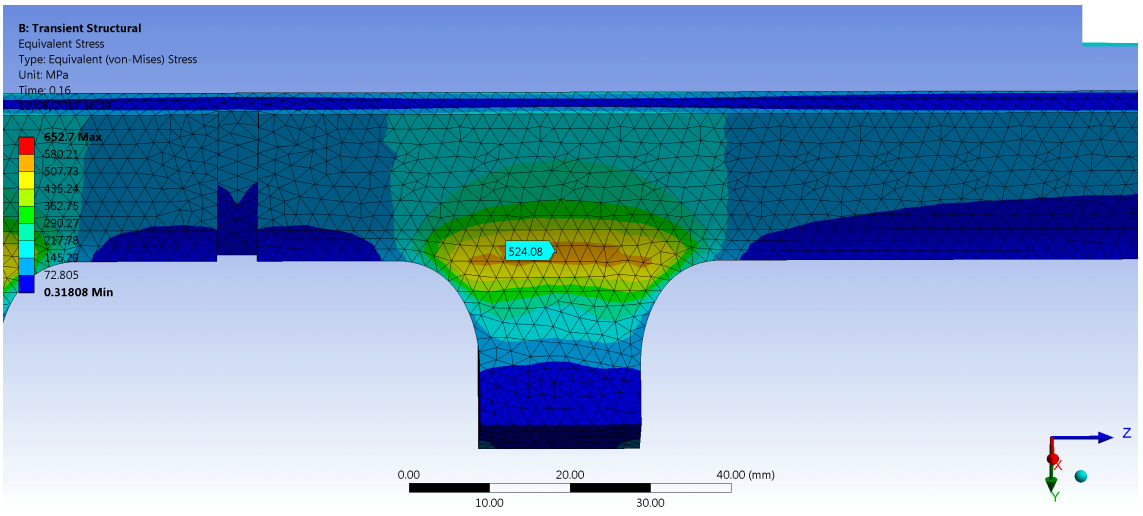
For the D1 beam screen the highest normal component is of compressive-type reaching 80 MPa during the quench and of tensile-type reaching 15 MPa after the quench, see Fig 5.46b and Fig. 5.46d, respectively. For all the beam screens, the interface stress during the quench is not deemed detrimental for the delamination of the copper layer. After the quench, the normal component of the stress results in a compression state for the Q1 and Q2 beam screen along the surfaces tilted at 45° angle. Any potential delamination is then avoided. For the D1 beam screen a residual tensile stress remains along the segments on the horizontal plane of the assembly. However, this is not high enough for the copper layer delamination.

Since the inner copper layer undergoes plastic deformations, an analysis to assess the number of cycles to fracture has been performed. To evaluate the fatigue life of the copper layer the Coffin-Manson relation [124] has been adopted:

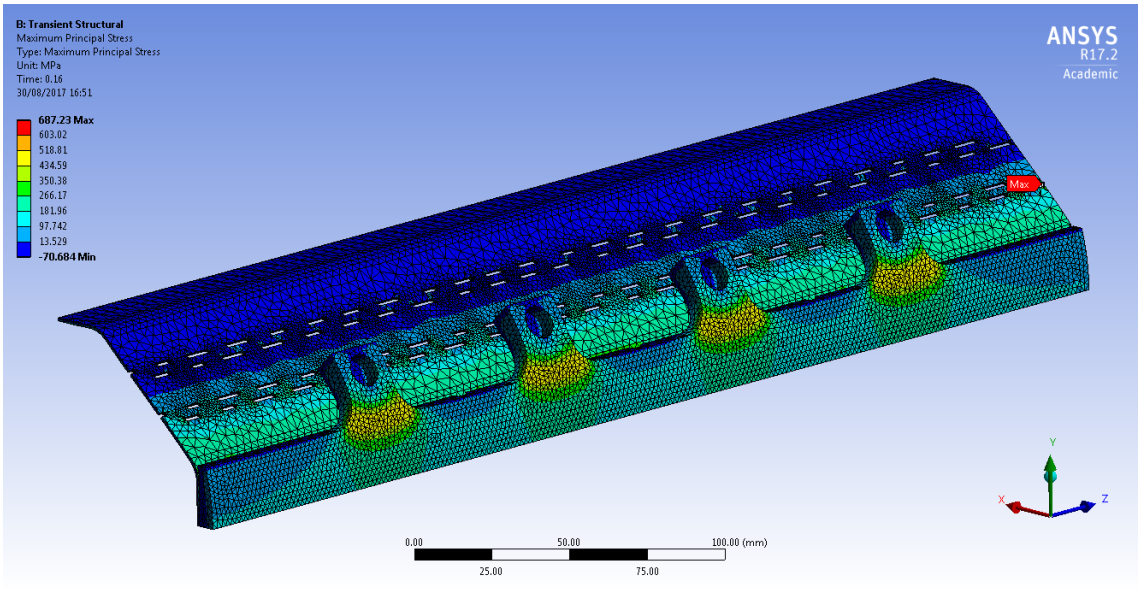
$$\frac{\Delta\epsilon_p}{2} = \epsilon_f (2N)^c \tag{5.59}$$



(A)



(B)



(C)

FIGURE 5.41: D1 heat absorber. From top to bottom: von Mises stress on the external side of the heat absorber; von Mises stress on the internal side of the heat absorber; maximum principal stress.

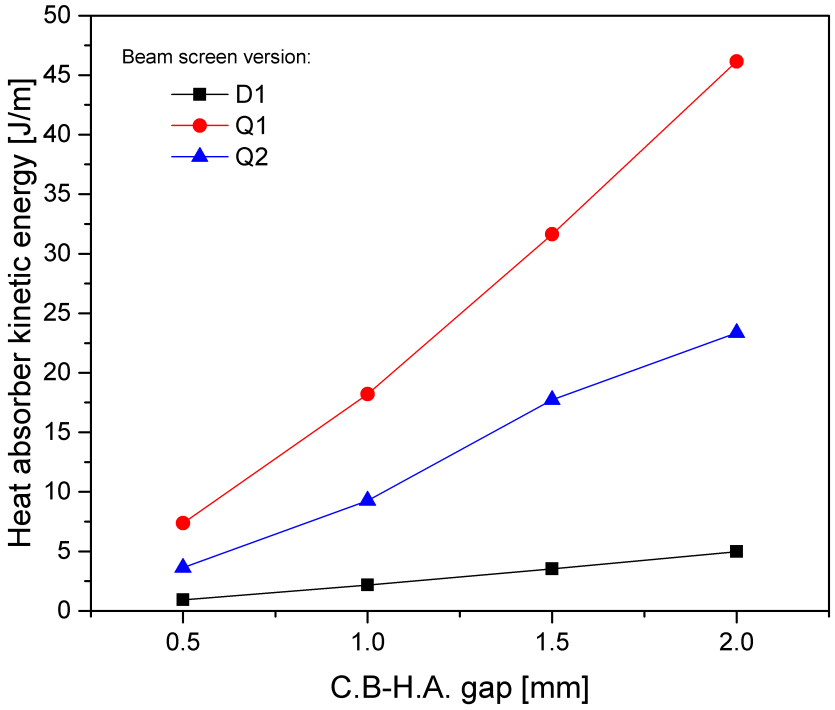


FIGURE 5.42: Kinetic energy of the heat absorber for the Q1, Q2, and D1 beam screen as a function of the gap between the cold bore and the heat absorber itself (in the x-axis C.B. and H.A. stand for cold bore and heat absorber, respectively).

where, $\frac{\Delta\epsilon_p}{2}$ is the plastic strain amplitude, ϵ_f is an empirical constant known as the fatigue ductility coefficient defined by the strain intercept at 2N =1, 2N is the number of reversals to failure (N cycles), c is an empirical constant known as the fatigue ductility exponent, commonly ranging from -0.5 to -0.7. Small c results in long fatigue life [125].

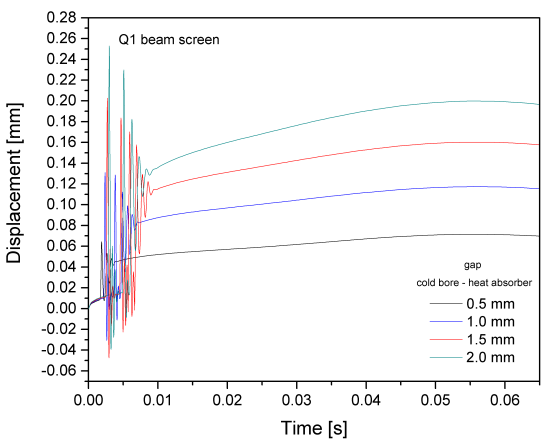
Such relation is based on low number of cycles to fracture (up to 10^5 cycles) and on plastic deformations in each cycle. The values of the strain-life equations constants for copper are reported in [126].

A fatigue process is characterised by three stages. The first one is the softening or hardening of the material according to the stress amplitude of the cyclic loading and the state of the material. The second stage is represented by the nucleation of the crack. The third stage is the propagation of the crack leading to failure. The nucleation site takes place where the cyclic-plastic deformation is the highest. The micro-crack propagates in the highly concentrated plastic deformations at the crack tip generally in the direction perpendicular to the stress axis. For the copper used in the inner layer the first stage is about 3 % of the total fatigue cycles [125].

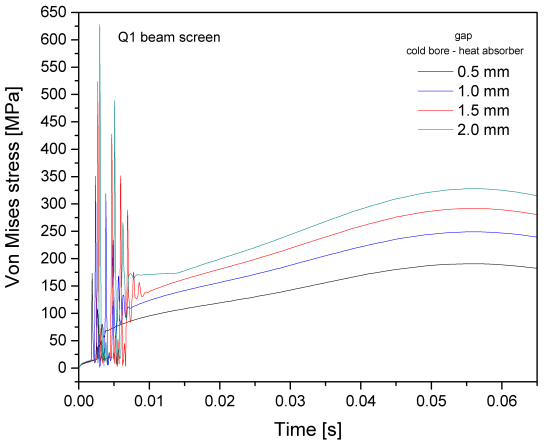
Copper becomes a fatigue hardened material when subject to cyclic loads [127]. However, this effect has not been accounted in the analysis performed to assess the fatigue life of the layer. It is assumed that the plastic deformation of copper is governed by a perfectly elasto-plastic behaviour with an elastic limit of 35 MPa. This assumption lead to more conservative results.

The most severe plastic strain amplitude are shown in Table 5.3 for the Q1, Q2, and D1 beam screen.

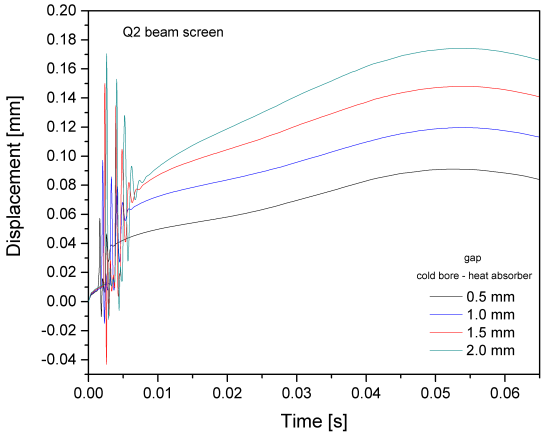
In the past multiple studies on the dependence of plastic strain amplitude upon number of cycles to failure have been performed [122, 128, 129, 130].



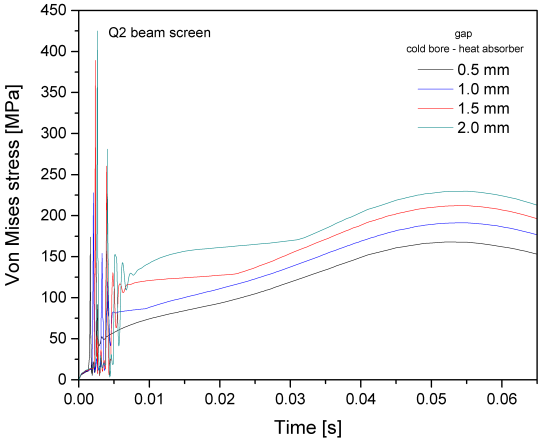
(A)



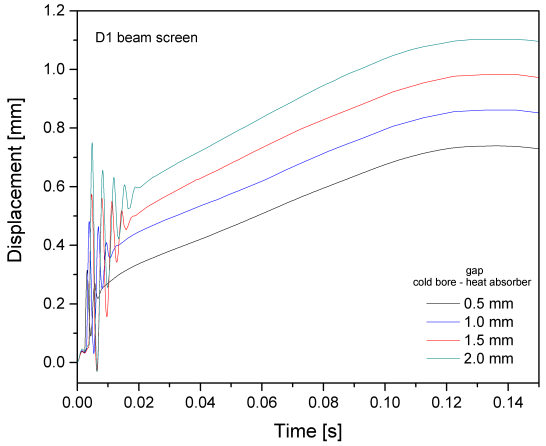
(B)



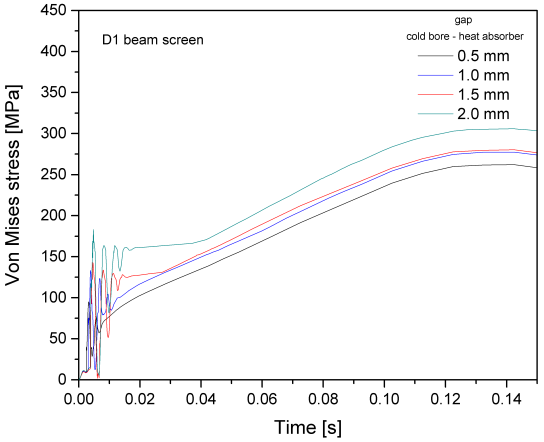
(C)



(D)



(E)



(F)

FIGURE 5.43: Maximum displacement and equivalent stress for the cold bore of the Q1, Q2, and D1 beam screen as a function of the gap between the cold bore and the heat absorber.

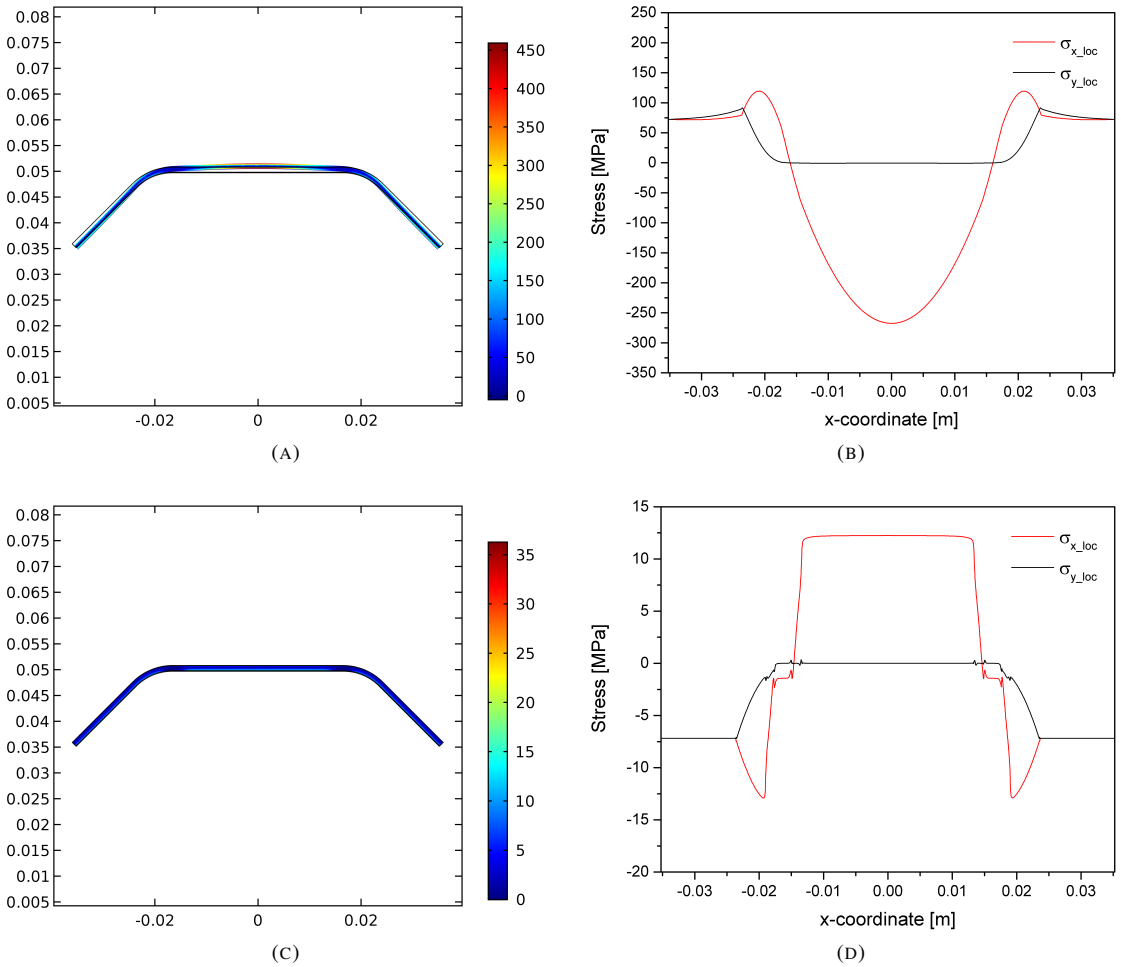


FIGURE 5.44: Local stress at the interface between the copper layer and the Q1 octagonal pipe during the quench at 55 ms (a,b) and after the quench (c,d). The x-axes of the graphs corresponds between each other.

Beam screen type	$\Delta\epsilon_p$ (%)
Q1	0.2131
Q2	0.2829
D1	0.1569

TABLE 5.3: $\Delta\epsilon_p$ of the Q1, Q2, and D1 beam screen during one quench-cycle.

Two curves related to the plastic strain amplitude of the oxigen-free high conductivity (OFHC) copper versus cycles to failure are shown in Fig. 5.47 [131]. Therefore, knowing the plastic strain amplitude it is possible to estimate the cycle number to failure which is between 5000 and 30000 cycles for all the beam screens. However, this prediction is based on tests performed in the air at room temperature, while the beam screen operates in vacuum between 50 and 80 K. In general, the cyclic stress-strain response is strongly temperature dependent from liquid helium temperature to creep temperature. Experiments have shown that the fatigue strength of S/N curves decreases when the temperature increases. However, the effects of temperature on the Coffin-Manson are not simple to determine. Sometimes the relation is temperature independent while other times the dependence is similar to the S/N curves. On a general basis, the temperature dependence for most metallic materials is related to the crack propagation. It changes from transcrystalline (slow propagation) at low temperatures to intercrystalline (fast propagation) at higher temperatures [132].

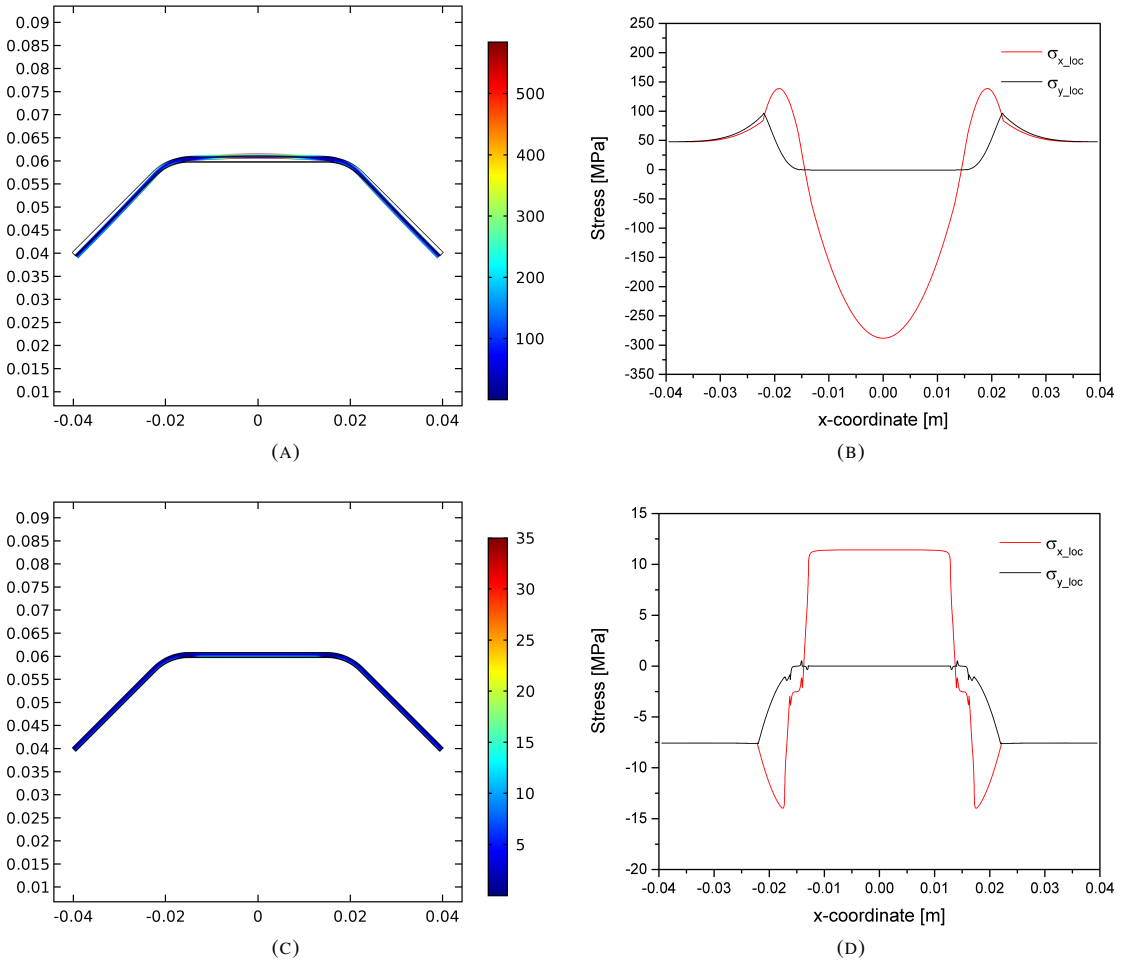


FIGURE 5.45: Local stress at the interface between the copper layer and the Q2 octagonal pipe during the quench at 55 ms (a,b) and after the quench (c,d). The x-axes of the graphs corresponds between each other.

Also vacuum affects the propagation of the crack within the material. In fact, it seems that the role of oxygen lowers the surface energy so that the crack propagates faster in air than in vacuum. In general, high vacuum can increase the low-cycle fatigue life by one order of magnitude [133].

5.6.7 Thermal link

The thermal link has been studied by means of the 3D version of the multiphysics model. As seen in chapter 2 and in chapter 4 the design of the thermal link is the outcome of a trade-off between its mechanical integrity during a quench, the efficient thermal transfer, and the manufacturing feasibility of the link itself. Only a quarter of the assembly has been considered to assess the response of the link subject to a quench. Periodic conditions have been assigned to avoid any border effects. By doing so, the current flow within the thermal link is not perturbed by any potential closure of the current loops of the heat absorber through the link. Moreover, this simplification is also beneficial to lower the computational cost of the simulation.

Different shapes and configurations of the thermal link have been simulated. However, the study of the component is presented only in its final shape. The thermal links adopted for the Q1 and Q2 beam screen, being connected to the cooling tubes at $45°$ are placed below the magnet poles. Therefore, each link can be seen as subject to a dipole magnetic field. As the Lorentz forces are mutually perpendicular to the current and the magnetic

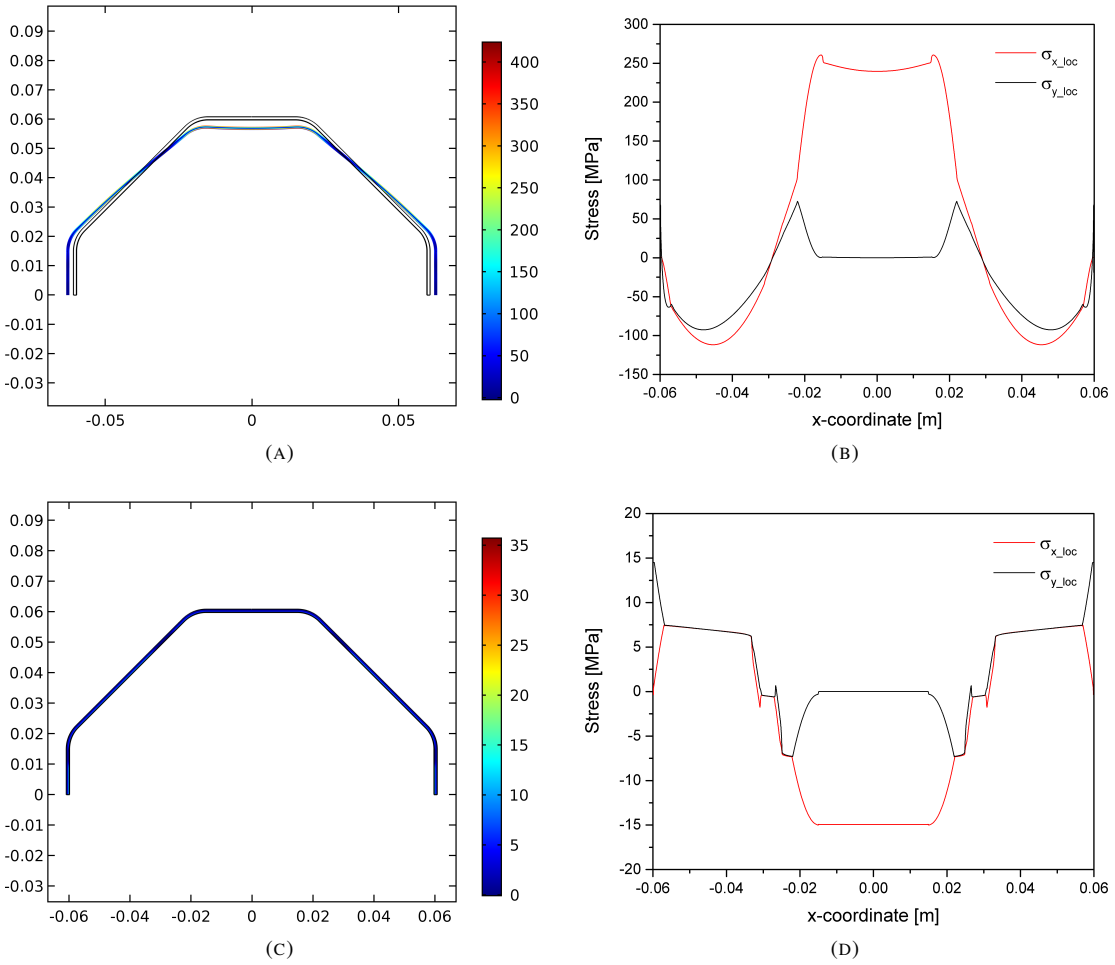


FIGURE 5.46: Local stress at the interface between the copper layer and the D1 octagonal pipe during the quench at 152 ms (a,b) and after the quench (c,d). The x-axes of the graphs corresponds between each other.

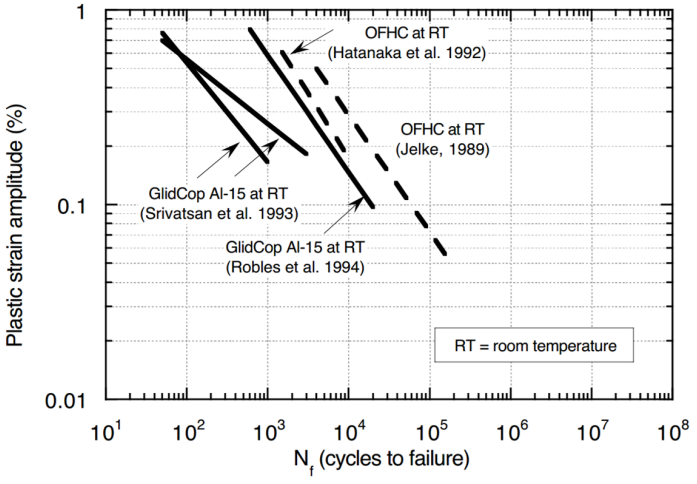


FIGURE 5.47: Plastic strain amplitude versus cycles to failure of OFHC copper at room temperature. Image taken from [131].

field, from the trajectories of the current it is possible to establish the direction of the forces. It turns out that the forces act mostly along the beam axis but in opposite direction in a way to stretch the thermal link. Hereafter, these forces are referred to as the longitudinal forces acting on the thermal link.

By way of example, the direction of the currents, forces and magnetic field in a thermal link is depicted in Fig. 5.48.

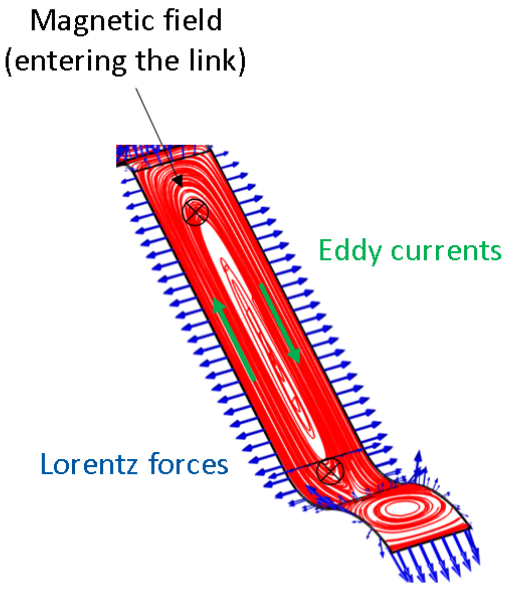


FIGURE 5.48: Currents, forces and magnetic field in a generic thermal link.

For symmetry reasons each thermal link around the Q1-Q2 beam screen behaves in the same way. In fact, as shown in Fig. 5.49 for the Q1 and in Fig. 5.50 for the Q2 beam screen, the magnetic field seen by each thermal link is the same. Conceptually, the forces of the D1 thermal link are induced in the same way as in the Q1-Q2 ones. However, the magnitude of such forces is not the same for all the links. In fact, as shown in Fig. 5.51, the magnetic flux seen by two consecutive links is different resulting in a dissimilar mechanical response.

Fig. 5.52 shows the comparison of the longitudinal forces induced in a quarter of thermal link of the Q1, Q2, and D1 version of the beam screen. These results refer to a thermal link made of copper RRR 100 whose electrical conductivity is $1.5 \cdot 10^9$ S m^{-1} (at 50 K). The forces are integrated over a quarter of the link as otherwise they will be zero (equal and opposite for the two sides). For all the links the width is 5 mm and the thickness is 1 mm. The highest integrated forces are 52.8 N for the Q2 links and 40.5 N for the Q1 links, both induced at around 55 ms. The forces induced in the D1 thermal link are reported for the link at the top and on the side. For the links at the top (and at the bottom) of the beam screen, the highest forces are 13.64 N while on the two sides these are 6.85 N, induced at 145 ms. Therefore, it turns out that most of the forces are induced in the Q2 version of the thermal link. In fact, even if the magnetic field decay is the same as for the Q1, the larger aperture of the Q2 beam screen implies that the thermal links are positioned further from the origin. In general, for both D1 links the forces are lower than the Q1-Q2 ones mainly because the decay of the dipolar magnetic field is smoother than the quadrupolar one.

Fig. 5.53 shows the forces integrated along the beam axis direction and induced in three Q2 thermal links 1 mm thick, whose widths are 3, 5, and 10 mm. The maximum force integrated in one link is 175 N for the 10 mm

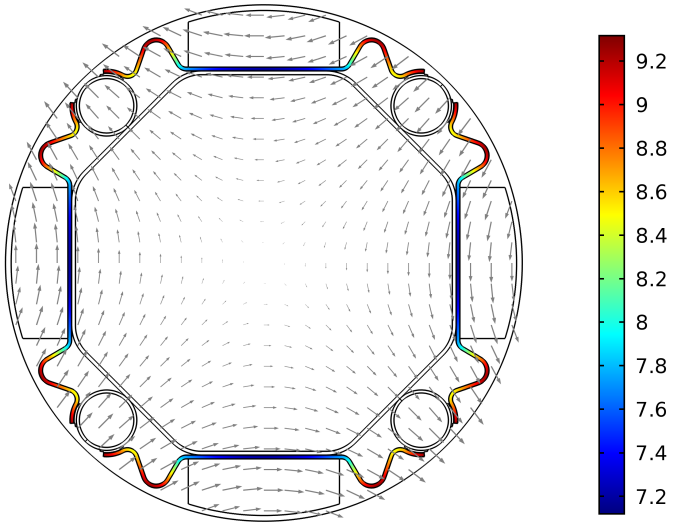


FIGURE 5.49: Distribution and norm of the magnetic field [T] for the Q1 beam screen.

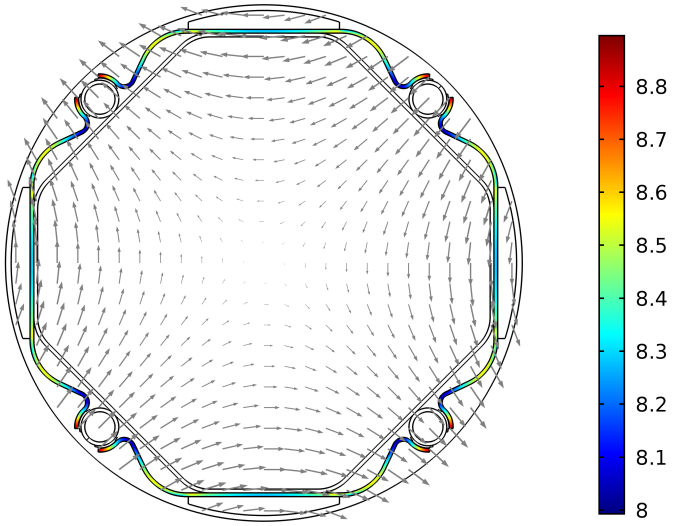


FIGURE 5.50: Distribution and norm of the magnetic field [T] for the Q2 beam screen.

width, 52.8 N for 5 mm width, and 22.4 N for 3 mm width. From these data it is possible to outline the second power dependence of the induced forces with the width, according to eq. 5.42.

To this purpose, the ratios between the maximum magnitude force induced in different thermal links are compared in Table 5.4 according to the analytical and numerical approach. The ratio of the forces related to the analytical expression is represented by the squared ratio of the widths. The numerical one is obtained by the ratio of the longitudinal forces integrated in a quarter of the link.

A big discrepancy emerges with the analytical approach if the forces are integrated over a quarter of the link. This is due to the typical loop of the eddy currents which are considered only in the numerical model but not in the analytical one. As seen in Fig. 5.54a, the direction of the forces changes according to the current path. In particular, the spatial rate of this change is larger for links of short width rather than large ones. This effect is

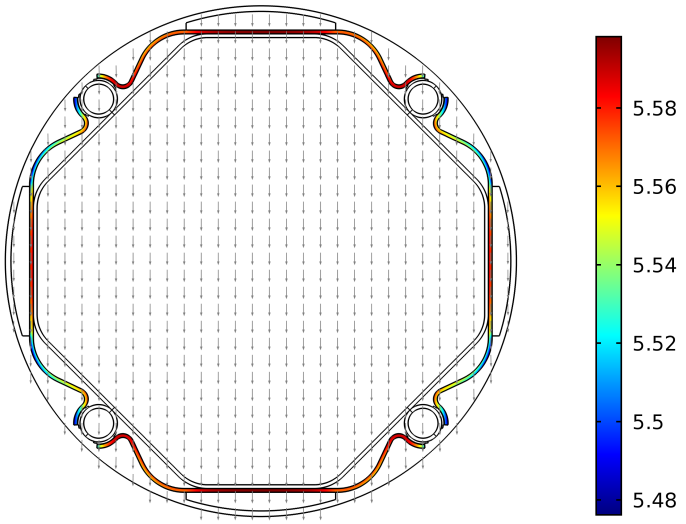


FIGURE 5.51: Distribution and norm of the magnetic field [T] for the D1 beam screen.

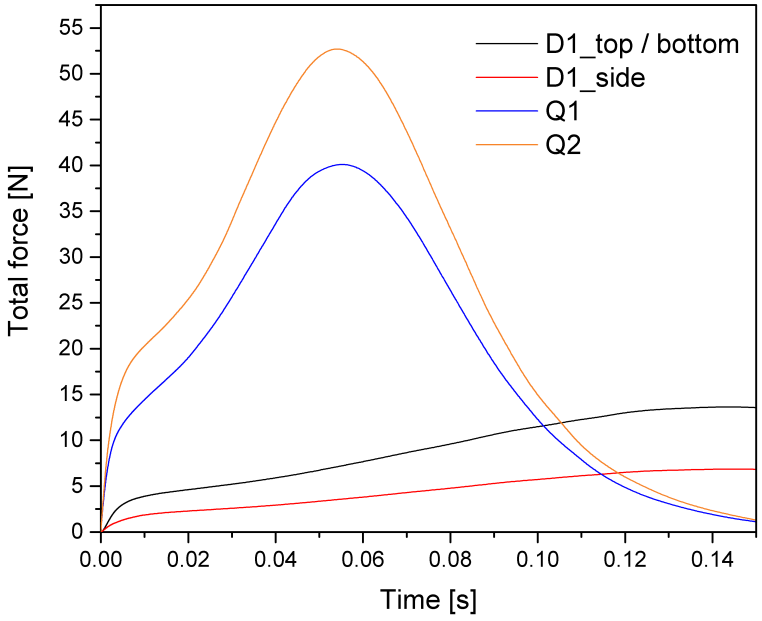


FIGURE 5.52: Profile of the total forces induced in the Q1, Q2, and D1 thermal links.

Ratio	Analytic	FEM (full link)	difference	FEM (partial link)	difference
3/5	0.36	0.42	17.6 %	0.368	2.3 %
3/10	0.09	0.13	42 %	0.099	11%
5/10	0.25	0.30	20.8 %	0.271	8.5 %

TABLE 5.4: Comparison of the forces induced in Q2 thermal link between the dipole-related analytical expression and the forces integrated over a quarter of the link and a portion of it. The comparison is between the ratio of thermal links of different widths.

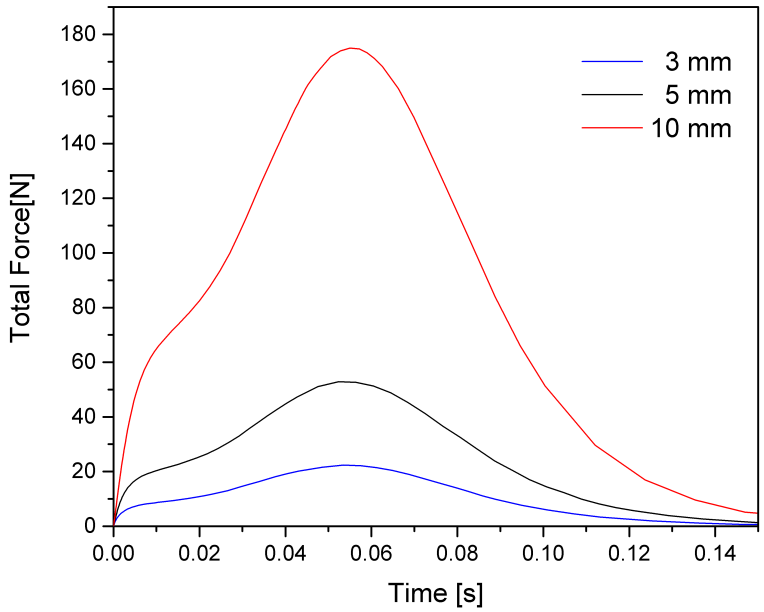
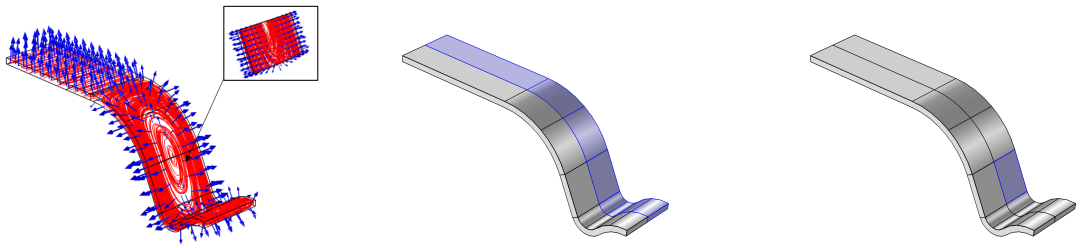


FIGURE 5.53: Profile of the total forces induced in the Q2 thermal links of width 3, 5, and 10 mm.



(A) (B) (C)

FIGURE 5.54: Current path and forces distribution in (a). Regions where the forces are integrated: over a quarter of the thermal link (b) or in a small portion to limit border effects (c).

captured by the numerical ratio resulting in a difference up to 42 % with the analytical one for the most severe comparison (3/10 mm).

An excellent agreement is found if the forces are integrated in a small portion of the thermal link to avoid border effects as shown in Fig. 5.54c rather than as in Fig. 5.54b. In fact, the small portion of the link, magnified in Fig. 5.54a, contains only a straight current flow. Therefore, the direction of the forces is mainly perpendicular to it and the closure of the currents does not take place. This condition makes the comparison with the analytical ratio more consistent.

Considering that the heat transfer depends on the cross section of the link this analysis gives an important hint for the thermal link design. In fact, for equal cross sections, it is more convenient to reduce the width rather than the thickness to lower the induced forces. The effects of the temperature increase on the induced forces is shown in Fig. 5.55. It is worth noting that for widths of 3 mm and 5 mm the temperature has no influence on the induced forces, while at 10 mm the forces are reduced of almost 10 %. This makes sense because the resistive losses depend on the magnitude of the induced currents, which are the largest for the 10 mm link.

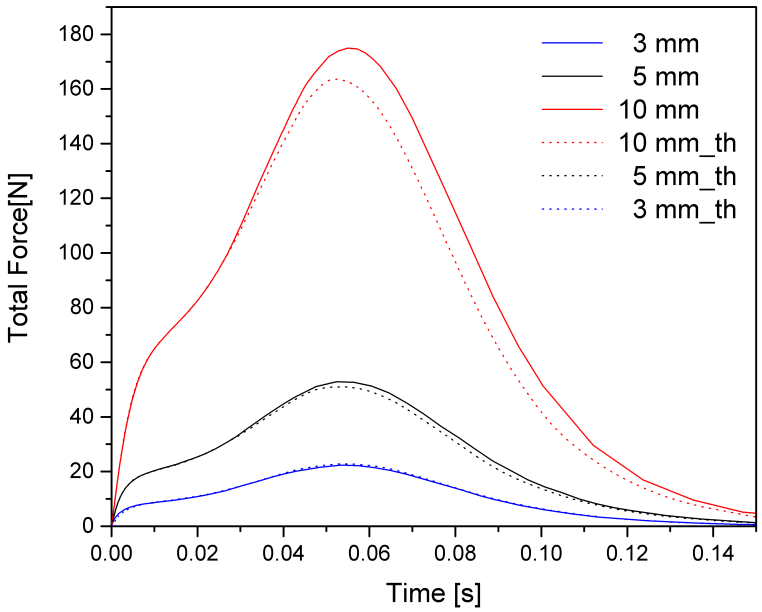


FIGURE 5.55: Profile of the total forces induced in the Q2 thermal links of width 3, 5, and 10 mm with and without the effects of the temperature increase.

Amongst the different types of thermal links, the highest forces are induced in the Q2 link. Therefore, the mechanical integrity is assessed only for such a link.

Only one layer, 0.1 mm thick, of the multi-layer link is examined in the analysis. In fact, the mesh of the whole link would have been troublesome because of the thin gaps between one layer and the other. Moreover, it would have not added any additional information as the forces induced in all the layers are equal. For this analysis the thermal module has not been considered because, as seen in Fig. 5.55, the temperature rise in the link is not sufficient to cause a considerable variation of the electrical resistivity and, in turn, of the forces. A constant and uniform temperature of 50 K is considered. A further simplification is obtained by running a static mechanical simulation rather than considering the mechanical dynamics during the quench decay. To this purpose, the largest field of forces during the quench is exported in a separate stationary study. A fixed constraint condition has been used for the portion of the link brazed to the heat absorber as well as to the extremities. These boundary conditions are shown in orange in Fig. 5.56. The mesh used for this analysis is composed of second order tetrahedral elements. As shown in Fig.5.57 two elements per thickness are used. The material model used for the copper is linear-elastic.

The equivalent von Mises stress is shown in Figs. 5.58a, 5.58b and 5.58c for the link of 3, 5, and 10 mm of width. The legend goes up to 35 MPa, to highlight the regions exceeding the elastic limit of copper.

It turns out that the stress in the link 3 mm wide is always below the elastic limit of copper. For the 5 mm wide link the elastic limit is exceeded locally along the bottom curvature reaching up to 60 MPa. This leads to a plastic deformation equal to 14 % of the representative portion outlined in Fig. 5.54c. For the 10 mm wide link an equivalent stress higher than 180 MPa is reached in the central part of the link, leading to a plastic deformation equal to 55 % of the representative portion outlined in Fig. 5.54a. However, this stress is not related only to the longitudinal forces but also to the bending caused by the forces perpendicular to the thermal link surface, see Fig. 5.59. In fact, if the thermal link is cut along the xy-planes one can observe the classical bending stress profile, see Fig. 5.59.

In conclusion, the thermal link that withstands the effects of a magnet quench with no plastic deformation is the one 3 mm wide. This represents the safest choice in the design of the beam screen.

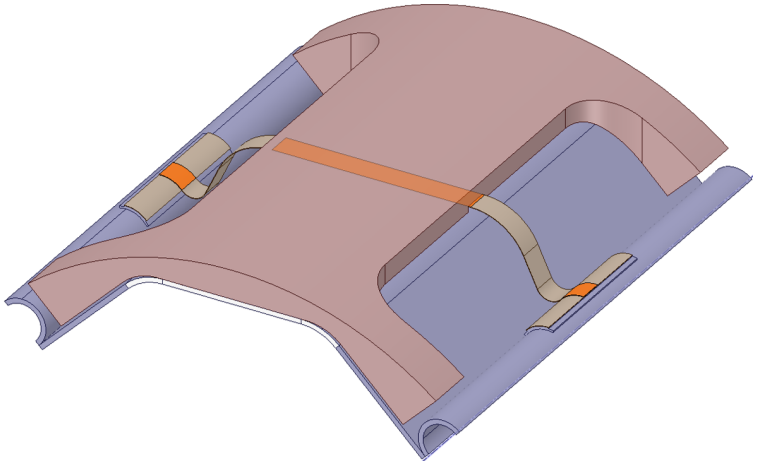


FIGURE 5.56: Fixed constraints (in orange) used in the mechanical analysis of the thermal link.

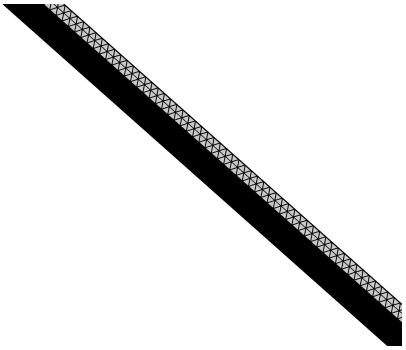


FIGURE 5.57: Domain discretisation of the thermal link along its thickness.

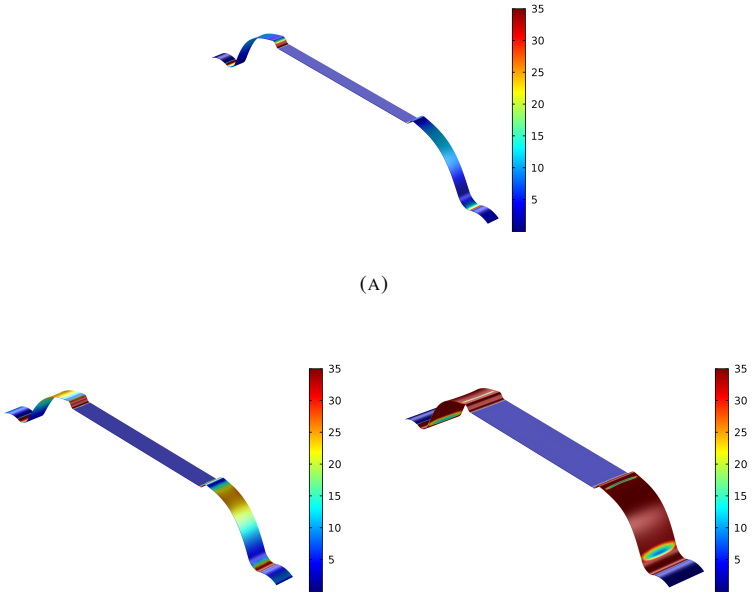


FIGURE 5.58: Von Mises stress for a thermal link of a width of 3 mm (a), 5 mm (b), and 10 mm (c).

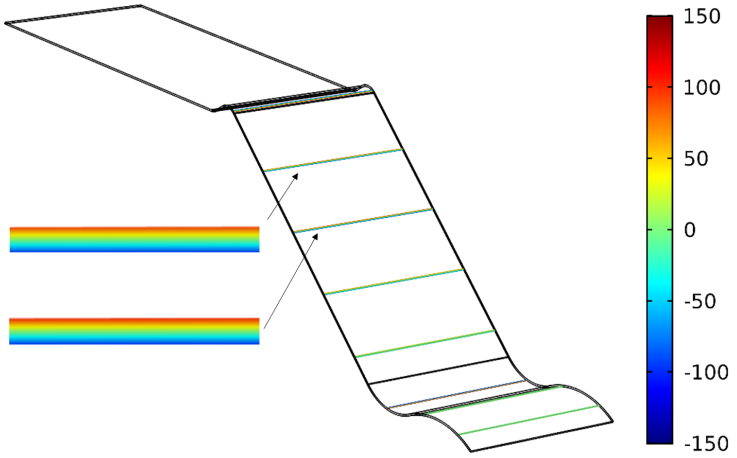


FIGURE 5.59: Axial stress in the thermal link cross section. It is worth noting the classical butterfly profile due to the bending.

Component	Q1			Q2			D1		
	$F_{r\ max}$ [N/mm]	σ_{max} [MPa]	δ_{max} [mm]	$F_{r\ max}$ [N/mm]	σ_{max} [MPa]	δ_{max} [mm]	$F_{r\ max}$ [N/mm]	σ_{max} [MPa]	δ_{max} [mm]
Cold bore st. st. 316 LN $\sigma_y = 860MPa$ (4 K)	59	524	0.2	61	390	0.15	15.3	280	0.98
Heat absorber Tungsten alloy $\sigma_y = 1284MPa$ (77 K)	233	61	1.7	108	138	1.65	18	280	2.47
Octagonal pipe st. st. P506 $\sigma_y = 1350MPa$ (50 K)	4.7	470	0.7	9	549	0.68	2.8	424	2.47
Inner layer Copper 0FE $\sigma_y = 35MPa$ (50 K)	37	35[a]	0.69	59	35[a]	0.68	24	35 [a]	2.47

TABLE 5.5: Comparison of the highest force, stress, displacement induced in each component of the Q1,Q2, and D1 beam screen subject to the relative magnetic field decay.

[a] limited by the elastic–perfectly plastic model.

5.6.8 Summary of the mechanical response

The multiphysics model presented in this chapter has allowed to get an insight on the magneto-thermo-mechanical behaviour of the beam screen during a magnet quench, whose protection system is based on quench heaters only.

In Table 5.5 a comparison between the Q1, Q2, and D1 beam screen is given by reporting the mechanical quantities of main interest, namely the highest radial force $F_{r\ max}$, the most severe stress σ_{max} and maximum deformation δ_{max} induced during the quench.

The mechanical integrity of the beam screens is demonstrated by simulation. Moreover, the highest displacement of the cold bore is within the safety margins (1.5 mm) to avoid the contact with the delicate magnet coils.

5.7 Conclusions

The modelling work performed on the beam screen so far is not sufficient to characterise the mechanical response of the HL-LHC beam screen during a magnet quench. Previous models are based on analytical formulations that do not take into account the reciprocal influence of the domains, two dimensional solving schemes, quasi-static mechanical analysis. Moreover, these present a limited exploitation of physics couplings. These limitations are too critical to be neglected in the design of the new beam screen. Therefore, a new fully coupled multiphysics model has been developed to assess the effects of a magnet quench on the HL-LHC beam screen.

The model is based on a reduced field formulation and, therefore, it works only when the magnetic field can be described according to the magnet vector potential. This is the case when the quench heaters only are used to protect the superconducting magnets. The final configuration of the model was obtained by setting up a two-way coupling between the magnetic and thermal module and a one-way coupling between the magnetic and mechanical module. This represents an effective compromise in terms of computational cost and significance of the results.

The application of the model has revealed three main unexpected phenomena. First, given that the model accounts for the reciprocal influence of multiple physics, self-inductance effects have been quantified in relation to an annulus geometry and as a function of the electrical conductivity. For values of electrical conductivity higher than 10^7 it was found that self-inductance effects are significant. In particular, the dependence of the induced forces on the electrical conductivity is not linear anymore. Second, as the heat absorbers are not welded on the octagonal pipe, an oscillatory behaviour of the cold bore and the heat absorber itself takes place in the first 20 ms of the quench. This is likely due to the excitation of the system natural modes. Third, the maximum displacement of the cold bore takes place in the first 20 ms rather than at 55 ms, *i.e.* when the highest Lorentz forces are induced in the beam screen materials.

The proposed model has demonstrated the mechanical integrity of the beam screen design in the event of a quench when the magnets are protected by quench heaters.

Chapter 6

Beam screen behaviour during a magnet quench with quench heaters and CLIQ

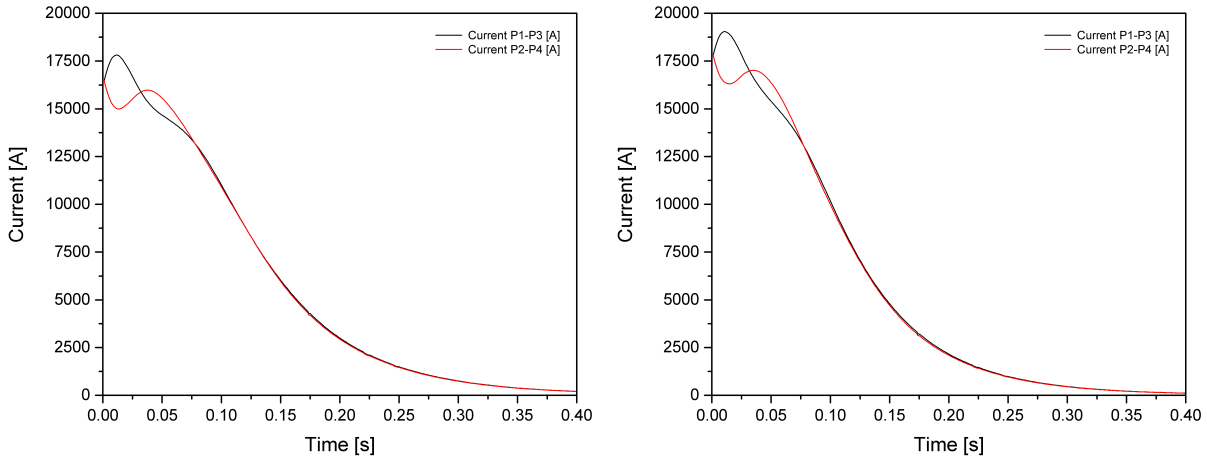
6.1 CLIQ

The Coupling-Loss-Induced Quench (CLIQ) protection scheme is a new system under development at CERN to protect high energy density superconducting quadrupole magnets [12] [134] [135]. In comparison with the quench heater technology, the CLIQ is expected to initiate faster and more homogeneous transitions to the resistive state of the magnet. When a sudden transition to the normal state of a superconducting coil occurs, fast bank capacitors are switched-in, introducing rapid time-oscillating currents. Therefore, coupling losses are induced uniformly in the inter-filaments of the coil so that the stored energy of the magnet can be released over a larger volume and not locally. At present, CLIQ has been optimised for the quadrupole magnet of the inner triplet area. The quench protection scheme based on CLIQ together with the outer quench heaters is a first candidate for the HL-LHC inner triplet magnets upgrade. The current discharge of this configuration is shown in Fig. 6.1 for nominal and ultimate conditions. It is noteworthy that the time derivative of the oscillating currents in the poles 1 and 3 is different from the one of the poles 2 and 4 during the first 100 ms from the quench initiation. The effects of the related magnetic field variations on the beam screen are treated in this chapter.

6.2 Model definition

The reduced vector magnetic potential (RVMP) formulation cannot be used to predict the behaviour of the Q1 and Q2 beam screen in case of the CLIQ discharge as the assumption of a monotonic magnetic field decay, on which the formulation is based, is not respected. In fact, as shown in Fig. 6.1, the current discharge of two consecutive poles is not the same for the first 100 ms of the quench. This calls for an independent control of each magnet coil.

An equivalent geometrical configuration to approximate the quadrupole magnetic field decay around the beam screen during the CLIQ discharge is shown in Fig. 6.2. Four permanent magnets tilted at $+/- 45^{\circ}$ angle are inserted into an iron cylinder whose purpose is to contain the field in accordance to its magnetic permeability. The internal part of the pole is hyperbolically shaped to better approximate the quadrupole field [136].



(A) (B)

FIGURE 6.1: Nominal (a) and ultimate (b) current discharge for the poles 1 - 3 and 2 - 4 upon the activation of CLIQ.

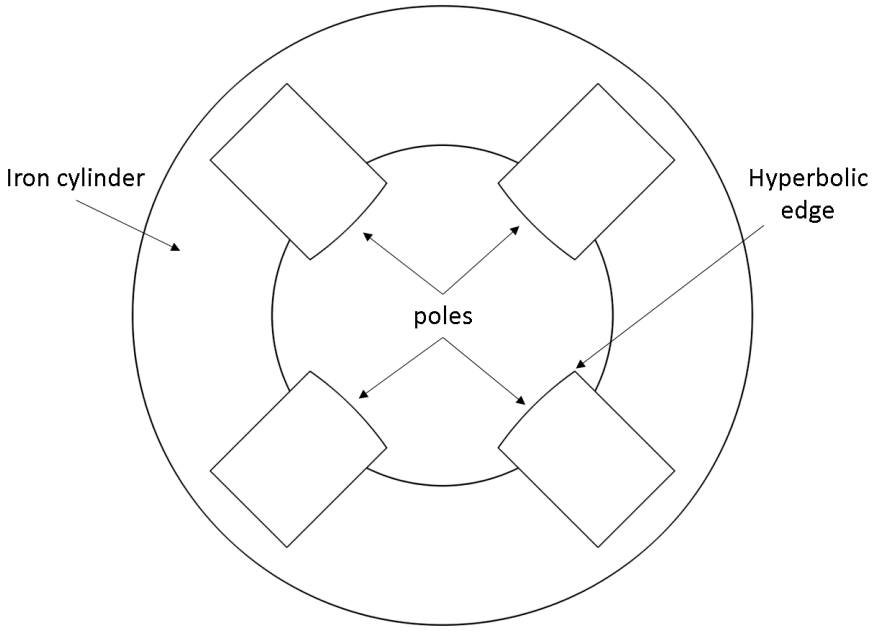


FIGURE 6.2: Geometrical structure of the model representing the quadrupole magnet.

The magnetic field generated by this configuration has been developed in COMSOL and gives a good approximation of the quadrupole field. The main advantage of this technique is that each magnet can be controlled independently. Moreover, the computational load of the multiphysics algorithm is only slightly increased as the complex definition of the magnet coils is still not modelled, which turns into a considerable gain of computational time.

The Maxwell's equations result in a set of governing laws for each region of the geometrical configuration shown in Fig. 6.3a. These are the conducting region of the beam screen Ω_c, the non-conducting region surrounding the beam screen Ω_n, the magnet region Ω_m, and the iron region Ω_i.

Defining μ as the magnetic permeability, σ the electrical resistivity, t the time, $\mathbf{A}$ the magnetic vector potential, and $\mathbf{M}$ the magnetisation vector, the equation of the conducting region Ω_c and of the iron region Ω_i reads to:

$$\nabla \times (\mu^{-1} \nabla \times \mathbf{A}) = -\sigma \frac{\partial(\mathbf{A})}{\partial t} \tag{6.1}$$

the equation of the non-conducting region Ω_n:

$$\nabla \times (\mu^{-1} \nabla \times \mathbf{A}) = 0 \tag{6.2}$$

the equation of the magnet region Ω_m:

$$\nabla \times \mu^{-1} \nabla \times \mathbf{A} - \mathbf{M} = -\sigma \frac{\partial(\mathbf{A})}{\partial t} \tag{6.3}$$

Each pole (P1, P2, P3, P4 in Fig. 6.3a) is magnetised through the magnetisation vector $\mathbf{M}$ [$\mathrm{A\,m^{-1}}$], which is defined for P1 as:

$$\mathbf{M}_{P1}(t) = k \begin{bmatrix} 0 \\ -I_{P1,3}(t) \\ -I_{P1,3}(t) \end{bmatrix} \tag{6.4}$$

for P2 as:

$$\mathbf{M}_{P2}(t) = k \begin{bmatrix} 0 \\ -I_{P2,4}(t) \\ I_{P2,4}(t) \end{bmatrix} \tag{6.5}$$

for P3 as:

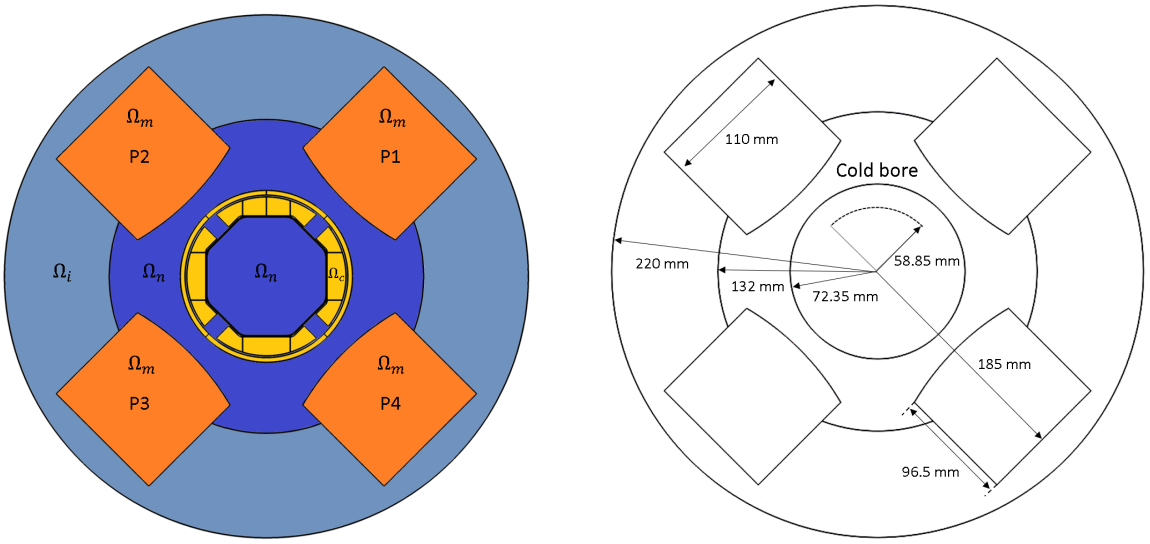
$$\mathbf{M}_{P3}(t) = k \begin{bmatrix} 0 \\ I_{P1,3}(t) \\ I_{P1,3}(t) \end{bmatrix} \tag{6.6}$$

and for P4 as:

$$\mathbf{M}_{P4}(t) = k \begin{bmatrix} 0 \\ I_{P2,4}(t) \\ -I_{P2,4}(t) \end{bmatrix} \tag{6.7}$$

where $I_{P1,3}$ and $I_{P2,4}$ are the CLIQ current discharge in the poles 1 - 3, and in the poles 2 - 4, respectively, while k is a fictitious parameter to calibrate the magnetic field with the one predicted by ROXIE.

ROXIE is a software developed internally at CERN for the electromagnetic simulation and optimization of accelerator magnets. All the superconducting magnets of the LHC except D1 and D2 have been designed using ROXIE [137].



(A) (B)

FIGURE 6.3: In (a) main regions of the equivalent quadrupole magnet. In (b) dimensions of the equivalent structure.

The calibration has been performed through a parametric study by varying the magnetic permeability of the iron cylinder, μ, the dimensions of the poles generating the field, the distance of the hyperbolic edge from the origin, and the proportionality factor of the current discharge input, k .

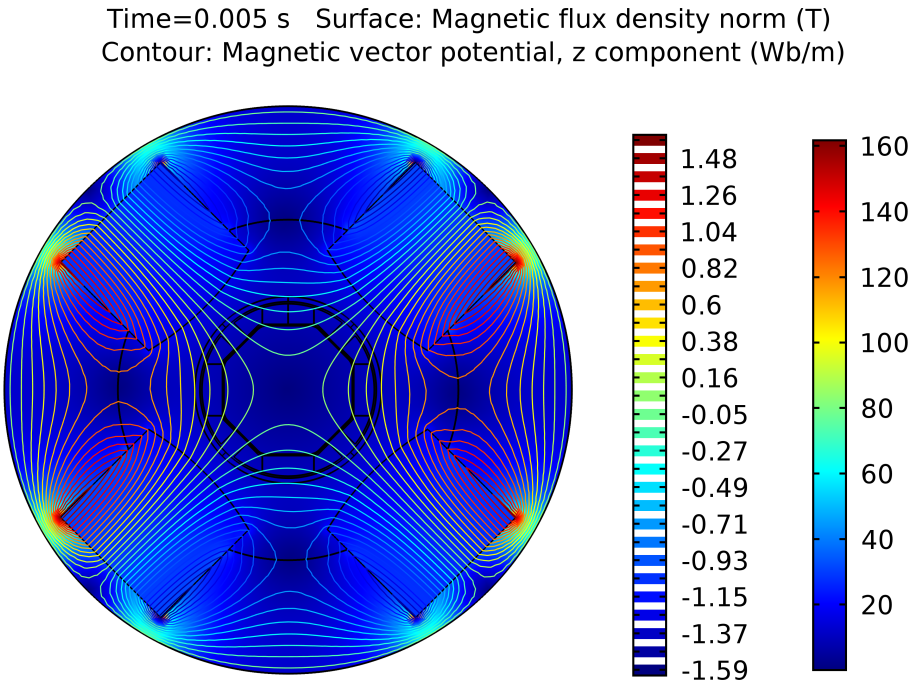
The model has been calibrated by means of a magnetic field cartography derived by ROXIE, see Fig.6.4. The x- and y-component of the **B** field and the $\mathbf{B}\dot{\mathbf{B}}$ factor have been compared in 26 points. Such points are uniformly distributed around a sector of circumference of radius 58.85 mm, ranging from $45°$ to $135°$, see Fig. 6.3b. The time chosen for the comparison corresponds to the highest $I\dot{I}$ factor and, therefore, to the highest forces induced in a conductive component, namely 2 ms after the current discharge.

The x- and y-component of the **B** field and the $\mathbf{B}\dot{\mathbf{B}}$ factor derived from the 26 points of COMSOL and ROXIE have been compared in Fig. 6.5a and in Fig. 6.5b, respectively.

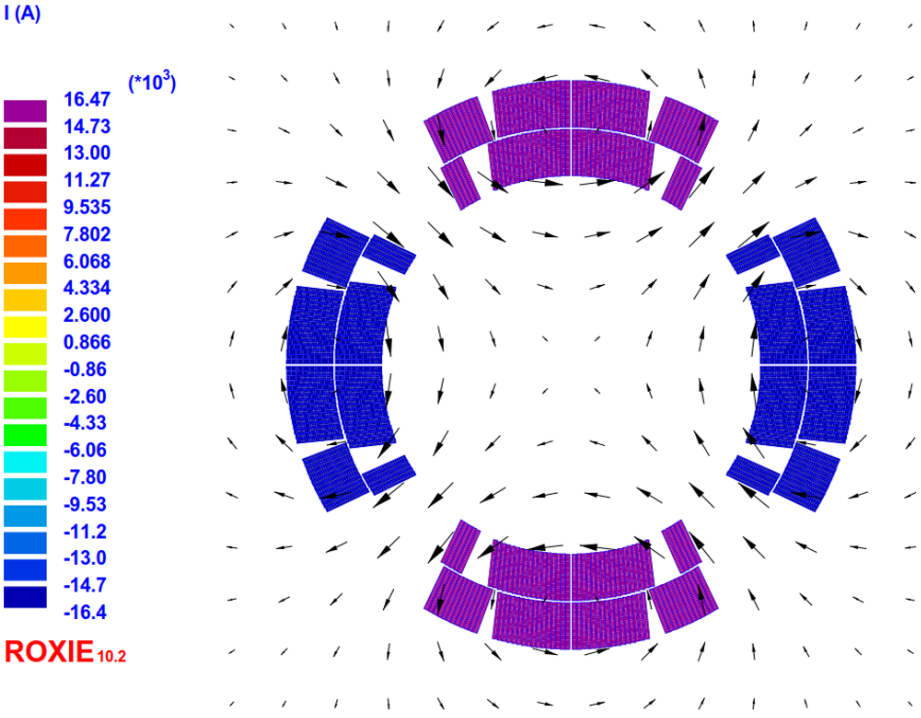
The percentage difference of B_x and B_y between COMSOL and ROXIE is -6.8 % and 4.5 %, respectively.

Another figure of merit to assess the approximation of the COMSOL model can be the $\mathbf{B}\dot{\mathbf{B}}$ factor. This is more important than **B** as the induced forces are ultimately proportional to such a factor. The analytical expression of the forces induced in a quadrupolar field (see section 5.4.6) is not valid because G is not uniform during the first phase of the CLIQ discharge, however, the expression derived from the dipole can be applied locally as a good indicator of the force intensity. The percentage difference of $B_x\dot{B}_x$ and $B_y\dot{B}_y$ between ROXIE and COMSOL has been found for all the 26 points as well as the average over such points. It turns out that COMSOL predicts slightly higher forces than ROXIE. In particular, 1.47 % more for the x-component and 4.05 % more for the y-component of the forces.

To obtain this approximation the magnetic permeability of the iron cylinder μ has been set to 5000 and the proportionality factor k to 955. The dimensions of the equivalent configuration are shown in Fig. 6.3b.

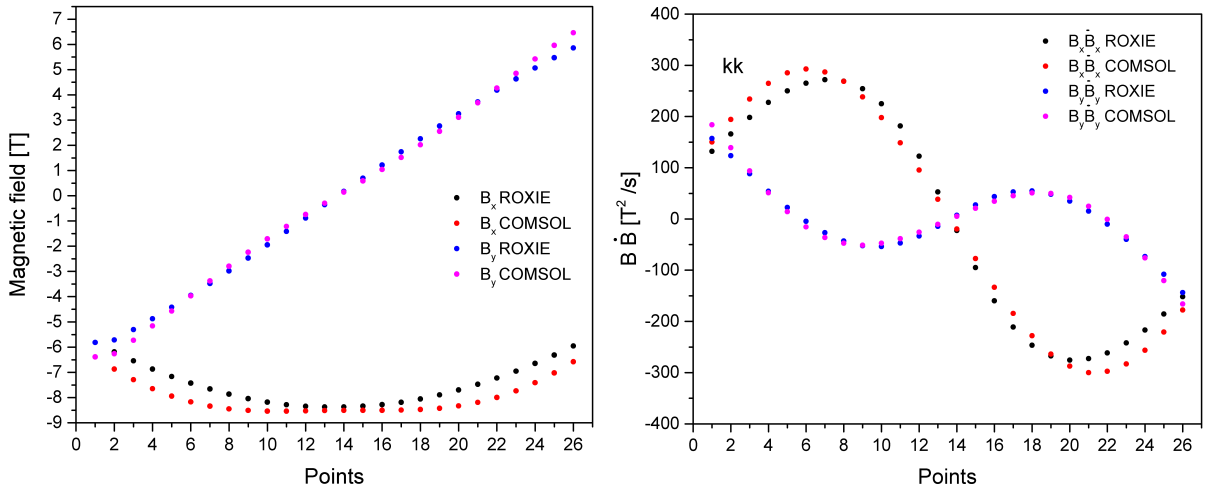


(A)



(B)

FIGURE 6.4: In (a) magnetic field lines generated by the equivalent COMSOL model. In (b) real coil structure generating the magnetic field in ROXIE, taken as reference.



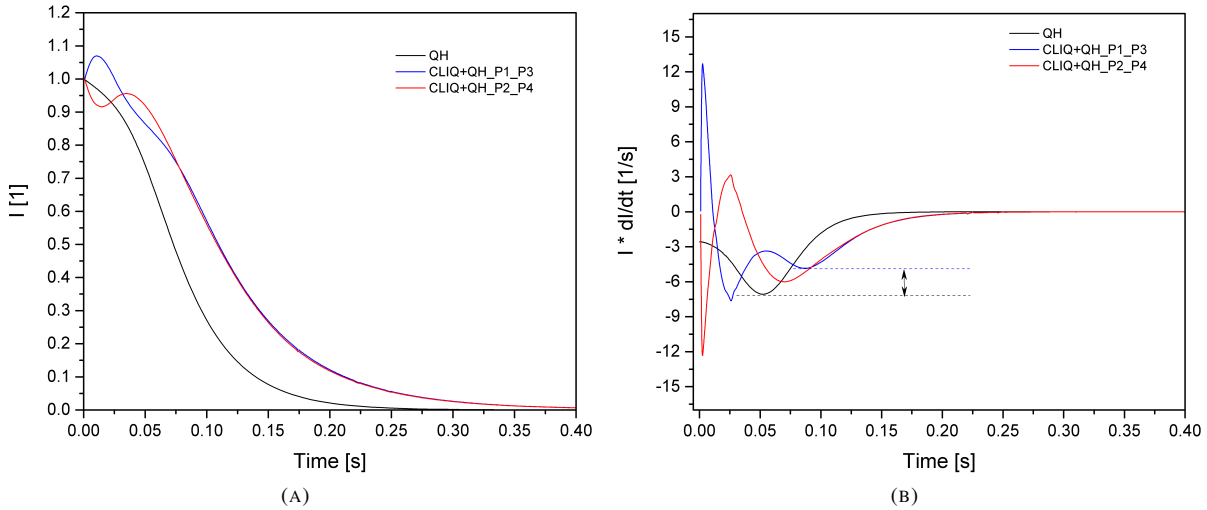
(A) (B)

FIGURE 6.5: In (a) comparison of **B** monitored on the 26 points between COMSOL and ROXIE. In (b) comparison of the $B\dot{B}$ factor monitored on the same points between COMSOL and ROXIE.

6.3 Preliminary considerations

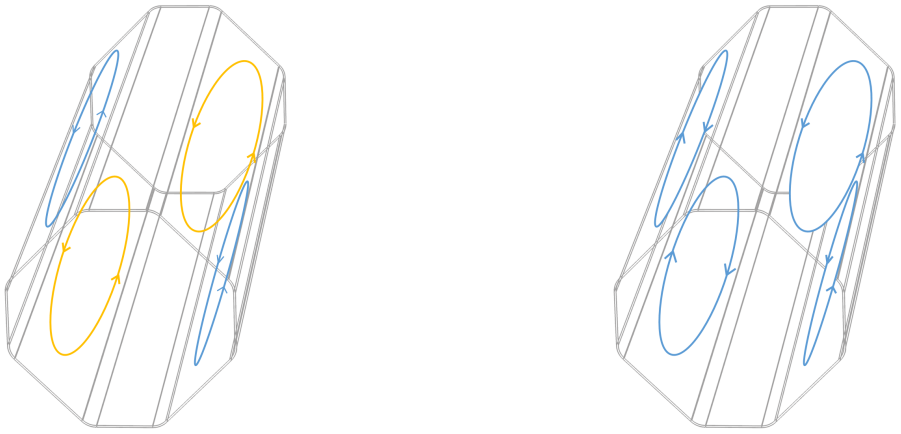
Fig. 6.6a shows the normalised profile of the magnet current discharge and of the relative $\mathbf{I\dot{I}}$ evolution in case of two different magnet protection schemes: the one based on the quench heaters and the one based on the quench heaters together with the CLIQ device. The former case has been treated in chapter 5 while the latter configuration is described in this chapter.

Under the assumption of proportionality between the discharge of the magnet current **I** and the magnet gradient G, some preliminary observations can be drawn from the comparison of $\mathbf{I\dot{I}}$ of the two quench protection schemes.



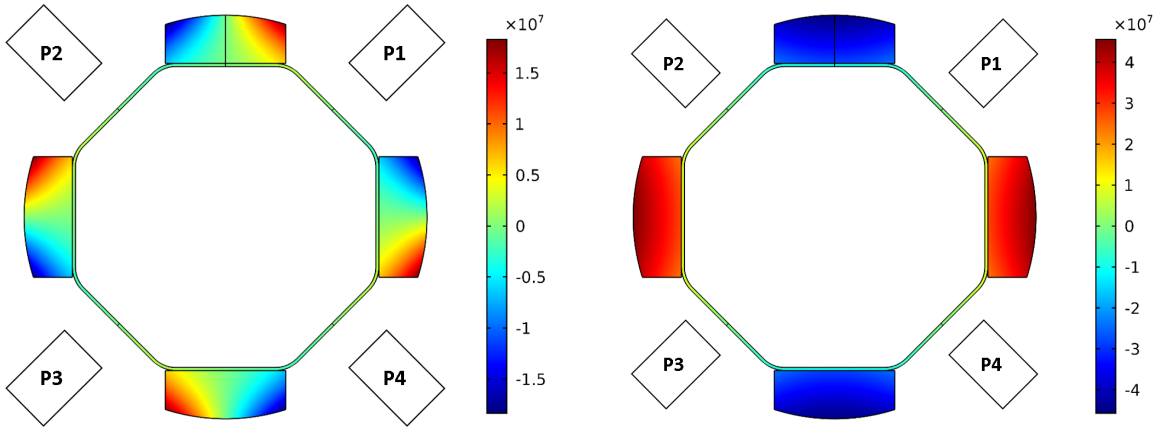
(A) (B)

FIGURE 6.6: In (a) the normalised profile of the magnet current discharge in case of CLIQ along with the quench heaters and in case of quench heaters only as a protection scheme. In (b) the $I\dot{I}$ factor for the current discharge of the two protection schemes.



(A) (B)

FIGURE 6.7: In (a) current loops in the octagonal pipe induced during the first phase of the CLIQ discharge. The adjacent flows of the (yellow and blue path) have opposite direction. In (b) the current loops induced in case of the quench heaters. The adjacent flows have the same direction.



(A) (B)

FIGURE 6.8: In (a) current density distribution induced at 5 ms in the beam screen inserted in a magnet equipped with CLIQ. In (b) current density distribution induced during a monotonic magnetic field decay.

Due to the initial increase of current injected in pole 1 and 3 and to the concurrent decrease of current in pole 2 and 4, the relative $\mathbf{I}\dot{\mathbf{I}}$ factor has opposite sign for two consecutive poles in the first 10 ms of the CLIQ discharge. Therefore, the eddy currents induced by two consecutive poles will flow in opposite direction as they depend on $\dot{\mathbf{I}}$.

For sake of simplicity, the eddy current paths corresponding to the highest and opposite $\mathbf{I}\dot{\mathbf{I}}$ peaks are depicted in Fig. 6.7a to highlight the orientation of the flows induced in the quadrants facing each pole. The current flow in case of an monotonic magnetic field decay (quench heaters and late phase of CLIQ) is shown in Fig. 6.7b instead.

Similarly, the current density is illustrated in Fig. 6.8 in the cross section of the Q1 beam screen when the $\mathbf{I}\dot{\mathbf{I}}$ factor has opposite sign in two consecutive poles and when it has the same sign, respectively. From here, it is also clear that one quarter of the beam screen is the smallest periodic unit to fully characterise the beam screen behaviour.

Once the unbalance of the forces due to the CLIQ discharge vanishes at around 10 ms, the beam screen behaves in the same way as described in chapter 5, namely in the case of a monotonic magnetic field decay. An indication of the total forces induced in each quadrant of the beam screen is given by $\mathbf{I\dot{I}}$. This is shown in Fig. 6.6b for CLIQ and the monotonic magnetic field decay (quench heaters). The $\mathbf{I\dot{I}}$ factor for the poles 1-3 and 2-4 is represented by the blue and red curve, respectively. The black curve represents the $\mathbf{I\dot{I}}$ factor when the quench heaters are used to protect the magnet. By comparing these curves, it turns out that the highest forces induced during a monotonic magnetic field decay are higher than those induced at the end of the CLIQ oscillations. This implies that only the unbalance of forces induced at the beginning of the CLIQ discharge needs to be studied to verify the mechanical integrity of the beam screen.

The main implication of the CLIQ discharge on the beam screen is that the induced field of forces, depending on the direction of the currents, leads to a torque load. This is a new load type that the beam screen would be subject to as it did not occur in the case of the quench heater technology only.

6.4 Magneto-thermal analysis

The evolution $\mathbf{I\dot{I}}$ of the poles 1-3 and 2-4 gives a useful insight to understand the force distribution in the beam screen. However, the change in direction of the forces during the first phase of the CLIQ discharge is smooth as the magnetic field is averaged in the regions equally distant from the poles.

The analysis of the current distribution in the assembly is needed to quantify the forces induced by the *diffusion* of the magnetic field.

Considering a periodic unit of the assembly, ranging from $45°$ to $135°$, the current flow transition occurs approximately at the interception with the y-axis from 1 ms up to 7 ms. Fig. 6.9 shows the current density induced in the unit at t=5 ms with the upper and bottom limits of the colour legend lowered on purpose to highlight the line of transition (from negative to positive current). The 5 ms time step is representative because it corresponds to the largest forces induced in the two sides of the unit. It turns out that the line of transition of the currents is located at + 0.4 mm from the y-axis. Such line has been identified by assessing where the current density is equal to 0. Therefore slightly more currents are induced in the left part of the unit than in the right one. This is due to the fact that in correspondence of the y-axis the time variation of the magnetic field, or equivalently the average of the P1-P3 and P2-P4 currents, is not zero but negative.

As shown in Fig. 6.10 for the heat absorber, the resultant of the forces induced in the two sides of the periodic unit are broken down into the normal and tangential components. It is worth noting that for each side of the unit, the normal components point in opposite directions, while the tangential ones point in the same direction. Therefore, for such a unit, the normal forces have to be integrated over the regions in which they are positive or negative. The tangential components can be integrated over each component of the periodic unit instead.

The magnitude of the volumetric forces is affected also by the intensity of the magnetic field according to $\mathbf{f} = \mathbf{j} \times \mathbf{B}$. The left side, where more currents are induced, is in correspondence of pole 2, whose magnetic field decays during the first bump, while the right side is in correspondence of pole 1, whose magnetic field increases, see Fig.6.1. This helps to balance the Lorentz forces with respect to the y-axis for the unit at the top and bottom side and to the x-axis for the unit on the right and left side, making the cartesian axes a convenient separation to integrate the forces during the CLIQ discharge. In Fig. 6.11 the percentage difference between the currents and the forces induced in the two sides of the heat absorber from 4 to 6 ms is shown. At 5 ms the current on the left side

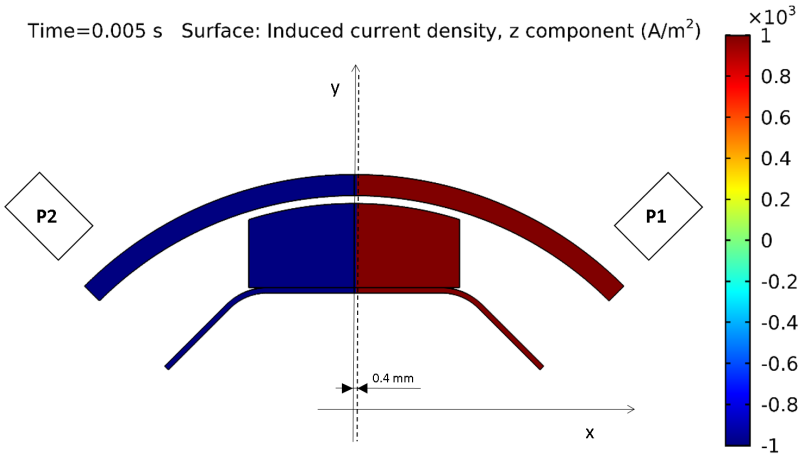


FIGURE 6.9: Current induced in a quarter of the beam screen whose limits in the colour map is set to $1 \cdot 10^3$ A and $-1 \cdot 10^3$ A.

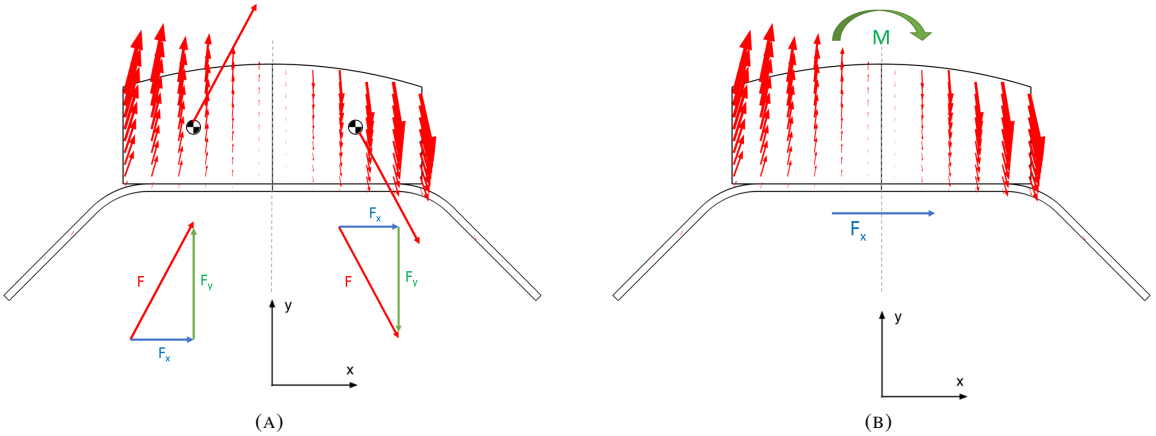


FIGURE 6.10: In (a) Lorentz force distribution induced in the heat absorber at 5 ms whose resultant force is decomposed in a normal and tangential component. In (b) it is shown the equivalent force distribution represented by a torque and a tangential force.

is about 6 % higher than the one on the right side, while the normal force is 5 % higher. The y-axis and the x-axis will be used as boundaries to integrate the forces over the two sides of the periodic unit for the whole evolution of the CLIQ discharge.

The magneto-thermal analysis has been performed in 2D in COMSOL. The wings of the heat absorbers are treated in the same way done for the study of the beam screen in chapter 5. Therefore, their electrical conductivity is 20 % of the tungsten alloy. The ultimate currents of the CLIQ discharge shown in Fig. 6.1b have been considered in the analysis. The interaction between the magnetic and thermal module has been set up with a two-way coupling.

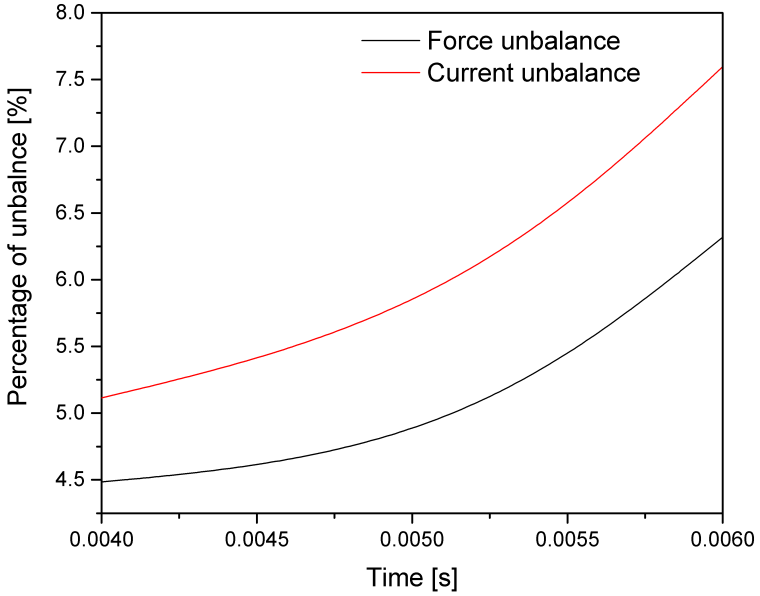


FIGURE 6.11: Percentage of current and force unbalance between the right and left side of the heat absorber delimited by the intersection with the y-axis.

6.4.1 Q1 beam screen

The two normal components and the single tangential component of the upper periodic unit are plotted in Fig. 6.12 for the inner copper layer, the octagonal pipe, the heat absorber, and the cold bore up to 0.2 s after the start of the quench.

Multiple observations can be derived from this profile of forces.

First, four regions can be identified by the evolution of the two normal components. The boundaries of such regions are given by vertical lines corresponding to the time where the two normal components have the same magnitude. Therefore, region 1 ranges from t=0 ms to t=15 ms, region 2 from 15 ms to 50 ms, region 3 from 50 ms to 91 ms, and region 4 from 91 ms up to the end of the quench. This is valid with a good approximation for all the beam screen components. In region 1 the forces are antisymmetric from 1 ms to 7 ms with respect to the y-axis. In region 2 and 3 there is no symmetry. In region 4 the unbalance of the forces due to the CLIQ discharge vanishes as the current decay becomes the same for each pole.

Second, for region 1, 2, and 3 the maximum difference of the normal forces between each side is reported in the graphs by red bars. For region 4 the difference is always zero as the profile of the two forces becomes identical. The largest difference of normal forces occurs in region 1 for all the beam screen components from 3 to 6 ms. In particular, for the inner copper layer it is 9.2 $\mathrm{N\,mm^{-1}}$, for the octagonal pipe 0.8 $\mathrm{N\,mm^{-1}}$, for the heat absorber 42 $\mathrm{N\,mm^{-1}}$, and for the cold bore 24 $\mathrm{N\,mm^{-1}}$. The maximum difference for region 2 occurs from 26 to 28 ms and for region 3 from 64 to 66 ms. By way of example, the force distribution of the heat absorbers only is shown in Fig. 6.13 in correspondence of the highest differences of forces in each region.

Third, as for the normal forces, the maximum tangential forces are induced in region 1. For the inner layer these are 3.6 $\mathrm{N\,mm^{-1}}$, for the octagonal pipe 0.3 $\mathrm{N\,mm^{-1}}$, for the heat absorber 10.3 $\mathrm{N\,mm^{-1}}$, and for the cold bore 8.5 $\mathrm{N\,mm^{-1}}$.

Fourth, region 4 is not a concern for the integrity of the beam screen as the induced forces are lower than the ones studied without CLIQ (see 6.6b).

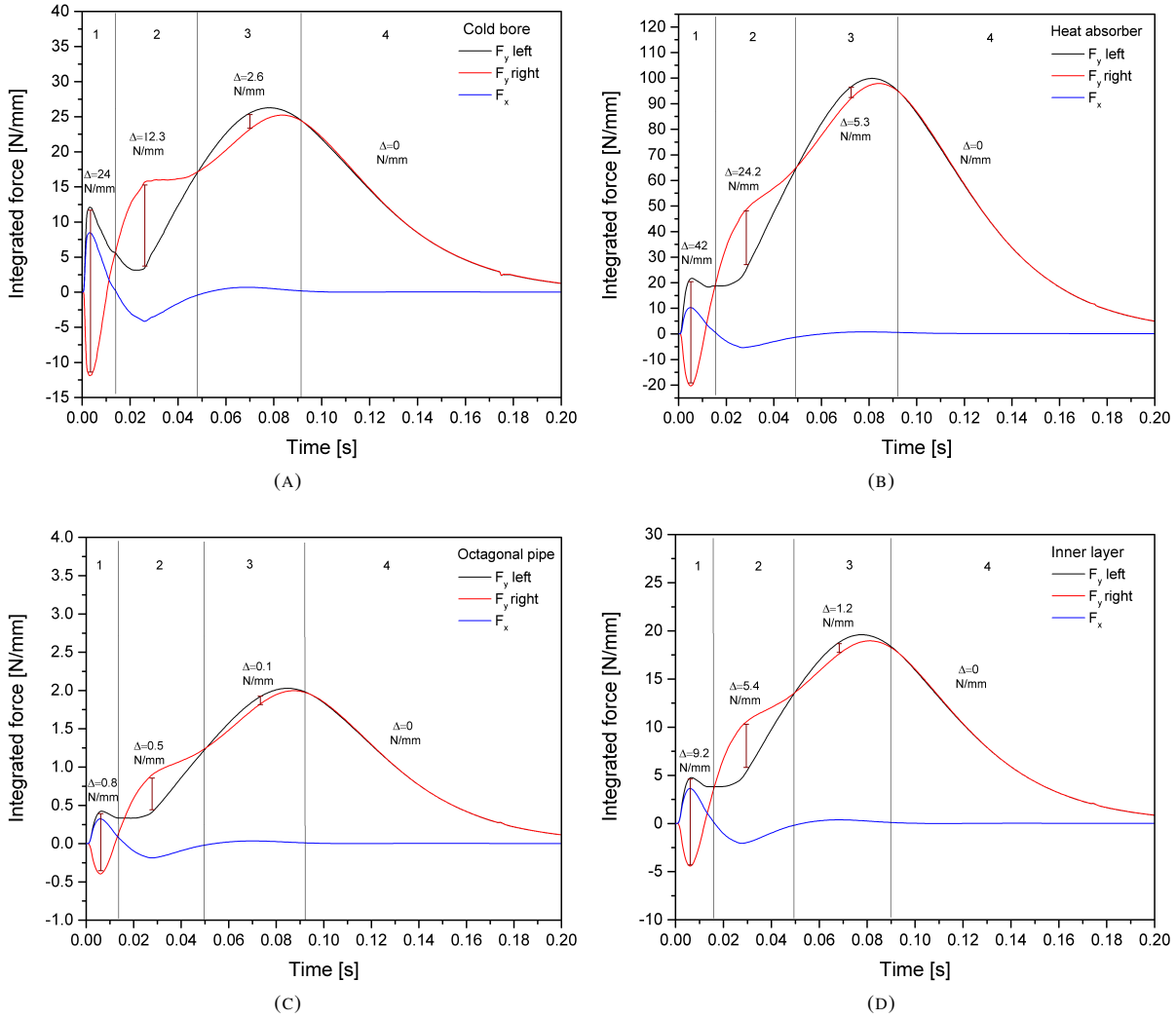
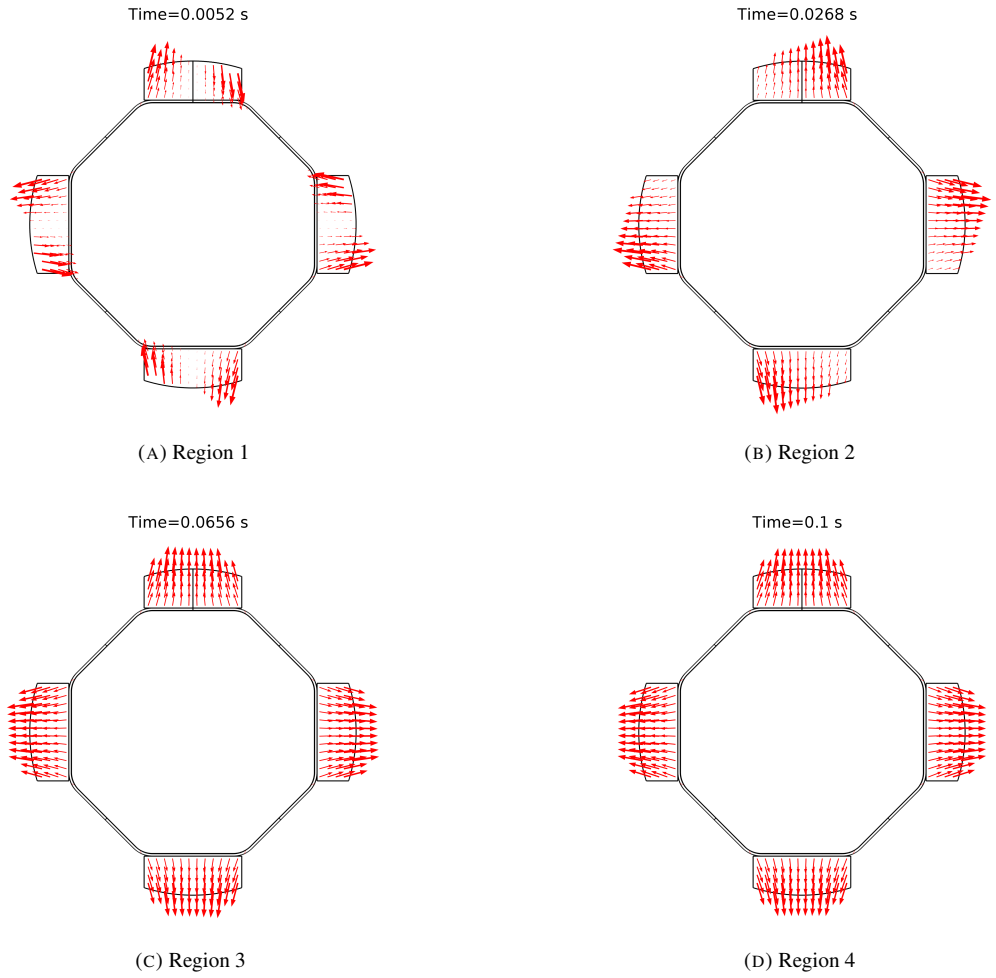


FIGURE 6.12: Evolution of the normal and the tangential forces induced in the Q1 cold bore (a), heat absorber (b), octagonal pipe (c), and inner layer (d) during the CLIQ discharge. Black vertical lines determine regions of interest of the CLIQ discharge. The red bars and their relative values indicate the highest difference of forces for each region.

The highest differences of normal forces and the longitudinal ones induced in the region 1, 2, 3 are summarised in Table 6.1. The highest normal component of the forces induced in a quarter of the beam screen undergoing a magnet quench without the CLIQ scheme is reported as well. By way of example, the forces induced in the heat absorber of region 4 are 15 % lower than those induced with the quench heaters (ultimate conditions).

The evolution of the induced currents, the heat losses and the maximum temperatures are shown in Fig. 6.14 for each beam screen component up to 0.2 s. The induced currents are integrated over the two sides of the beam screen components separated by the y-axis to capture the direction of the current flow as well. The maximum total current is 4011 A for the cold bore and 17413 A for the heat absorber, see Fig. 6.14a, while it is 406 A for the octagonal pipe and 3602 A for the inner layer, see Fig. 6.14b. The maximum heat losses are 17.6 $\mathrm{kW\,m^{-1}}$ for the cold bore, 64.4 $\mathrm{kW\,m^{-1}}$ for the heat absorber, 1 $\mathrm{kW\,m^{-1}}$ for the octagonal pipe and 8.1 $\mathrm{kW\,m^{-1}}$ for the inner layer, see Fig. 6.14c. The maximum temperature is 57.3 K for the cold bore, 64.3 K for the heat absorber, 61.2 K for the octagonal pipe and the inner layer, see Fig. 6.14d.



(A) Region 1

(B) Region 2

(C) Region 3

(D) Region 4

FIGURE 6.13: Distributions of the forces induced in the heat absorbers of the Q1 beam screen with respect to each region of the CLIQ discharge.

Component	Region 1			Region 2			Region 3			Region 4		NO CLIQ	
	t [ms]	ΔF_n [N/mm]	F_t [N/mm]	t [ms]	ΔF_n [N/mm]	F_t [N/mm]	t [ms]	ΔF_n [N/mm]	F_t [N/mm]	t [ms]	F_n [N/mm]	t [ms]	F_n [N/mm]
Cold bore	3.2	24	8.5	26	12.3	-4.2	64.4	2.6	0.6	80.4	51.3	55	58.7
Heat absorber	5.2	42	10.3	26.8	24.2	-5.4	65.6	5.3	0.4	82.8	197.5	55	233.4
Octagonal pipe	6	0.8	0.3	27.6	0.5	-0.2	65.6	0.1	0.03	84.8	4	59	4.7
Inner layer	6.4	9.2	3.6	27.6	5.4	-2	65.6	1.2	0.4	79.6	38.5	50	36.9

TABLE 6.1: Summary of the highest forces (ΔF_n and F_t) induced in the Q1 beam screen with respect to the four regions of the CLIQ discharge. The normal forces induced during the monotonic magnetic field decay analysed in chapter 5 (NO CLIQ) are presented for comparative purposes.

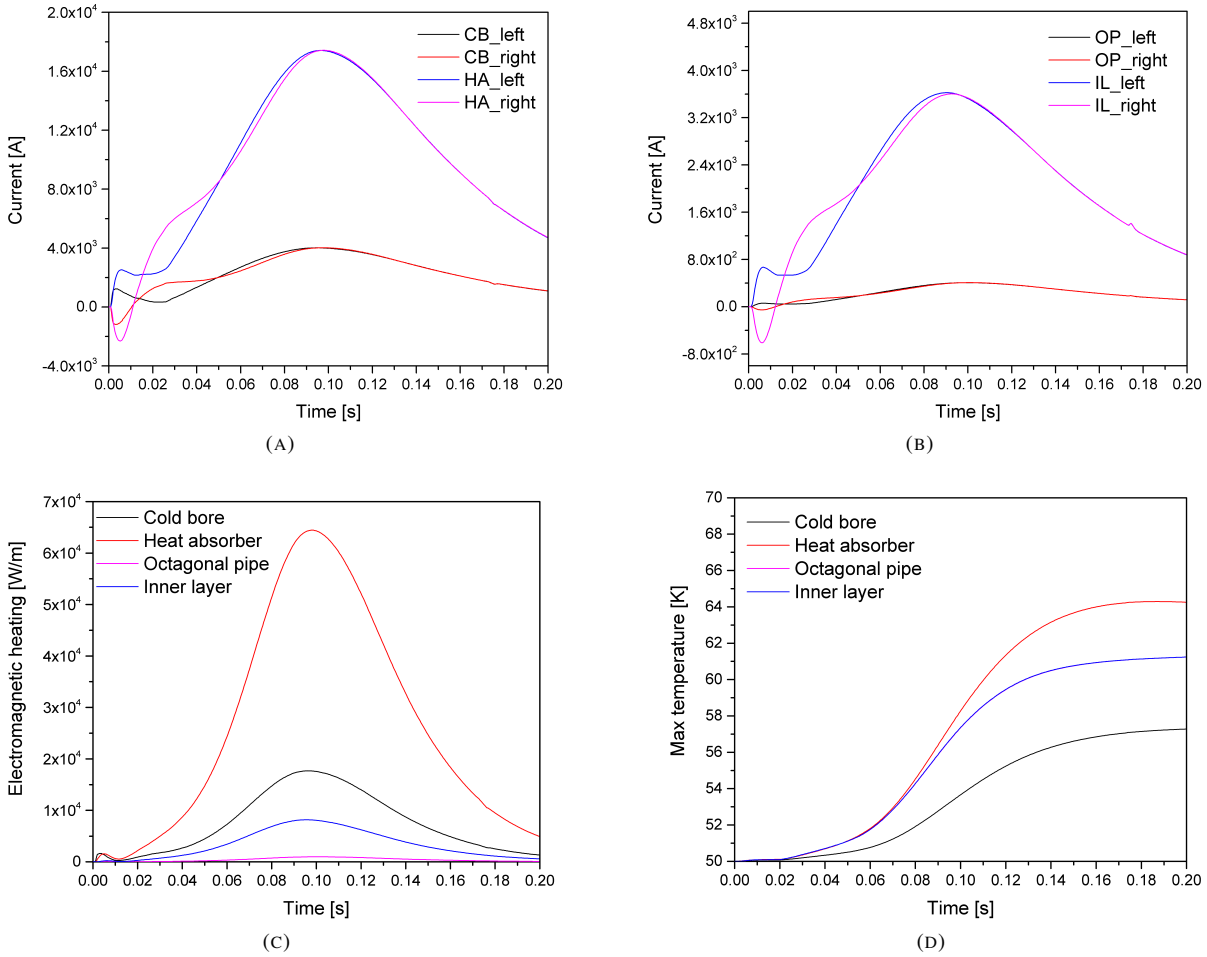


FIGURE 6.14: Evolution of the induced currents integrated over the two sides of the Q1 cold bore (CB) and heat absorber (HA) in (a), the octagonal pipe (OP) and the inner layer (IL) in (b). The electromagnetic heating (c) and the maximum temperature (d) refer to each quarter of the beam screen components.

6.4.2 Q2 beam screen

Analogous observations to the Q1 beam screen can be derived from the profile of forces induced in Q2 beam screen during the CLIQ discharge, see Fig. 6.15. The boundaries of region 1 are from t=0 ms to t=15 ms, region 2 from 15 ms to 50 ms, region 3 from 50 ms to 95 ms, and region 4 from 95 ms up to the end of the quench.

The largest difference of normal forces occurs in region 1 for all the beam screen components from 3 to 6 ms. For the inner copper layer this is 24.4 $\mathrm{N\,mm^{-1}}$, for the octagonal pipe 2.1 $\mathrm{N\,mm^{-1}}$, for the heat absorber 21.6 $\mathrm{N\,mm^{-1}}$, and for the cold bore 24 $\mathrm{N\,mm^{-1}}$. The maximum difference for region 2 occurs from 26 to 28 ms and for region 3 from 64 to 66 ms.

The highest tangential forces in region 1 are 8.5 $\mathrm{N\,mm^{-1}}$ for the inner layer, 0.7 $\mathrm{N\,mm^{-1}}$ for the octagonal pipe, 5.5 $\mathrm{N\,mm^{-1}}$ for the heat absorber, and 8 $\mathrm{N\,mm^{-1}}$ for the cold bore.

The highest difference of the normal forces and the longitudinal ones induced in the region 1, 2, 3 are summarised in Table 6.2. The highest normal component of the forces induced in the beam screen undergoing a magnet quench without the CLIQ scheme are reported as well. By way of example, the forces induced in the heat absorber of region 4 are 17.55 % lower than those induced with the quench heaters (ultimate conditions).

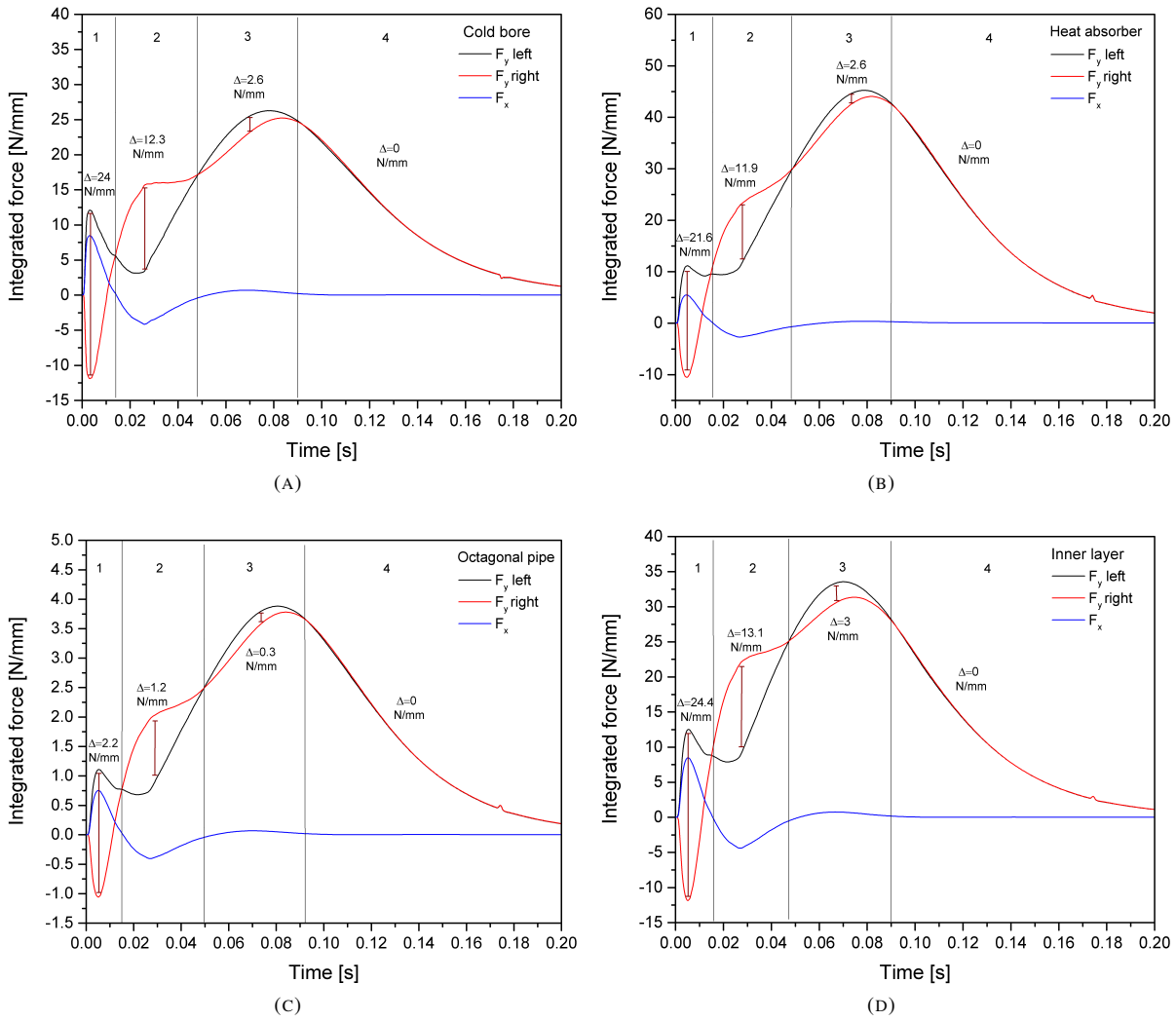


FIGURE 6.15: Evolution of the normal and the tangential forces induced in the Q2 cold bore (a), heat absorber (b), octagonal pipe (c), and inner layer (d) during the CLIQ discharge. The regions of the CLIQ dischargeare identified by the black vertical line. The red bars and their relative values indicate the highest difference of the normal forces.

Component	Region 1			Region 2			Region 3			Region 4		NO CLIQ	
	t [ms]	ΔF_n [N/mm]	F_t [N/mm]	t [ms]	ΔF_n [N/mm]	F_t [N/mm]	t [ms]	ΔF_n [N/mm]	F_t [N/mm]	t [ms]	F_n [N/mm]	t [ms]	F_n [N/mm]
Cold bore	4	24	8	26	12.3	-4.2	64.4	2.6	0.6	80.4	51.3	55	58.7
Heat absorber	4.8	21.6	5.5	26.4	11.9	-2.7	64.8	2.6	0.2	80.4	89.2	55	108.2
Octagonal pipe	5.2	2.2	0.7	26.8	1.2	-0.4	65.6	0.3	0.06	81.2	7.6	55	9
Inner layer	5.2	24.4	8.5	26.8	13.1	-4.4	62.4	3	0.7	72.8	64.7	44.2	59.4

TABLE 6.2: Summary of the highest forces (ΔF_n and F_t) induced in the Q2 beam screen with respect to the four regions of the CLIQ discharge. The normal forces induced during the monotonic magnetic field decay analysed in chapter 5 (NO CLIQ) are presented for comparative purposes.

The evolution of the induced currents, the heat losses and the maximum temperatures are shown in Fig. 6.16 for each beam screen component up to 0.2 s. The induced currents are integrated over the two sides of the beam screen components separated by the y-axis in order to capture the direction of the current flow as well. The maximum total current is 4011 A for the cold bore and 7271 A for the heat absorber, see Fig. 6.16a, while it is 662 A for the octagonal pipe and 5087 A for the inner layer, see Fig. 6.16b. The maximum heat losses are 17.6 $\mathrm{kW\,m^{-1}}$ for the cold bore, 30.6 $\mathrm{kW\,m^{-1}}$ for the heat absorber, 2.2 $\mathrm{kW\,m^{-1}}$ for the octagonal pipe and 15.8 $\mathrm{kW\,m^{-1}}$ for the inner layer, see Fig. 6.16c. The maximum temperature is 57.3 K for the cold bore, 67 K for the heat absorber, 68.2 K for the octagonal pipe and the inner layer, see Fig. 6.16d.

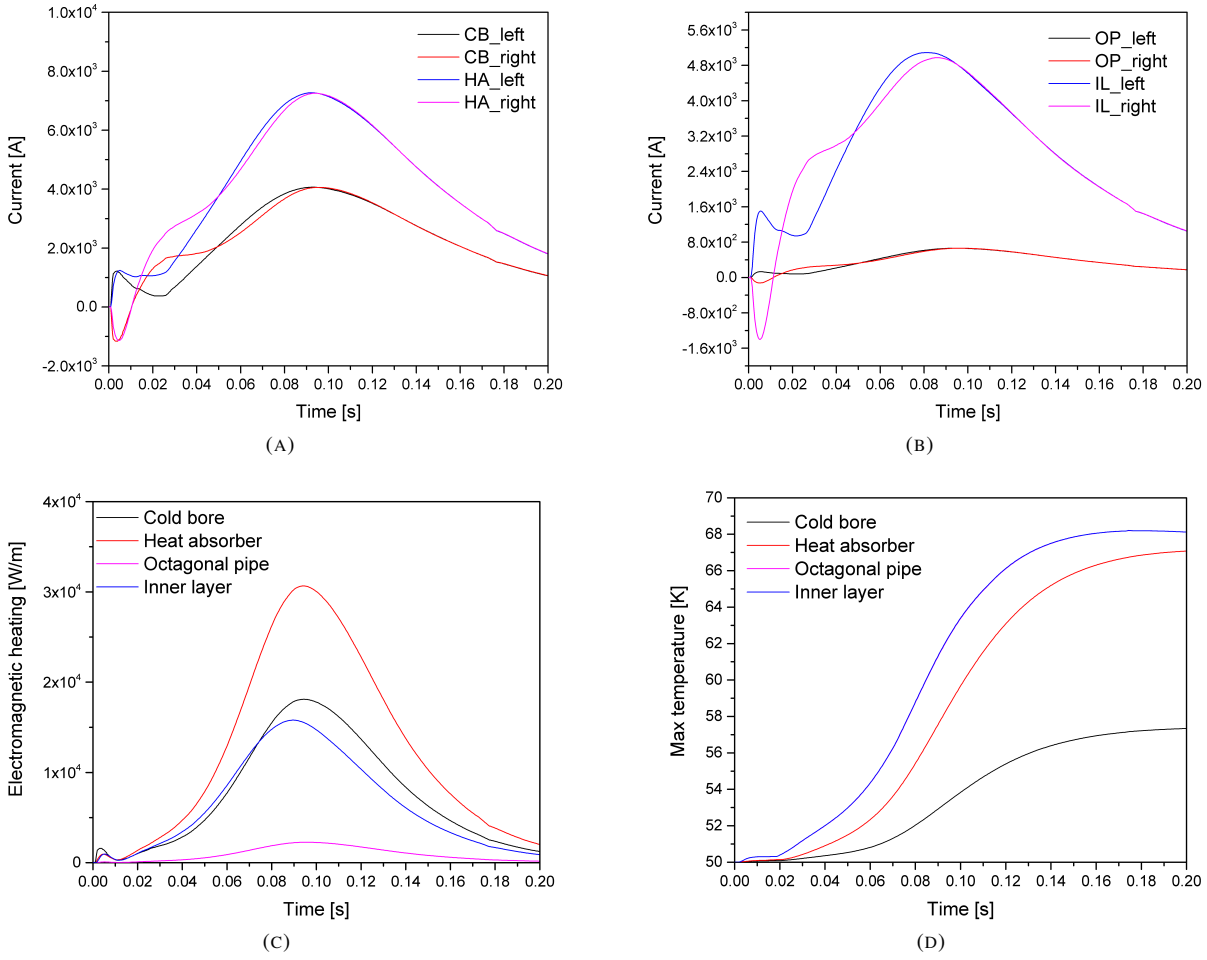


FIGURE 6.16: Evolution of the induced currents integrated over the two sides of the Q2 cold bore (CB) and heat absorber (HA) in (a), the octagonal pipe (OP) and the inner layer (IL) in (b). The electromagnetic heating (c) and the maximum temperature (d) refer to each quarter of the beam screen components.

6.5 Mechanical analysis

Three torques of different magnitude and orientation are generated in the first three regions of the CLIQ discharge.

According to the poles configuration shown in Fig. 6.8 the periodic unit rotates in a clockwise direction in region 1, counter-clockwise in region 2, and again slightly clockwise in region 3. In region 4 there are no rotations but the classical outward deformation along the y-axis and x-axis as described in chapter 5.

The heat absorber, being simply laid on the octagonal pipe, is constrained to the rotation by the centring pins only. This represents a new scenario for the beam screen originally designed to withstand outward forces. Therefore, two main problems arise: 1) the pin welded on the octagonal pipe, whose function is to align the heat absorbers, is now loaded and its design needs to be re-studied; 2) the impact dynamics between the heat absorber and the cold bore are more intense and need to be re-assessed.

The number of mechanical contacts increases in comparison with the no-CLIQ case because of the interaction of the heat absorber with the pin and the octagonal pipe. This calls for a 3D dynamic evaluation of the mechanical response of the beam screen. The multiphysics nature of the problem would increase considerably the overall computational load of the simulation making the study of the 3D contacts more challenging in COMSOL. Therefore, the problem is split in two platforms: the magneto-thermal analysis is computed in COMSOL in 2D (as done in section 6.4) while the mechanical one is computed in Ansys in 3D. Ansys is of great help because its solver is more efficient to handle 3D contacts.

The effects of CLIQ are studied only for region 1 where the most critical torques take place at 5.2 ms. The behaviour of region 4 is not studied as the integrated radial force induced in the beam screen components are lower to the ones induced without CLIQ (see Table 6.1 and Table 6.2).

Due to magnetic and mechanical symmetries one quarter of the beam screen is sufficient to fully assess the behaviour of the beam screen. However due to the force distribution induced in the first phase of CLIQ, the mechanical symmetries of the beam screen quarter have to be necessarily tilted by a $+/- 45°$ angle. Mechanical anti-symmetry conditions could have been used on a portion ranging from $0°$ to $90°$ but since the displacements and rotations for such boundaries are expected to be large, anti-symmetry conditions are not recommended [138]. Therefore, the beam screen portion ranging from $45°$ to $135°$ is the periodic unit taken as a reference to study the mechanical response of the whole beam screen during the CLIQ discharge.

6.5.1 Equivalent force method

The distribution of the body forces from the 2D magneto-thermal analysis of COMSOL needs to be transferred to the 3D mechanical model in Ansys. To this end, the forces per unit length integrated in COMSOL have been scaled according to the length of the 3D model and applied in Ansys as concentrated loads. It is noteworthy that the forces have been applied on specific edges or faces of the beam screen components in a way to have the same mechanical response as if the problem would have been studied accounting for the real force distribution of COMSOL.

As described in section 6.4.1, the Lorentz force distribution is with a good approximation antisymmetric only in region 1 from 1 to 7 ms. As shown in Fig. 6.10, this is equivalent to a torque and a tangential force induced on each periodic unit of the beam screen.

For the periodic unit of Fig. 6.9, the torque acts around an axis parallel to the z-axis whose exact position is determined by the distribution of the forces itself.

It is fundamental to find a method to quantify the torque for each beam screen component in COMSOL to then apply an equivalent system of forces in Ansys. To this purpose, the centroid position relative to the resultant forces of the right and left side of the periodic unit is determined for each component. It turns out that the centroids are with good approximation symmetric with respect to the y-axis up to 7 ms. The distance between these two points determines the arm of the normal component of the total forces by which the torque can be derived as:

$$\mathbf{M} = \mathbf{F}_{tot} \times \mathbf{OC} \tag{6.8}$$

where **M** is the torque, $\mathbf{F}_{tot}$ is the total force induced for each component in one side of the unit, and **OC** is the arm, namely the distance of the centroid from the x- or y-axis.

The body loads computed by COMSOL can be treated as discrete quantities and can be exported in relation to each node of the mesh. The total force can be calculated as:

$$\mathbf{F}_{tot} = \sum_{n=1}^{N_{nodes}} \mathbf{f}_n \tag{6.9}$$

The equality between the torques related to the discrete quantities and the integrated ones can be written as [139]:

$$\mathbf{OC} \times \mathbf{F}_{tot} = \sum_{n=1}^{N_{nodes}} \mathbf{oc} \times \mathbf{f} \tag{6.10}$$

Therefore, the centroid position of the equivalent force of each beam screen component calculates to:

$$OC_x = \frac{\sum_{n=1}^{N_{nodes}} oc_x f_y}{F_{tot\ y}} \tag{6.11}$$

$$OC_y = \frac{\sum_{n=1}^{N_{nodes}} oc_y f_x}{F_{tot\ x}} \tag{6.12}$$

Overall, two torques can be estimated from the decomposition of the induced forces in each quadrant of the beam screen assembly. By way of example, these are illustrated in Fig. 6.17 for the cold bore. One torque is generated by the normal forces in each quadrant and the other one is generated by the tangential forces acting on two alternate quadrants. However, concerning the heat absorber only the normal forces generate a torque as these components are not rigidly connected with the rest of the assembly.

As the heat absorber is not fully constrained to the octagonal pipe, its torque is of great concern for the mechanical integrity of the assembly.

Table 6.3 summarises the torques generated by the normal components of the forces in each beam screen component with respect to the length of the heat absorber (40 cm). The forces and the arm considered to estimate such torques are with respect to the left side of the periodic unit shown in Fig. 6.9 where the forces are slightly higher than in the right side, see Fig. 6.11. Moreover, considering geometric non-linearities of the cold bore and the octagonal pipe, this method over-estimates further the respective torques. Non-linearities are negligible only for the heat absorber.

6.5.2 Calibration between the 2D and 3D FEM model

The calibration has been performed to verify if the equivalent system of forces assigned in Ansys-3D gives the same mechanical output (displacement - stress) of the real force distribution calculated by COMSOL-2D.

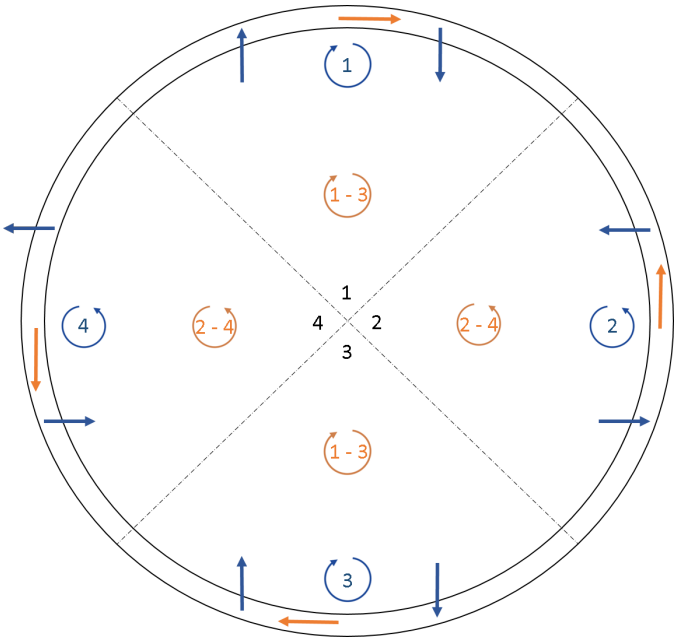


FIGURE 6.17: Integrated forces induced in the cold bore decomposed in the normal (blue) and tangential (orange) component. The normal forces generate a torque (blue circles) in each quadrant, numbered from 1 to 4. The tangential forces generate two counteracting torques (orange circles) numbered as 1-3 and 2-4.

Component	Q1 beam screen Torque / 40 cm [N m]	Q2 beam screen Torque / 40 cm [N m]
Cold bore	253	253
Heat absorber	280	148.5
Octagonal pipe [a]	81.5	231

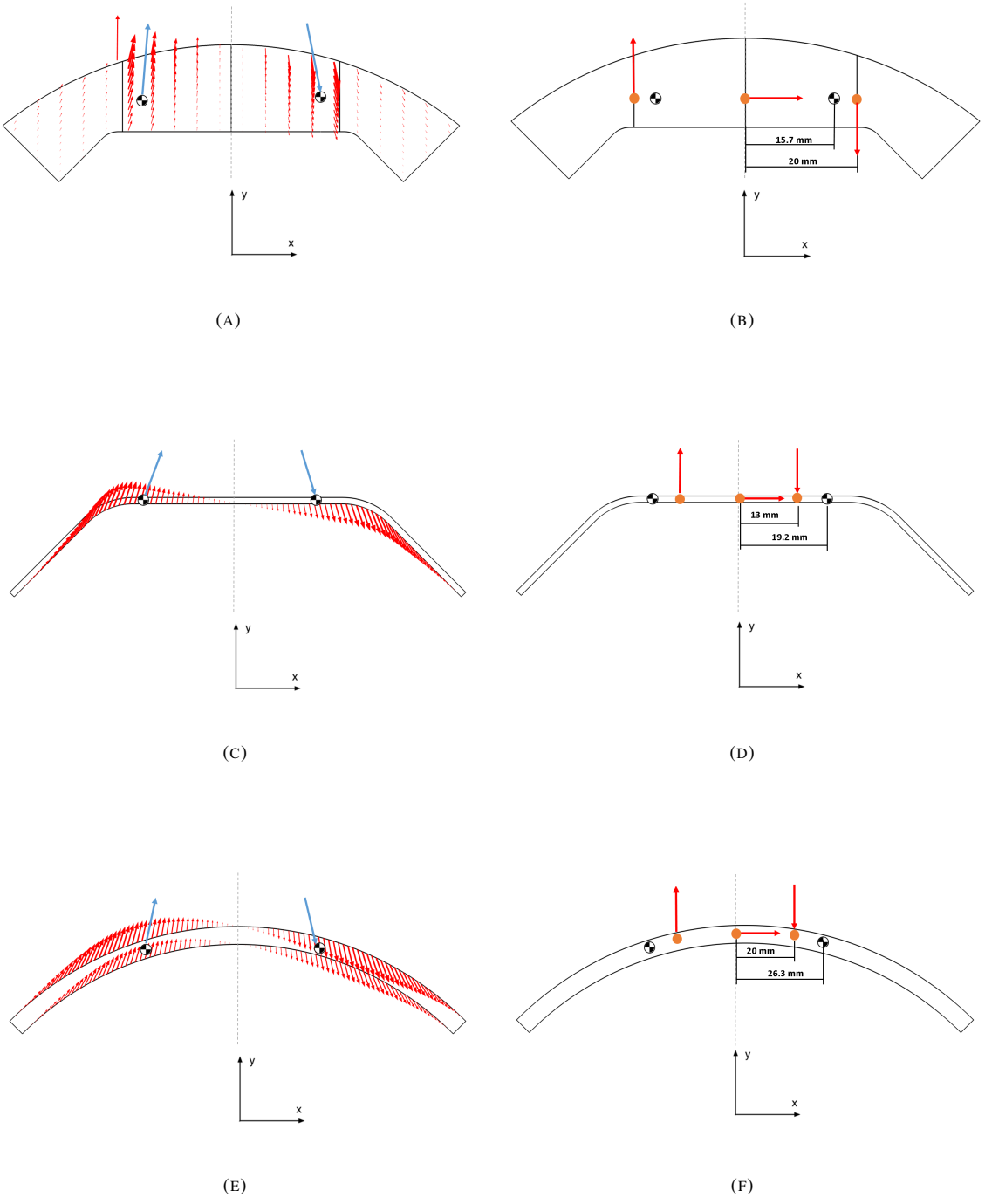
TABLE 6.3: Maximum torque induced in the Q1 and Q2 beam screen components during the CLIQ discharge of region 1.

[a] the inner copper layer is included.

To compare the 2D and 3D models the boundary conditions have to be necessarily identical. Therefore, in COMSOL the heat absorber has been considered bonded on the octagonal pipe as otherwise the convergence would have not been obtained due to an intrinsic lack of constraints of the problem.

Fig. 6.18 shows the position of the centroids of the equivalent force for each side of the periodic unit. As the most critical torque is the one generated by the normal forces, only the distance from the y-axis is shown. The arm of the forces that allows the same mechanical response between the 2D and 3D model is found by a parametric study described in this section. Such an arm is represented by the distance of the orange points from the y-axis shown in Fig. 6.18.

The useful interval of time selected for the analysis is within region 1, namely from 0 to 6 ms. The equivalent system of forces can be easily applied to the heat absorber since this can be considered as a rigid body with no



(A) (B) (C) (D) (E) (F)

FIGURE 6.18: Real force distribution and equivalent system of forces for the heat absorber (a-b), octagonal pipe (b-c) and cold bore (d-e). The distance of the centroids and the equivalent one (represented by orange dots) is indicated.

geometric non-linearities. As shown in Fig. 6.18b the total longitudinal force has been applied on the internal face intersecting the yz-plane, while the normal forces to the lateral faces of the absorber. As the lateral faces of the heat absorber are distant 20 mm from the y-axis, while the centroids are at 15.7 mm, the forces have been scaled accordingly in order to have the original torque evolution.

For the cold bore and the octagonal pipe, this method overestimates the relative torques as not all the forces act in a way to generate a torque load type. In fact, due to the shape of these components the distribution of the forces induced in the tilted areas at $+/-\ 45°$ angle act only as tensile load. To take into account this phenomenon, both the torque and the longitudinal force are reduced by a characteristic factor. This factor is 1.5 for the octagonal pipe and 1.3 for the cold bore. However, the torque is reduced by shortening the arm but not the force. Therefore, for the octagonal pipe the arm of the force becomes 13 mm instead of 19.2 mm, see Fig. 6.18d, while for the cold bore 20 mm instead of 26.3 mm, see Fig. 6.18f. The longitudinal forces are applied on the internal faces of the components intersecting the yz-plane.

These equivalent distances have been obtained by comparing the displacement of specific vertexes and the equivalent stress state between COMSOL and Ansys, see Fig. 6.19.

In particular, the calibration has been performed by applying the equivalent forces to each beam screen component separately and to the whole assembly afterwards. Four vertexes of the octagonal pipe have been monitored to calibrate the mechanical response of the pipe itself, while one vertex for the heat absorber and the cold bore.

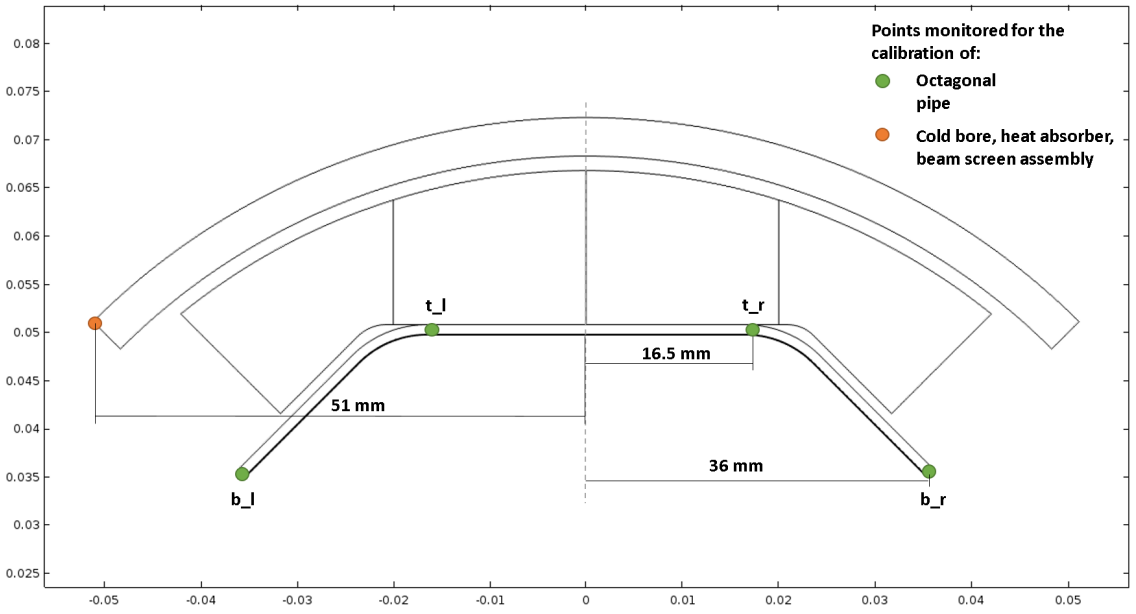


FIGURE 6.19: Specific vertexes of the beam screen section chosen to monitor the deformation of the beam screen components during the CLIQ discharge between COMSOL and Ansys.

For the octagonal pipe the evolution of the total displacement of the selected vertexes is shown in Fig. 6.20a. The agreement turns out to be good. At 5 ms the difference in terms of displacement between the two platforms for the four vertexes is between 2 and 7 %.

For the cold bore the evolutions of the radial displacements and of the stress state are in good agreement, see Fig. 6.20b and Fig. 6.22, respectively.

For the heat absorber the radial displacement of the cold bore in COMSOL is not in a good agreement with Ansys, see Fig.6.20c. In addition, the response in Ansys is anticipated in time which gives a good hint to understand

the mismatch. Due to the very short time scale (in the order of a few ms), dynamic effects need to be accounted for. Therefore, since the wings of the heat absorber are considered in COMSOL (so as if the absorber were uniform along the beam axis), the weight of the heat absorber is much higher than that in Ansys (real geometry as it is in 3D). The increased weight (or inertia) explains the delay of the displacement as well as the higher peak value due to a higher impact energy. To demonstrate this hypothesis, a heat absorber with a uniform cross section including the wings has been considered in Ansys and the comparison of the total displacement is shown in Fig.6.20d. As expected, the match is in an excellent agreement.

Fig.6.20e shows the evolution of the radial displacement of the cold bore when all the beam screen components are loaded according to the real force distribution in COMSOL and to the equivalent system of forces in Ansys. In this case the heat absorber considered in Ansys is the real one. The two profiles agree well for the first bump and less for the second one. The first bump is related to the forces induced in the cold bore and, therefore, as seen in Fig. 6.20b, the match is good. The second one is caused by the hit of the heat absorber and, as seen in Fig. 6.20c, there is a mismatch due to the different inertia. However, if the cross section taken into account was uniform also in Ansys, the evolution of the displacement profiles would become almost the same, see Fig.6.20f. On this latter case, the maximum evolution of the von Mises stress and stress map of the cold bore calculated by COMSOL and Ansys are reported in Fig. 6.21 and in Fig. 6.21, respectively. This comparison shows an excellent agreement as well.

Therefore, the method based on the equivalent system of forces in Ansys seems to reproduce well the real force distribution in COMSOL. Therefore, such a method is deemed to be fully applicable for the study of the real beam screen configuration, *i.e.* heat absorbers in contact to the octagonal pipe.

6.6 Results and discussion

6.6.1 Q1 beam screen

Original design

The torque generated during the first phase of the CLIQ discharge is applied to the original design of the Q1 beam screen according to the method presented in section 6.5.1. The centring pin welded on the octagonal pipe is now loaded and its mechanical integrity might be compromised, see Fig. 6.23.

The stress state of the octagonal pipe is shown in Fig. 6.24 at 5 ms. The elastic limit of the material has been set up as the upper limit of the colour map to highlight plastic deformations. Severe plastic deformations (red regions) are visible on a wide region of the screen and across the thickness of the pipe. This would cause permanent distortion of the beam aperture as well as damage to the pin itself. In addition, the heat absorber might permanently get in contact with the cold bore. This does not comply with the requirements of the beam screen and a new solution has to be found.

New design

The modifications required for the beam screen to withstand the CLIQ discharge consist of on a new design of the pin and its integration with the heat absorbers. The new solution is proposed in Fig. 6.25. In comparison with the straight pin seen in Fig. 6.23, the new one presents an increased diameter at the base. The idea is to transfer

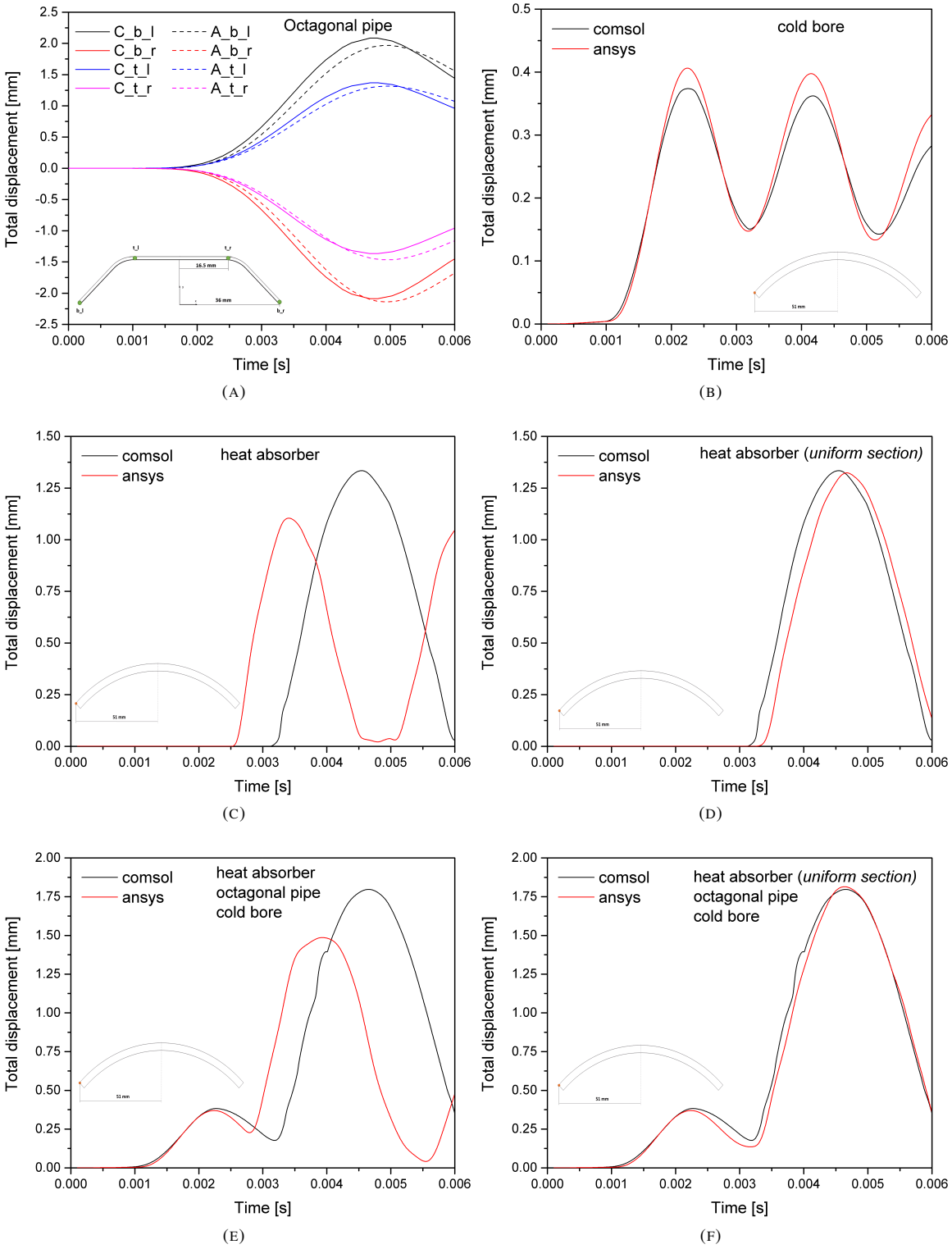


FIGURE 6.20: Comparison of the radial displacement of the vertexes chosen to monitor the mechanical response of each beam screen component between COMSOL and Ansys. The component is shown at the top-right of each graph.

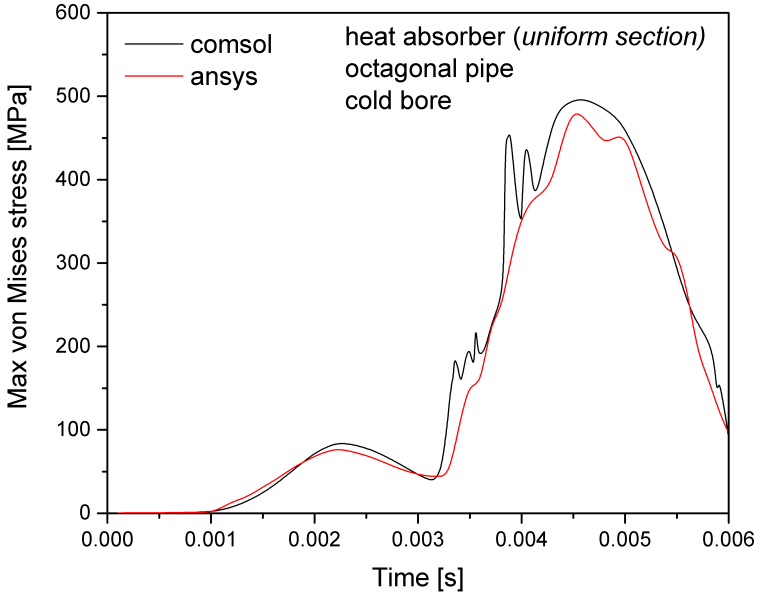


FIGURE 6.21: Evolution of the highest von Mises stress in the cold bore computed by Ansys and COMSOL.

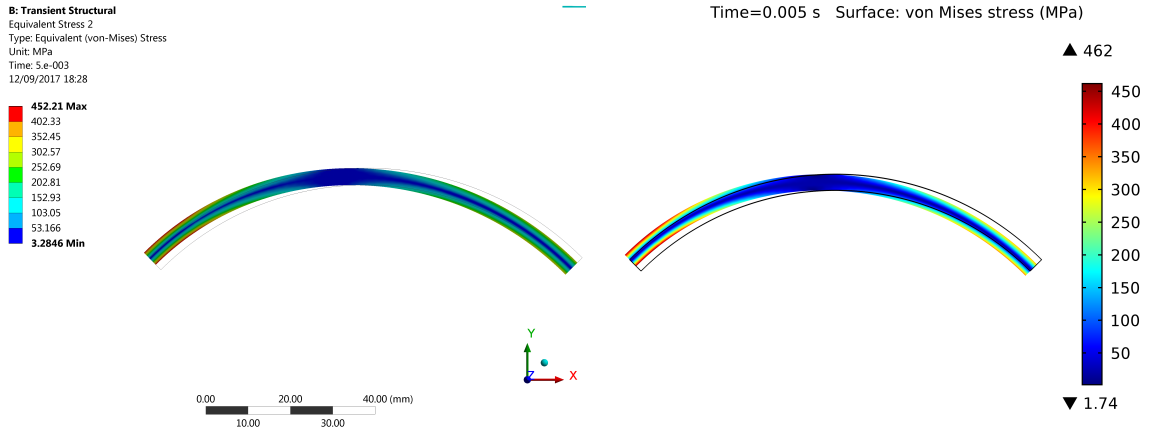
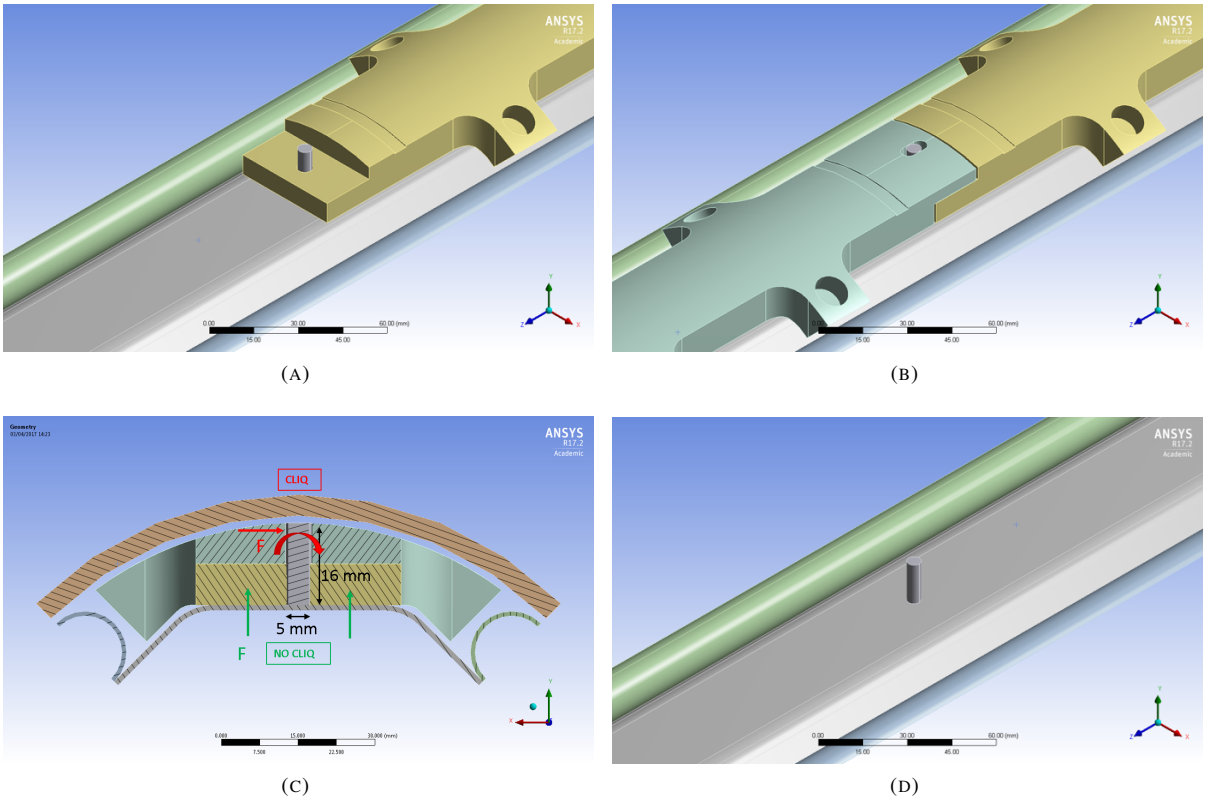


FIGURE 6.22: Stress state of the cold bore hit by the heat absorber at 5 ms in Ansys in (a) and in COMSOL in (b).

the forces at a shorter distance from the octagonal pipe (from 16 mm to 4 mm) in order to reduce the torque to be absorbed locally by the pin. In addition, the larger diameter (from 5 mm to 8 mm) guarantees an increased robustness of the weld at the interface with the octagonal pipe.

The stress state of the new pin and of the region nearby it, is reported in Fig. 6.26. In general, even if the extension of the plastic regions is smaller than in the case of the straight pin, the induced plastic deformations are still not acceptable.



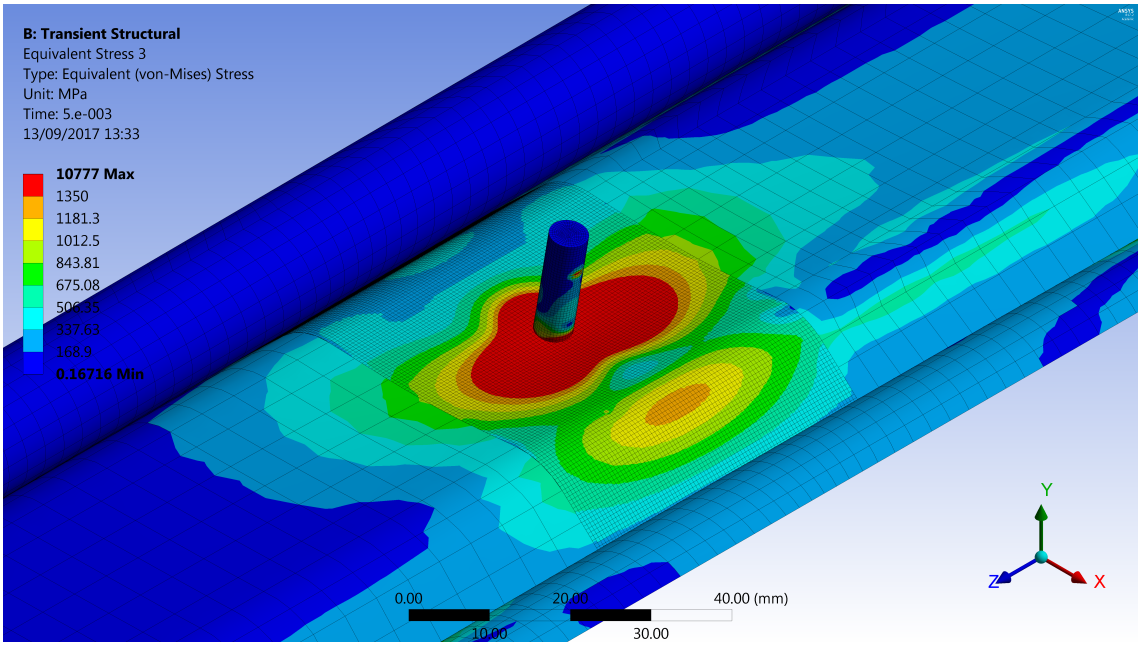
(A) (B)

(C) (D)

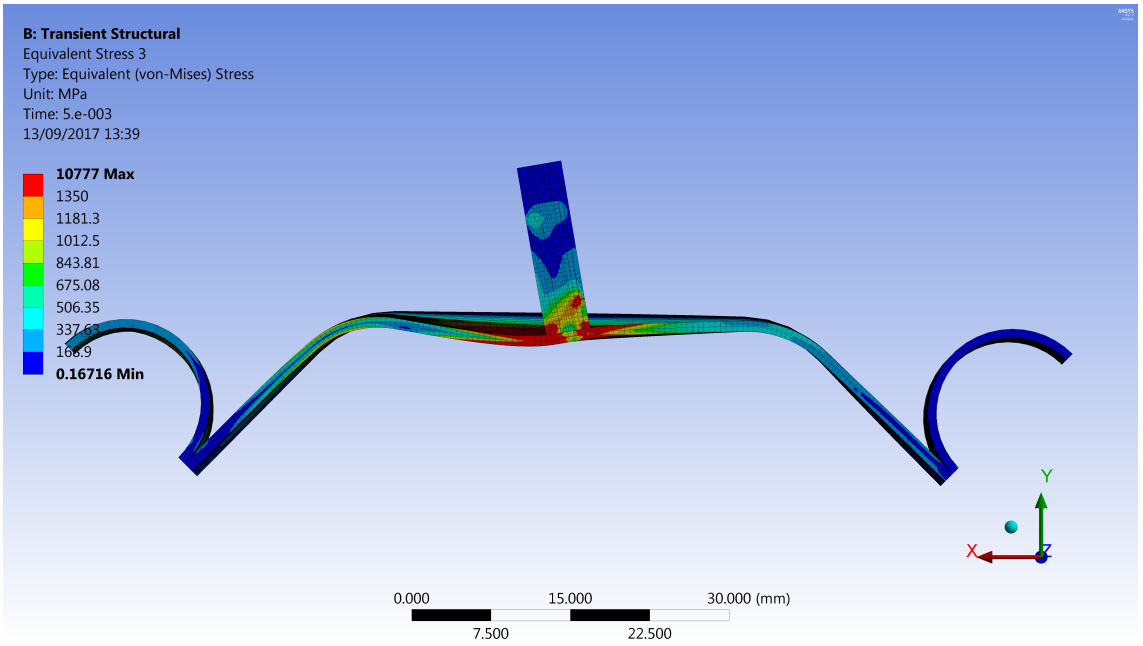
FIGURE 6.23: Original pin design and integration with the interfacing systems. In (c) the force distribution around the pin with or without CLIQ.

To lower the stress in the octagonal pipe another solutions has been simulated. A reinforcement plate 1 mm and 2 mm thick has been added to the pipe to increase locally the stiffness of the area on which the pin is welded, see Fig. 6.27.

The stress state of the pin welded on the reinforcement plate 1 mm thick and of the nearby region is reported in Fig. 6.28. The region exceeding the elastic limit (in red) is now reduced but still present. The elastic limit is exceeded locally mainly on the surface of the reinforcement plate and partly along its thickness.

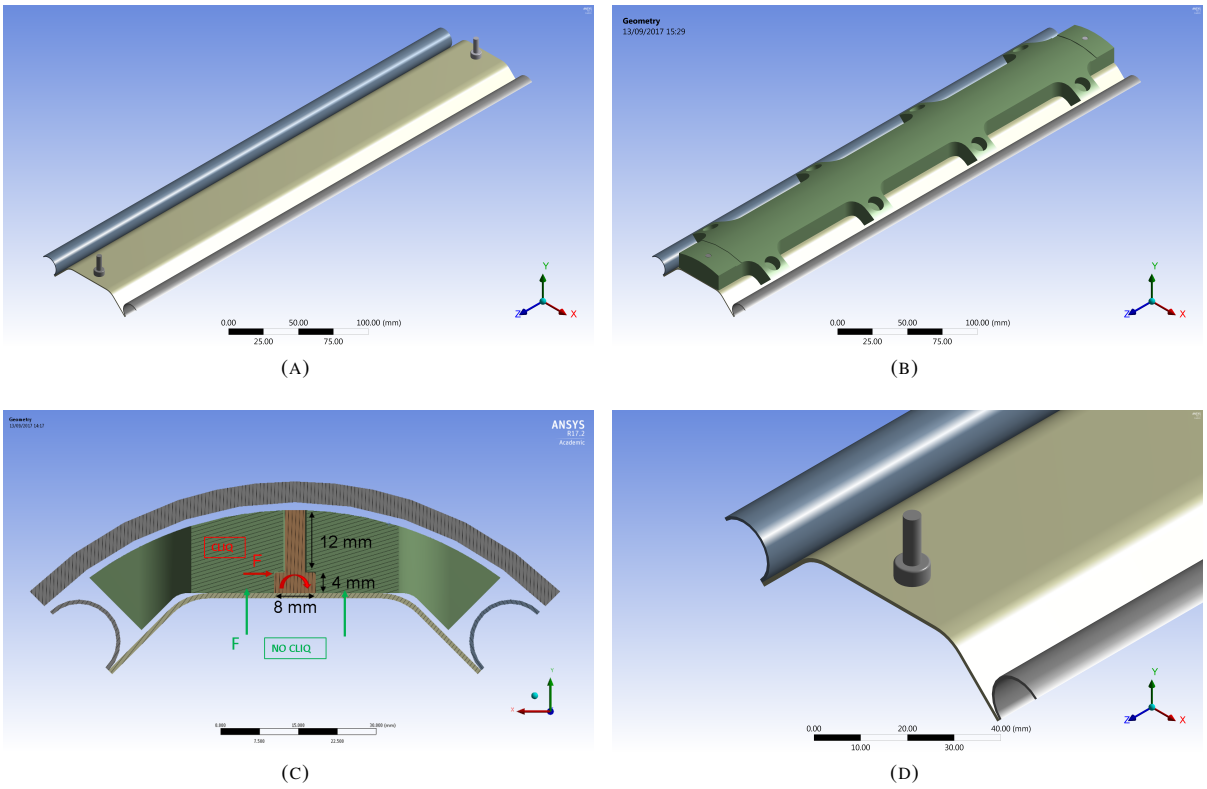


(A)



(B)

FIGURE 6.24: On top, von Mises stress state of the Q1 octagonal pipe at 5 ms. On the bottom, cross section view of the octagonal pipe. The upper bound of the legend is set to 1350 MPa, elastic limit of the material, to highlight plastically deformed regions.

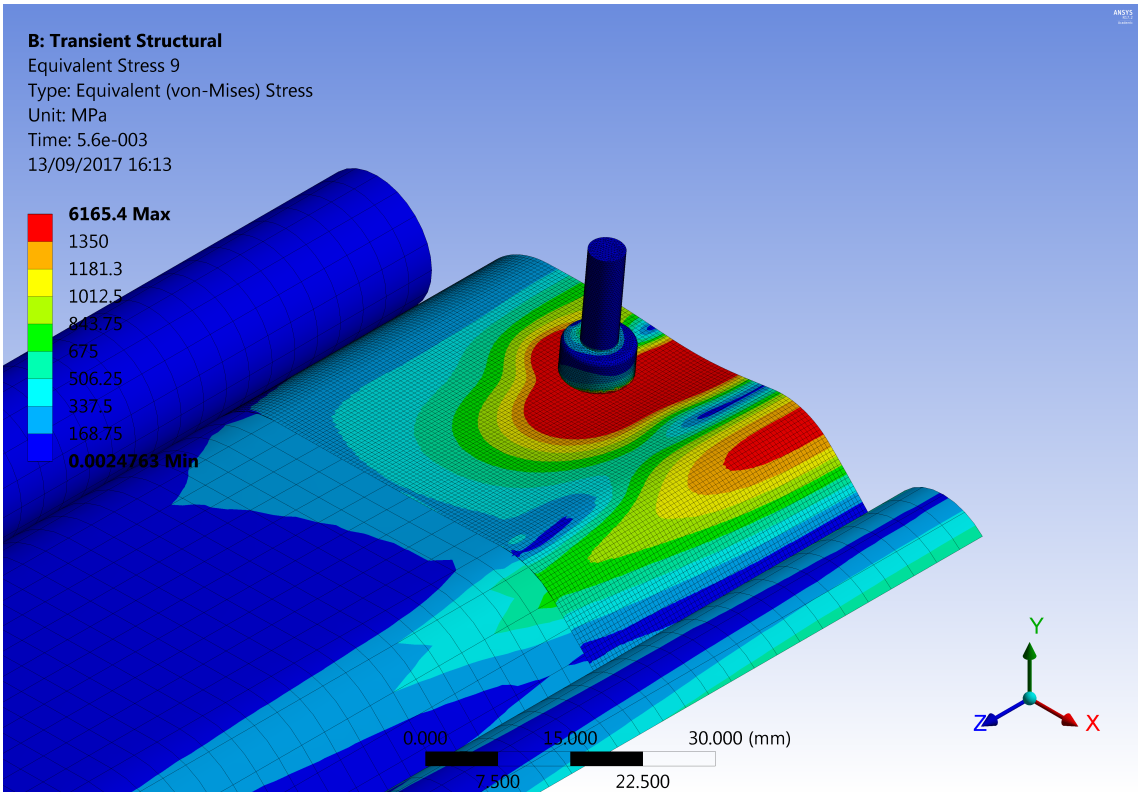


(A) (B)

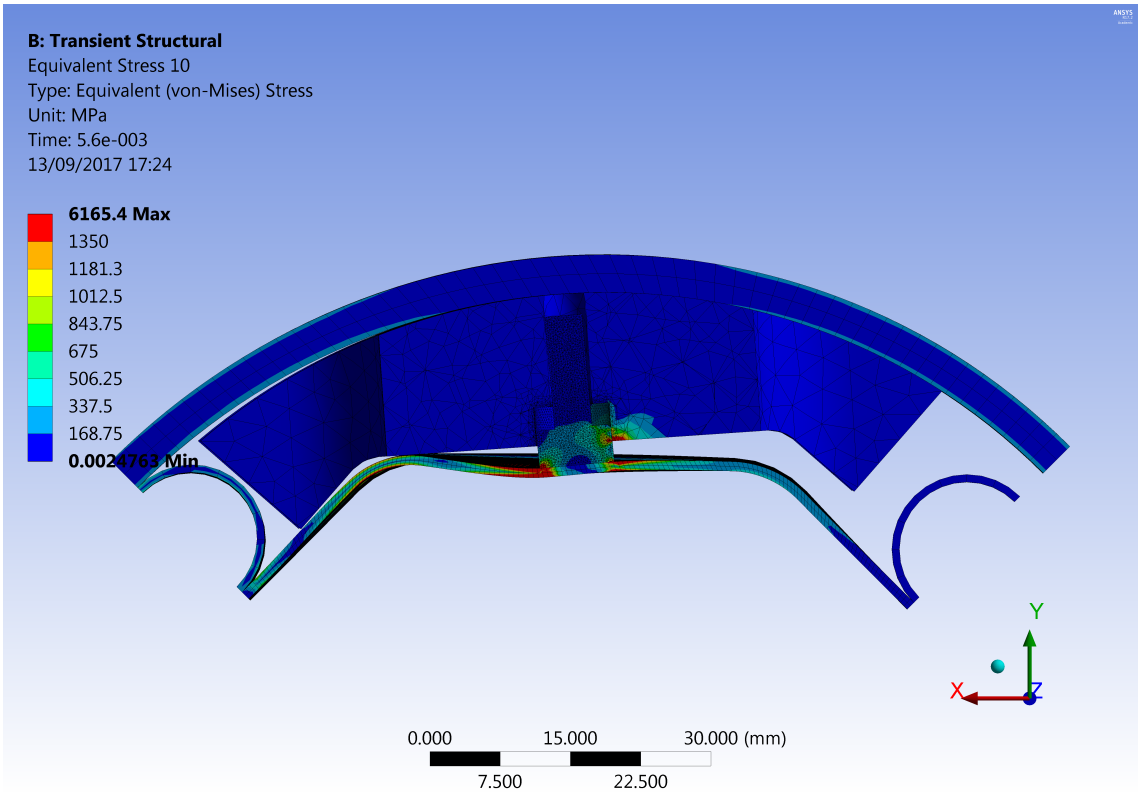
(C) (D)

FIGURE 6.25: New concept of the pin to withstand the CLIQ discharge and integration with the interfacing systems. In (c) the force distribution around the pin with or without CLIQ.

The stress state of the pin welded on the reinforcement plate 2 mm thick and of the nearby region is reported in Fig. 6.29. The region exceeding the elastic limit (in red) are now almost absent. The elastic limit is partially exceeded only on the surface of the reinforcement plate and at the extremities of the welding lines. This solution guarantees the mechanical integrity of the Q1 beam screen during a CLIQ discharge.

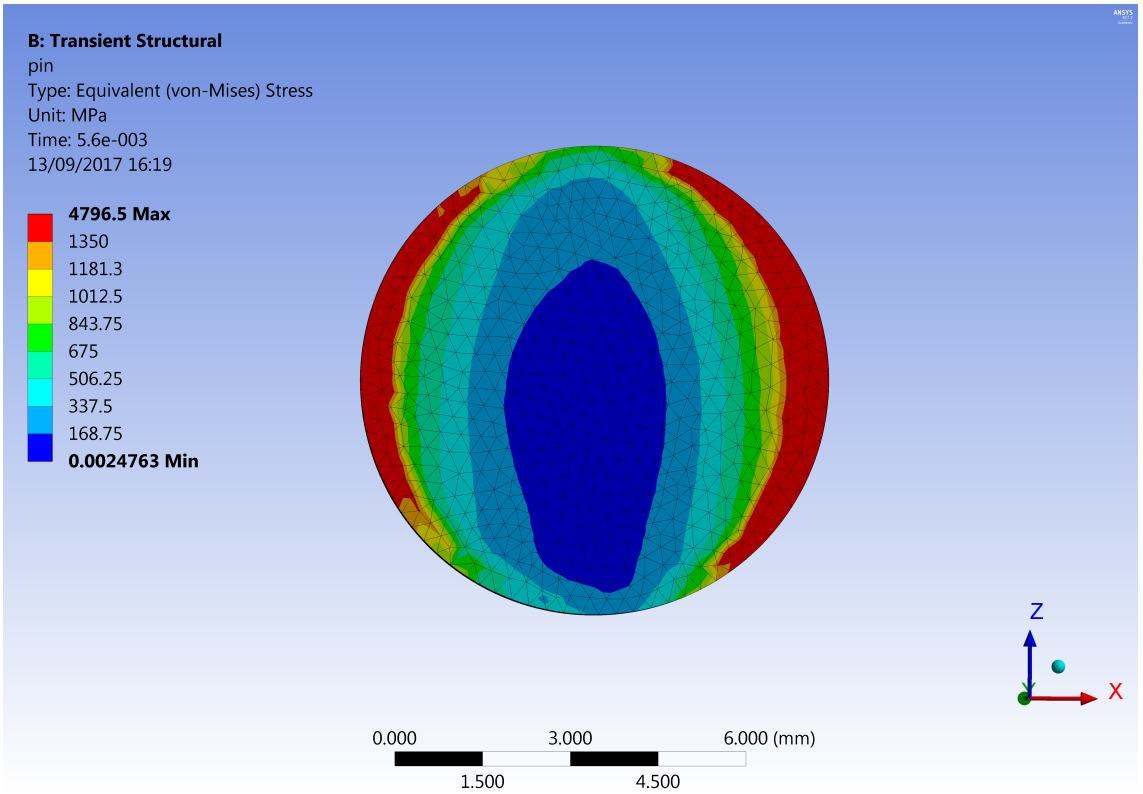


(A)

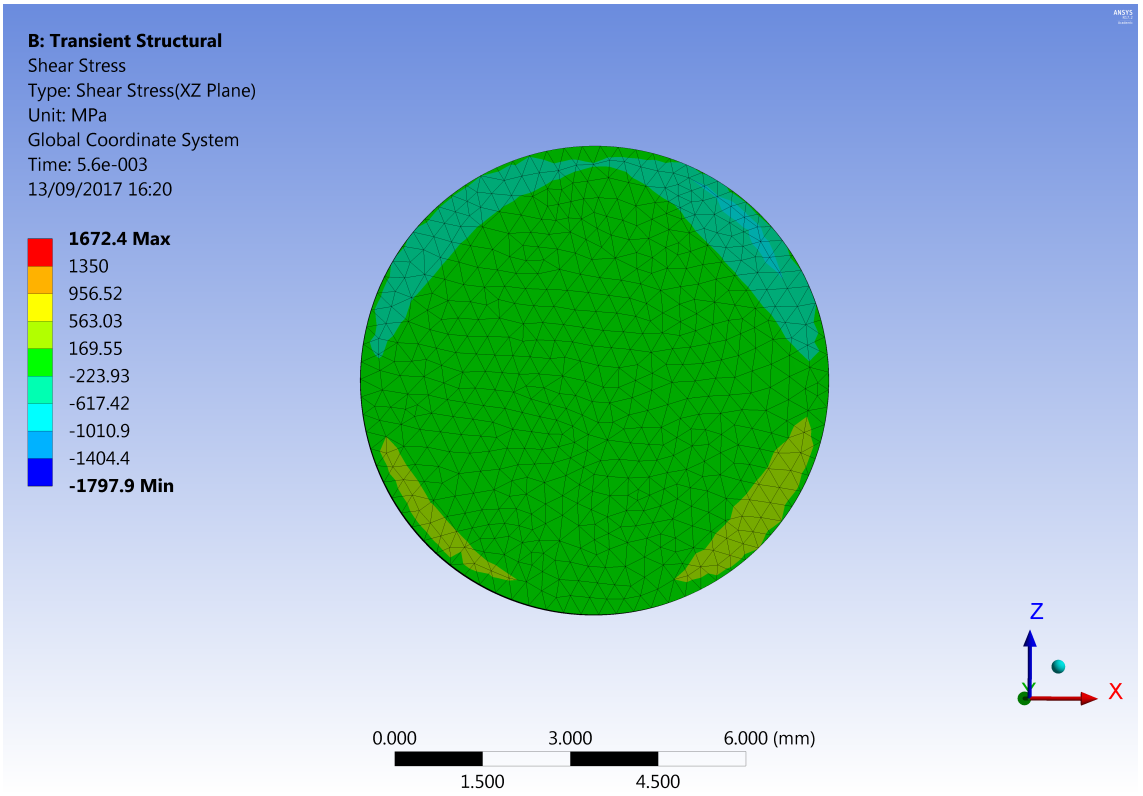


(B)

FIGURE 6.26: Equivalent stress of the Q1 beam screen, in particular: octagonal pipe (a), cross section of the beam screen (b), bottom face of the pin (c), cross section of the octagonal pipe and pin (e), and cross section of the pin itself (f). The shear stress of the bottom face of the pin on the XZ plane is in (d). The elastic limit is set to 1350 MPa on the legend to highlight the regions that undergo plastic deformations (in red).

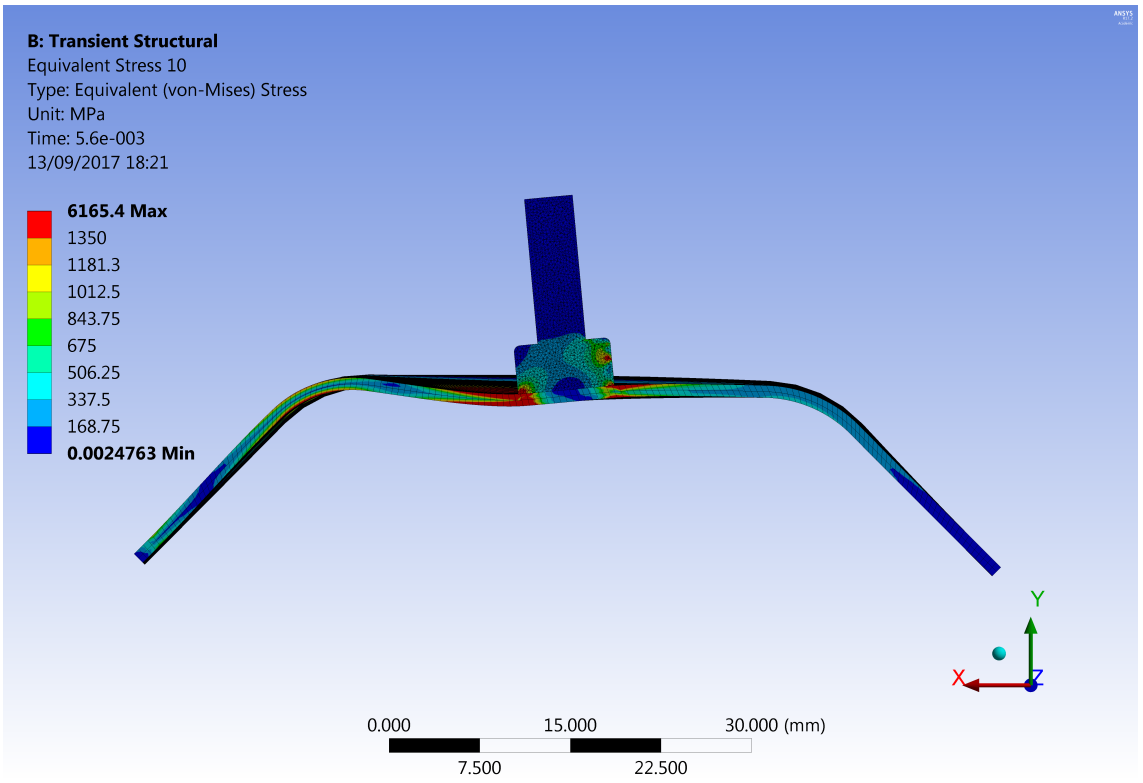


(C)

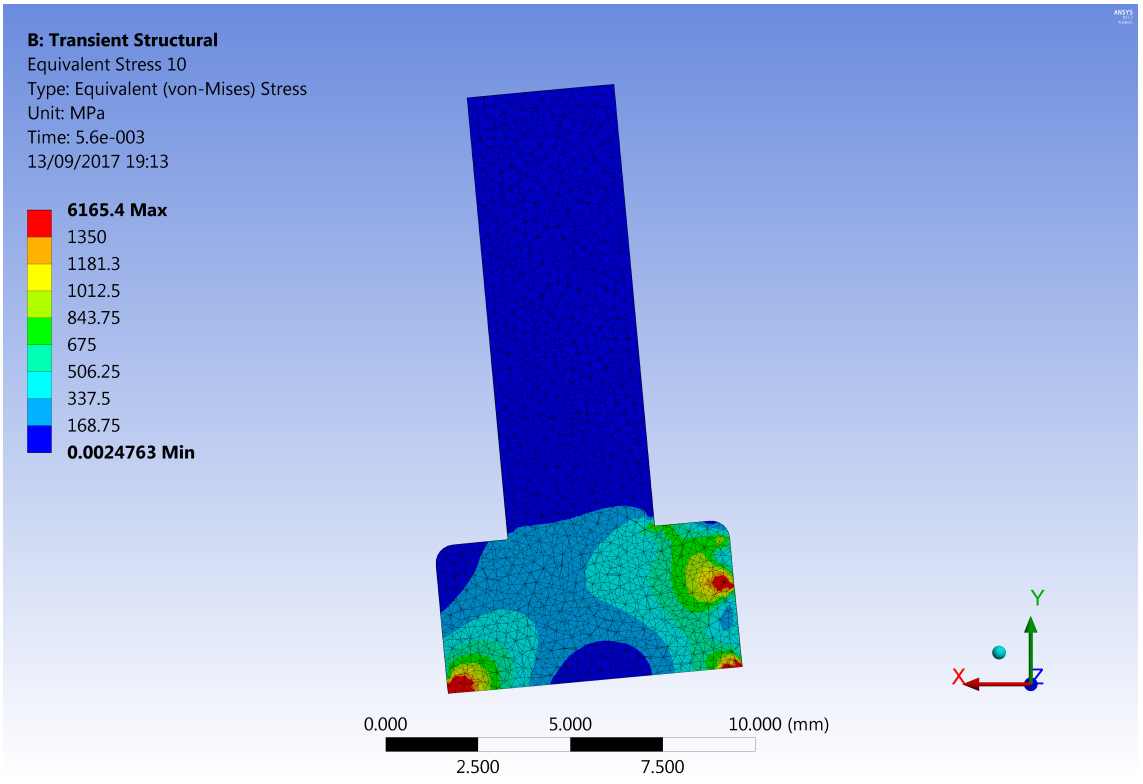


(D)

FIGURE 6.26: (continued) Equivalent stress of the Q1 beam screen, in particular: octagonal pipe (a), cross section of the beam screen (b), bottom face of the pin (c), cross section of the octagonal pipe and pin (e), and cross section of the pin itself (f). The shear stress of the bottom face of the pin on the XZ plane is in (d). The elastic limit is set to 1350 MPa on the legend to highlight the regions that undergo plastic deformations (in red).

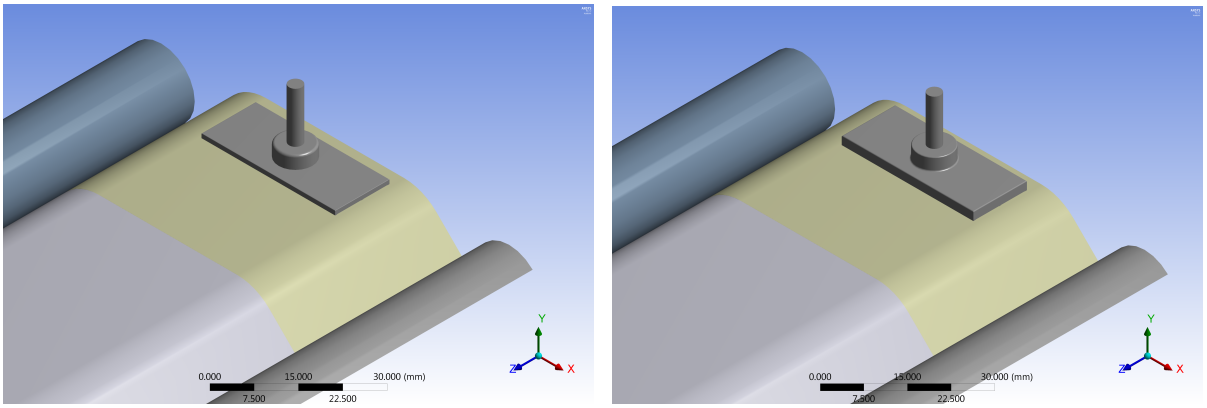


(E)



(F)

FIGURE 6.26: (continued) Equivalent stress of the Q1 beam screen, in particular: octagonal pipe (a), cross section of the beam screen (b), bottom face of the pin (c), cross section of the octagonal pipe and pin (e), and cross section of the pin itself (f). The shear stress of the bottom face of the pin on the XZ plane is in (d). The elastic limit is set to 1350 MPa on the legend to highlight the regions that undergo plastic deformations (in red).



(A) (B)

FIGURE 6.27: Reinforcement plates added on the octagonal pipe. In (a) the thickness is 1 mm while in (b) it is 2 mm.

6.6.2 Q2 beam screen

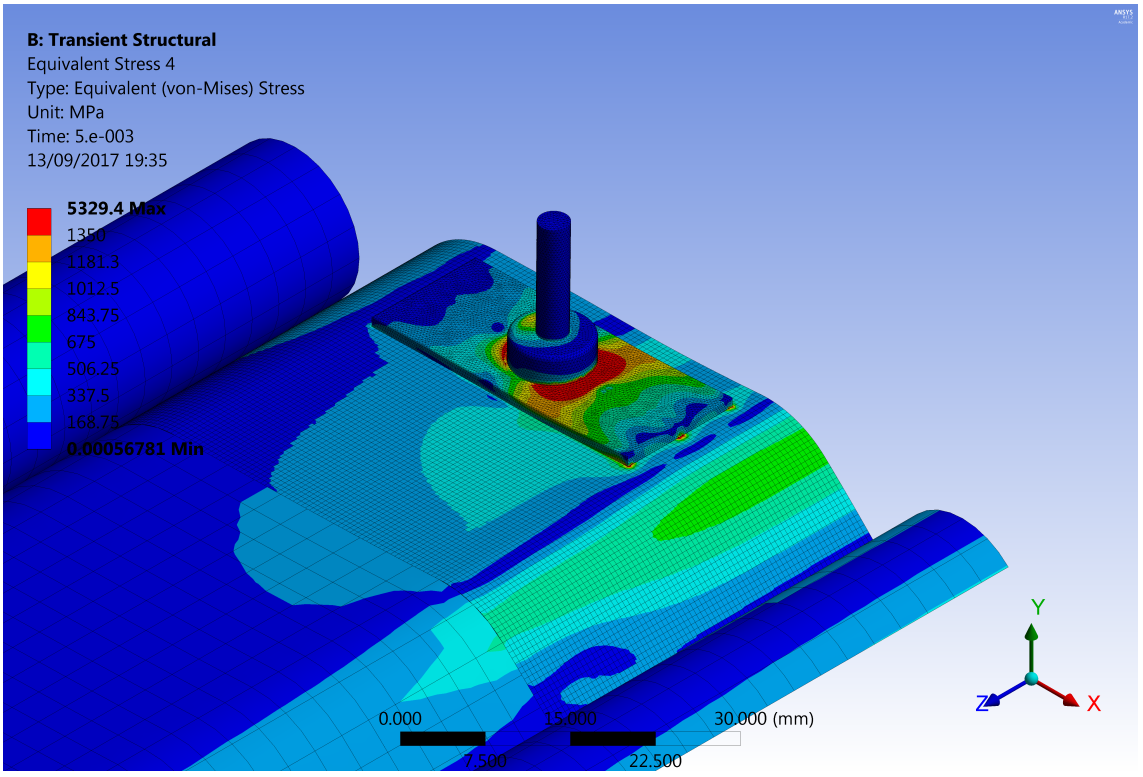
Original design

The torque generated during the first phase of the CLIQ discharge is applied to the original design of the Q2 beam screen. As seen for the Q1, the centring pin welded on the octagonal pipe is now loaded and its mechanical integrity might be compromised. Fig. 6.30 shows the differences between the straight and the new pin with different loading conditions. As for the Q1 pin, the Q2 pin presents an increased diameter at the base (from 5 mm to 8 mm) and a height of 3 mm in order to reduce the torque to be absorbed locally by the pin itself.

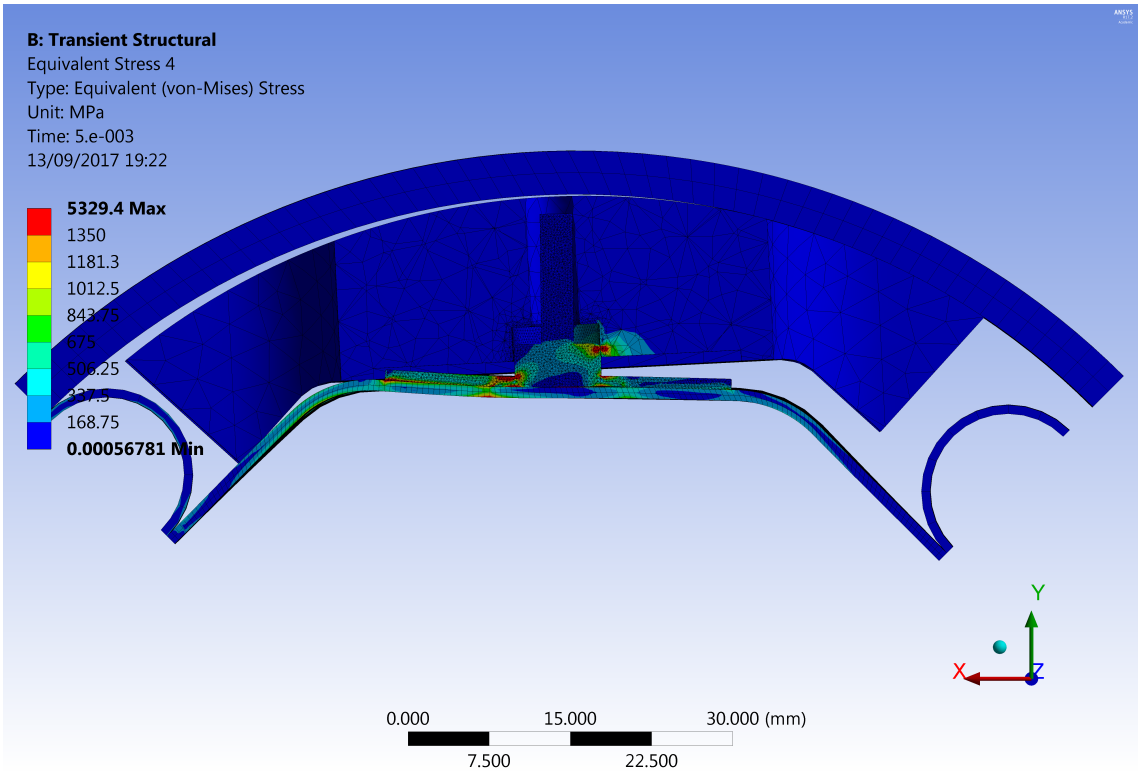
The stress state of the octagonal pipe is shown in Fig. 6.31 at 5 ms. Severe plastic deformations (red regions) are visible on a limited region of the screen and across the thickness of the pipe. As for the Q1 octagonal pipe, this would cause permanent distortion of the beam aperture as well as damage to the pin.

New design

The stress state of the new pin and of the region nearby it, is reported in Fig. 6.32. Due to the lower torque exerted by the heat absorber, the elastic limit is not exceeded anywhere and therefore the reinforcement plate.

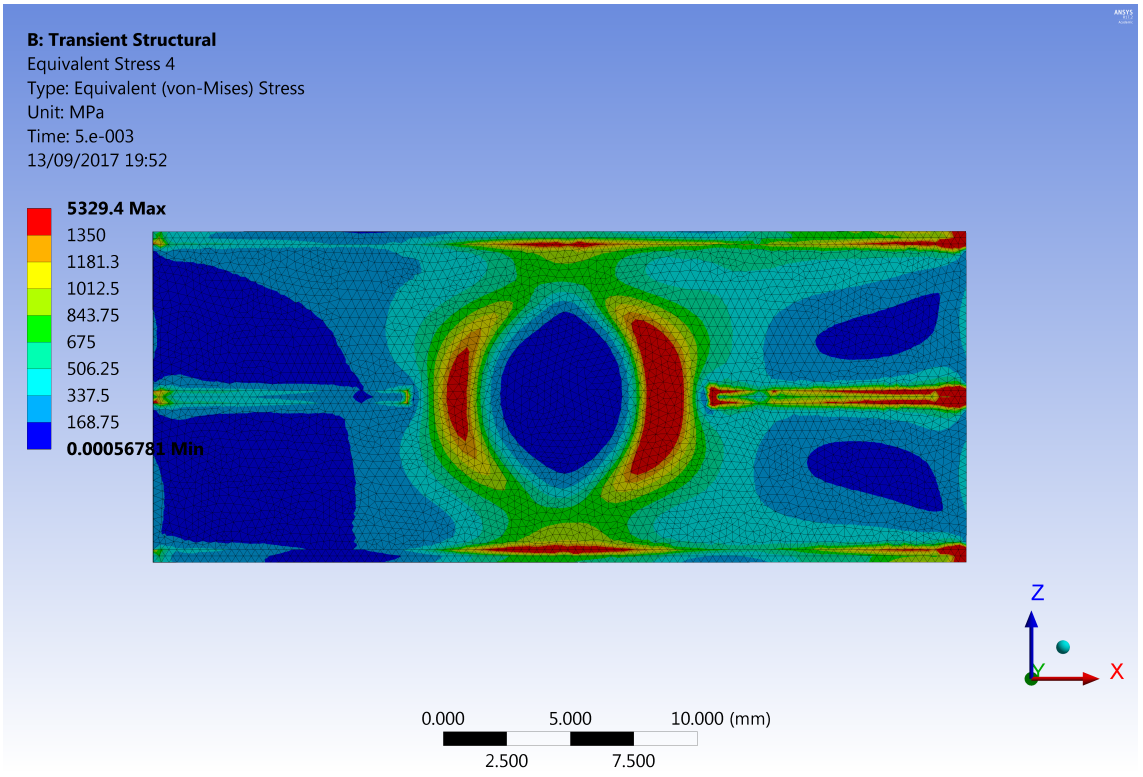


(A)

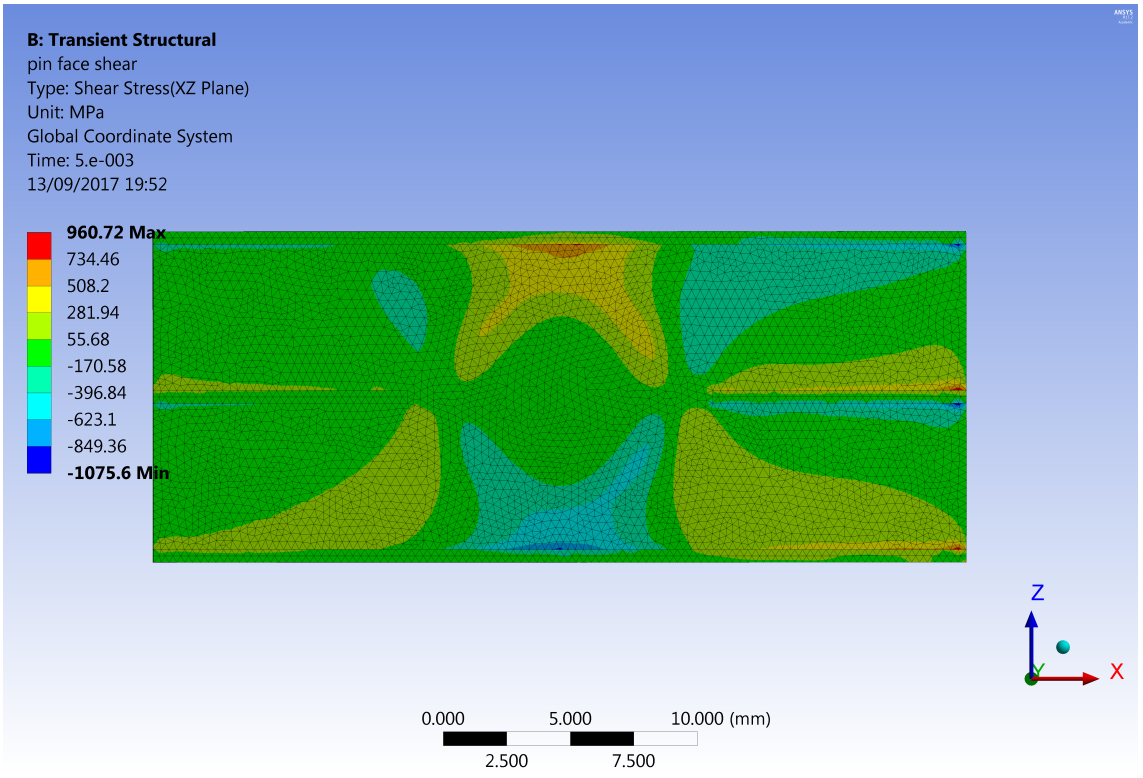


(B)

FIGURE 6.28: Equivalent stress of the Q1 beam screen equipped with a reinforcement plate 1 mm thick: octagonal pipe (a), cross section of the beam screen (b), bottom face of the reinforcement plate (c), cross section of the octagonal pipe and pin (e), and cross section of the pin itself (f). The shear stress of the bottom face of the reinforcement plate on the XZ plane is in (d). The elastic limit is set to 1350 MPa on the legend to highlight the regions that undergo plastic deformations (in red).

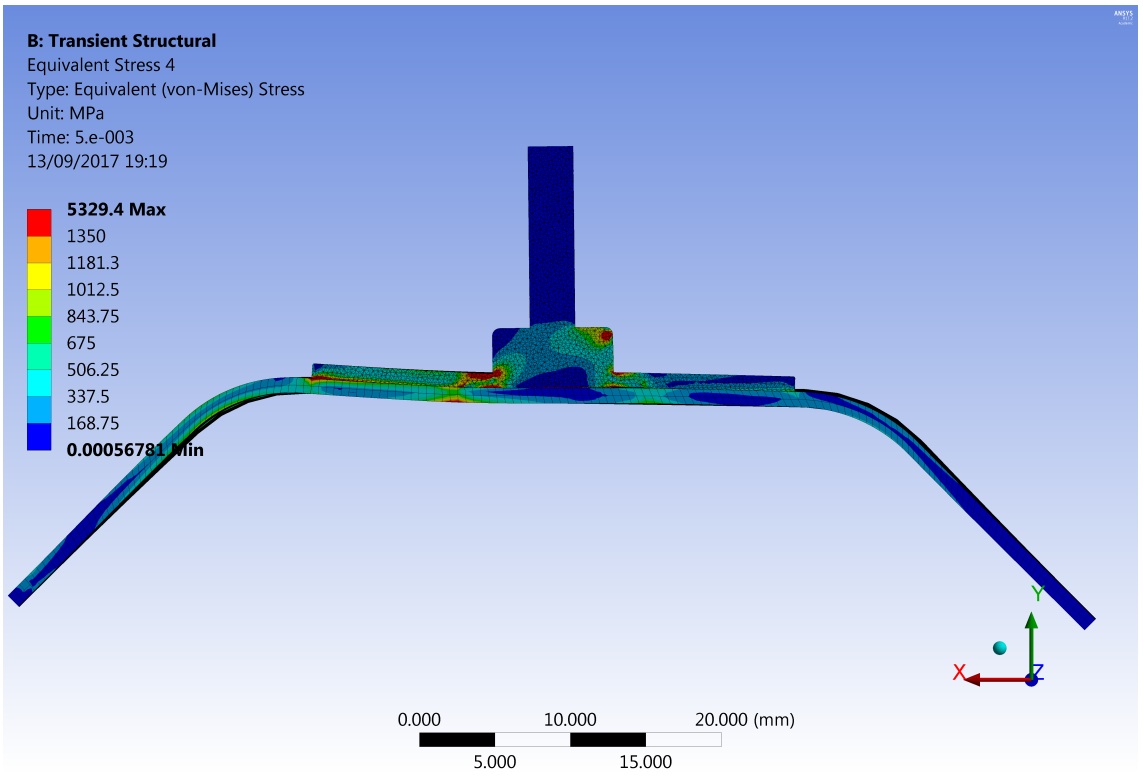


(C)

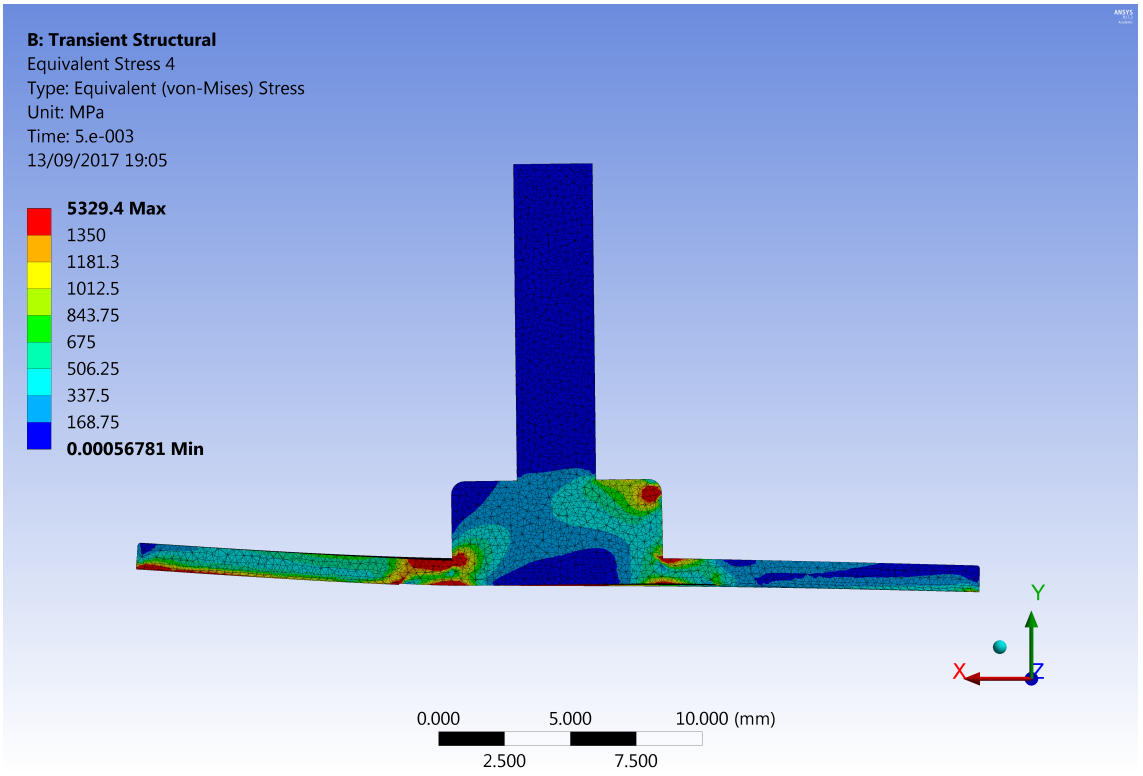


(D)

FIGURE 6.28: (continued) Equivalent stress of the Q1 beam screen equipped with a reinforcement plate 1 mm thick: octagonal pipe (a), cross section of the beam screen (b), bottom face of the reinforcement plate (c), cross section of the octagonal pipe and pin (e), and cross section of the pin itself (f). The shear stress of the bottom face of the reinforcement plate on the XZ plane is in (d). The elastic limit is set to 1350 MPa on the legend to highlight the regions that undergo plastic deformations (in red).

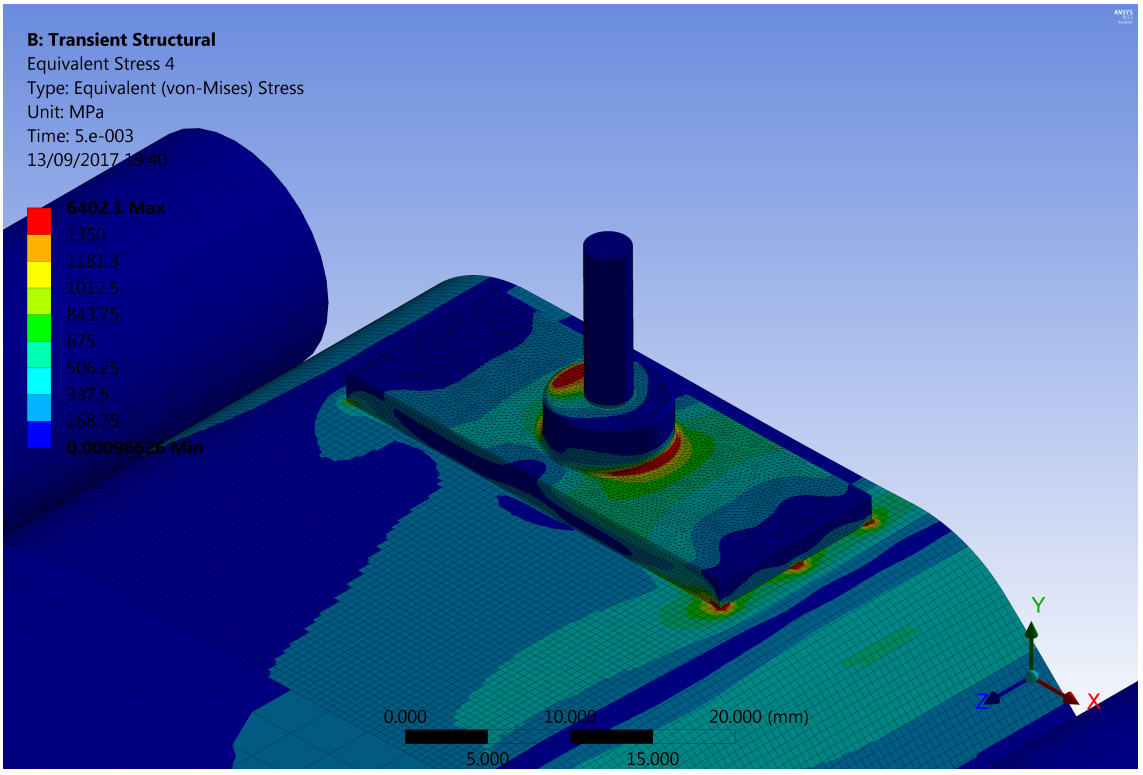


(E)

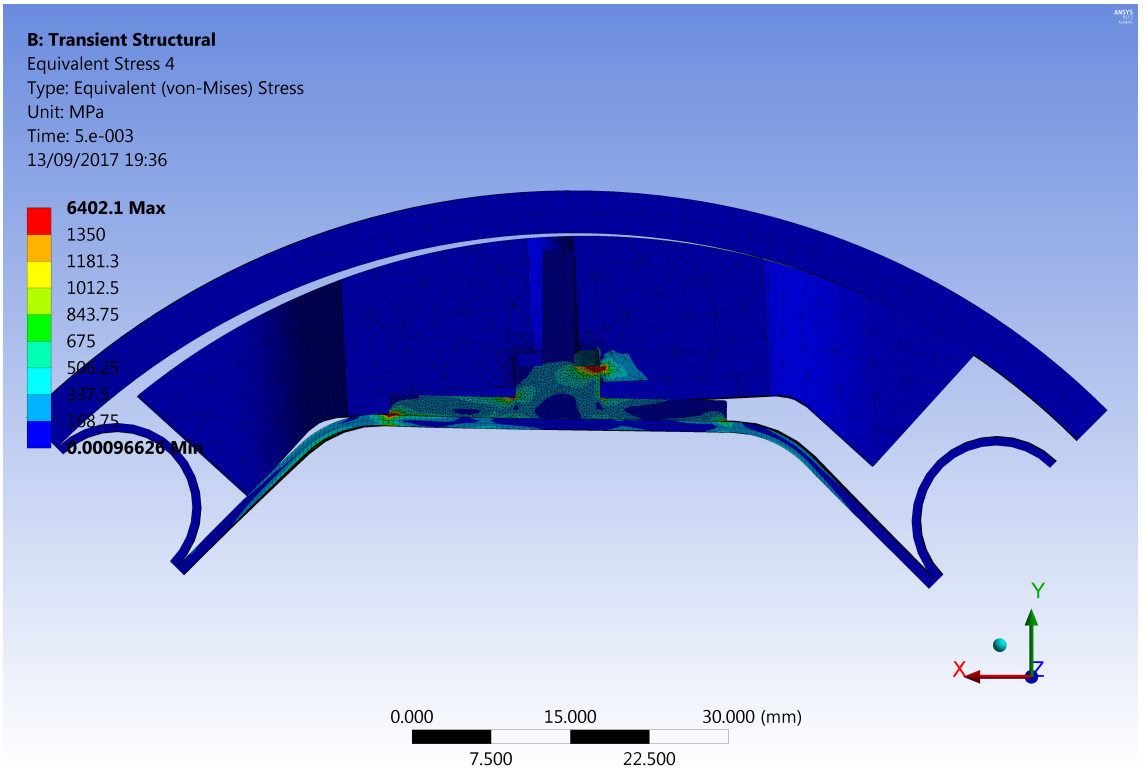


(F)

FIGURE 6.28: (continued) Equivalent stress of the Q1 beam screen equipped with a reinforcement plate 1 mm thick: octagonal pipe (a), cross section of the beam screen (b), bottom face of the reinforcement plate (c), cross section of the octagonal pipe and pin (e), and cross section of the pin itself (f). The shear stress of the bottom face of the reinforcement plate on the XZ plane is in (d). The elastic limit is set to 1350 MPa on the legend to highlight the regions that undergo plastic deformations (in red).

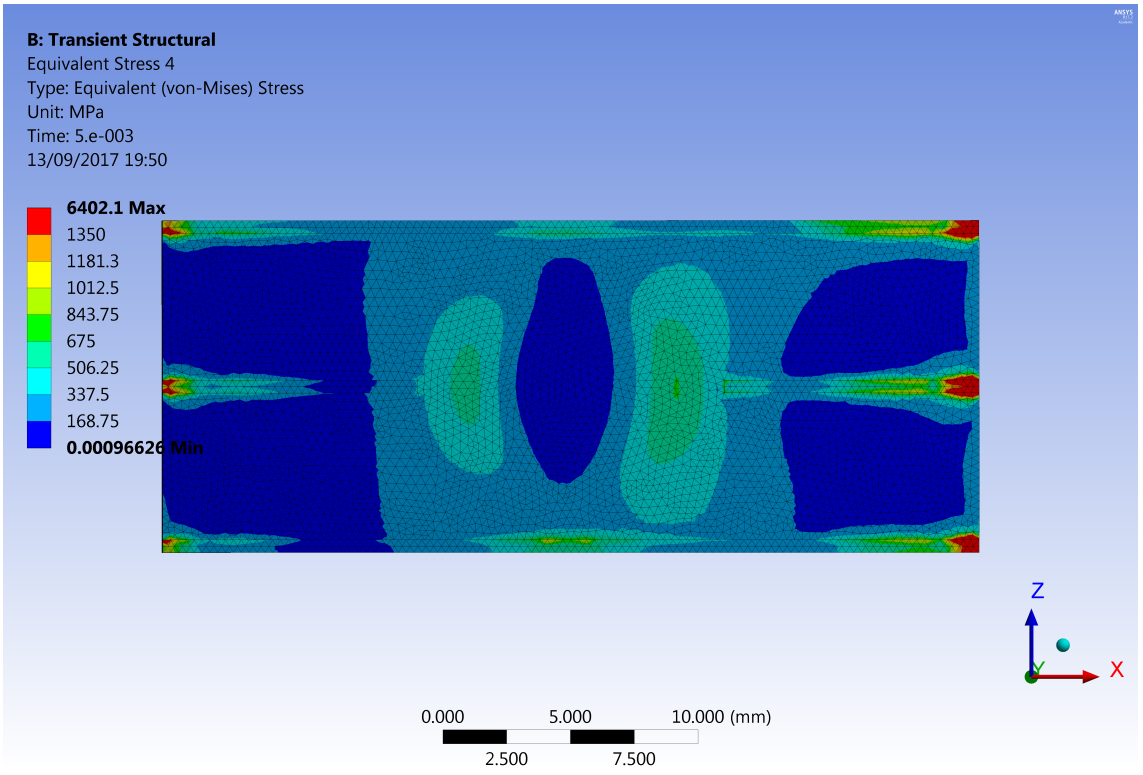


(A)

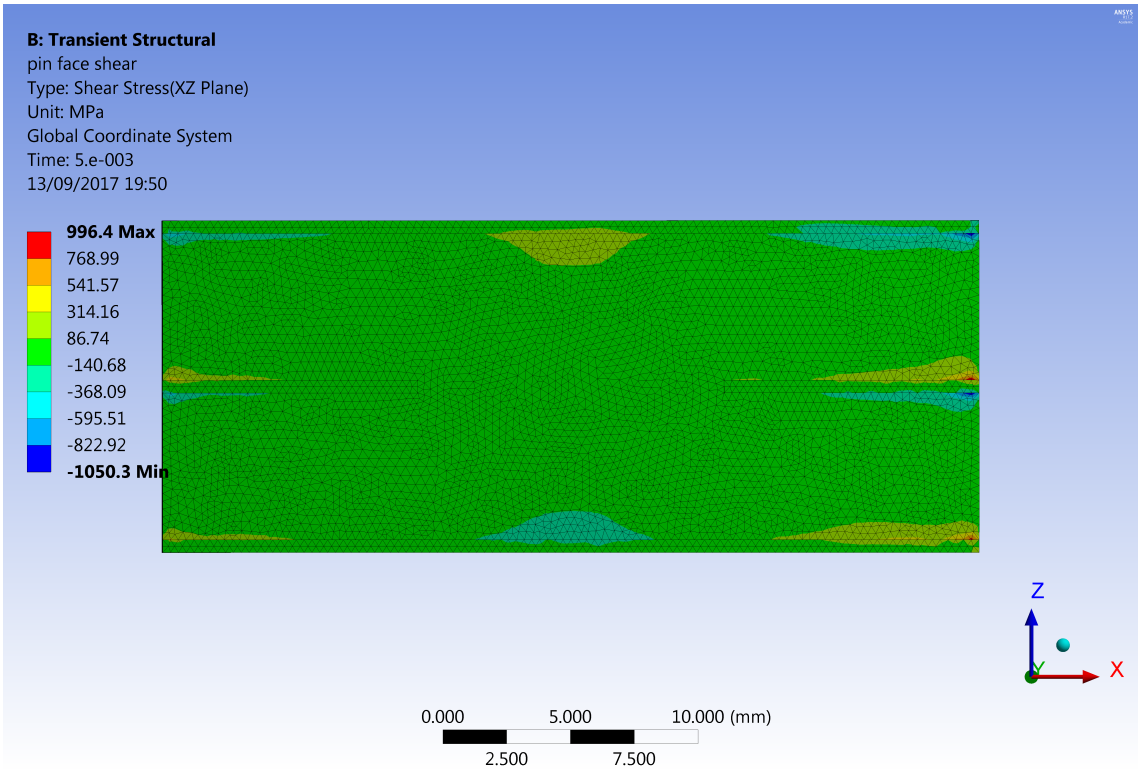


(B)

FIGURE 6.29: Equivalent stress of the Q1 beam screen equipped with a reinforcement plate 2 mm thick: octagonal pipe (a), cross section of the beam screen (b), bottom face of the reinforcement plate (c), cross section of the octagonal pipe and pin (e), and cross section of the pin itself (f). The shear stress of the bottom face of the reinforcement plate on the XZ plane is in (d). The elastic limit is set to 1350 MPa on the legend to highlight the regions that undergo plastic deformations (in red).

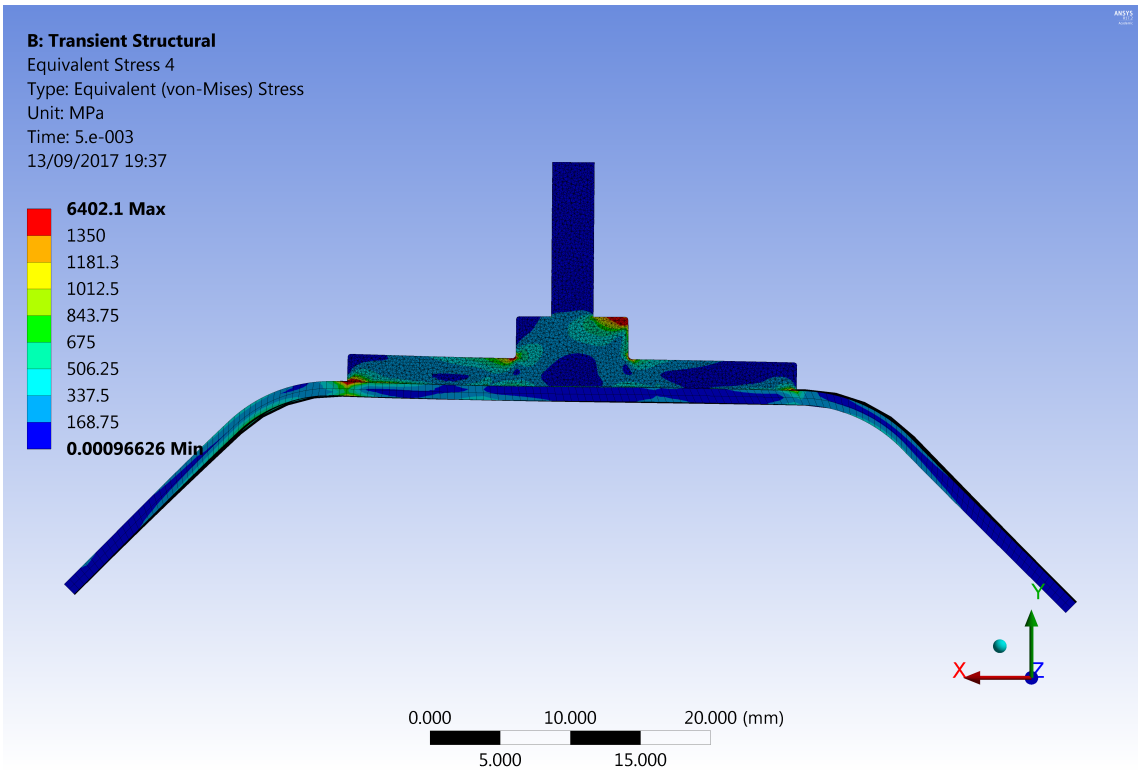


(C)

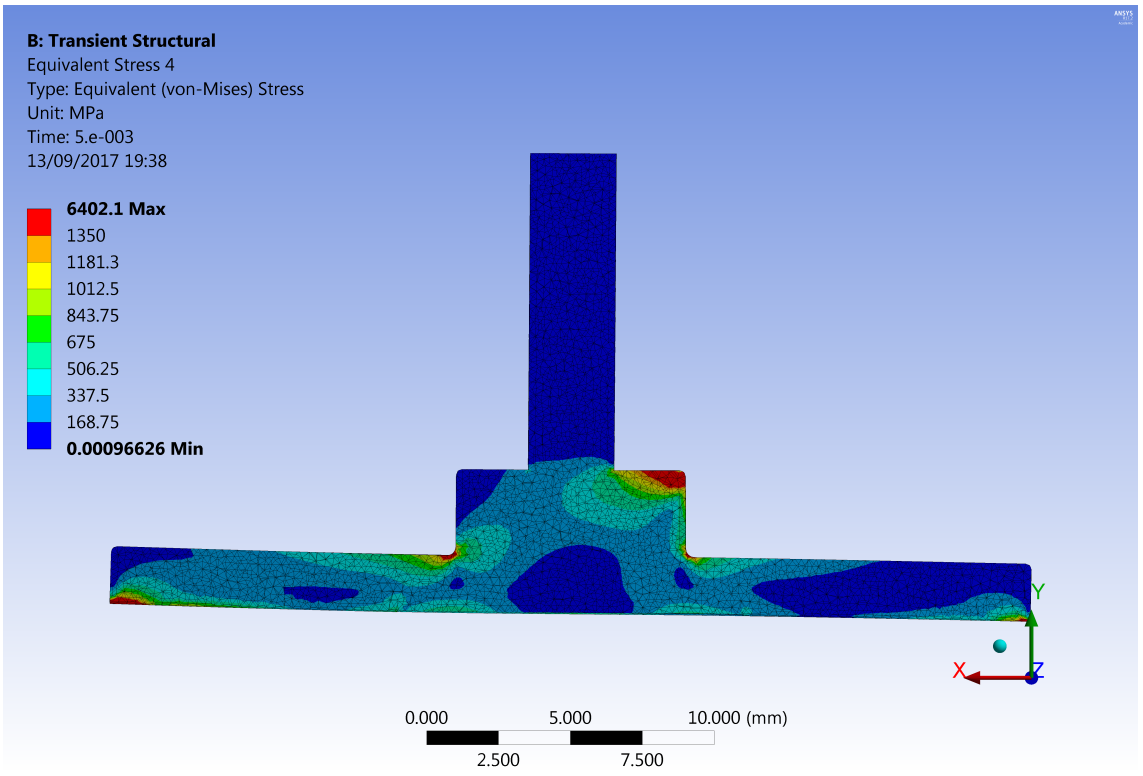


(D)

FIGURE 6.29: (continued) Equivalent stress of the Q1 beam screen equipped with a reinforcement plate 2 mm thick: octagonal pipe (a), cross section of the beam screen (b), bottom face of the reinforcement plate (c), cross section of the octagonal pipe and pin (e), and cross section of the pin itself (f). The shear stress of the bottom face of the reinforcement plate on the XZ plane is in (d). The elastic limit is set to 1350 MPa on the legend to highlight the regions that undergo plastic deformations (in red).

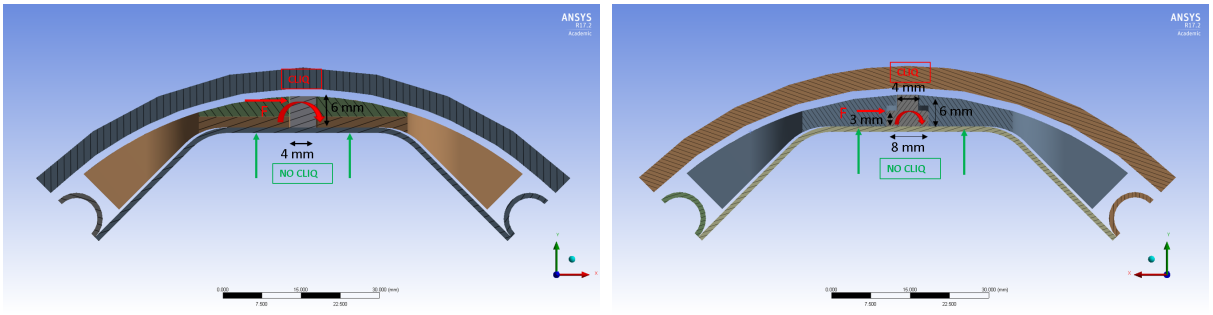


(E)



(F)

FIGURE 6.29: (continued) Equivalent stress of the Q1 beam screen equipped with a reinforcement plate 2 mm thick: octagonal pipe (a), cross section of the beam screen (b), bottom face of the reinforcement plate (c), cross section of the octagonal pipe and pin (e), and cross section of the pin itself (f). The shear stress of the bottom face of the reinforcement plate on the XZ plane is in (d). The elastic limit is set to 1350 MPa on the legend to highlight the regions that undergo plastic deformations (in red).



(A) (B)

FIGURE 6.30: Cross section of the Q2 beam screen equipped with the straight pin in (a) and with the double diameter pin in (b).

6.6.3 Heat absorber - cold bore interaction

The analyses of the interaction between the heat absorber and the cold bore for the Q1 and Q2 beam screen are described in this section. As shown in Fig. 6.33, the highest displacement of the cold bore takes place at $+/-45°$ angle. The time evolution of the radial displacement of the cold bore vertex placed at $45°$ angle is shown in Fig. 6.34 for the Q1 and Q2 beam screen. For the Q1 assembly, the cold bore displacement is shown when the pin is welded on the octagonal pipe and on the reinforcement plate, whose thickness is 1 mm and 2 mm. In general, the maximum radial displacement occurs at around 3 ms and is approximately 1.5 mm. It is slightly reduced when the reinforcement plates is used. For the Q2 assembly, the maximum displacement of the cold bore is 1.1 mm and takes place at around 5 ms.

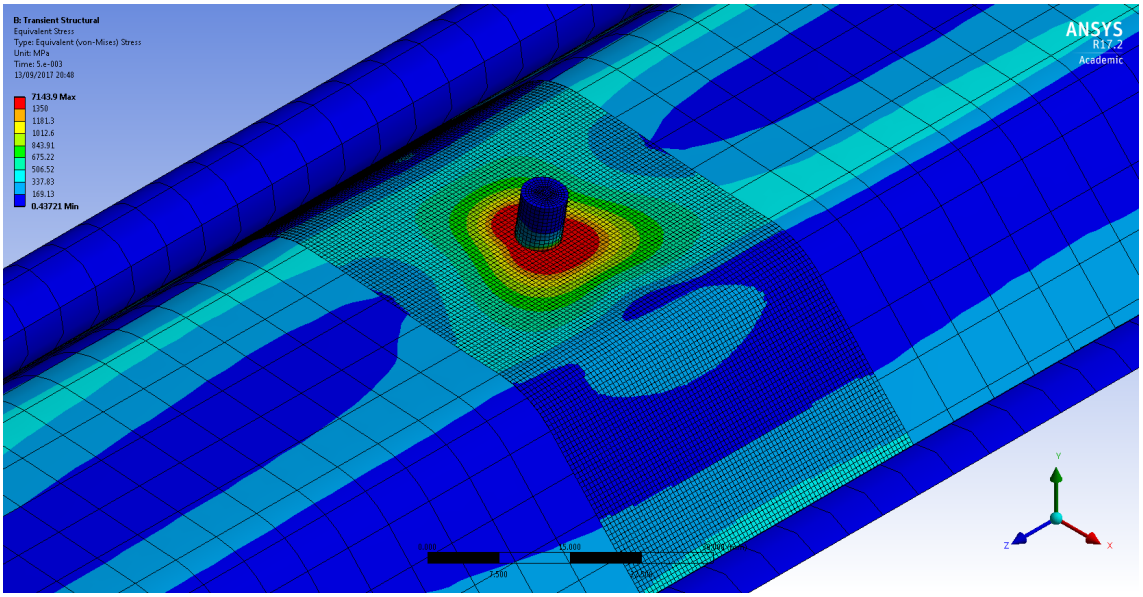
The highest stress of the heat absorber in terms of von Mises and maximum principal stress is shown in Fig. 6.35 in correspondence of the maximum radial displacement of the cold bore. The stress in the Q2 heat absorber wing, being thinner, is higher than that of the Q1 absorbers. However, as the elastic limit is not exceeded anywhere, the cold bore is not damaged during the CLIQ discharge.

The highest von Mises stress is shown in Fig. 6.36 for the cold bore hit by the Q1 heat absorber and by the Q2 heat absorber, respectively. For both the cases, the highest equivalent stress is well below the elastic limit.

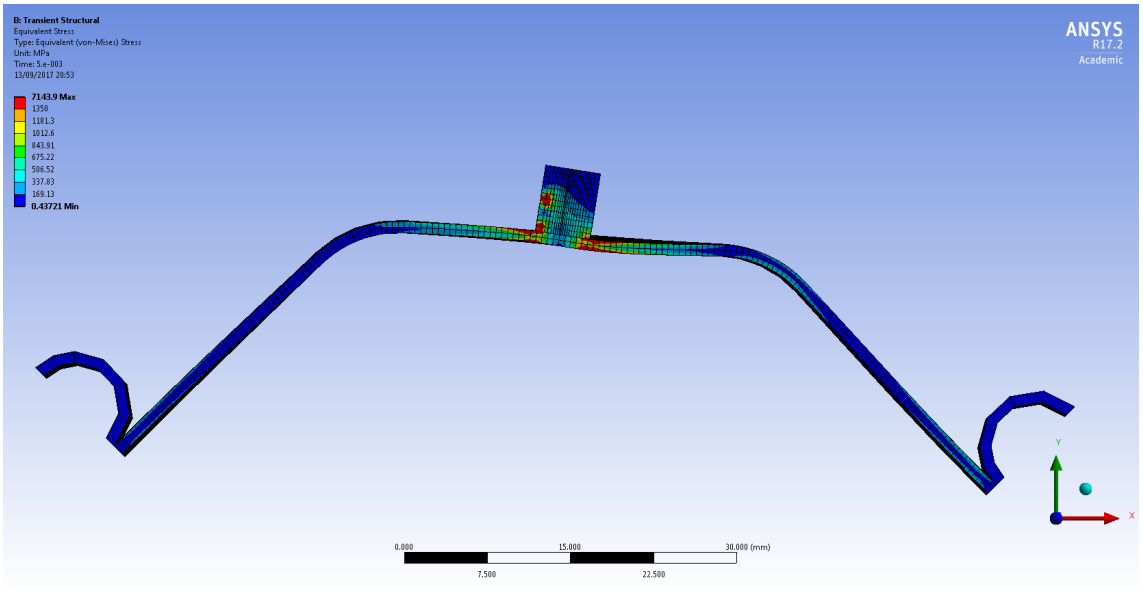
6.6.4 Cold bore - magnet coil interaction

In comparison with the deformations of the cold bore due to a monotonic magnetic field decay seen in chapter 5, the deformations relative to the CLIQ discharge, and in particular to its first region, are larger. In fact, even if the forces of the first region are less intense than the case without CLIQ, the cold bore is loaded alternatively only along a line tilted at $45°$ angle.

Considering that the beam screen assembly is supported by pins placed in the magnet pole at $+/-45°$ angle, the forces to be absorbed by such pins are of interest and need to be determined. To this purpose, an analysis to assess the forces transferred to the pins in the first region of the CLIQ discharge has been performed. The model used for the analysis is the same as the one used to characterise the effects of the CLIQ discharge. Two pins, considered as fixed, have been added at $45°$ and $135°$ angle to quantify the magnitude of the forces transferred when the absorber hits the cold bore, see Fig. 6.37. Periodic conditions are applied on the longitudinal and lateral faces of the 20 cm long assembly. This symmetry results in a quarter of a pin placed in correspondence of each magnet poles every 40 cm.

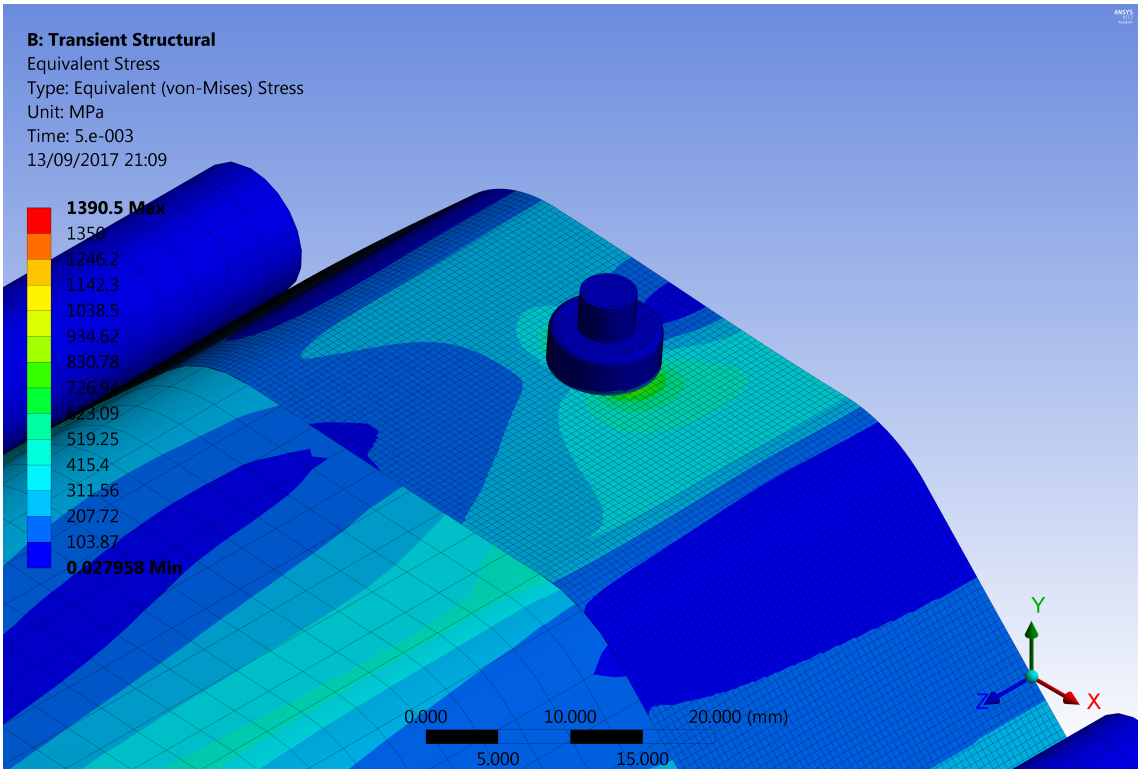


(A)

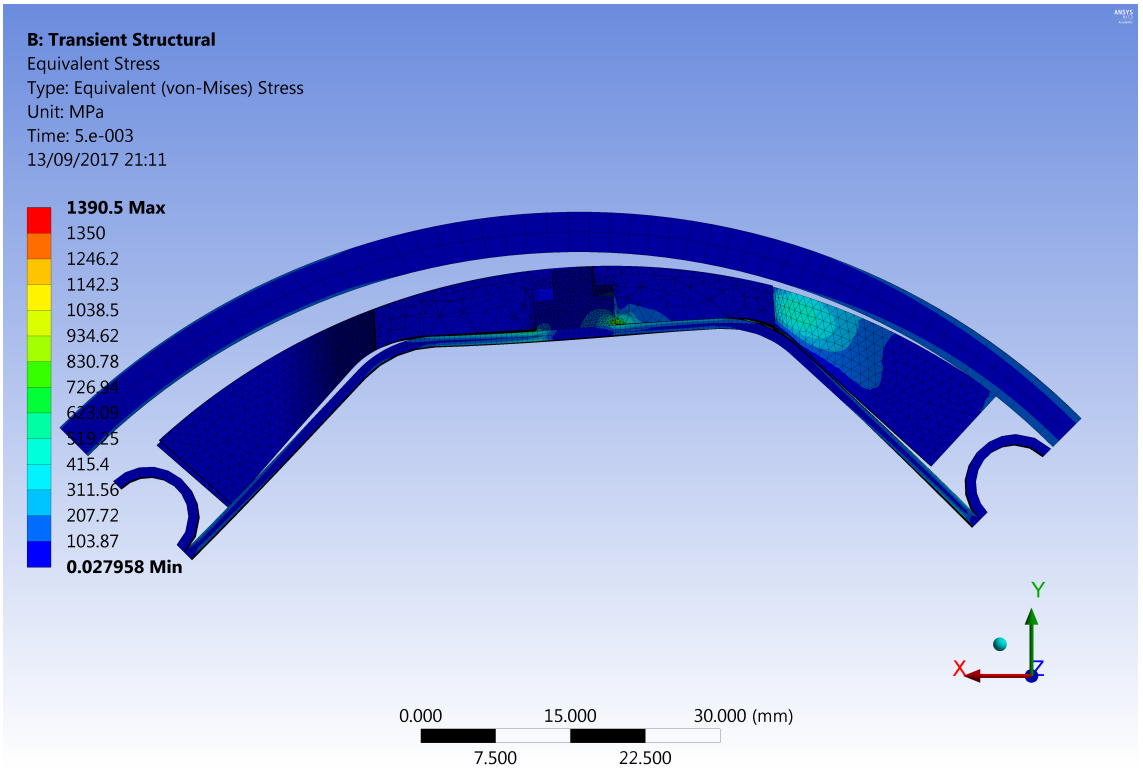


(B)

FIGURE 6.31: In (a) von Mises stress state of the Q2 octagonal pipe at 5 ms. In (b) cross section view of the octagonal pipe. The upper bound of the legend is set to 1350 MPa, elastic limit of the material, to highlight plastically deformed regions.

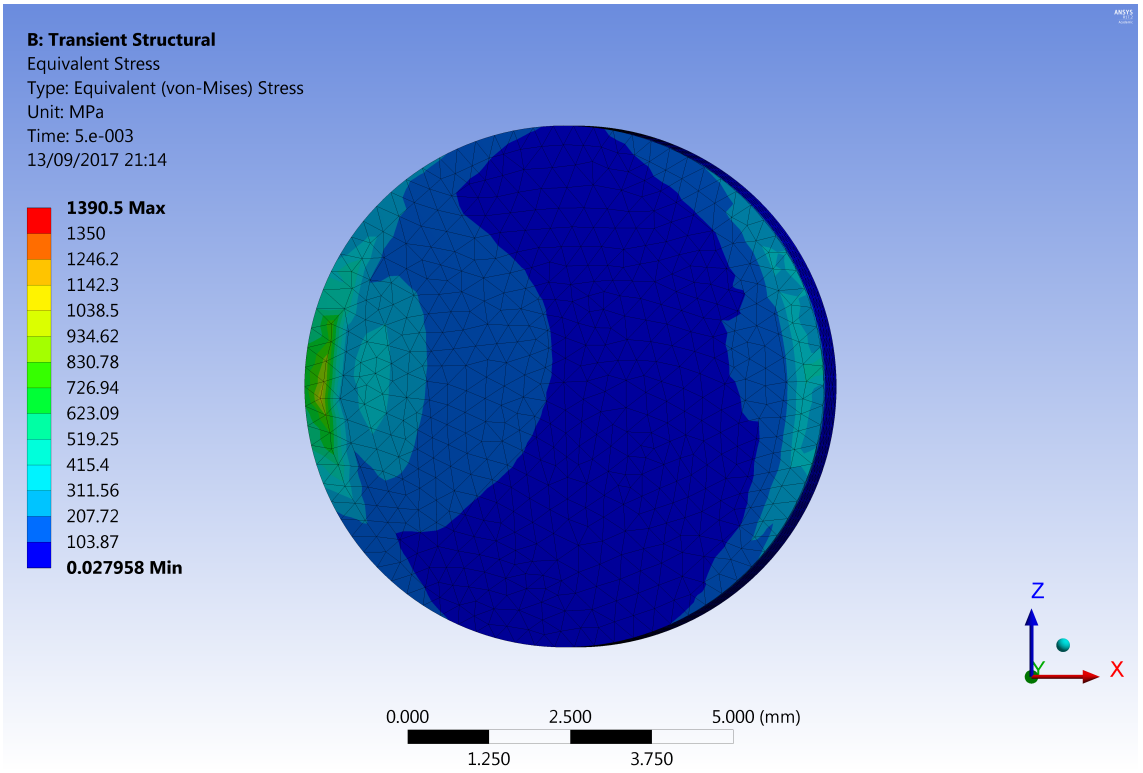


(A)

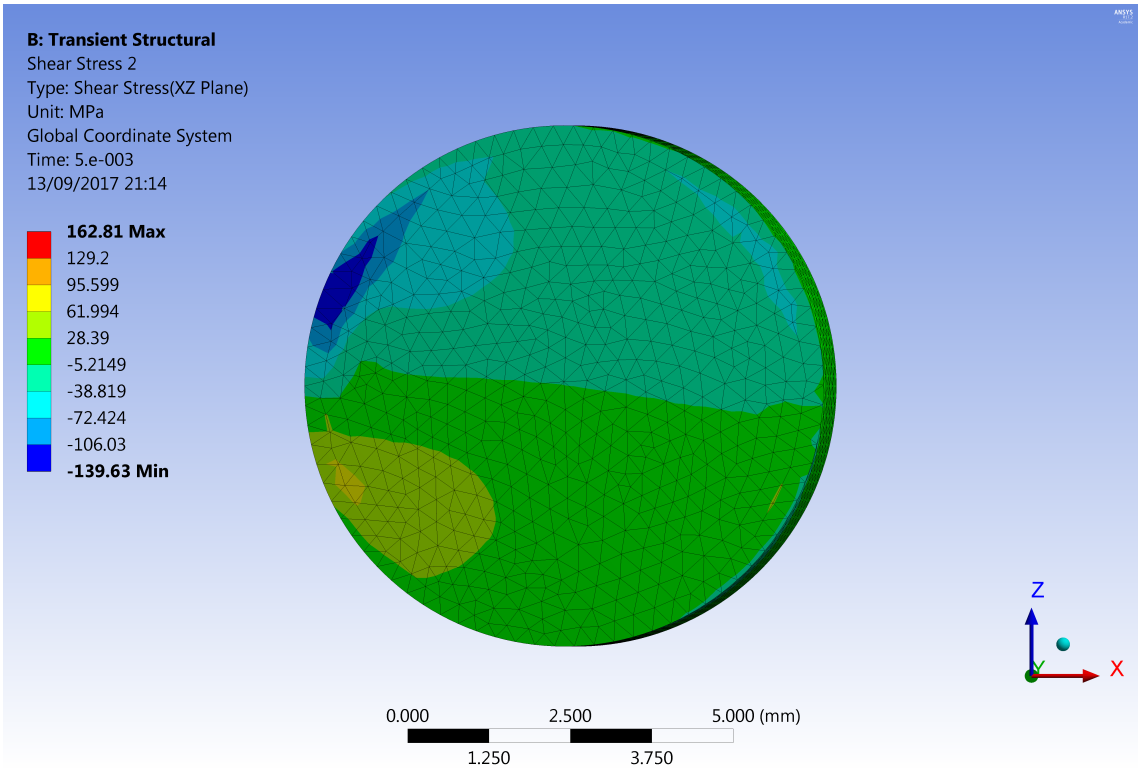


(B)

FIGURE 6.32: Equivalent stress of the Q2 beam screen, in particular: octagonal pipe (a), cross section of the beam screen (b), bottom face of the pin (c), cross section of the octagonal pipe and pin (e), and cross section of the pin itself (f). The shear stress of the bottom face of the pin on the XZ plane is in (d). The elastic limit is set to 1350 MPa on the legend to highlight the regions that undergo plastic deformations (in red).

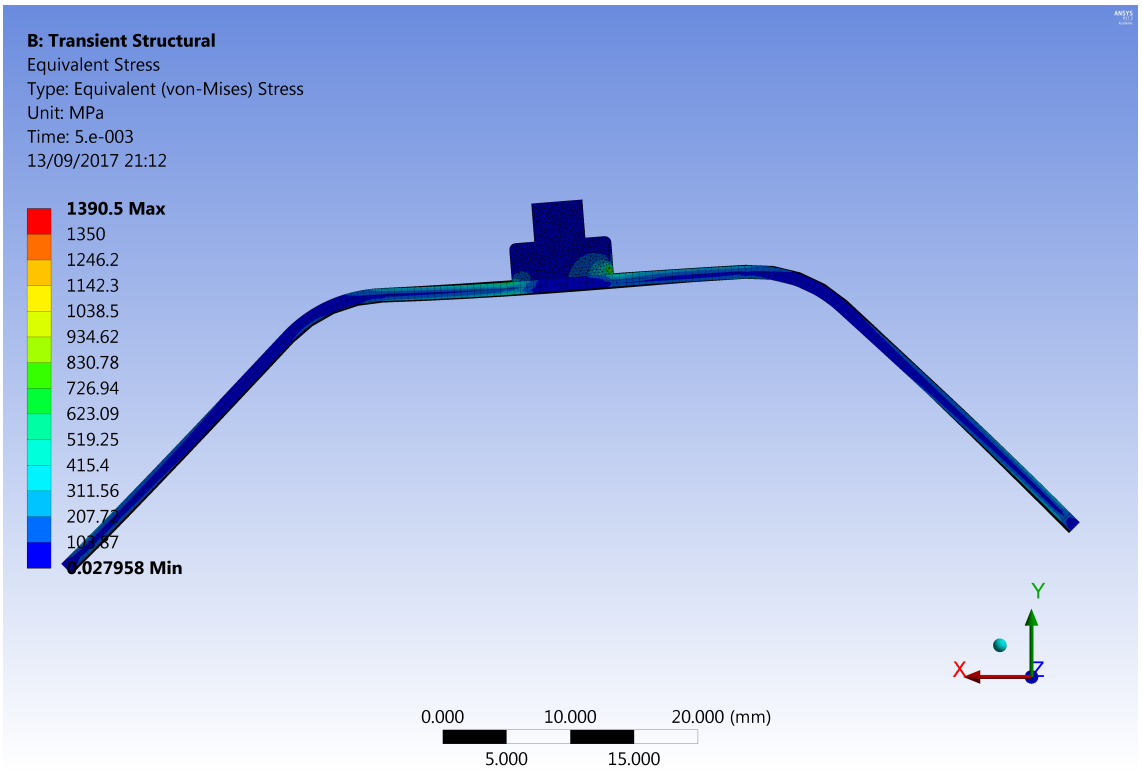


(C)

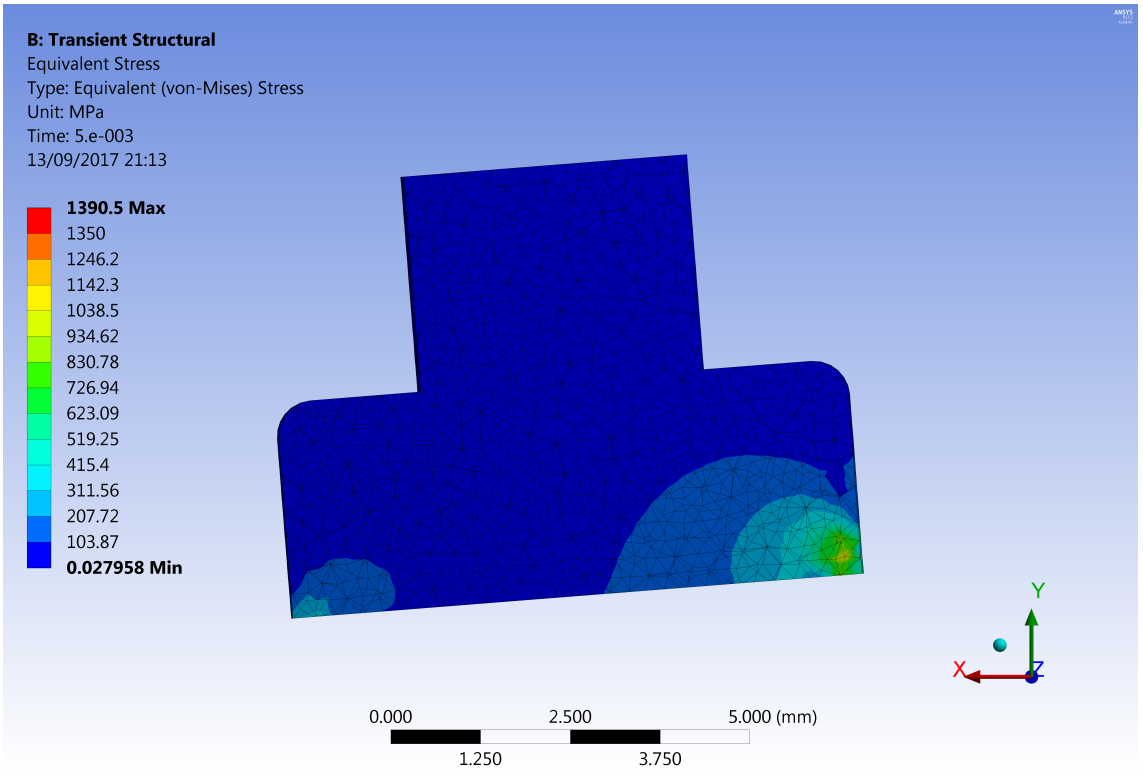


(D)

FIGURE 6.32: (continued) Equivalent stress of the Q2 beam screen, in particular: octagonal pipe (a), cross section of the beam screen (b), bottom face of the pin (c), cross section of the octagonal pipe and pin (e), and cross section of the pin itself (f). The shear stress of the bottom face of the pin on the XZ plane is in (d). The elastic limit is set to 1350 MPa on the legend to highlight the regions that undergo plastic deformations (in red).



(E)



(F)

FIGURE 6.32: (continued) Equivalent stress of the Q2 beam screen, in particular: octagonal pipe (a), cross section of the beam screen (b), bottom face of the pin (c), cross section of the octagonal pipe and pin (e), and cross section of the pin itself (f). The shear stress of the bottom face of the pin on the XZ plane is in (d). The elastic limit is set to 1350 MPa on the legend to highlight the regions that undergo plastic deformations (in red).

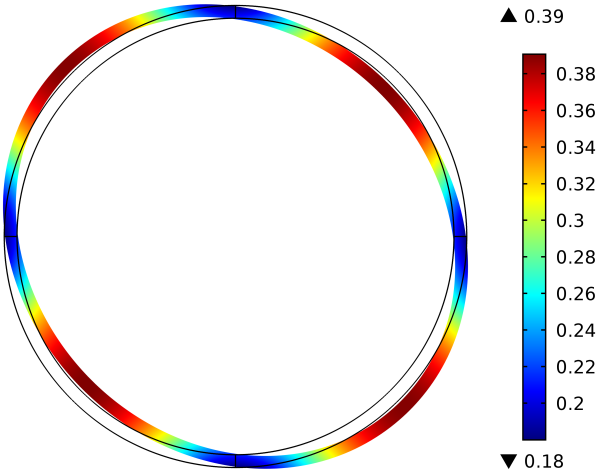


FIGURE 6.33: Shape of the cold bore squeezed at 45° angle in the first region of the CLIQ discharge.

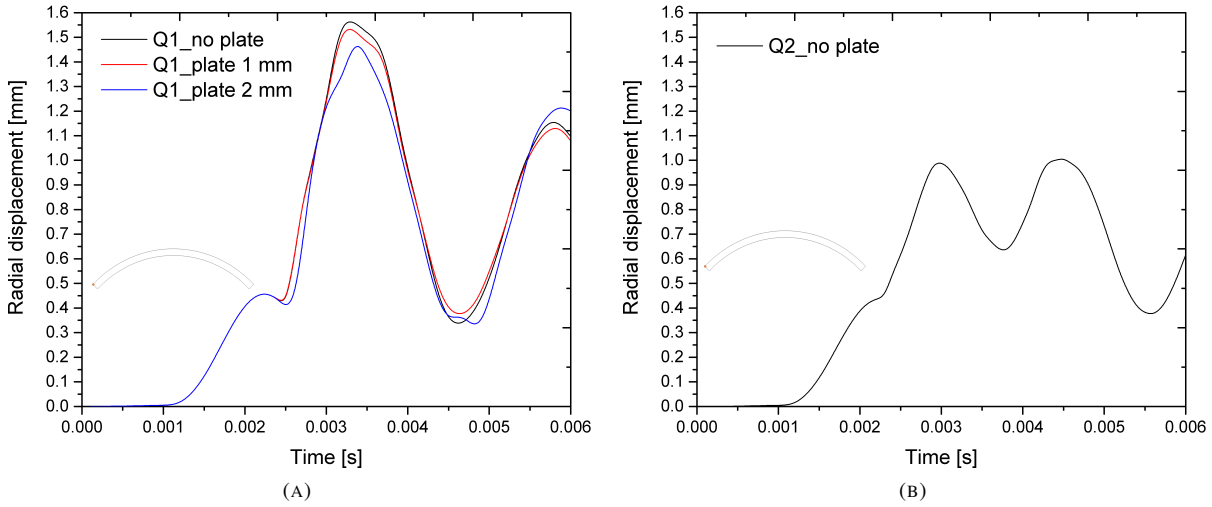


FIGURE 6.34: In (a) radial displacement of the cold bore during the CLIQ discharge for the Q1 cold bore in case of the Q1 beam screen equipped with or without reinforcements plate. In (b) radial displacement of the Q2 cold bore.

The cross section of the beam screen quarter equipped with the supporting pins is shown in Fig. 6.38. Only one supporting pin is loaded according to the classical deformation of the cold bore subject to the CLIQ discharge. The analysis of the forces is carried out as a function of the gap between the cold bore and the pin.

Three gaps are considered, 0.1 mm, 0.25 mm and 1 mm and the maximum forces transferred to the pin turn out to be 26.4 kN, 23.2 kN, and 11 kN, respectively. As expected, the larger the gap the lower the force to be absorbed by the pin.

6.6.5 Fracture mechanics analysis

The heat absorber block might be subject to a fracture failure when it hits the cold bore. The fracture mechanics analysis has been performed only for the absorber as the tungsten alloy at cryogenic temperatures is the most brittle material amongst the materials used for the beam screen (see Table 3.2).

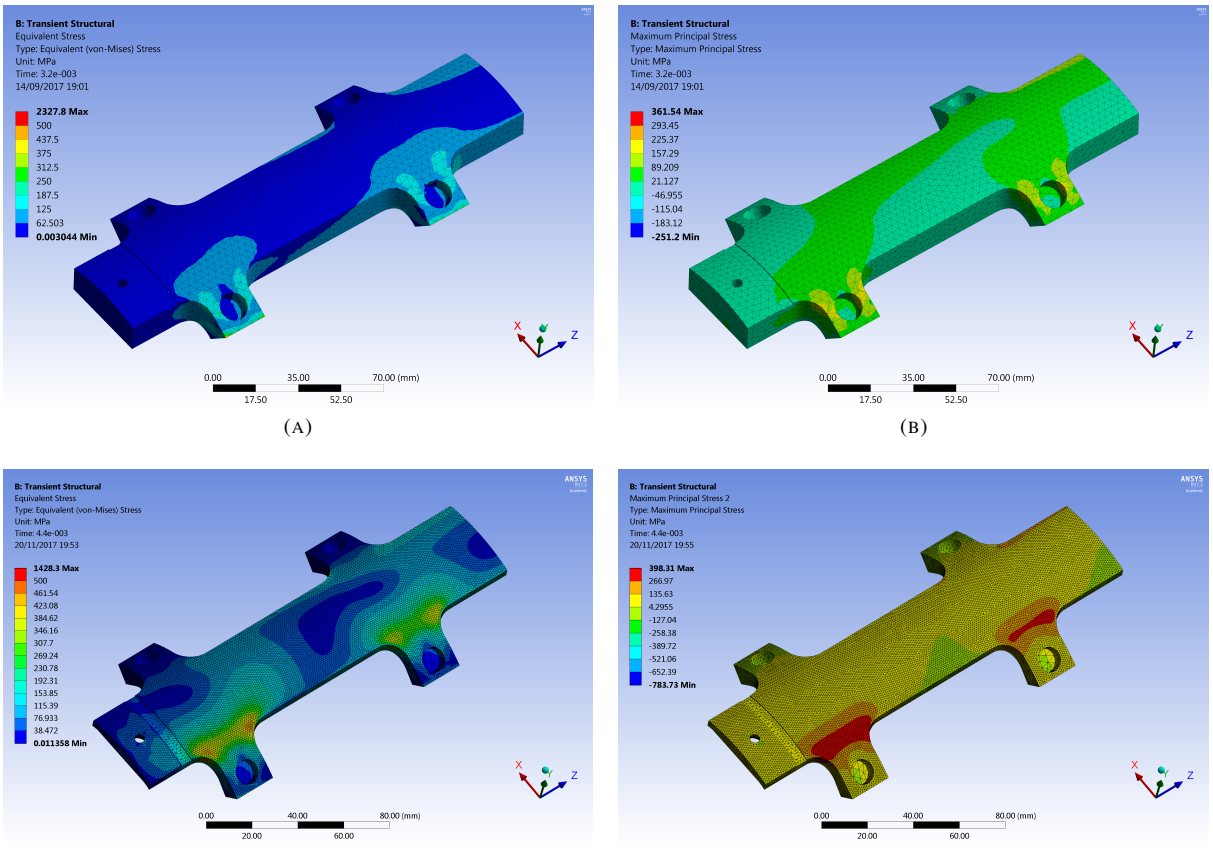


FIGURE 6.35: Equivalent and maximum principal stress of the Q1 heat absorber (a,b) and of the Q2 heat absorber (c,d), respectively. The upper bound of the legend is set to 500 MPa to better visualise high-stress regions.

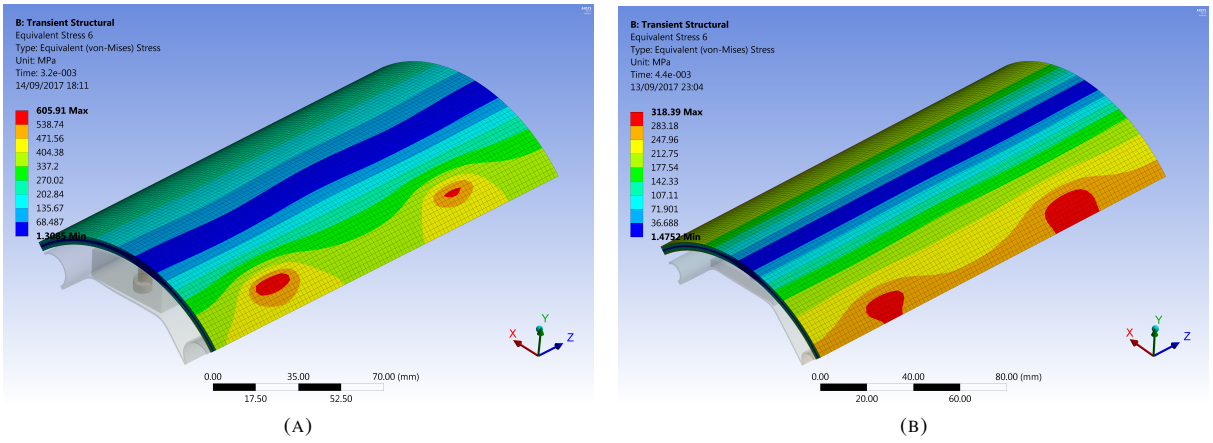


FIGURE 6.36: In (a) equivalent stress of the cold bore hit by the Q1 heat absorber. In (b) equivalent stress of the cold bore hit by the Q2 heat absorber.

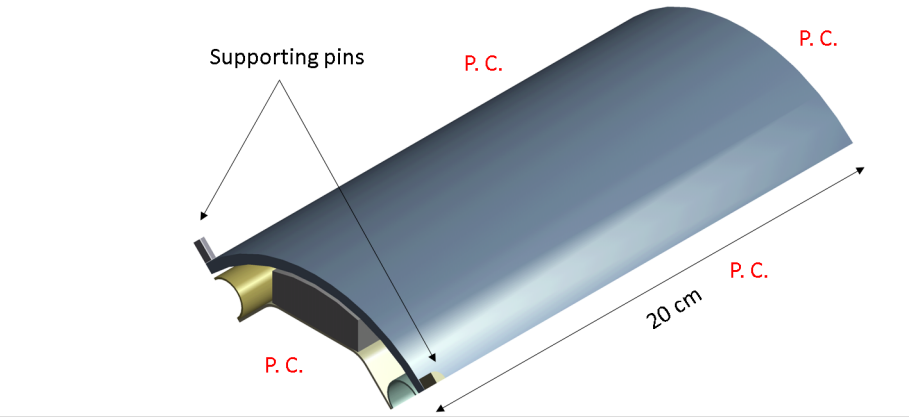


FIGURE 6.37: Ansys model to account for the force transmitted to the supporting pin placed at $+/-\ 45^{\circ}$ angle in the magnet poles. Periodic conditions (PC) are applied on the eternal faces of the assembly.

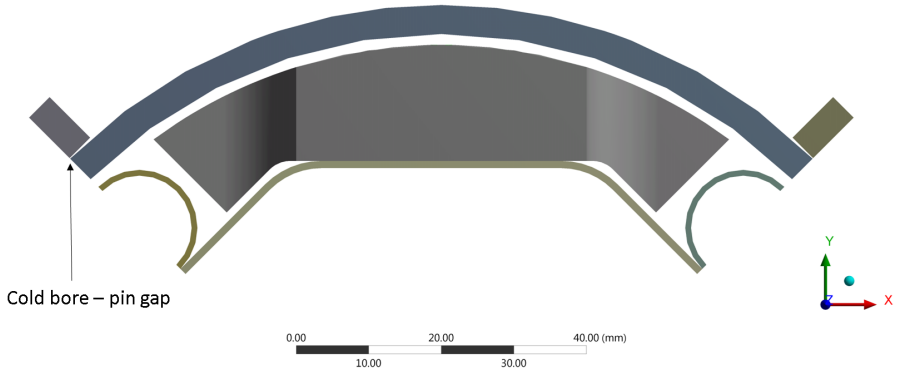


FIGURE 6.38: Cross section of one quarter of the Q1 beam screen assembly which includes the supporting pins.

The analytical expression of the Stress Intensity Factor (SIF) of a bar subject to bending has been used for the analysis [140]:

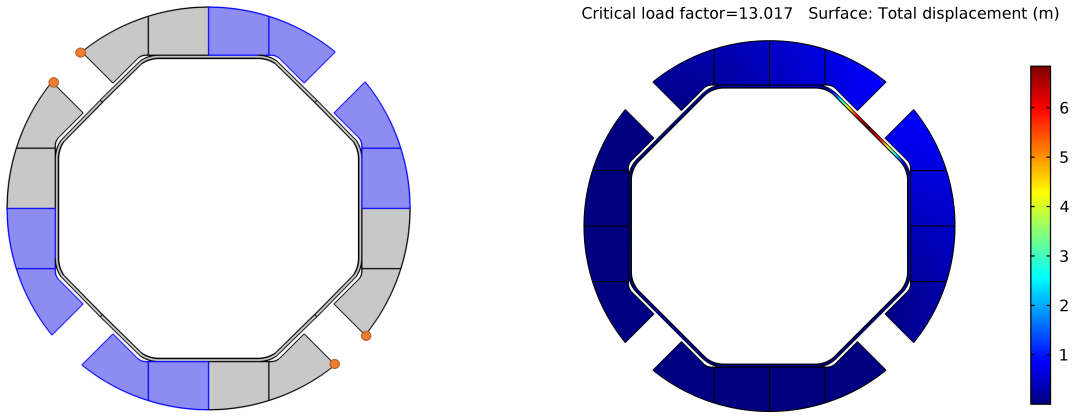
$$K_I = \sigma_{MAX}\sqrt{\pi a} \times [1.112 - 1.4\frac{a}{b} + 7.33(\frac{a}{b})^2 - 13.08(\frac{a}{b})^3 + 14(\frac{a}{b})^4] \tag{6.13}$$

Moreover, the analysis is performed only for the Q2 block due to its reduced thickness, and therefore, higher stress. A value of σ_{MAX} equal to 850 MPa has been derived from the mechanical analysis carried out in Ansys. By comparing K_I with K_{IC} = 29 [MPa m^{-1}] measured at 77 K it turns out that the critical crack size, a_c, that might initiate a sudden fracture in the block is 35 µm.

This information is useful to define the surface roughness of the heat absorbers. Therefore, the adopted ISO grade N8 (R_a =3.2 µm) guarantees a sufficient safety margin.

6.6.6 Buckling analysis

The octagonal pipe is subject to compressive loads during the first phase of the CLIQ discharge that might buckle the pipe itself. For this reason, a linear buckling analysis has been performed on the octagonal pipe to assess its critical load factor. This is obtained through the approximated and simplified configuration shown in Fig. 6.39a, which is capable to capture the most severe Lorentz force distribution without modelling any mechanical contacts. Therefore, the distribution of the highest compressive forces is applied on the octagonal pipe and on the heat absorber through a stationary analysis. Only the rotations of the heat absorber vertexes impacting the cold bore, in orange in Fig. 6.39a, have been enabled. As shown in Fig. 6.39b the critical load factor is above any critical value, i.e. 13.



(A) (B)

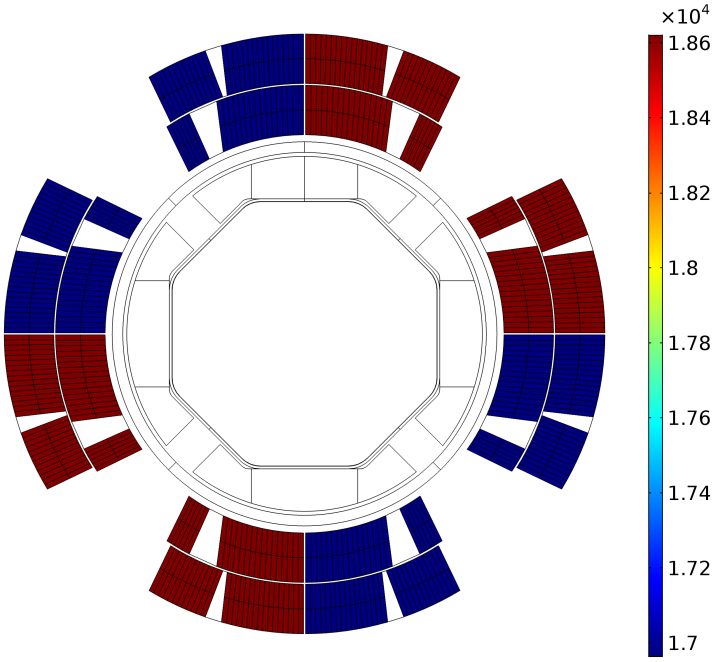
FIGURE 6.39: In (a) regions of the beam screen (in violet) where the force distribution of the octagonal pipe and the inner layer cause the compression of the pipe itself. In (b) critical load factor and total displacement calculated through the linear buckling analysis.

6.6.7 Magnet coil electrodynamcis

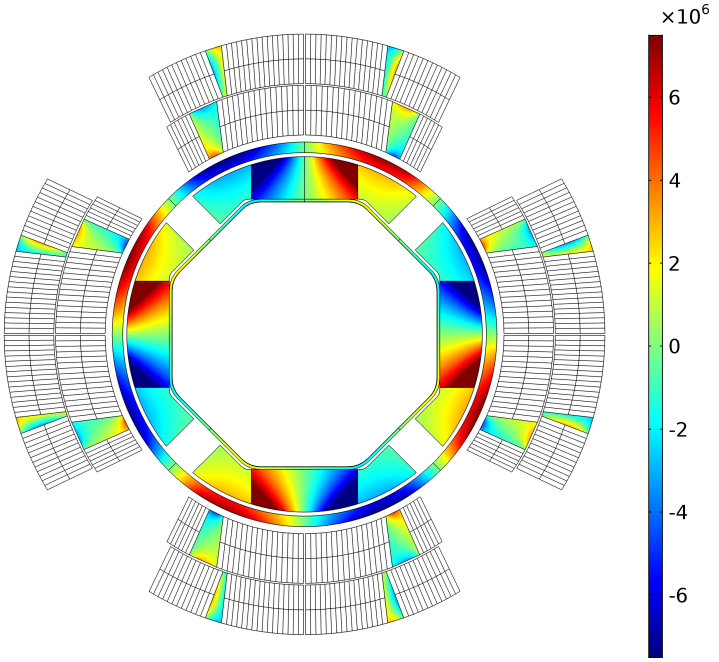
Inter-filament coupling currents (IFCC) and inter-strand coupling currents (ISCC) are induced in the strands and filaments of the superconducting magnets during a fast magnetic field variation [141]. In addition to that, high-intensity currents are induced in the copper wedges of the magnet structure. Such currents oppose the decay of the magnetic field resulting in softening the intensity of the Lorentz forces [142] [143] [141]. To assess the intensity of these effects, the complex magnet coil needs to be modelled and the electrodynamics of the superconducting filaments has to be efficiently setup to avoid solving the coil at a micro-metric scale. To this purpose, the 2D model developed by Bortot et al. [123] to study the quench protection systems of the new HL-LHC magnet has been further extended by including the beam screen in the magnet aperture, see Fig. 6.40.

Such a model accounts for:

- Saturation of the iron yoke **B(H)**;
- Magneto-thermal properties of the materials $c_p(T, B)$, $k_p(T, B)$;
- Coil electrodynamic IFCC - ISCC;



(A)



(B)

FIGURE 6.40: Current $[A]$ circulating in the HL-LHC magnet coil after 5 ms the initiation of the CLIQ discharge in (a). Current density $[A/m^2]$ induced in the beam screen after 5 ms the initiation of the CLIQ discharge in (b).

- Quench transition $\mathbf{Q}_{joule}$;
- Eddy currents in conductive domains $\mathbf{j}_{eddy}$;
- CLIQ co-simulation;

The discharge of the current accounted in this model occurs under the assumption of a CLIQ unit of 600 V and 40 mF. It turns out that the torque induced in one heat absorber (40 cm long) results to be 186 N m, namely 33 % less than the one calculated by the model described in this chapter, which does not account for the magnet electrodynamics. However, further analyses and measurements are needed to prove these results.

In addition, the electrodynamic model turns out to be also a very important tool to validate the calibration of the magnetic field between ROXIE and COMSOL. In fact, the arm of the torque induced in the heat absorber calculated through the proposed COMSOL model is 15.76 mm, while by considering the real coil structure is 15.72 mm.

6.6.8 Thermal link

The mechanical behaviour of the thermal link during the CLIQ discharge is analysed for three widths, 3 mm, 5 mm, and 10 mm at 50 K. The effects of the temperature on the electrical resistivity are not considered as these are negligible for the widths analysed here, see section 5.6.7. As seen for the thermal links under a evenly decaying magnetic field decay, the forces are induced along the beam axis direction and, therefore, are integrated in each half portion of the link (these forces are referred to as longitudinal forces throughout the text). However, since the magnetic field is not always decaying during the CLIQ discharge, the thermal links in correspondence of the poles 1-3, behave differently from those of poles 2-4. In fact, during the first oscillation, the time derivative of the magnetic field is positive for the poles 1 and 3 and negative for the poles 2 and 4, see Fig. 6.1 and Fig. 6.41.

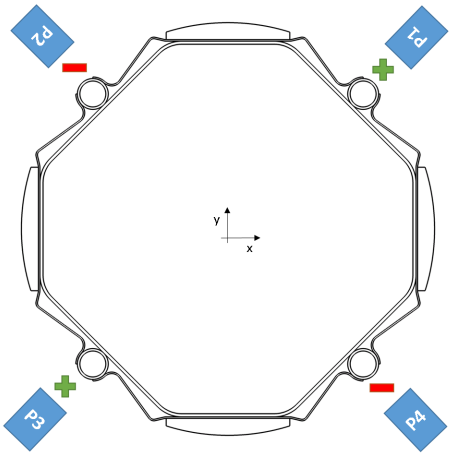


FIGURE 6.41: Thermal link position with respect to the magnet poles. In the links facing the poles 1 and 3 the magnetic field increases locally, while for the poles 2 and 4 it decreases.

Since the magneto-thermo-mechanical behaviour of the beam screen is fully characterised by the periodic unit ranging from $45°$ to $135°$ the thermal link placed between the poles 1 and 2 is then analysed. As shown in Fig. 6.42, the principal consequence of the first CLIQ discharge oscillation is that the distribution of the longitudinal forces is of compressive type for the links facing the poles 1-3 (due to the positive time variation of the field), while it is of tensile type for the links facing the poles 2 and 4 (due to the negative time variation of the field).

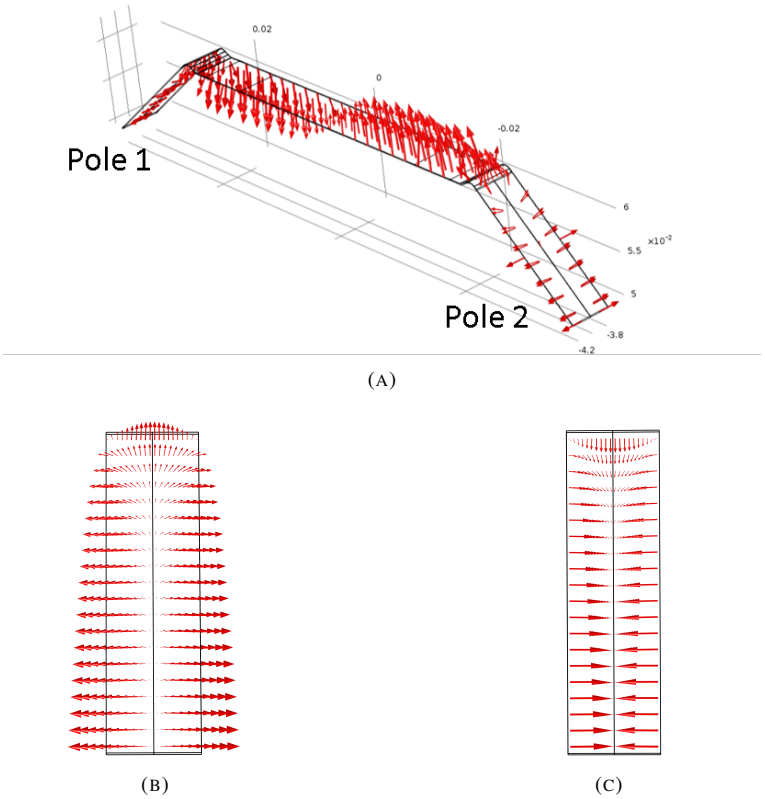


FIGURE 6.42: Distribution of the forces in the thermal link side brazed underneath the heat absorber (a), facing the poles 2 or 4 (b), and the poles 1 or 3 (c).

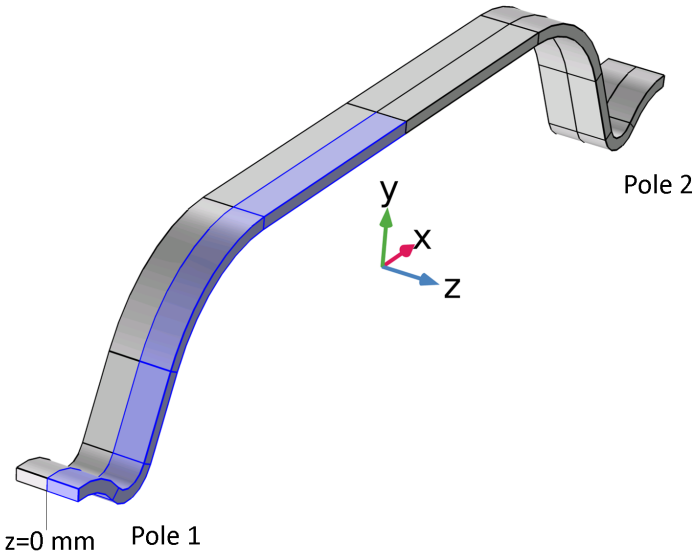


FIGURE 6.43: Portion of the thermal link used to integrate the Lorentz forces.

The thermal link is symmetric along two mutually perpendicular planes (the xy- and yz- planes in Fig. 6.43), resulting in a portion of the link over which the induced forces can be better analysed, see Fig. 6.43. The longitudinal forces are integrated over each of these portions identified with respect to their position on the z-axis and to the pole. By way of example, the portion of the thermal link outlined in Fig. 6.43 being on the positive side of the z-axis and under the influence of pole 1, is referred to as p1p3_z+ because it behaves at the same way as the link in front of pole 3.

As seen in chapter 5, the most critical thermal link is the one adopted in the Q2 beam screen and it is, therefore, analysed in this section. The longitudinal forces are integrated in thermal links 1 mm thick and 3 mm wide in Fig. 6.44, 5 mm wide in Fig. 6.45, and 10 mm wide in Fig. 6.46. The total longitudinal forces are reported up to 100 ms for each portion of the thermal link according to the above described convention.

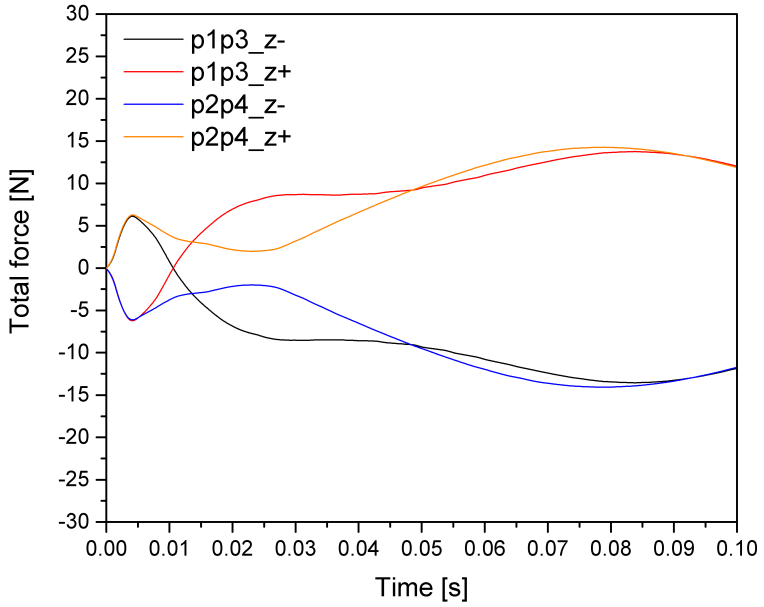


FIGURE 6.44: Evolution of the longitudinal forces integrated over each portion of the thermal link 1 mm thick and 3 mm wide facing the poles 1 or 3, and 2 or 4.

It is worth noting that the highest forces in each thermal link portion are induced when the CLIQ unbalance vanishes at around 80 ms. However, a compressive load condition is present in the thermal links below the poles 1 and 3 that might induce buckling due to the very thin layer of the link (0.1 mm). For this reason, a linear buckling analysis is performed with respect to the distribution of the highest compressive forces induced in one layer 10 mm wide. As shown in Fig. 6.47, the critical buckling load for the link is 1.86. Therefore, as the 10 mm wide thermal link should not buckle, the stability for the shorter links is met a fortiori.

The von Mises stress is calculated with respect to the highest forces and shown in Fig. 6.48 for one layer of the thermal link (0.1 mm thick) and widths of 3 mm, 5 mm, and 10 mm. The boundary conditions are the same as the ones depicted in Fig. 5.56 of chapter 5. It turns out that the elastic limit of copper, 35 MPa, is exceeded only in the thermal link 10 mm wide.

The percentage of plastic deformation of the central portion of the link is shown in Table 6.4. For comparative purposes such a portion is the same as the one of the Q2 thermal link undergoing a evenly decaying magnetic field, see Fig. 5.54c.

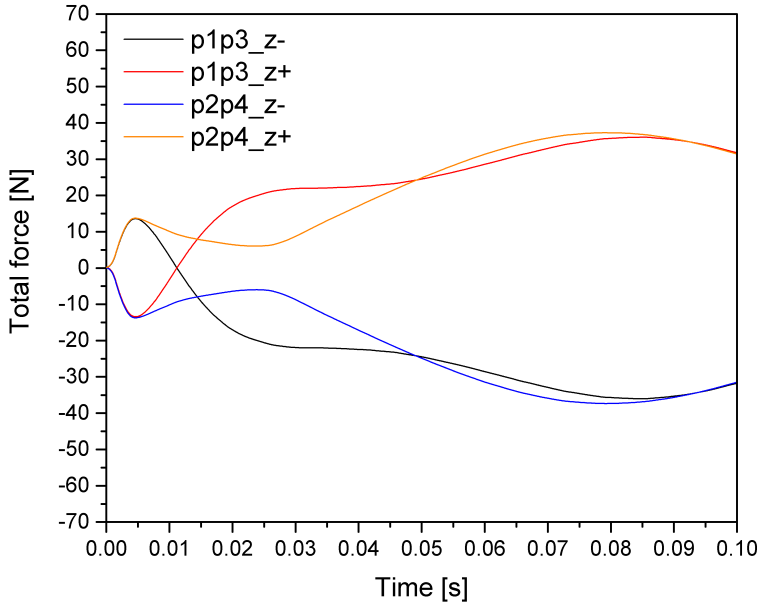


FIGURE 6.45: Evolution of the longitudinal forces integrated over each portion of the thermal link 1 mm thick and 5 mm wide facing the poles 1 or 3, and 2 or 4.

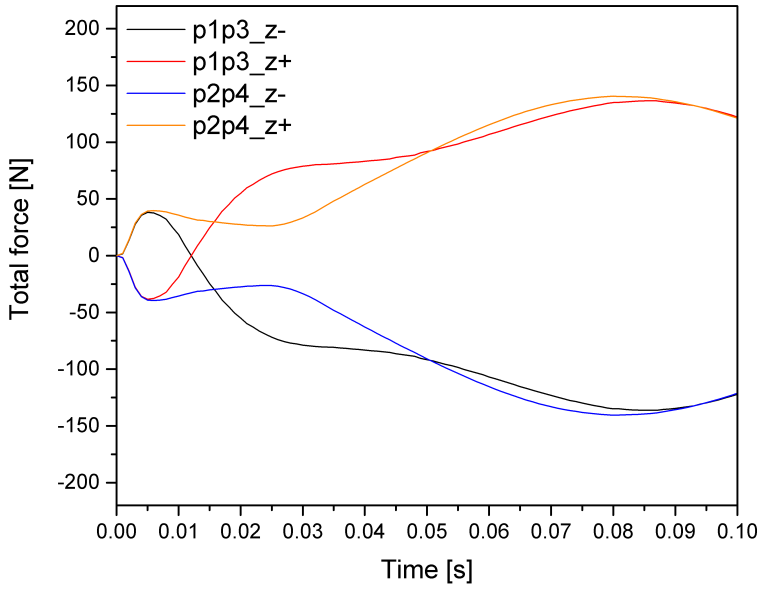


FIGURE 6.46: Evolution of the longitudinal forces integrated over each portion of the thermal link 1 mm thick and 10 mm wide facing the poles 1 or 3, and 2 or 4.

Beam screen width	plastic deformation (%)
3	0
5	0
10	43.4

TABLE 6.4: Plastic deformation percentage as function of the width of a thermal link layer 1 mm thick.

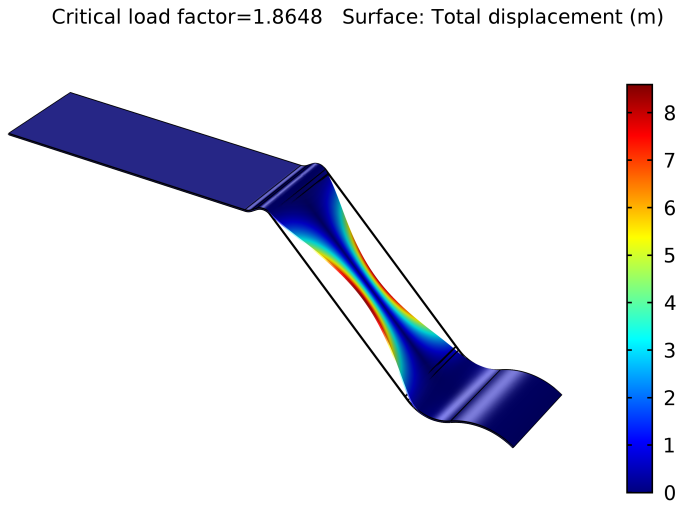
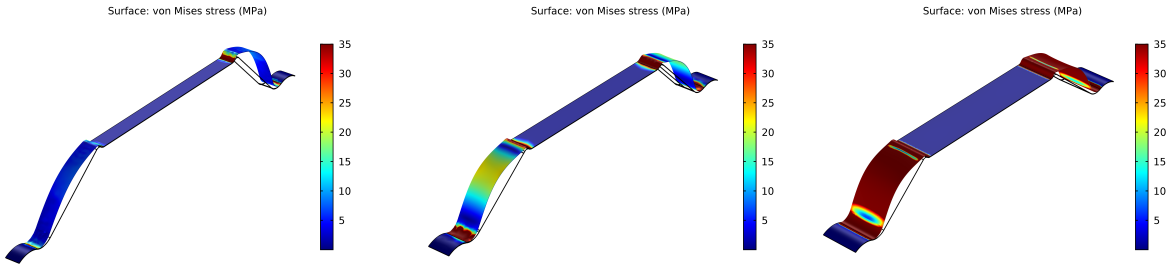


FIGURE 6.47: Buckling analysis performed on a 10 mm wide thermal link.



(A) (B) (C)

FIGURE 6.48: Von Mises stress for a thermal link layer 0.1 mm thick and 3 mm wide in (a), 5 mm in (b), and 10 mm in (c). The upper limit of the colour map is set to 35 MPa to highlight the regions of plastic deformations.

In comparison with the thermal link 5 mm wide analysed in chapter 5, the link 5 mm wide subject to the ultimate current discharge of CLIQ does not undergo any plastic deformation and, therefore, can be adopted safely.

6.6.9 Summary of the mechanical response

The maximum normal force, equivalent stress, and displacement of the Q1 and Q2 beam screen are reported in Table 6.5 with respect to the first region of the CLIQ discharge. For the Q1 beam screen, the data correspond to the case with a reinforcement plate 1 mm thick. Only for the most critical beam screen, the Q1 type, the results derived from the FEM model accounting for the coil electrodynamics are provided as well. In such a case, no reinforcement plate has been considered.

6.6.10 Summary of the changes of the beam screen design due to CLIQ

The modifications introduced by the quench protection system CLIQ in the design of the beam screen are therefore:

Component	Q1			Q1 - coil electrodynamic			Q2		
	$\Delta F_{n\ max}$ [N/mm]	σ_{max} [MPa]	δ_{max} [mm]	$\Delta F_{n\ max}$ [N/mm]	σ_{max} [MPa]	δ_{max} [mm]	$\Delta F_{n\ max}$ [N/mm]	σ_{max} [MPa]	δ_{max} [mm]
Cold bore st. st. 316 LN $\sigma_y = 860MPa$ (4 K)	24	620	1.5	16.7	445	1.06	24	280	1
Heat absorber Tungsten alloy $\sigma_y = 1284MPa$ (77 K)	42	650 (loc.)	-	30	600 (loc.)	-	21.7	400 (loc.)	-
Octagonal pipe * st. st. P506 $\sigma_y = 1350MPa$ (50 K)	10	> 1350 (loc.)	-	7.3	> 1350 (loc.)	-	26.6	1000 (loc.)	-

TABLE 6.5: Comparison of the highest force, stress, and displacement induced in each component of the Q1 (reinforcement plate 1 mm thick) and Q2 beam screen subject to the CLIQ discharge. For the Q1 beam screen, these quantities are reported also by considering the magnet electrodynamics. * The forces induced in the inner layer are included.

- New shape of the centring pin designed to withstand the effects of the torque;
- Double number of pins welded on the octagonal pipe for the Q1 and Q2 beam screen;
- Reinforcement plates for the Q1 beam screen;
- New shape of the heat absorber for the Q1 and Q2 beam screen.

As shown in Fig. 6.49, the extremities of the heat absorber are no longer shaped in a way to allow the overlapping of two consecutive blocks. This solution, aimed at reducing the number of pins, cannot be used for the new beam screen design as the pins are loaded during the CLIQ discharge. Therefore, the number of pins doubles as each block needs to be positioned independently. Each absorber features one oval slot to guarantee the sliding of the absorber on the octagonal pipe during the cooling down. The reinforcement plates of the Q1 beam screen are laser welded on the octagonal pipe, while, subsequently, the pins are stud welded on the plates. To better visualise the differences between the original version of the beam screen and the one compatible with the CLIQ discharge, the 3D models of the Q1 and Q2 design are shown with and without heat absorbers in the next subsections.

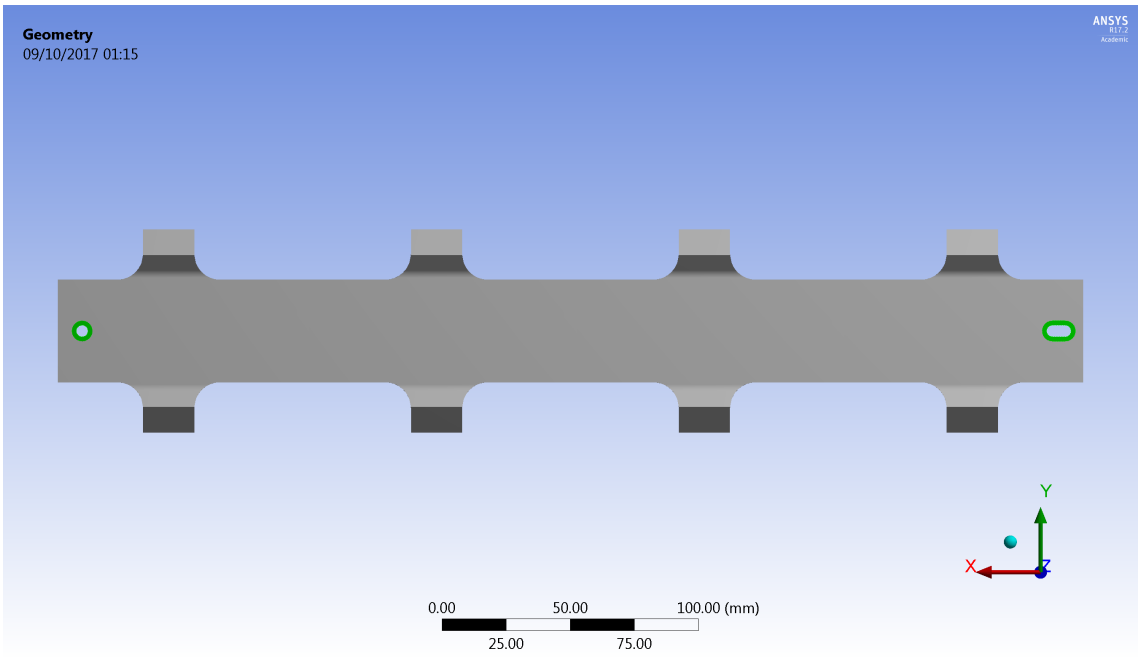
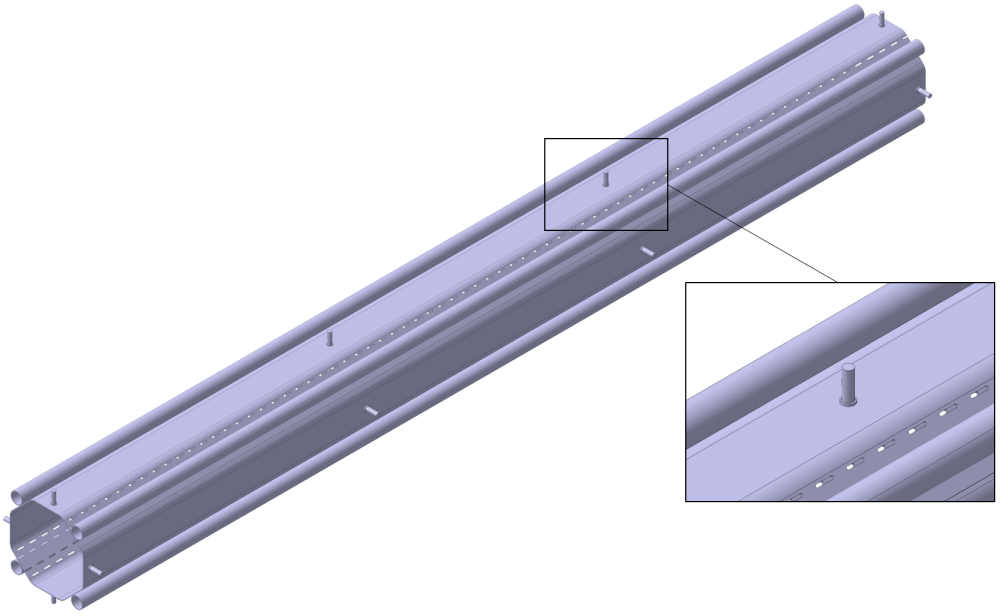


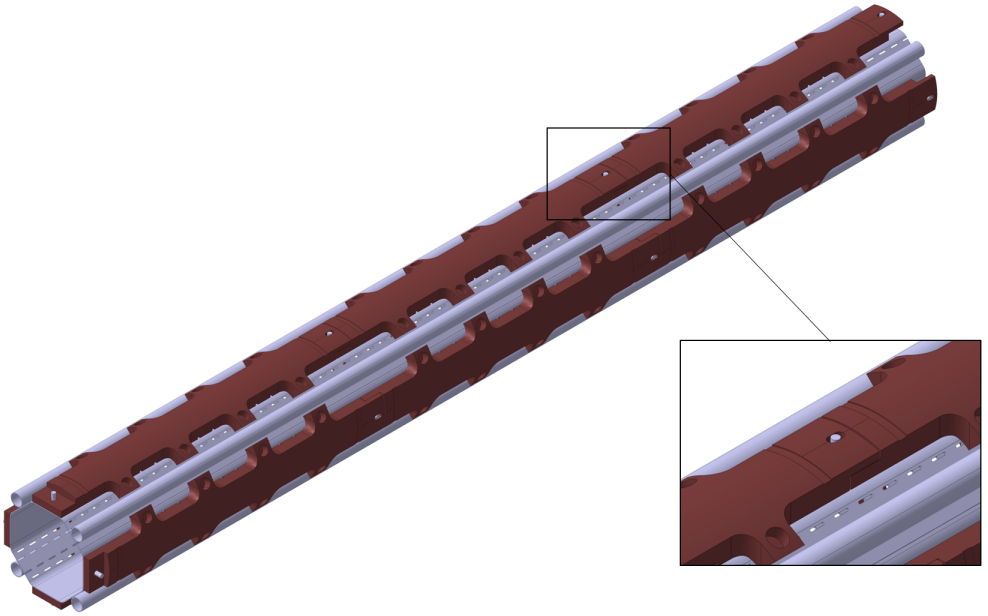
FIGURE 6.49: Bottom side of the heat absorber. One slot of the pins is ovally shaped to allow a stress-free thermal contraction during the cooling down of the magnet.

Q1 beam screen: Design based on the quench heaters

The design of the Q1 beam screen subject to a monotonic magnetic field decay (magnet protection scheme: quench heaters) is shown in Fig. 6.50 without and with the heat absorbers, respectively.



(A)

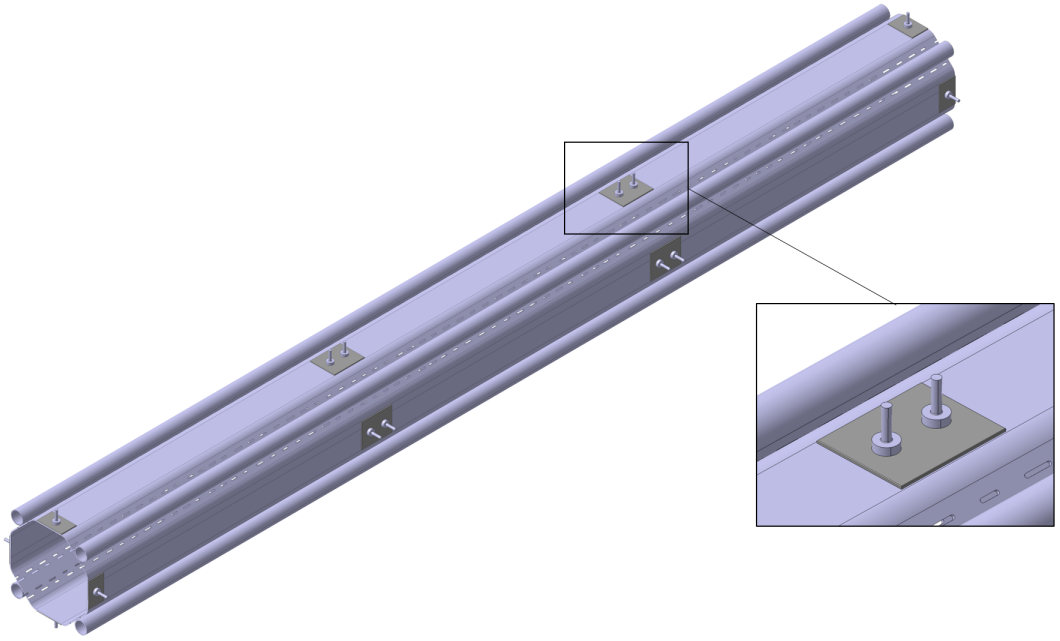


(B)

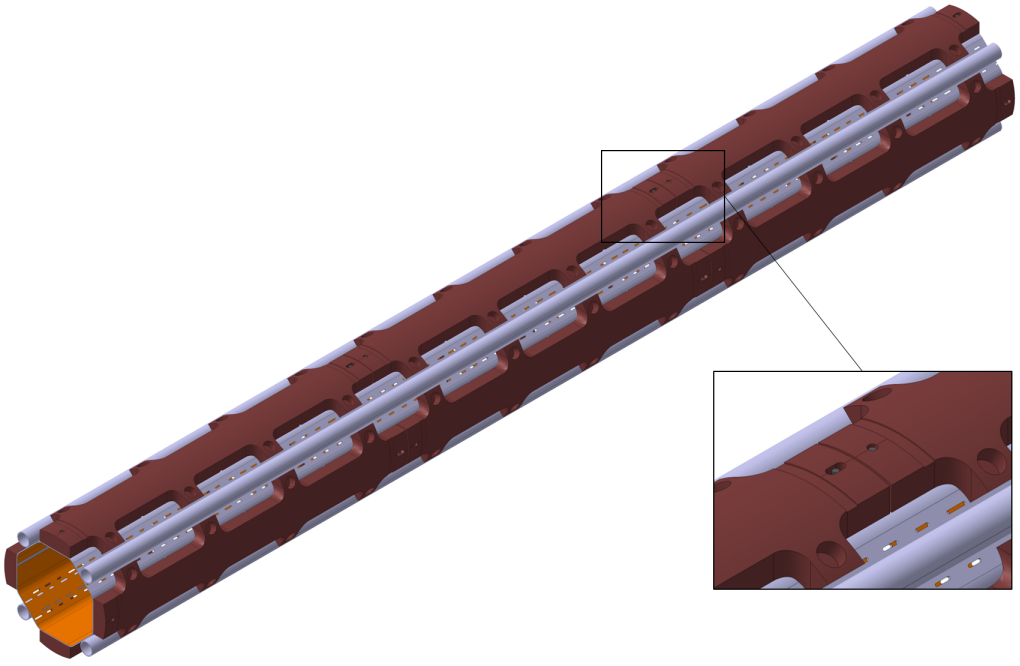
FIGURE 6.50: Octagonal pipe of the Q1 beam screen in (a), equipped with the heat absorbers in (b) in the case of quench heaters used as a quench protection scheme.

Q1 beam screen: Design based on the quench heaters + CLIQ

The design of the Q1 beam screen subject to a not monotonic magnetic field decay (magnet protection scheme: quench heaters + CLIQ) is shown in Fig. 6.51 without and with the heat absorbers, respectively. Some rendered images are shown in Fig. 6.52.

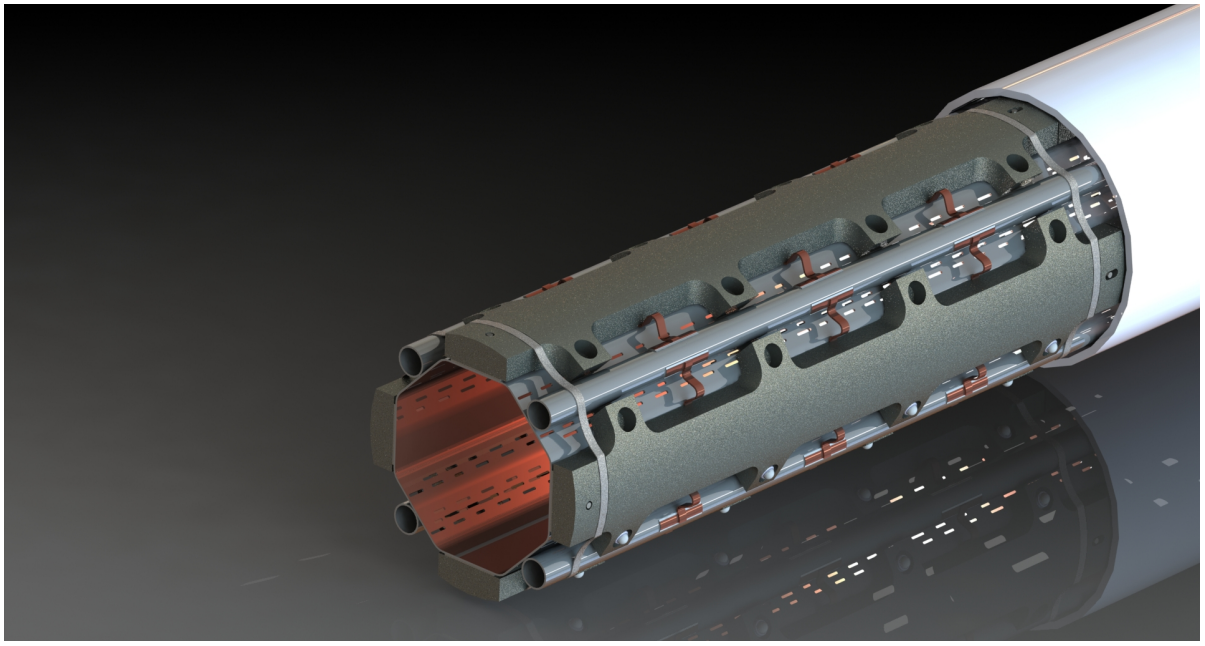


(A)

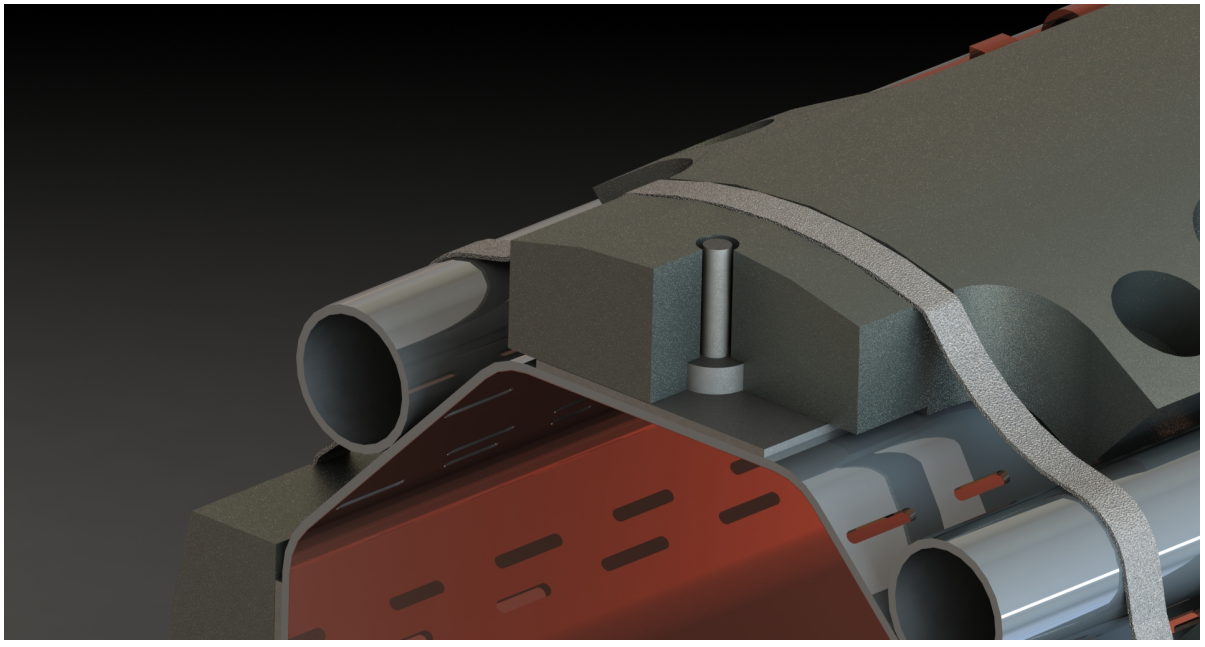


(B)

FIGURE 6.51: Octagonal pipe of the Q1 beam screen in (a), equipped with the heat absorbers in (b) in the case of CLIQ used as a quench protection scheme.



(A)

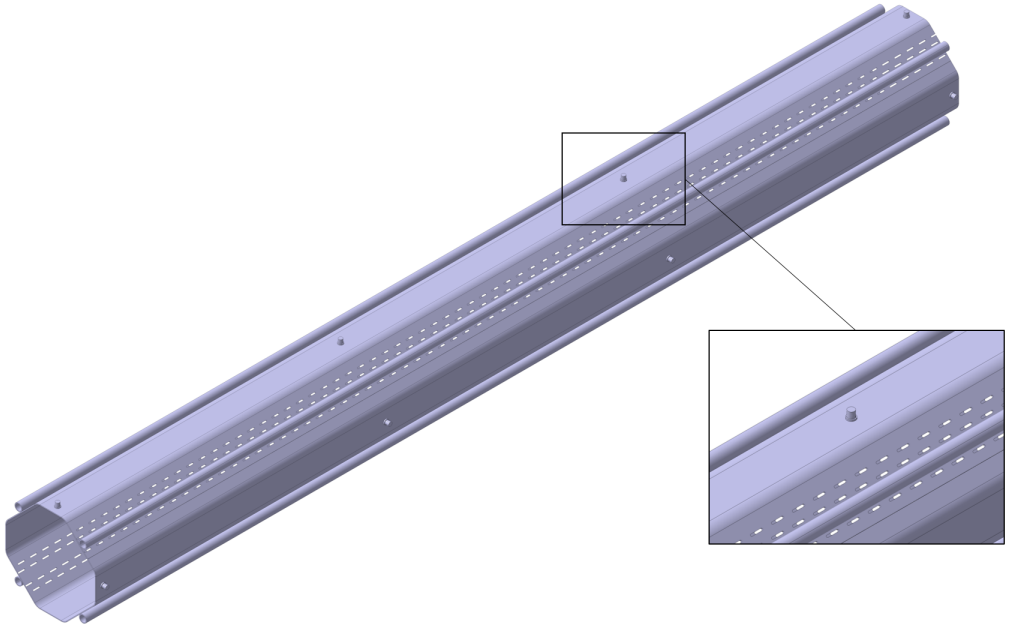


(B)

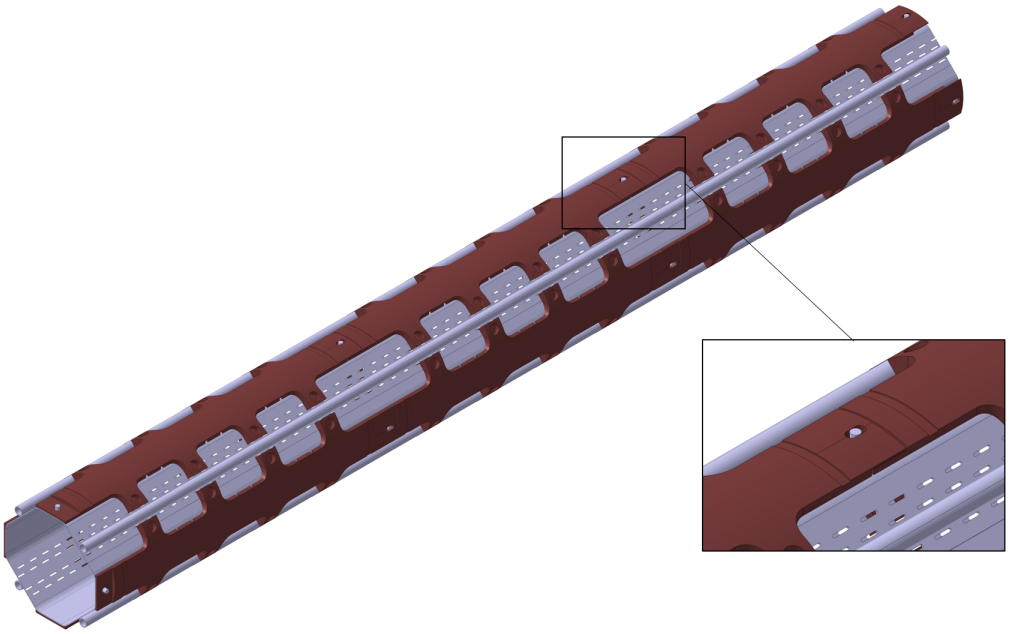
FIGURE 6.52: Rendering of the Q1 beam screen inserted in the cold bore in (a) and of the new pin geometry in (b).

Q2 beam screen: Design based on the quench heaters

The design of the Q2 beam screen subject to a not monotonic magnetic field decay (magnet protection scheme: quench heaters) is shown in Fig. 6.53 without and with the heat absorbers, respectively. Some rendered images are shown in Fig. 6.55.



(A)

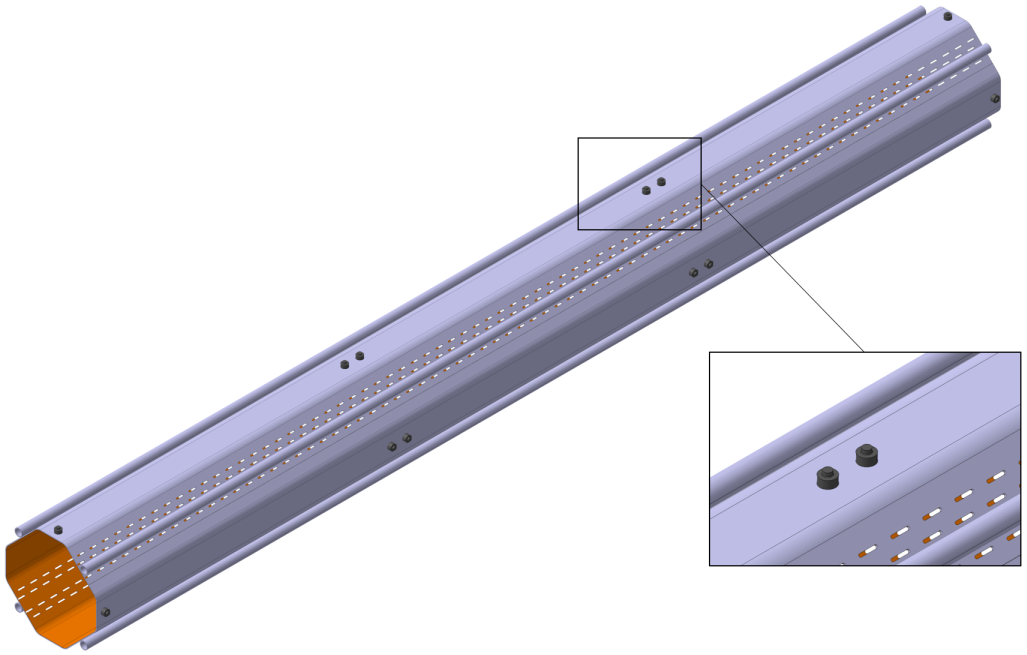


(B)

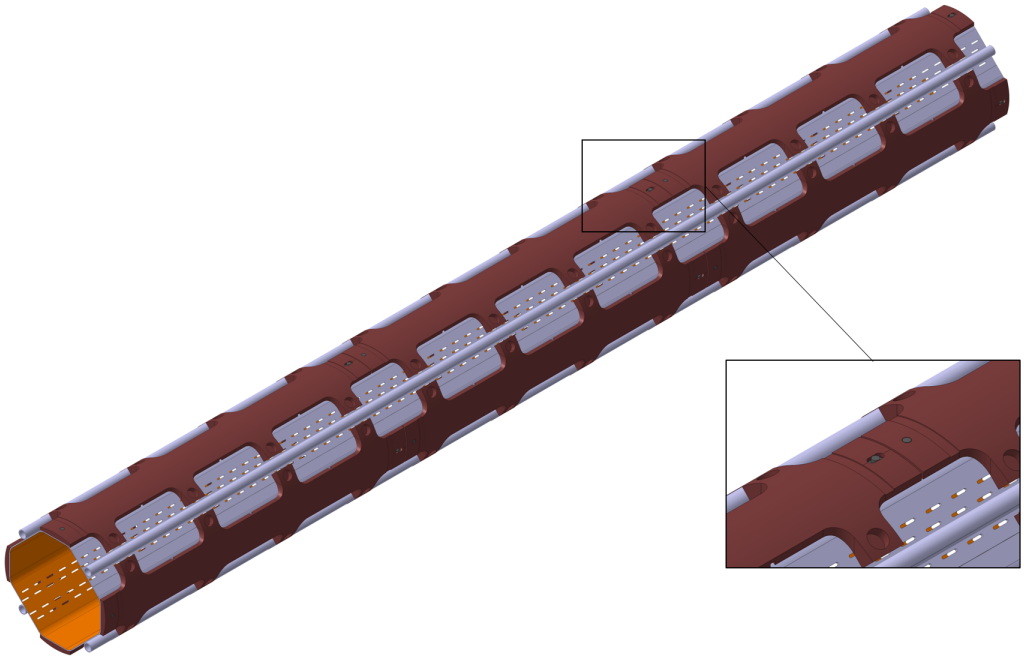
FIGURE 6.53: Octagonal pipe of the Q2 beam screen in (a), equipped with the heat absorbers in (b) in the case of quench heaters used as a quench protection scheme.

Q2 beam screen: Design based on the quench heaters + CLIQ

The design of the Q2 beam screen subject to a not monotonic magnetic field decay (magnet protection scheme: quench heaters + CLIQ) is shown in Fig. 6.54 without and with the heat absorbers, respectively.

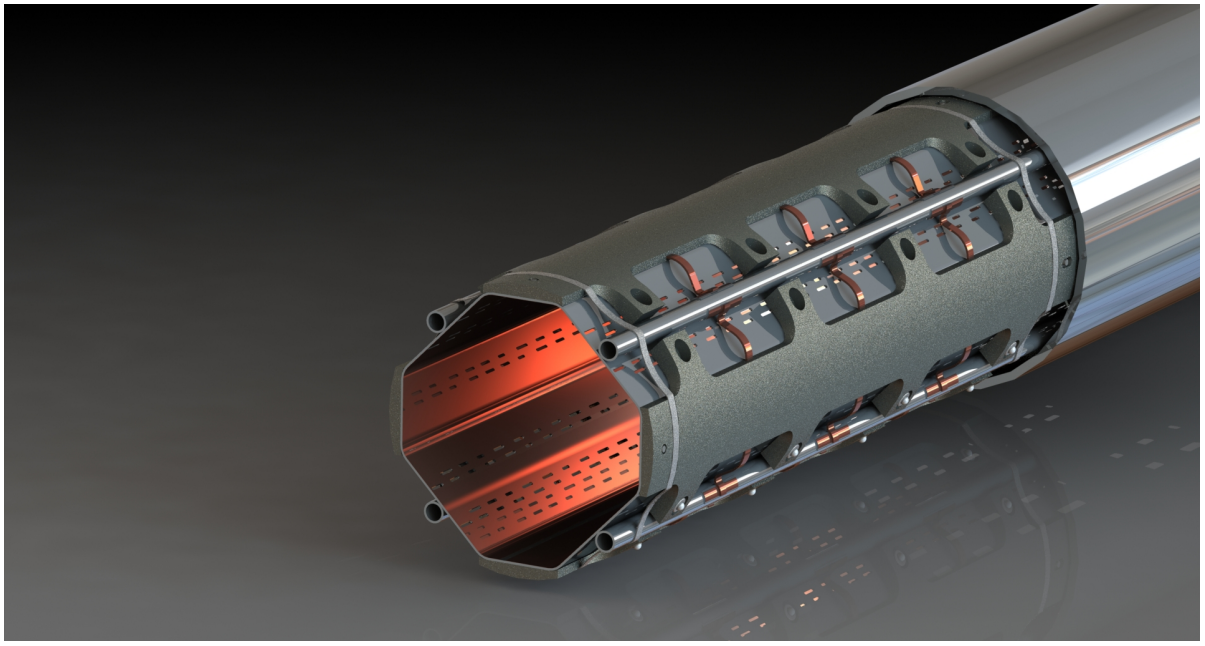


(A)

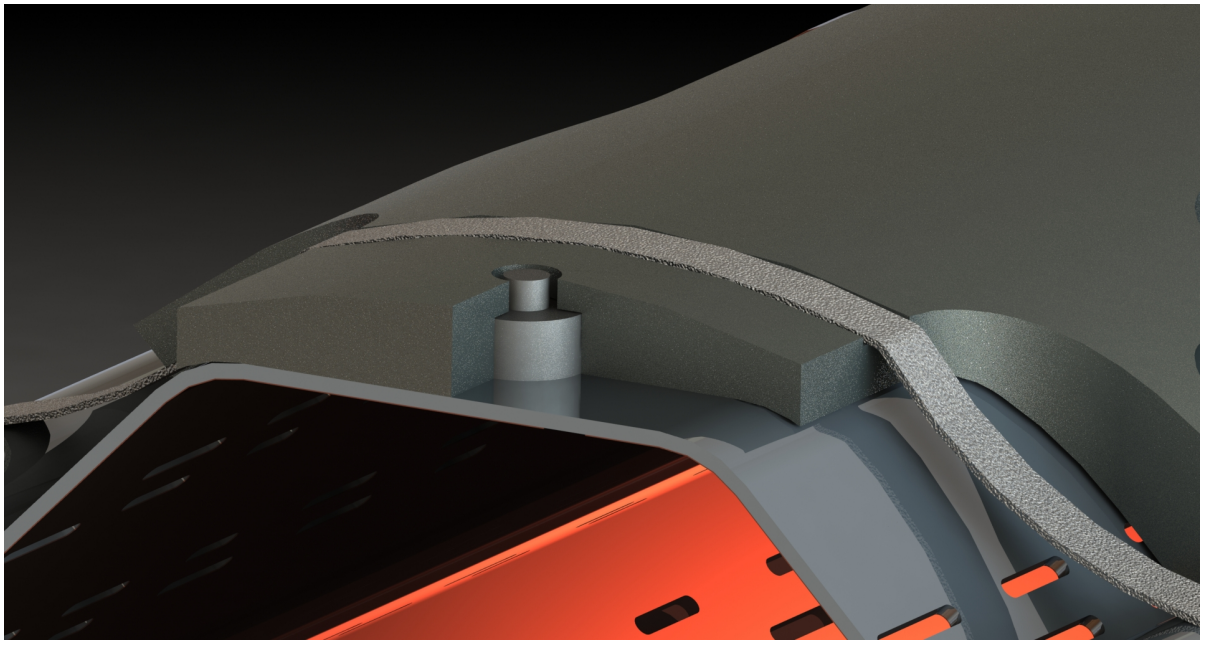


(B)

FIGURE 6.54: Octagonal pipe of the Q2 beam screen in (a), equipped with the heat absorbers in (b) in the case of CLIQ used as a quench protection scheme.



(A)



(B)

FIGURE 6.55: Rendering of the Q1 beam screen inserted in the cold bore in (a) and of the new pin geometry in (b).

6.7 Experimental setup of the magnet quench test

The Q1 and Q2 beam screen mechanical response during a magnet quench will be measured by July 2018. To this purpose the HL-LHC triplet magnet, known as MQXFS magnet and shown in Fig. 6.56, will be equipped with CLIQ as a quench protection scheme. Two flanges will align the cold bore within the magnet. The first flange is welded on the cold bore and connected to the end-plates of the magnet, while the second flange is connected to the front plate of the magnet to better support the cold bore. In turn, the alignment of the beam screen is obtained by two octagonally-shaped cups inserted within the beam screen and fixed at the two extremities of the cold bore.

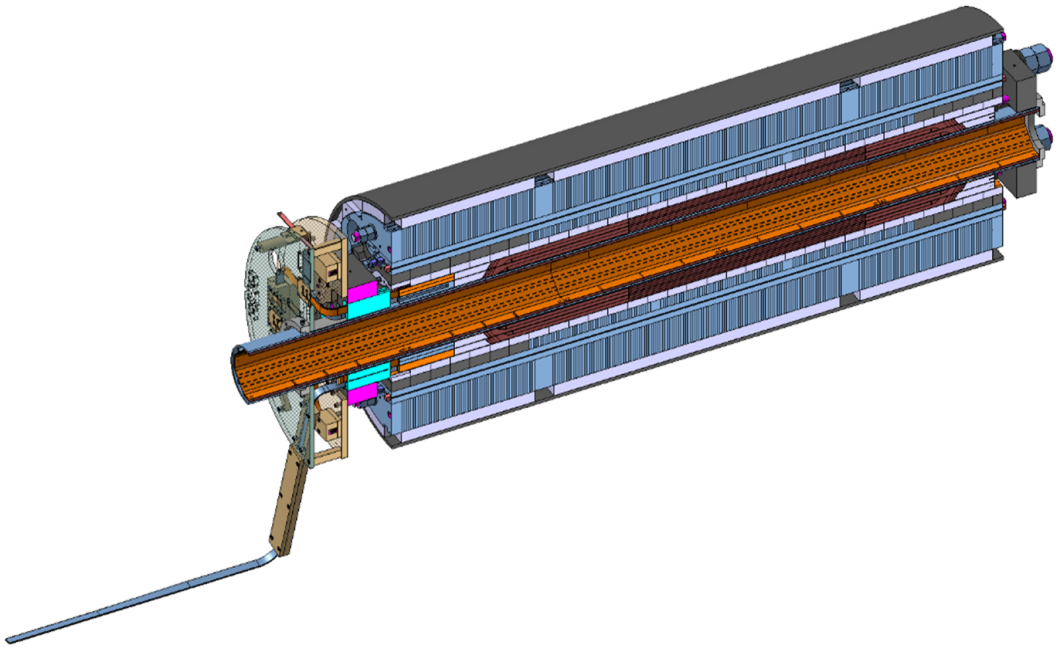


FIGURE 6.56: Cross section of the MQXFS magnet whose aperture accommodates the beam screen.

As shown in Fig. 6.57 and in Fig. 6.58, an auto-equilibrated probe will be inserted in the beam screen to measure the displacement of the octagonal pipe and of the heat absorber during a quench. The rotation of the heat absorbers and the displacement of the octagonal pipe will be obtained by means of pins positioned on elastic titanium strips. Moreover, several strain gauges will be installed on the octagonal pipe. The longitudinal and azimuthal deformations of the cold bore will be measured via optical fibres.

The beam screen will be inserted in the magnet horizontally. However, the test will be performed vertically as the magnet needs to be immersed in a cryostat filled with super-fluid helium at 1.9 K. This implies that the beam screen will not be in vacuum and that its temperature will be 1.9 K, *i.e.* much lower than during operation (60-80 K). The temperature of the super-fluid helium represents an unavoidable constraint which translates into a lower electrical resistivity of the materials and, therefore, higher forces induced in the beam screen components. A work-around, consisting in reducing the thickness of the inner copper layer (from 80 µm to 18 µm) and the width of the thermal links (from 5 mm to 2 mm), has been adopted. The resistivity of the tungsten alloy and of the stainless steel shows a plateau from 1.9 K to 80 K, see Fig. 3.6. Therefore, no other modifications are necessary.

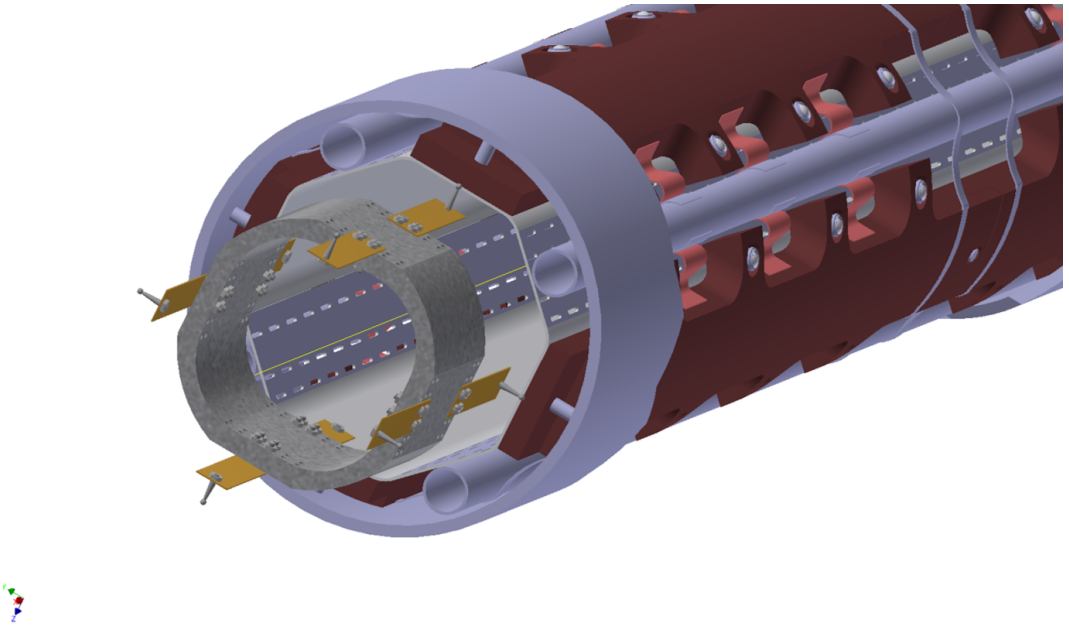


FIGURE 6.57: Measuring probe inserted in the the beam screen.

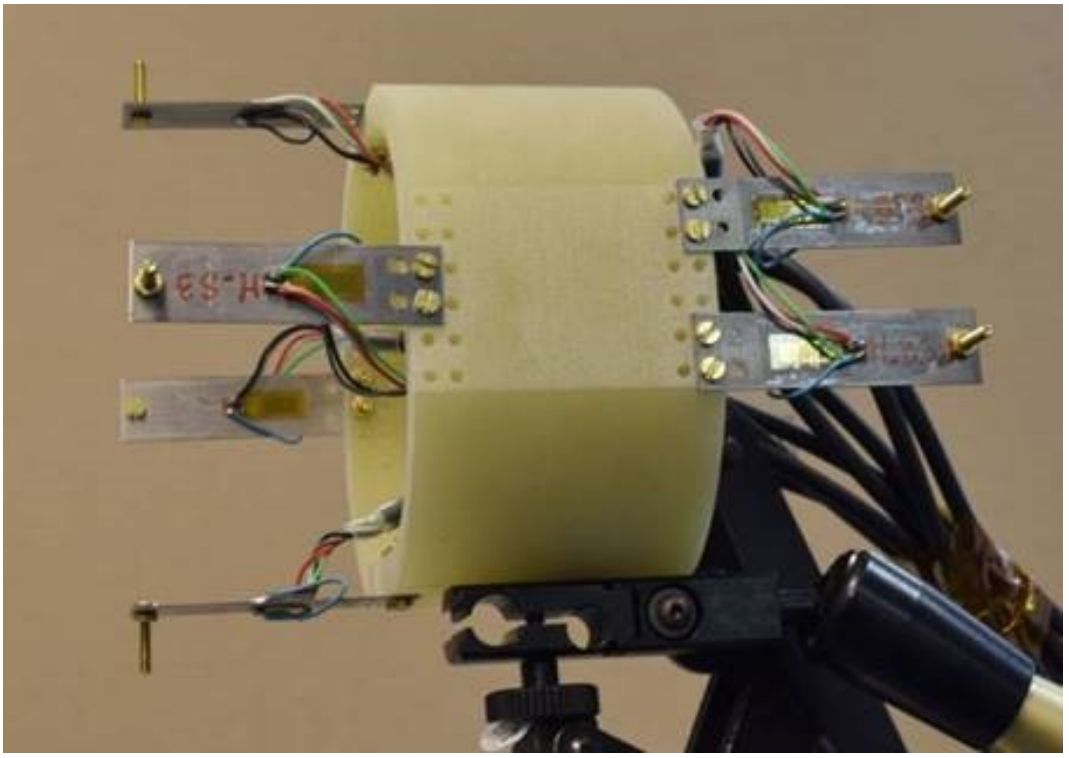


FIGURE 6.58: Measuring probe instrumented with 8 titanium strips. The right side measures the rotation of the heat absorber while the left side measures the displacement of the octagonal pipe.

6.8 Conclusions

This chapter has investigated the behaviour of the HL-LHC beam screen during a magnet quench when the quench heaters and CLIQ are used to protect the superconducting magnets. The CLIQ device introduces an oscillatory current discharge that heats up by induction the magnet in a faster and more homogeneous way than by quench heaters only. As the profile of the current discharge is not equal for all the poles of the magnet (but only for alternate poles), the magnetic field cannot be described by a reduced field formulation. Therefore, each pole of the magnet is controlled independently by magnetization. A new fully coupled multiphysics model has, therefore, been developed and verified with ROXIE, the software used at CERN for magnetic field quality analyses. It turns out that a torque load type is induced for each quarter of the beam screen assembly. A buckling analysis has been performed due to a compression stress state induced by the torque. However, no instabilities have been revealed by simulation. The beam screen design, originally developed to cope with an outward force distribution was found not to withstand the effects of CLIQ without plastic deformations. Therefore, the design of the beam screen has been modified. Specifically, the shape of the centring pins and that of the heat absorbers have been varied. In addition, a reinforcement plate has been introduced for the Q1 beam screen to increase the strength of the octagonal pipe along the direction of the torque. With these changes the mechanical integrity of the beam screen undergoing a magnet quench has been demonstrated. Moreover, since the CLIQ discharge occurs in the order of time of a few ms the electrodynamics of the magnet coil has been considered. From preliminary analysis it has been found that the Lorentz forces induced in the beam screen are about 33% lower than those obtained without magnet coil. Therefore, the fast dynamics of the CLIQ discharge can result in lower forces induced in the beam screen assembly. The behaviour of the thermal link has been studied and its shape to withstand a magnet quench has been determined.

Chapter 7

Conclusions and discussion

7.1 Summary of key results

The following results are presented as answers to the research objectives of the thesis defined in chapter 1.

7.1.1 Beam screen design

The conceptual design of the beam screen has been extended and new features have been developed and implemented. The aperture reduction of the beam screen due to the weight of the Q1 and Q2 heat absorbers has been calculated and accounted for. For the Q1 and Q2 beam screen this is 0.2 mm and 0.07 mm, respectively.

The flexibility of the heat absorber, being related to the thermal links, is an important feature of the whole assembly as the absorber has to return to its original position after a quench for shielding and thermal requirements. To this purpose, a flexible multilayer structure has been proposed for the lateral sides of the thermal link. The simulations and experiments have permitted to verify that the multilayer structure allows the absorber to freely return to its original position after a quench.

The beam screen is supported by a conical spring inserted in dedicated holes of the absorbers. The spring is coupled with a ceramic sphere to limit the heat load to the superconducting magnet. The geometry of the springs that guarantees the required 1.5 mm gap between the absorbers and the cold bore has been developed through simulations. The stiffness measured for the Q1 spring is 16.3 N/mm, while for the Q2 spring is 15.7 N/mm resulting in a good agreement with the required one. The von Mises stresses of the Q1 and Q2 springs with respect to their maximum compression in operation are 1350 MPa and 1300 MPa, respectively, which is below the elastic limit at 100 K. No contact between the spires was observed at their maximum compression.

7.1.2 Beam screen material characterisation

The properties of beam screen material are a fundamental input to conduct the simulations. Therefore, the physical properties of the beam screen materials not found in the literature have been measured. A lack of information was found at cryogenic temperatures for the heat absorbers material, namely a tungsten alloy composed by 95 % of tungsten and the remaining 5 % by copper and nickel. At 4.2 K, 77 K, and 293 K the tensile strength is 1085 MPa,

1284 MPa, and 973 MPa, respectively, while the fracture toughness is 21.3 $\mathrm{MPa\,m^{-1}}$, 29 $\mathrm{MPa\,m^{-1}}$, and 34.2 $\mathrm{MPa\,m^{-1}}$, respectively. The thermal conductivity ranges from 5 $\mathrm{W\,m^{-1}\,K^{-1}}$ at 4 K to 75 $\mathrm{W\,m^{-1}\,K^{-1}}$ at 80 K. The electrical resistivity ranges from $3.1 \cdot 10^{-8}$ at 40 K to $5.2 \cdot 10^{-8}$ at 100 K. The relative magnetic permeability in the temperature window from 7 K to 300 K is always below 1.005.

The thermal conductivity of zirconia was not known and therefore has been measured as well. It goes from 0.5 $\mathrm{W\,m^{-1}\,K^{-1}}$ at 4 K to 3 $\mathrm{W\,m^{-1}\,K^{-1}}$ at 80 K.

7.1.3 Beam screen behaviour during normal operation

The thermal profile of the beam screen during normal operation has been assessed through a FEM model which allows to specify the thermal contacts between the heat absorbers and the octagonal pipe. Assuming six thermal links per heat absorber and a thickness of 1 mm, it has been found that the main thermal requirements, *i.e.* an increase of the copper inner layer temperature no larger than 5 K, is satisfied through a link at least 3 mm wide. The maximum temperature difference between measurement and simulation of a small-scale beam screen sample is 25 $\%$. From simulation the temperature of the real-scale Q1 heat absorber is around 76 K, while the one for the Q2 heat absorber is 87 K. From measurement and simulations it turns out that the heat load transferred by the ceramic spheres to the cold bore varies between 5 mW and 7 mW.

7.1.4 Beam screen behaviour during a magnet quench (quench heaters)

A fully coupled multiphysics model has been developed in COMSOL Multiphysics to assess the magnetic, thermal, and mechanical behaviour of the beam screen during a magnet quench with quench heaters. The model is based on a reduced field formulation, which decreases the computational time of the simulation as no magnet coil needs to be modelled. The beam screens inserted in quadrupole magnets deform outwardly along the horizontal and vertical planes, while the beam screen inserted in the dipole magnet deforms only along the horizontal plane. For both cases the triplet area beam screens deform elastically. The highest radial displacement of the cold bore is 0.2 mm for the Q1 beam screen, 0.15 mm for the Q2 beam screen and 1 mm for the D1 beam screen. The cold bore does not come in contact with the magnet coil as the 1.5 mm distance is never exceeded. The thermal link deforms elastically up to a width of 3 mm.

7.1.5 Beam screen behaviour during a magnet quench (quench heaters + CLIQ)

A second fully coupled model has been developed in COMSOL Multiphysics and in Ansys to evaluate the behaviour of the Q1 and Q2 beam screens during a quench when the magnet is protected by quench heaters and CLIQ. It turns out that each quarter of the beam screen containing the heat absorbers is subject to a torque-load type. However, the overall response of the assembly is self-balanced. A new beam screen design capable to cope with the effects of CLIQ has been proposed. The deformations are elastic and the highest radial displacement of the cold bore is 1.5 mm for the Q1 beam screen and 1.06 mm for the Q2 beam screen. The thermal link deforms elastically up to a width of 5 mm.

7.2 Discussion

The research and development phase of the HL-LHC beam screen has started in 2014 and is still underway. The main challenges for the design of the beam screen have been the optimisation of the thermal transfer during normal conditions and the characterisation of the electromagnetic and thermomechanical behaviour during a magnet quench. The beam screen has come a long way from its first conceptual design consisting of a circular pipe and round absorbers [26]. This solution was abandoned due to an increased complexity of the manufacturing process of the heat absorbers and the assembly of the beam screen. The first evolution of the design, therefore, follows the demand to simplify the geometry of the heat absorbers. For this purpose an octagonally-shaped pipe has been developed. In this way, the surface of the heat absorber, leaning on the pipe, is flat and therefore easier to manufacture. The second evolution of the design has been driven by the need to increase the flexibility of the beam screen assembly. This has been obtained by connecting through elastic rings the heat absorbers to the octagonal pipe (and not by brazing as initially foreseen). This has allowed a reduction of the octagonal pipe thickness and therefore a gain in aperture as the Lorentz forces induced during a quench can be transferred to the cold bore. This evolution represents a more reliable assembly process as the heat absorbers are not suitable for soldering (tungsten vs stainless steel). The third evolution of the beam screen design is related to CLIQ, a recently developed quench protection system. Compared to the previous design based on quench heaters only, the positioning pins have been modified and doubled in number. In addition, the geometry of the heat absorbers has been changed as well. The newly proposed design is also compatible with the beam screen placed in magnets protected by quench heaters only.

The thermal behaviour of the beam screen has been studied through simulations and validated by measurements. A FEM model has been developed to optimise the heat transfer from the heat absorbers to the cooling tubes during normal operation. An important feature of the model is the possibility to specify the thermal contacts in terms of contact pressure, material hardness and surface roughness properties. The thermal transfer from the heat absorbers to the cooling tubes has been optimised through the thermal link design. Such a component has to fulfil three main functions: guarantee a proper thermal transfer from the heat absorber to the cooling tube in normal working conditions, exhibit an elastic behaviour during a magnet quench, and be flexible enough to allow the heat absorber to return to its original position after a quench. The best trade-off is represented by a 1 mm thick and 3 mm or 5 mm wide thermal link (depending on the quench protection scheme) made by a multilayer structure composed by ten 0.1 mm thick strips. This design was chosen because a uniformly thick thermal link would have made the assembly very stiff not allowing the heat absorber to return to its original positions after a quench. Moreover, a wider link would have not withstood a magnet quench without plastic deformations as the Lorentz forces depend on the second power of the width. Finally, a thicker link would have resulted in a deeper groove in the heat absorber and therefore a higher risk of fracture during a quench. An experimental campaign using small-scale samples has validated the simulations at temperatures ranging from 40 K to 80 K. An excellent agreement has been obtained between the experimental and numerical results concerning the thermal link welded on the beam screen. A worse trend has resulted in the case of the link welded on the cooling tube. This might be due to a full penetrating centering link which has not been considered in the simulation. The experimental results confirmed the fulfilment of the thermal requirement, *i.e.* during normal operation the temperature of the inner copper layer does not increase more than 5 K. However, it is noteworthy that the mechanical integrity of the thermal link during a magnet quench has not been validated experimentally yet.

The supporting system is composed of a titanium spring and a zirconia sphere to limit the heat load to the cold bore. It has been designed in a way to guarantee a gap of 1.5 mm between the heat absorber and the cold bore in normal working conditions. However, during a magnet quench the springs are compressed into their dedicated

slots to prevent damage. Kinematic analyses have demonstrated that the spires of the conical-shaped spring do not come in contact during a full contraction. 3D printing technology has been used to obtain the customised spring.

A full characterisation of the physical properties of the tungsten alloy was important to safely design the beam screen. An experimental campaign has been conducted at ambient and cryogenic temperatures. As expected, at cryogenic temperatures the mechanical properties of the tungsten alloy show better performance than at room temperature [39]. However, at 4.2 K there is a drop of mechanical strength and fracture toughness compared to the values obtained at 77 K [39]. This is due to an intra-grain fracture propagation, which prevails on the inter-grain mechanism. The electrical resistivity is rather flat in the temperature range of interest, namely from 40 K to 100 K.

During a magnet quench, where the magnets are protected by quench heaters, the magnetic field has been conveniently assigned through a reduced field formulation. Therefore, no magnet coil has been modelled resulting in a considerable gain of computational time. However, this is possible if the quench heaters only are used to protect the magnet as for each time step the magnet gradient remains monotonic. The interaction between the magnetic and the thermal physics has been set up according to a two-way coupling, while that between the mechanical and magnetic ones through a one-way coupling. Both couplings have been fully implemented within COMSOL Multiphysics. In this way, the electrical and thermal properties of the beam screen components are constantly updated during the magnet quench and the Lorentz forces are transferred linearly to the solid mechanics interface. This approach turns out to be the best trade-off in terms of computational load and significance of the results. In particular it has been found that the effects of a two-way coupling between the magnetic and mechanical interface are negligible. Since the beam screen is a flexible assembly, the mechanical response has been evaluated dynamically. This has revealed, for the first time, critical values of the stress and displacement at the beginning of the quench rather than at the moment when the highest forces are induced. Since the model allows studying three dimensional geometries, the design of the thermal link placed along the beam axis direction has been optimised. The model has been verified by comparison to a closed form expression. In particular, the integrated forces of the model and the closed form expression are shown to be in excellent agreement for values of electrical conductivity up to 10^7 S/m. Between the two methods, the relative error is below 1 %. At higher values of electrical conductivity, due to the effects of self-inductance the forces predicted by the proposed FEM models are lower by a few order of magnitude and delayed in time. A limitation of the model is that the magnetic field needs to be monotonic over the air domain region.

In case of the magnet protection scheme based on quench heaters together with CLIQ, the magnet gradient of the quadrupoles does not remain monotonic during the current discharge. Therefore, the magnetic field has not been assigned by means of a reduced field formulation. A solution based on four bars placed in an iron annulus with the scope to confine the field has been adopted. To this purpose, each bar can be magnetised by a factor proportional to the currents independently. Moreover, the magnetic field can be further tuned by varying the geometrical and physical parameters of the model configuration. The magnetic field generated by the proposed configuration has been verified with ROXIE, the software used at CERN for field quality analysis, resulting in a relative error lower than 1.1 %. The unbalance of the magnetic field during the first phases of the CLIQ discharge results in a torque induced in each quadrant of the assembly. As the complexity of the mechanical analysis increases, the problem has been split in two FEM platforms. The thermo-magnetic analysis has been carried out in COMSOL Multiphysics accounting for a two-way coupling and self-inductance phenomena, while the mechanical analysis has been performed dynamically in Ansys, which provides a more robust solver to handle the increased number of mechanical contacts. The torque load has called for a change of the original design of the beam screen, which was conceived to withstand only the Lorentz forces distribution corresponding to a magnet protected by quench heaters. The fast electrodynamics of the CLIQ discharge has been further analysed

by considering the structure of the magnet coil and its interaction with the beam screen. Preliminary analyses have revealed a damping effect of around 33 % in terms of induced forces. Therefore, if these calculations will be confirmed by experiments the coil electrodynamic will play an important damping role.

7.3 Future work

The effects of translational and rotational misalignments of the beam screen within the cold bore need to be studied to investigate a detrimental unbalance of the induced forces on the fixed point of the assembly. Further analyses of the magnet coil electrodynamics is also necessary to get an insight on the mechanisms of the Lorentz forces damping. The temperature distribution over the beam screen in actual operating conditions will be measured by mid 2018. In parallel, an experimental campaign to assess the behaviour of the Q1, Q2, and D1 beam screens during a magnet quench will be performed. The aim of this test is to demonstrate the mechanical integrity of the beam screens whose design is based on the fully coupled multiphysic models described in this thesis. The mechanical response of the beam screen will be measured for a quench protection scheme based on quench heaters and CLIQ for the Q1 and Q2 beam screens and only with quench heaters for the D1 beam screen.

7.4 Conclusions

Magnetic, mechanical, and electro-thermal physical properties of the materials used for the beam screen were unknown and therefore have been measured. The properties of the selected materials have been found to be suitable for the beam screen application. The fulfilment of the thermal requirements during normal operation conditions has been successfully demonstrated by simulation and experiments. The models proposed in this thesis introduce a step change in our understanding of the behaviour of the beam screen during a magnet quench as they are more comprehensive and powerful than previously developed formulations.

Compared to the analytical formulations used to design the beam screen currently installed in the LHC [64] [63], the multiphysics FEM models developed in this research introduces multiple elements of novelty and improved performance. First, self-inductance effects are accounted for and found to reduce the induced forces up to approximately 2000 % at high electrical conductivity values. Second, the one-way and two-way coupling of the magnetic with the mechanical and thermal interfaces are explored and the best trade-off is defined. Third, the mechanical response of the assembly is evaluated dynamically over the evolution of the magnetic field decay rather than just in a quasi-static manner. Fourth, three dimensional geometries can also be studied enabling the design of the components to be placed along the beam axis.

Finally, a design of the beam screen capable to withstand the effects of a magnet quench is provided for two quench protection schemes: quench heaters and these used together with CLIQ. The mechanical integrity of the beam screen placed in the Q1, Q2a, Q2b, Q3, and D1 is demonstrated by simulations.

7.5 Contributions and impact

This work constitutes the first effort in the complete analysis of the behaviour and response of a complex assembly to a magnet quench as well as in the development of a guide for the design of devices subject to a magnetic field

variation. The major contribution of this thesis results in the development of two new multiphysics FEM models. The first model has been developed to study the behaviour of the beam screen placed in a magnet protected by quench heaters, while the second model to assess the behaviour of the beam screen placed in a magnet protected by quench heaters and CLIQ. The models have been verified by comparison to a closed form expression showing the advantages of considering self-inductance phenomena. Such models can be therefore used to study multiphysics problems related to power converter technology, nuclear power plant applications and induction heating devices. Important insights on the magnetic, thermal, and mechanical behaviour of the HL-LHC beam screen during a magnet quench have been obtained. In particular, the understanding of the mechanical response in the case of CLIQ has called for a new design of the positioning pins from a straight cylinder to one consisting of two co-axial cylinders of different diameter welded on the octagonal pipe. The number of pins has doubled in comparison with the design based on quench heaters only and the geometry of the heat absorbers has been adapted accordingly.

The design of the beam screen has been largely supported by the proposed models and, at present, it is the final version before the launch of the experimental campaign provided that no changes of the quench protection systems take place.

To date the models have already been adopted to support the conceptual design of an *ad-hoc* beam screen for the Future Circular Collider (FCC) [144] [145], to assess the magnetic frequency response of the assembly due to power converter noise [146] [147], and to compensate the effects of the eddy currents induced in the Proton Synchrotron (PS) vacuum chambers during the magnetic field ramp-up [148] [149].

7.6 Publications and awards

The publications written during the doctoral project and the awards received are listed in this section.

Journal papers:

- Morrone, M., Garion, C., Aurisicchio, M. and Chiggiato, P. A coupled multiphysics FEM model to investigate electromagnetic, thermal and mechanical effects in complex assemblies: the design of th High-Luminosity LHC beam screen, *Applied Mathematical Modelling*;
- Morrone, M., Martino, M., Garion, C., Fitterer, M. and De Maria, R. Magnetic Frequency Response of HL-LHC Beam Screens, *Physical Review Accelerators and Beams* (under review).

Conference papers:

- Garion, C., L. Dufay-Chanat, T. Koettig, W. Machiocha, and M. Morrone. "Material characterisation and preliminary mechanical design for the HL-LHC shielded beam screens operating at cryogenic temperatures." In IOP Conference Series: Materials Science and Engineering, vol. 102, no. 1, p. 012013; IOP Publishing, 2015.
- Morrone, Marco, Cedric Garion, Paolo Chiggiato, and Marco Aurisicchio. "Mechanical Design of the High-Luminosity Large Hadron Collider (HL-LHC) Beam Screen through a Multiphysics Model." PoS (2016): 914.

- de Sousa, P. Borges, M. Morrone, N. Hovenga, C. Garion, R. van Weelderen, T. Koettig, and J. Bremer. "Parametric study on the thermal performance of beam screen samples of the High-Luminosity LHC upgrade." In IOP Conference Series: Materials Science and Engineering, vol. 278, no. 1, p. 012053. IOP Publishing, 2017.

Posters:

- Mechanical design of the HL-LHC beam screens, presented at the International Conference on High Energy Physics (ICHEP) 2016, Chicago, USA, on the 6^{th} of August 2016;
- Unveiling the Origin of the Universe: Mechanical Design of the Future LHC Beam Screen, presented at the House of Parliament, London on the 7^{th} of March 2016.

Awards:

- Distinguished Poster Award at ICHEP 2016;
- Selected student to showcase his own research at the event SET FOR BRITAIN in the House of Parliament, London.

References

[1] L. Evans and P. Bryant, "Lhc machine," *Journal of Instrumentation*, vol. 3, no. 08, p. S08001, 2008. [Online]. Available: http://stacks.iop.org/1748-0221/3/i=08/a=S08001

[2] G. Aad, T. Abajyan, B. Abbott, J. Abdallah, S. A. Khalek, A. Abdelalim, O. Abdinov, R. Aben, B. Abi, M. Abolins *et al.*, "Observation of a new particle in the search for the standard model higgs boson with the atlas detector at the lhc," *Physics Letters B*, vol. 716, no. 1, pp. 1–29, 2012.

[3] W. Herr and B. Muratori, "Concept of luminosity," Tech. Rep., 2006, Availabe from: https://cds.cern.ch/record/941318.

[4] L. Rossi and O. Brüning, "The high luminosity large hadron collider: The new machine for illumination the mysteries of the universe," *The High Luminosity Large Hadron Collider: The New Machine for Illumination the Mysteries of the Universe. Edited by ROSSI LUCIO & BRUNING OLIVER. Published by World Scientific Publishing Co. Pte. Ltd., 2015. ISBN# 9789814675475*, vol. 1, 2015.

[5] G. Apollinari, I. Bejar Alonso, O. Brüning, P. Fessia, M. Lamont, L. Rossi, and L. Tavian, *High-Luminosity Large Hadron Collider (HL-LHC). Technical Design Report V.0.1*, ser. CERN Yellow Reports: Monographs. CERN, 2017, vol. 4. [Online]. Available: http://dx.doi.org/10.23731/CYRM-2017-004

[6] G. Apollinari, I. Béjar Alonso, O. Brüning, M. Lamont, and L. Rossi, *High-Luminosity Large Hadron Collider (HL-LHC): Preliminary Design Report*, ser. CERN Yellow Reports: Monographs. Geneva: CERN, 2015. [Online]. Available: https://cds.cern.ch/record/2116337

[7] L. Rossi and O. Brüning, *The High Luminosity Large Hadron Collider: the new machine for illuminating the mysteries of Universe*, ser. Advanced series on directions in high energy physics. Hackensack, NJ: World Scientific, 2015, will also be published as a special issue of International journal of modern physics A. [Online]. Available: https://cds.cern.ch/record/1995532

[8] O. Grobner, "The lhc vacuum system," in *Particle Accelerator Conference, 1997. Proceedings of the 1997*, vol. 3. IEEE, 1997, pp. 3542–3546.

[9] S. Claudet, P. Gayet, and U. Wagner, "Specification of four new large 4.5 k helium refrigerators for the lhc," in *Advances in cryogenic engineering*. Springer, 2000, pp. 1269–1276.

[10] L. Bottura, "Magnet Quench 101. Magnet Quench 101," no. arXiv:1401.3927, pp. 1–9. 9 p, Jan 2014, comments: 9 pages, Contribution to WAMSDO 2013: Workshop on Accelerator Magnet, Superconductor, Design and Optimization; 15 - 16 Jan 2013, CERN, Geneva, Switzerland. [Online]. Available: http://cds.cern.ch/record/1643429

[11] K. Dahlerup-Petersen, R. Denz, J. Gomez-Costa, D. Hagedorn, P. Proudlock, F. Rodrinuez-Mateos, R. Schmidt, and F. Sonnemann, "The protection system for the superconducting elements of the large hadron collider at cern," in *Particle Accelerator Conference, 1999. Proceedings of the 1999*, vol. 5. IEEE, 1999, pp. 3200–3202.

[12] E. Ravaioli, "Cliq. a new quench protection technology for superconducting magnets," Ph.D. dissertation, 2015.

[13] V. Baglin, L. Tavian, P. Lebrun, and R. van Weelderen, "Cryogenic beam screens for high-energy particle accelerators," Tech. Rep., 2013, Availabe from: https://cds.cern.ch/record/1507613.

[14] G. Iadarola, "Electron cloud studies for cern particle accelerators and simulation code development," Ph.D. dissertation, 2014.

[15] F. Zimmermann, "Electron cloud effects in the lhc," Tech. Rep., 2002, Availabe from: https://cds.cern.ch/record/585562.

[16] A. Tsinganis and F. Cerutti, "Energy deposition in the hl-lhc experimental irs (v1.3)," Tech. Rep., 2017, Availabe from: https://indico.cern.ch/event/676089/contributions/2767533.

[17] R. Kersevan, "Synchrotron radiation distribution and related outgassing and pressure profiles for the hl-lhc final focus magnets," Tech. Rep., 2015, Available from: https://cds.cern.ch/record/2141878?ln=en.

[18] G. Iadarola, "Beam induced heat loads on hl-lhc beam screens," Tech. Rep., 2017, Availabe from: https://indico.cern.ch/event/676089/contributions/2767533.

[19] O. Brüning, P. Collier, P. Lebrun, S. Myers, R. Ostojic, J. Poole, and P. Proudlock, "Lhc design report vol. 1," *CERN, Geneva, Switzerland*, vol. 157, p. 170, 2004.

[20] V. Baglin, "Vacuum transients during lhc operation," 2004, Available from: https://cds.cern.ch/record/726331.

[21] V. Anashin, G. Derevyankin, V. Dudnikov, O. Malyshev, V. Osipov, C. Foerster, F. Jacobsen, M. Ruckman, M. Strongin, R. Kersevan *et al.*, "Cold beam tube photodesorption and related experiments for the superconducting super collider laboratory 20 tev proton collider," *Journal of Vacuum Science & Technology A: Vacuum, Surfaces, and Films*, vol. 12, no. 4, pp. 1663–1672, 1994.

[22] L. S. G. Collaboration *et al.*, "Lhc—the large hadron collider accelerator project," CERN-AC-93-03 (known as the "White Book"), http://cdsweb. cern. ch/record/87244, Tech. Rep., 2003.

[23] Y. Baconnier, J. Jeanneret, and A. Poncet, "Lhc beam aperture and beam screen geometry," CERN-LHC-Note-326, Tech. Rep., 1995.

[24] E. Luigi, "3rd joint hilumi lhc-larp annual meeting," https://indico.cern.ch/event/257368/contributions., Tech. Rep., 2013.

[25] V. Baglin and C. Garion, "Draft conceptual specification hl-lhc shielded beam screen [lhc-vsm]- wp12," Tech. Rep., 2013, Available from: https://edms.cern.ch/document/1361079/0.2.

[26] R. Kersevan, C. Garion, and N. Kos, "Preliminary design of the hilumi-lhc triplet area beam screen," Tech. Rep., 2014, Available from: http://cds.cern.ch/record/1968539?ln=en.

[27] C. Garion, "Mechanical design of the hl triplet beam screen," Tech. Rep., 2014, Available from: https://indico.cern.ch/event/339901/.

[28] R. Salemme, R. Kersevan, G. Bregliozzi, P. Chiggiato, and V. Baglin, "Amorphous carbon coatings at cryogenic temperatures with lhc type beams: first results with the coldex experiment," Tech. Rep., 2015, Available from: http://cds.cern.ch/record/2141874?ln=sk.

[29] P. Fessia, P. Thonet, and E. Skordis, "Radiation shielding installation for the mbw and mqw magnets in ir 3 and 7 of the lhc." Tech. Rep., 2013, Available from: https://edms.cern.ch/ui/ Document number: 1321044.

[30] M. Reytier, F. Kircher, and B. Levesy, "Characterization of titanium alloys for cryogenic applications," in *AIP Conference Proceedings*, vol. 614, no. 1. AIP, 2002, pp. 76–83.

[31] E. S. P. Fessia, P. A. Thonet, "Radiation shielding installation for the mbw and mqw magnets in ir 3 and 7 of the lhc," Tech. Rep., 2013, Available from: https://edms.cern.ch/ui/file/1321044/1.0/LHC-MW-EC-0001-10-00.pdf.

[32] S. Sgobba and G. Hochortler, "New non-magnetic stainless steel for very low temperature applications," in *Associazione Italiana di Metallurgia, International Congress Stainless Steel'99 Science and Market 3 rd European Congress Proceedings,*, vol. 2, 1999, pp. 391–401.

[33] J. Sa, H. Kim, C. Choi, H. Kim, K. Hong, H. Park, J. Bak, K. Lee, and E. Ha, "Mechanical characteristics of austenitic stainless steel 316ln weldments at cryogenic temparature," in *Fusion Engineering 2005, Twenty-First IEEE/NPS Symposium on*. IEEE, 2005, pp. 1–4.

[34] N. Simon, "Properties of copper and copper alloys at cryogenic temperatures," *NIST monograph*, vol. 177, 1992.

[35] SCERAM website, "Zirconia data sheet," 2017, http://sceram.com.

[36] P. Lorenzo, M. Miralda, S. Iyengar, S. Melin, and E. Noah, "Fatigue properties and characterization of tungsten heavy alloys it180 & d176," *International Journal of Refractory Metals and Hard Materials*, vol. 41, pp. 250–258, 2013.

[37] M. Scapin, "Mechanical characterization and modeling of the heavy tungsten alloy it180," *International Journal of Refractory Metals and Hard Materials*, vol. 50, pp. 258–268, 2015.

[38] J. Das, G. A. Rao, and S. Pabi, "Microstructure and mechanical properties of tungsten heavy alloys," *Materials Science and Engineering: A*, vol. 527, no. 29, pp. 7841–7847, 2010.

[39] C. Garion, L. Dufay-Chanat, T. Koettig, W. Machiocha, and M. Morrone, "Material characterisation and preliminary mechanical design for the hl-lhc shielded beam screens operating at cryogenic temperatures." in *IOP Conference Series: Materials Science and Engineering*, vol. 102, no. 1. IOP Publishing, 2015, p. 012013.

[40] S. Sgobba, "Physics and measurements of magnetic materials," *arXiv preprint arXiv:1103.1069*, 2011.

[41] N. Wilson and P. Bunch, "Magnetic permeability of stainless steel for use in accelerator beam transport systems," *PAC1991–2322*, 1991.

[42] S. Sgobba, "Materials for high vacuum technology, an overview," Cern, Tech. Rep., 2006, Available from: https://cds.cern.ch/record/983744/files/p117.pdf.

[43] Amatweb website, "Titanium grade 5 data sheet," 2017, http://asm.matweb.com/.

[44] P. Duthil, "Material Properties at Low Temperature," no. arXiv:1501.07100. arXiv:1501.07100, pp. 77–95. 18 p, Jan 2015, comments: 18 pages, contribution to the CAS-CERN Accelerator School: Superconductivity for Accelerators, Erice, Italy, 24 April - 4 May 2013, edited by R. Bailey. [Online]. Available: https://cds.cern.ch/record/1973682

[45] O. Umezawa and K. Ishikawa, "Electrical and thermal conductivities and magnetization of some austenitic steels, titanium and titanium alloys at cryogenic temperatures," *Cryogenics*, vol. 32, no. 10, pp. 873–880, 1992.

[46] J. Ho, G. King, and F. Fickett, "Low temperature specific heat of two stainless steels," *Cryogenics*, vol. 18, no. 5, pp. 296–298, 1978.

[47] W. Ziegler and J. Mullins, "Final rept., proj. no. a-504, p1-54, georgia inst. technology," 1961.

[48] G. K. White and S. Collocott, "Heat capacity of reference materials: Cu and w," *Journal of physical and chemical reference data*, vol. 13, no. 4, pp. 1251–1257, 1984.

[49] M. Rouby and P. Blanchard, "Physical and mechanical properties of stainless steels," *Les Editions de Physique Les Ulis, Cedex A, France*, p. 139, 1993.

[50] V. Baglin, "Optimal temperature window of the beam screens in the IT," Tech. Rep., 2017, Available from: https://indico.cern.ch/event/590398/contributions/2463698.

[51] E. Hatchadourian, L. Tavian, and P. Lebrun, "Supercritical helium cooling of the lhc beam screens," Tech. Rep., 1998, Available from: https://cds.cern.ch/record/364733.

[52] F. Dittus and L. Boelter, "Heat transfer in automobile radiators of the tubular type," *International Communications in Heat and Mass Transfer*, vol. 12, no. 1, pp. 3–22, 1985.

[53] A. P. Colburn, *A method of correlating forced convection heat transfer data and a comparison with fluid friction*. Elsevier, 1933.

[54] M. Cooper, B. Mikic, and M. Yovanovich, "Thermal contact conductance," *International Journal of heat and mass transfer*, vol. 12, no. 3, pp. 279–300, 1969.

[55] M. Grujicic, C. Zhao, and E. Dusel, "The effect of thermal contact resistance on heat management in the electronic packaging," *Applied Surface Science*, vol. 246, no. 1, pp. 290–302, 2005.

[56] J. Zheng, Y. Li, P. Chen, G. Yin, and H. Luo, "Measurements of interfacial thermal contact conductance between pressed alloys at low temperatures," *Cryogenics*, vol. 80, pp. 33–43, 2016.

[57] T. Koettig, W. Maciocha, S. Bermudez, J. Rysti, S. Tavares, F. Cacherat, and J. Bremer, "Thermal conductivity measurements of impregnated nb3sn coil samples in the temperature range of 3.5 k to 100 k," in *IOP Conference Series: Materials Science and Engineering*, vol. 171, no. 1. IOP Publishing, 2017, p. 012103.

[58] P. B. de Sousa, M. Morrone, N. Hovenga, C. Garion, R. van Weelderen, T. Koettig, and J. Bremer, "Parametric study on the thermal performance of beam screen samples of the high-luminosity lhc upgrade," in *IOP Conference Series: Materials Science and Engineering*, vol. 278, no. 1. IOP Publishing, 2017, p. 012053.

[59] L. Tavian, "Beam screen regenerative heating: cryogenic impact and feasibility," CERN-LHC-Project-Note-330, Tech. Rep., 2003, Available from: http://cds.cern.ch/record/689958?ln=sk.

[60] W. E. Forsythe and A. Worthing, "The properties of tungsten and the characteristics of tungsten lamps," *The Astrophysical Journal*, vol. 61, p. 146, 1925.

[61] Z. Charifoulline, L. Bortot, R. Denz, F. R. Mateos, A. Siemko, J. Steckert, A. Verweij, and G. Willering, "Overview of the performance of quench heaters for high-current lhc superconducting magnets," *IEEE Transactions on Applied Superconductivity*, vol. 27, no. 4, pp. 1–5, 2017.

[62] F. Rodriguez-Mateos and F. Sonnemann, "Quench heater studies for the lhc magnets," in *Particle Accelerator Conference, 2001. PAC 2001. Proceedings of the 2001*, vol. 5. IEEE, 2001, pp. 3451–3453.

[63] C. Rathjen, "Mechanical behaviour of vacuum chambers and beam screens under quench conditions in dipole and quadrupole fields," Tech. Rep., 2002, Available from: https://accelconf.web.cern.ch/accelconf/e02/PAPERS/WEPDO039.pdf.

[64] R. Valbuena, "Calcul des courants de foucault et analyse mecanique de l'ecran de faisceau des quadrupoles < low-beta > supraconducteurs du lhc en cas de transition resistive," Tech. Rep., 2002, CERN note EST-ESI/2000-005 revl.

[65] "Castem software," Availabe from: http://www-cast3m.cea.fr/.

[66] J.-B. Ferrer, "Finite element analysis on thee lhc dipole screen in quench situation." Tech. Rep., 1993, CERN note MT-ESH/93-26.

[67] J. M. Darve, "Fe analysis of the beam screen for cross-checking of the quench tests in a short model magnet and in the 15 metre long lhc dipole magnet," Tech. Rep., 2001, CERN note EST-ME/2001-001.

[68] P. Monk, *Finite element methods for Maxwell's equations*. Oxford University Press, 2003.

[69] A. Bossavit, *Computational electromagnetism: variational formulations, complementarity, edge elements*. Academic Press, 1998.

[70] P. D. Ledger, A. J. Gil, R. Poya, M. Kruip, I. Wilkinson, and S. Bagwell, "Solution of an industrially relevant coupled magneto–mechanical problem set on an axisymmetric domain," *Applied Mathematical Modelling*, vol. 40, no. 3, pp. 1959–1971, 2016.

[71] P. Ledger and K. Morgan, "An adjoint enhanced reduced-order model for monostatic rcs computation," *Electromagnetics*, vol. 28, no. 1-2, pp. 54–76, 2008.

[72] A. Bossavit and J.-C. Verite, "A mixed fem-biem method to solve 3-d eddy-current problems," *IEEE Transactions on Magnetics*, vol. 18, no. 2, pp. 431–435, 1982.

[73] T. Morisue and M. Fukumi, "3-d eddy current calculations using the magnetic vector potential," *IEEE Transactions on magnetics*, vol. 24, no. 1, pp. 106–109, 1988.

[74] A. Kameari, "Three-dimensional eddy current calculation using finite element method with av in conductor and omega in vacuum," *IEEE Transactions on magnetics*, vol. 24, no. 1, pp. 118–121, 1988.

[75] O. Biro and K. Preis, "On the use of the magnetic vector potential in the finite-element analysis of three-dimensional eddy currents," *IEEE Transactions on magnetics*, vol. 25, no. 4, pp. 3145–3159, 1989.

[76] O. Biro, K. Preis, and W. Renhart, "Finite element analysis of 3d multiply connected eddy current problems," *IEEE transactions on magnetics*, vol. 25, no. 5, pp. 4009–4011, 1989.

[77] J. Webb and B. Forghani, "A scalar-vector method for 3d eddy current problems using edge elements," *IEEE Transactions on Magnetics*, vol. 26, no. 5, pp. 2367–2369, 1990.

[78] H. Kanayama, D. Tagami, K. Imoto, and S.-i. Sugimoto, "Finite element computation of magnetic field problems with the displacement current," *Journal of computational and applied mathematics*, vol. 159, no. 1, pp. 77–84, 2003.

[79] W. Zheng, Z. Chen, and L. Wang, "An adaptive finite element method for the h-ψ formulation of time-dependent eddy current problems," *Numerische Mathematik*, vol. 103, no. 4, pp. 667–689, 2006.

[80] Q. Luo and L. Tong, "Multi-physics field models of photostrictive unimorphs and heterogeneous bimorphs subjected to light illumination and mechanical loading," *International Journal of Solids and Structures*, vol. 47, no. 16, pp. 2006–2016, 2010.

[81] C. Oskay and M. Haney, "Computational modeling of titanium structures subjected to thermo-chemo-mechanical environment," *International Journal of Solids and Structures*, vol. 47, no. 24, pp. 3341–3351, 2010.

[82] M. Scapin, L. Peroni, and A. Dallocchio, "Effects induced by lhc high energy beam in copper structures," *Journal of Nuclear Materials*, vol. 420, no. 1, pp. 463–472, 2012.

[83] Y. P. Jiang, D. Wang, Q. H. Zhang, and J. Q. Chen, "Electromagnetic-thermal coupling simulation by ansys multiphysics of induction heater," in *Applied Mechanics and Materials*, vol. 701. Trans Tech Publ, 2015, pp. 820–825.

[84] O. C. Zienkiewicz and R. L. Taylor, *The finite element method: solid mechanics*. Butterworth-heinemann, 2000, vol. 2.

[85] R. Haj-Ali, H. Zemer, R. El-Hajjar, and J. Aboudi, "Piezoresistive fiber-reinforced composites: a coupled nonlinear micromechanical–microelectrical modeling approach," *International Journal of Solids and Structures*, vol. 51, no. 2, pp. 491–503, 2014.

[86] J. Aboudi and R. Haj-Ali, "A fully coupled thermal–electrical–mechanical micromodel for multi-phase periodic thermoelectrical composite materials and devices," *International Journal of Solids and Structures*, vol. 80, pp. 84–95, 2016.

[87] C. Kaufmann, M. Günther, D. Klagges, M. Knorrenschild, M. Richwin, S. Schöps, and E. J. Ter Maten, "Efficient frequency-transient co-simulation of coupled heat-electromagnetic problems," *Journal of Mathematics in Industry*, vol. 4, no. 1, pp. 1–13, 2014.

[88] Y. Li, Z. Wang, and S. Yang, "3d electromagnetic and thermal field analysis of edge induction heater," in *Electrical Machines and Systems (ICEMS), 2014 17th International Conference on*. IEEE, 2014, pp. 3463–3468.

[89] J. Nerg and J. Partanen, "Numerical solution of 2d and 3d induction heating problems with nonlinear material properties taken into account," *IEEE transactions on magnetics*, vol. 36, no. 5, pp. 3119–3121, 2000.

[90] F. Bay, V. Labbé, Y. Favennec, and J.-L. Chenot, "A numerical model for induction heating processes coupling electromagnetism and thermomechanics," *International Journal for Numerical Methods in Engineering*, vol. 58, no. 6, pp. 839–867, 2003.

[91] M. Kaltenbacher, R. Landes, and R. Lerch, "An efficient calculation scheme for the numerical simulation of coupled magnetomechanical systems," *IEEE Transactions on Magnetics*, vol. 33, no. 2, pp. 1646–1649, 1997.

[92] M. Rausch, M. Gebhardt, M. Kaltenbacher, and H. Landes, "Magnetomechanical field computations of a clinical magnetic resonance imaging (mri) scanner," *COMPEL-The international journal for computation and mathematics in electrical and electronic engineering*, vol. 22, no. 3, pp. 576–588, 2003.

[93] S. Bagwell, P. D. Ledger, A. J. Gil, M. Mallett, and M. Kruip, "A linearised hp–finite element framework for acousto-magneto-mechanical coupling in axisymmetric mri scanners," *International Journal for Numerical Methods in Engineering*.

[94] M. Rausch, M. Gebhardt, M. Kaltenbacher, and H. Landes, "Computer-aided design of clinical magnetic resonance imaging scanners by coupled magnetomechanical-acoustic modeling," *IEEE transactions on magnetics*, vol. 41, no. 1, pp. 72–81, 2005.

[95] M. Schinnerl, J. Schoberl, M. Kaltenbacher, and R. Lerch, "Multigrid methods for the three-dimensional simulation of nonlinear magnetomechanical systems," *IEEE transactions on magnetics*, vol. 38, no. 3, pp. 1497–1511, 2002.

[96] W. F. Brown Jr, "Theory of magnetoelastic effects in ferromagnetism," *Journal of Applied Physics*, vol. 36, no. 3, pp. 994–1000, 1965.

[97] M. Besbes, Z. Ren, and A. Razek, "Finite element analysis of magneto-mechanical coupled phenomena in magnetostrictive materials," *IEEE Transactions on Magnetics*, vol. 32, no. 3, pp. 1058–1061, 1996.

[98] L. Gros, G. Reyne, C. Body, and G. Meunier, "Strong coupling magneto mechanical methods applied to model heavy magnetostrictive actuators," *IEEE Transactions on magnetics*, vol. 34, no. 5, pp. 3150–3153, 1998.

[99] P.-S. Shin and H.-J. Cheung, "A magnetostrictive force and vibration mode analysis of 3 kw bldc motor by a magneto-mechanical coupling formulation," *Journal of Electrical Engineering and Technology*, vol. 6, no. 1, pp. 76–80, 2011.

[100] Q. Yang, R. Yan, C. Fan, H. Chen, F. Liu, and S. Liu, "A magneto-mechanical strongly coupled model for giant magnetostrictive force sensor," *IEEE Transactions on Magnetics*, vol. 43, no. 4, pp. 1437–1440, 2007.

[101] R. Lerch, M. Kaltenbacher, H. Landes, M. Hofer, J. Hoffelner, M. Rausch, and M. Schinnerl, "Advanced computer modeling of magnetomechanical transducers and their sound fields," in *Ultrasonics Symposium, 2000 IEEE*, vol. 1. IEEE, 2000, pp. 747–758.

[102] M. Kaltenbacher, *Numerical simulation of mechatronic sensors and actuators*. Springer, 2007, vol. 2.

[103] A. El-Azab, M. Garnich, and A. Kapoor, "Modeling of the electromagnetic forming of sheet metals: state-of-the-art and future needs," *Journal of Materials Processing Technology*, vol. 142, no. 3, pp. 744–754, 2003.

[104] J. R. Alves Z and F. Bay, "Magnetic pulse forming: Simulation and experiments for high-speed forming processes," *Advances in Materials and Processing Technologies*, vol. 1, no. 3-4, pp. 560–576, 2015.

[105] H. A. Haus and J. R. Melcher, *Electromagnetic fields and energy*. Prentice Hall, 1989.

[106] A. A. Bernal and L. L. García, "The modelling of an electromagnetic energy harvesting architecture," *Applied Mathematical Modelling*, vol. 36, no. 10, pp. 4728–4741, 2012.

[107] C. G. Someda, *Electromagnetic waves*. Crc Press, 2006.

[108] Z. Zeng, L. Udpa, S. S. Udpa, and M. S. C. Chan, "Reduced magnetic vector potential formulation in the finite element analysis of eddy current nondestructive testing," *IEEE transactions on magnetics*, vol. 45, no. 3, pp. 964–967, 2009.

[109] E. X. Xu and J. Simkin, "Total and reduced magnetic vector potentials and electrical scalar potential for eddy current calculation," *IEEE transactions on magnetics*, vol. 40, no. 2, pp. 938–940, 2004.

[110] O. Biro and K. Preis, "An edge finite element eddy current formulation using a reduced magnetic and a current vector potential," *IEEE Transactions on Magnetics*, vol. 36, no. 5, pp. 3128–3130, 2000.

[111] "Comsol multiphysics software," Availabe from: https://www.comsol.com.

[112] Z. Wei and L. K. Weavers, "Combining comsol modeling with acoustic pressure maps to design sonoreactors," *Ultrasonics sonochemistry*, vol. 31, pp. 490–498, 2016.

[113] M. Schwertz, A. Katz, E. Sorrel, S. Lemonnier, E. Barraud, A. Carradò, S. d'Astorg, A. Leriche, M. Nardin, M.-F. Vallat *et al.*, "Coupled electro-thermo-mechanical finite element modeling of the spark plasma sintering technique," *Metallurgical and Materials Transactions B*, vol. 47, no. 2, pp. 1263–1273, 2016.

[114] T. A. Jankowski, N. H. Pawley, L. M. Gonzales, C. A. Ross, and J. D. Jurney, "Approximate analytical solution for induction heating of solid cylinders," *Applied Mathematical Modelling*, vol. 40, no. 4, pp. 2770–2782, 2016.

[115] B. Shen, L. Fu, J. Geng, X. Zhang, H. Zhang, Q. Dong, C. Li, J. Li, and T. Coombs, "Design and simulation of superconducting lorentz force electrical impedance tomography (lfeit)," *Physica C: Superconductivity and its Applications*, vol. 524, pp. 5–12, 2016.

[116] S. sandoval Torres, W. Jomaa, J.-R. Puiggali, and S. Avramidis, "Multiphysics modeling of vacuum drying of wood," *Applied Mathematical Modelling*, vol. 35, no. 10, pp. 5006–5016, 2011.

[117] N. Xoubi and A. Y. Soliman, "Neutronic modeling and calculations of the etrr-2 mtr reactor using comsol multiphysics code," *Annals of Nuclear Energy*, vol. 109, pp. 667–674, 2017.

[118] "Ansys software," Availabe from: https://www.ansys.com.

[119] "Opera simulation software," Availabe from: http://operafea.com/.

[120] "Nacs finite element analysis software," Availabe from: https://www.simetris.de/.

[121] "COMSOL Multiphysics, AC/DC User's Guide, Documentation within Software Package, Ver. 5.2, 2016."

[122] E. Drexler, N. Simon, and R. Reed, "Properties of copper and copper alloys at cryogenic temperatures," NIST, Tech. Rep., 1992.

[123] L. Bortot, M. Maciejewski, M. Prioli, A. M. F. Navarro, J. B. Ghini, B. Auchmann, and A. P. Verweij, "A consistent simulation of electrothermal transients in accelerator circuits," *IEEE Transactions on Applied Superconductivity*, vol. 27, no. 4, pp. 1–5, 2017.

[124] S. Manson, "National advisory commission on aeronautics: Report 1170," *Lewis Fight Propulsion Laboratory, Cleveland*, 1954.

[125] W. O'Donnell and B. Langer, "Fatigue design basis for zircaloy components," *Nuclear Science and Engineering*, vol. 20, no. 1, pp. 1–12, 1964.

[126] A. Singhal, J. Stubbins, B. Singh, and F. Garner, "Room temperature fatigue behavior of ofhc copper and cual25 specimens of two sizes," *Journal of nuclear materials*, vol. 212, pp. 1307–1312, 1994.

[127] F. Bullen, A. K. Head, and W. Wood, "Structural changes during the fatigue of metals," in *Proceedings of the Royal Society of London A: Mathematical, Physical and Engineering Sciences*, vol. 216, no. 1126. The Royal Society, 1953, pp. 332–343.

[128] M. Klesnil and P. Lukáš, *Fatigue of metallic materials*. Elsevier, 1992, vol. 71.

[129] B. E. Jelke, "Low cycle fatigue and crack growth in oxygen free high conductivity copper," 1991.

[130] K. Hatanaka and Y. Ishimoto, "An analysis of strain rate dependent cyclic stress-strain response and fatigue life in copper," in *Proc. of the 1992 Joint ASME/JSME Conference on Electronic Packaging*, 1992, pp. 813–818.

[131] G. Li, B. G. Thomas, and J. Stubbins, "Modeling creep and fatigue of copper alloys," *Metallurgical and materials transactions A*, vol. 31, no. 10, pp. 2491–2502, 2000.

[132] Z. Wang and R. J. Zhang, "Microscopic characteristics of fatigue crack propagation in aluminum alloy based particulate reinforced metal matrix composites," *Acta metallurgica et materialia*, vol. 42, no. 4, pp. 1433–1445, 1994.

[133] R. Honeycombe, "The plastic deformation of metals, edward arnold (publishers) ltd," *London Google Scholar*, 1968.

[134] E. Ravaioli, V. I. Datskov, V. Desbiolles, J. Feuvrier, G. Kirby, M. Maciejewski, K. A. Sperin, H. H. ten Kate, A. P. Verweij, and G. Willering, "Towards an optimized coupling-loss induced quench protection system (cliq) for quadrupole magnets," *Physics procedia*, vol. 67, pp. 215–220, 2015.

[135] E. Ravaioli, V. Datskov, A. Dudarev, G. Kirby, K. Sperin, H. ten Kate, and A. Verweij, "First experience with the new coupling loss induced quench system," *Cryogenics*, vol. 60, pp. 33–43, 2014.

[136] S. Russenschuck, *Field computation for accelerator magnets: analytical and numerical methods for electromagnetic design and optimization*. John Wiley & Sons, 2011.

[137] "Roxie software," Available from https://espace.cern.ch/roxie/default.aspx.

[138] O. C. Zienkiewicz and R. L. Taylor, *The finite element method for solid and structural mechanics*. Butterworth-heinemann, 2005.

[139] R. A. Johnson, *Advanced euclidean geometry*. Courier Corporation, 2013.

[140] J. Lemaître, J.-L. Chaboche, R. Desmorat, and A. Benallal, "Solid material mechanics," 2004.

[141] M. N. Wilson, "Superconducting magnets," 1983.

[142] A. P. Verweij, "Electrodynamics of superconducting cables in accelerator magnets," CM-P00081075, Tech. Rep., 1995.

[143] G. Morgan, "Theoretical behavior of twisted multicore superconducting wire in a time-varying uniform magnetic field," *Journal of Applied Physics*, vol. 41, no. 9, pp. 3673–3679, 1970.

[144] J. F. Topham, "Fcc-hh beam screen design, eurocircol wp4," Tech. Rep., 2017, Available from: https://indico.cern.ch/event/556692/.

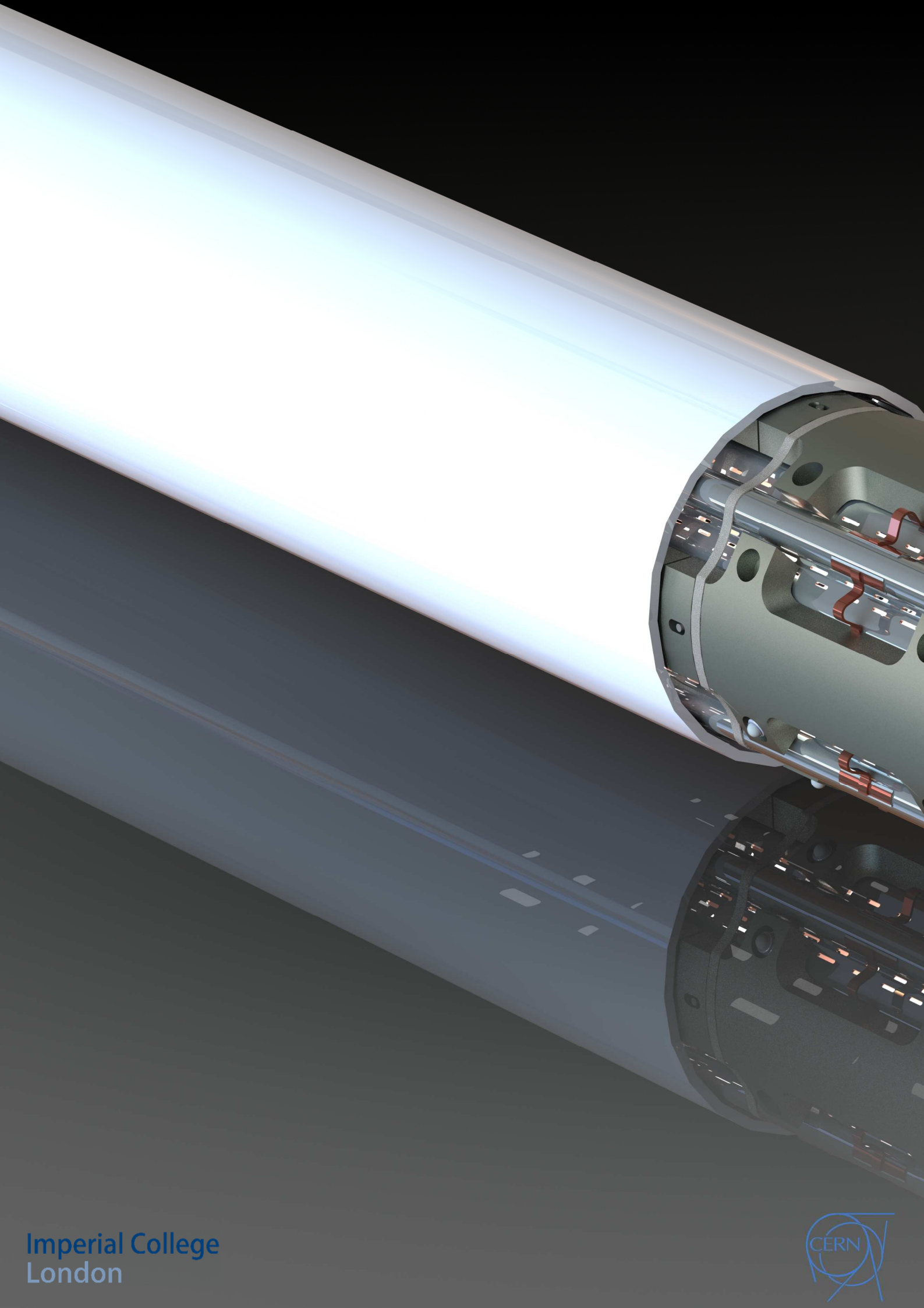
[145] J. F. Topham *et al.*, "Preliminary beam screen and beam pipe engineering design," Cern, Tech. Rep., 2017, Available from :https://fcc.web.cern.ch/eurocircol/Documents/WP4/Milestone

[146] M. Martino, "Recent changes in the HL-LHC powering and WP6B highlights," Cern, Tech. Rep., 2016, Available from: http://indico.cern.ch/event/549979/.

[147] M. Morrone, M. Martino, R. De Maria, M. Fitterer, and C. Garion, "Magnetic frequency response of high luminosity large hadron collider beam screens," *Physical Review Accelerators and Beams*, APS, under review.

[148] F. Sperati, "Effect of the eddy currents induced in the ps vacuum chamber on the magnetic field," Cern, Tech. Rep., 2017, Available from: https://edms.cern.ch/ui/file/1849643.

[149] F. Sperati *et al.*, "Compensation of eddy currents in the ps with PFWs," Tech. Rep., 2017, Available from: https://indico.cern.ch/event/680471/.



Imperial College
London

CERN